Vrije Universiteit Brussel

Doctoral Thesis

Merging Neutrino Astronomy with the Extreme Infrared Sky

A Search for Cosmic Neutrinos from Ultra-Luminous Infrared Galaxies with the IceCube Observatory

Author:
Pablo Correa Camiroaga

Promotor:
Prof. Dr. Nick van Eijndhoven

Co-promotor:
Prof. Dr. Krijn D. de Vries

A thesis submitted in fulfillment of the requirements for the degree of Doctor of Sciences

in the

Sciences & Bio-Engineering Sciences
Interuniversity Institute for High Energies

September 2022

Doctoral examination commission:

Chair: Prof. Dr. Jorgen D'Hondt
Interuniversity Institute for High Energies – Vrije Universiteit Brussel

Secretary: Prof. Dr. Stijn Buitink
Interuniversity Institute for High Energies – Vrije Universiteit Brussel

Promotor: Prof. Dr. Nick van Eijndhoven
Interuniversity Institute for High Energies – Vrije Universiteit Brussel

Co-promotor: Prof. Dr. Krijn D. de Vries
Interuniversity Institute for High Energies – Vrije Universiteit Brussel

Internal faculty member: Prof. Dr. Dominique Maes
Department of Bio-Engineering Sciences – Vrije Universiteit Brussel

External expert: Prof. Dr. Mauricio Bustamante
Niels Bohr Institute – University of Copenhagen

External expert: Prof. Dr. Anna Franckowiak
Faculty of Physics and Astronomy – Ruhr University Bochum

External expert: Prof. Dr. Annarita Margiotta
Department of Physics and Astronomy – University of Bologna

Credit cover art: NASA/ESA & IceCube/NSF.

Dedicado a mi abuela
y a todos con quien he compartido una risa

Voor mijn oma
en voor iedereen met wie ik een lach heb gedeeld

À ma grand-mère
et à tous ceux avec qui j’ai partagé un rire

To my grandmother
and to everyone with whom I shared a laugh

Abstract

The field of neutrino astronomy was born in 2013 when a diffuse flux of high-energy astrophysical neutrinos was discovered by the IceCube Neutrino Observatory at the South Pole. So far, only a few hints have been reported for possible sources of these high-energy neutrinos, such that their origin remains largely unidentified. A promising class of neutrino-source candidates consists of ultra-luminous infrared galaxies (ULIRGs). With infrared luminosities exceeding 10^{12} solar luminosities in the wavelength range 8–1000 μm, these spiral-galaxy mergers are the most luminous object in the infrared sky. ULIRGs are mostly powered by starbursts that produce an equivalent of over 100 solar masses per year, and active galactic nuclei (AGN) can yield secondary contributions to the infrared luminosity of these sources. Both starburst regions and AGN constitute promising environments for the production of high-energy neutrinos.

This thesis presents a novel IceCube study searching for high-energy neutrinos from ULIRGs. First, a dedicated selection of 75 ULIRGs, distributed over the full sky, is made using three catalogs based on data of the Infrared Astronomical Satellite (IRAS). This selection yields a representative sample of the local ULIRG source population within a redshift $z \leq 0.13$. Second, 7.2 years of high-quality IceCube data is used for the search for high-energy astrophysical neutrinos from this ULIRG sample. For this purpose, a stacking analysis is developed to enhance the sensitivity for a small signal of ULIRG neutrinos in data that is dominated by atmospheric backgrounds.

No high-energy neutrinos from ULIRGs are identified in the stacking search. These null results allow to set upper limits on the neutrino flux from the selection of 75 ULIRGs. Moreover, these results are extrapolated to upper limits on the diffuse neutrino flux of the full ULIRG source population accumulated over cosmic history. As such, the first ever constraints are set on the contribution of ULIRGs to the diffuse astrophysical neutrino flux detected by IceCube. For an $E_\nu^{-2.5}$ neutrino energy spectrum, the ULIRG contribution to the diffuse neutrino flux is restricted to $\lesssim$10% at 90% confidence level. In addition, these limits are used to constrain several model predictions of high-energy neutrino emission from ULIRGs, providing novel insights into the high-energy astrophysics of these sources.

Samenvatting

In 2013 rapporteerde het IceCube Neutrino Observatorium aan de Zuidpool de ontdekking van hoogenergetische astrofysische neutrino's. Sindsdien heeft IceCube een diffuse flux van deze neutrino's waargenomen, maar blijft hun oorsprong grotendeels onbekend. Ultra-heldere infraroodstelsels (ULIRGs) vormen een veelbelovende bronklasse die de huidige neutrino-observaties zou kunnen verklaren. Deze interagerende sterrenstelsels hebben een karakteristieke infraroodhelderheid die meer dan 100 keer groter is dan de totale helderheid in elektromagnetische straling uitgestraald door ons eigen melkwegstelsel. Het gigantische vermogen van ULIRGs is voornamelijk te wijten aan de vorming van 100 zonsmassa's aan sterren per jaar. Bovendien kan een supermassief zwart gat dat actief materie opslorpt (AGN) een tweede contributie geven aan de infraroodhelderheid. De extreme stervorming en AGN creëren ideale omgevingen waarin hoogenergetische neutrino's geproduceerd kunnen worden.

Dit proefschrift omvat een eerste IceCube zoektocht naar hoog-energetische neutrino's afkomstig van ULIRGs. Eerst wordt een selectie van 75 ULIRGs gemaakt, die voornamelijk gebaseerd is op data van de infraroodsatelliet IRAS. Deze selectie is representatief voor de volledige bronpopulatie van ULIRGs binnen een roodverschuiving $z \leq 0.13$. Vervolgens wordt een IceCube analyse opgesteld om hoogenergetische neutrino's te identificeren die afkomstig zijn van deze 75 geselecteerde ULIRGs. Hiervoor wordt kwaliteitsvolle IceCube data gebruikt, die geregistreerd werd tussen 2011–2018. Bovendien wordt de cumulatieve neutrinoflux van ULIRGs onderzocht in plaats van elke bron apart te analyseren. Deze methode optimaliseert de gevoeligheid van de analyse om een signaal van ULIRG neutrino's waar te nemen in de data, die gedomineerd wordt door atmosferische achtergronden.

Er worden geen hoogenergetische astrofysische neutrino's van ULIRGs geïdentificeerd in deze analyse. Desondanks kan dit resultaat gebruikt worden om nooit eerder bepaalde limitien te plaatsen op de neutrino-emissie van deze bronnen. In het bijzonder worden er limieten geplaatst op de contributie van de volledige populatie van ULIRGs aan de diffuse neutrino observaties van IceCube. Indien ULIRGs neutrino's zouden produceren volgens een $E_\nu^{-2.5}$ energiespectrum, dan kan deze bronklasse $\lesssim$10% van de diffuse IceCube observaties verklaren met een betrouwbaarheidsniveau van 90%. Bovendien levert dit resultaat beperkingen op voor verschillende modellen die hoogenergetische neutrino's van ULIRGs voorspellen. Op deze manier worden er nieuwe inzichten verworven in de hoogenergetische astrofysica van deze objecten.

Acknowledgments

I vividly recall my very first physics lecture on classical mechanics at the VUB, ten years ago. I remember sitting there, looking at our professor Alex Sevrin solving differential equations of motion, and thinking to myself: *What the hell have I done?* And here I am. A decade later, writing the final words of a PhD thesis that will conclude my current VUB/IIHE journey, and therefore close a significant chapter of my life. During these five PhD years, I was able to perform fundamental research in a young and thriving field that fascinates me. I was able to showcase my work to various audiences, from fellow peers to young future scientists, which also gave me the opportunity to travel all across the world. For that I want to thank the Flemish Research Foundation (FWO), who funded the majority of this PhD project and made many of these experiences possible.

Although I did love the work of my PhD, be it research, teaching, or outreach—the writing not as much though, but let's ignore that—what I will cherish most of these past five years are the wonderful people I have been able to create great memories with, both in and outside of academic circles. Unfortunately, it is impossible for me to acknowledge each and every one of you. That is why I first want to express my immense overall gratitude to everyone that I had the pleasure to share these memories with. Even if you're not really interested in what I do, or if you're just opening this manuscript to read the acknowledgments—trust me, I do too!—thank you for all the good times we had together. Nevertheless, in the following I want to thank some people that have strongly shaped these past five years of my PhD.

Let me start with my supervisors, Nick and Krijn, two Dutch gentlemen who share one thing in particular: a love for cigars accompanied by a smooth cognac! Thank you for all the guidance since my bachelor years, and for supporting and reassuring me whenever I faced any adversity or insecurity. You've always treated me as an equal, which is something that I highly appreciate. Aan jullie allebei: nogmaals heel erg bedankt voor alles! We houden zeker nog contact om toffe fysicaprojecten te bespreken en af en toe een lekkere sigaar op te steken.

Apart from my supervisors, who revised many versions of this manuscript, I would like to thank all members of my PhD jury for thoroughly reading through this work. I have learned a lot from our very pleasant discussions, which have lead to several improvements of this thesis. In particular, I would like to thank Jorgen for teaching me a lot about the political side of academics without loosing sight of the passion for science—and beer. Jorgen, bedankt voor alle gezellige gesprekken in de IIHE keuken, zeker na langedurige (en soms erbarmelijke) faculteitsraden!

Next in line are my amazing colleagues at the VUB and the IIHE in particular. I feel privileged to have spent so many years in such a wonderful work environment, where one thing stands out for me above all: doing science and having fun *can* go hand in hand! This experience would not have been possible without our (ex)-secretaries—Marleen, Sofie, Nina, Merel, and Audrey—and all IT guys behind the scenes that make sure everything works smoothly for us helpless scientists. I also want to thank Freya, with whom I had the pleasure to teach first-year labs, for many insightful lessons about life, education, and academia. Bedankt voor de super toffe en leerrijke samenwerking! And to all the students I have had over the years: thank you for keeping it fun—never forget that you are our future!

Moving deeper into the IIHE dungeon, we find the astroparticle family, whom I have shared many precious moments with, from our small corridor all the way to the Land of the Rising Sun. The infamous vlogs exist thanks to many of you, with which we can relive our beautiful memories—until we get bored of all the memes. Special mentions go to Orazio, Simon, Rose, Quique, Dani, Nadège, Sebastian, Koun, Chris, Giovanni, Gwen, Nico, Mauricio, Ioana, Juanan, Simona, Catherine, Godwin, Uzair: thanks for all the good times! Also much love to all the wonderful IceCubers and Marsala people I met during my travels—you know who you are!

I would like to dedicate some extra words the best office mates ever. Paul, thanks for being such an amazing travel buddy (a.k.a. vlog protagonist) during the four-and-a-half years we spent together—on top of the five years in the same class—and for always being willing to help me out whenever I faced a problem of any kind. Als er iets bestaat dat groter is dan jouw gestalte, dan is het jouw hart! Yarno, it's great to see how far you've come since your bachelor years. You started as my pupil, and ended up being my main boo with whom I had the pleasure to share an office with these last few months. Vergeet nooit: je bent van meer in staat dan je zelf beseft!

Now it's time for me to acknowledge the people that have shaped my life outside of academia. Many of us have shared ecstatic highs and the heartbreaking lows, and your unwavering support means the world to me. First, my old classmates and company: Timmy, Jonas, Jonathan, Daphné, Cynthia, Charlotte, Pieter, Dina, Carlo, Brecht, Marine. Bedankt voor alle gezellige avonden met of zonder gezelschapsspelletjes! Special shout-out to Maurits, thanks for being the best Japan guide ever and remember that I will always love you baby! Second, my friends and roommates Alexandre, Noah, and Viktor—it was an absolute pleasure to spend these years living with you, we had some great times and kept it real during the pandemic! And third, old friends that by now have become fundamental pillars of my life: Filip, Grisha, Anna, Kero, Bram, Laurens, Florian, Marie, Edo, Alec, Odrade, Ruben, Ben, Alexander, and Alessio. Bedankt aan jullie allen voor alle zalige herinneringen, ik kijk uit naar onze toekomstige avonturen!

Finally, I want to express my deepest appreciation for the people that have quite literally shaped my life: my family. Without their love and support, but also *their* hard work and dedication, this PhD would not have been possible, and that's something that I will never forget. Rafa, Nele, Paqui, Nana, Mon, Aiyana, Jeannine, Fabienne, Juan: thanks for always being there and making my life so much richer! A toda la familia en Chile, España, y Vilvoorde, ¡muchísimas gracias por todo vuesto apoyo y amor! And lastly, the people closest to me. Mamá, papá, abuelo, tito, y también abuela: no existen palabras que puedan expresar lo que vosotros significáis para mí. Al fin, éste trabajo no tendría mucho valor personal si no fuera por ustedes. Gracias por todo, os quiero con todo mi corazón. Y ahora, ¡a pasárselo bien!

One last time, thanks to all of you from the bottom of my heart, even to those who caused me to be at my lowest points during these years. In the end, it's part of life; time goes on, and there's no point in lingering thoughts about such unpleasant experiences. I will always aim to cherish the good moments we shared. But to end on a high note, we're all here to make the best of life. Thanks to vast majority of you, my life has been truly amazing and I'm sure there's still a lot of that to come! Love you all, now let's go and have some fun baby!

Contents

List of Constants and Units

Unit	Symbol	Conversion to SI units
Astronomical unit	AU	1.500×10^{11} m
Barn	b	10^{-28} m^2
Electronvolt	eV	1.602×10^{-19} J
Erg	erg	10^{-7} J
Gauss	G	10^{-4} T
Hour	h	3.6×10^{3} s
Jansky	Jy	10^{-26} W m^{-2} Hz^{-1}
Lightyear	ly	9.460×10^{15} m
Parsec	pc	3.086×10^{16} m
Photoelectron	PE	1.602×10^{-19} C
Year	yr	3.154×10^{6} s

Non-SI units

Physical constant	Symbol	Value
Elementary charge	e	1.602×10^{-19} C
Hubble constant	H_0	67.8 km s^{-1} Mpc^{-1}
Planck constant	$h \equiv 2\pi\hbar$	6.626×10^{-34} J s
Solar mass	$M_\odot$	1.988×10^{30} kg
Solar luminosity	$L_\odot$	3.828×10^{26} W
Speed of light in vacuum	c	3.000×10^{8} m s^{-1}

Physical constants

List of Acronyms

Acronym	Full name
AGN	**A**ctive **G**alactic **N**ucleus
BDT	**B**oosted **D**ecision **T**ree
BL Lac	**BL Lac**ertae
CC	**C**harged **C**urrent
CDF	**C**umulative **D**istribution **F**unction
CMB	**C**osmic **M**icrowave **B**ackground
CL	**C**onfidence **L**evel
CR	**C**osmic **Ray**
DAQ	**D**ata **AQ**uisition
DIS	**D**eep **I**nelastic **S**cattering
DOM	**D**igital **O**ptical **M**odule
EBL	**E**xtragalactic **B**ackground **L**ight
EGB	**E**xtragalactic **G**amma-ray **B**ackground
GFU	**G**amma-ray **F**ollow-**U**p
GRB	**G**amma-**R**ay **B**urst
GZK	**G**reisen **Z**atsepin **K**uzmin
FSRQ	**F**lat-**S**pectrum **R**adio **Q**uasar
HAGS	**HA**dronically-powered **G**amma-ray Galaxie**S**
HESE	**H**igh-**E**nergy **S**tarting **E**vents
HLC	**H**ard **L**ocal **C**oincidence
ICL	**I**ce**C**ube **L**ab
IGRB	**I**sotropic **G**amma-**R**ay **B**ackground
IR	**I**nfra**R**ed
LED	**L**ight **E**mitting **D**iode
LIRG	**L**uminous **I**nfra**R**ed **G**alaxy
MC	**M**onte **C**arlo
MPE	**M**ultiple **P**hoto**E**lectron
NC	**N**eutral **C**urrent
PDF	**P**robability **D**ensity **F**unction
PMT	**P**hoton **M**ultiplier **T**ube
PnF	**P**rocessing a**n**d **F**iltering
PS	**P**oint **S**ource
SFG	**S**tar-**F**orming **G**alaxy
SFR	**S**tar-**F**ormation **R**ate
SLC	**S**oft **L**ocal **C**oincidence

Main abbreviations
(excluding names of experiments, source catalogs, and software)
(Continued on next page)

Acronym	Full name
SMBH	**S**uper**M**assive **B**lack **H**ole
SMT	**S**imple **M**ultiplicity **T**rigger
SNR	**S**uper**N**ova **R**emnant
SoB	**S**ignal **o**ver **B**ackground
SPE	**S**ingle **P**hoto**E**lectron
sps	**s**amplings **p**er **s**econd
TDE	**T**idal **D**isruption **E**vent
TS	**T**est **S**tatistic
UHE	**U**ltra-**H**igh **E**nergy
UHECR	**U**ltra-**H**igh-**E**nergy **C**osmic **R**ay
ULIRG	**U**ltra-**L**uminous **I**nfra**R**ed **G**alaxy
UV	**U**ltra**V**iolet
VHE	**V**ery-**H**igh **E**nergy

Main abbreviations
(excluding names of experiments, source catalogs, and software)

Preface

High-energy astrophysical neutrinos were discovered by the IceCube Neutrino Observatory in 2013—the only fully-operational 1-km^3 optical neutrino telescope currently in existence—marking the birth of neutrino astronomy. This young field has grown significantly over the past decade, thanks to the characterization of this diffuse astrophysical neutrino flux. However, one of the major questions in neutrino astronomy is yet to be answered: *Where do high-energy astrophysical neutrinos come from?* Recent studies have found first hints for potential sources of neutrinos, although their origin remains largely unknown. In fact, after 10 years of observations, various constraints have been set on the sources that could be responsible for the diffuse astrophysical neutrino flux. The current status of neutrino astronomy, and how it fits within the overarching fields of astroparticle physics and multimessenger astronomy, is reviewed in Chapter 1.

In this thesis, an IceCube search is performed for astrophysical neutrinos originating from ultra-luminous infrared galaxies (ULIRGs). These are the most luminous astrophysical objects in the infrared sky. Not only are ULIRGs promising neutrino-source candidates, but their neutrino emission has not been constrained in previous studies. In principle, the ULIRG source class as a whole could be responsible for the diffuse astrophysical neutrino flux observed by IceCube. The properties of ULIRGs and possible neutrino emission mechanisms are outlined in Chapter 2. In addition, a dedicated selection of ULIRGs is performed, which lays the foundation for the IceCube analysis of this work.

Chapter 3 is dedicated to the IceCube experiment and how it functions as an optical-Cherenkov neutrino telescope. The various types of detection patterns are covered, as well as the main backgrounds for studies of astrophysical neutrinos. Particular attention is devoted to tracks, which are the events in IceCube that yield the best angular resolution, making them ideal for neutrino-source studies. A detailed description is therefore given of the GFU dataset, which consists of high-quality IceCube tracks that are used for the analysis in this work. A short comparative study is also presented between the GFU sample and another dataset that is widely used in neutrino-source searches with IceCube.

The statistical analysis used to search for high-energy neutrino from the selected ULIRGs is described in Chapter 4. More specifically, a stacking analysis is developed, where the contribution of ULIRGs to the analysis is given a weight based on their observed infrared flux. The performance of the stacking analysis is tested using simulations. In particular, sensitivities are computed for neutrino emission from the selection of ULIRGs under consideration in this work. Furthermore, the first compatibility check is presented between two software packages used in IceCube searches in the context of a stacking analysis.

Finally, Chapter 5 presents the results of the IceCube stacking search for high-energy neutrinos from the selection of ULIRGs using the GFU data sample. Null results are reported, and upper limits are computed on the neutrino flux originating from the ULIRG selection. Systematic effects on these results are investigated, and the neutrino energy range covered by the upper limits is also determined. Moreover, the results are extrapolated to upper limits on the diffuse neutrino flux of the full population of ULIRGs over cosmic history. As such, the first ever constraints are obtained on the contribution of ULIRGs to the diffuse IceCube observations. On top of that, these upper limits are used to constrain several model predictions of neutrinos from ULIRGs.

The scientific efforts of this work have been published in a peer-reviewed article [1] and several conference proceedings [2–5]. Therefore, the reader should be aware that some passages in this thesis will strongly resemble the content of these publications. As a last remark, it should be noted that all cosmological computations in this thesis use the 2015 results of the *Planck* mission for a ΛCDM cosmology [6].

Chapter 1

Neutrino Astronomy in the Multimessenger Era

> *Somewhere, something incredible is waiting to be known.*
>
> **— Carl Sagan**

Introduction

Astronomy finds its origins at the dawn of human civilization. Although for several millennia the study of the night sky was limited to observations of electromagnetic radiation, the past decade saw major breakthroughs in modern astronomy with the discovery of high-energy astrophysical neutrinos and gravitational waves in 2013 and 2015, respectively [7–9]. These discoveries opened up new windows to the Universe that complement the photon sky. A gravitational-wave signal was observed in coincidence with photons from the neutron-star merger GW170817 in August 2017 [10, 11]. Roughly one month later, a high-energy neutrino was observed in coincidence with photons originating from the blazar TXS 0506+056 [12, 13]. These observations marked the birth of multimessenger astronomy, the study of the Universe through the combination of different cosmic messengers—photons, neutrinos, gravitational waves, and cosmic rays.

Cosmic rays[1] were actually the first extraterrestrial particles to be observed other than photons, as they are in fact charged atomic nuclei.[2] They were discovered by Hess in 1912 [15], from which the field of astroparticle physics emerged.[3] With energies reaching[4] 10^{20} eV ≈ 16 J, they are the most energetic particles ever to be detected. However, because cosmic rays carry an electric charge, they are deflected by magnetic fields on their trajectory through space (Figure 1.1). Consequently, they do not point back to their source when observed at Earth, and their origin thus remains an unsolved mystery. Fortunately, cosmic rays are expected to interact within their source environments, producing gamma rays (high-energy photons) and neutrinos, which do not carry an electric charge and therefore point back to their source. Gamma rays, however, are not solely produced in processes involving cosmic rays,

[1] The term "cosmic ray" stems from the fact that they were originally believed to be some form of electromagnetic radiation.

[2] Generally, cosmic rays can also refer to charged (anti)leptons and antinuclei that reach Earth from space, but these will not be considered in this work. See [14] and references therein for more details.

[3] Photons, like all quanta, possess both particle and wave characteristics. However, in 1912 the idea of wave-particle duality was not yet confirmed, such that astronomical observations relied solely on the wave properties of electromagnetic radiation. Only in later years, astronomers started to exploit the particle characteristics of light, especially at higher energies (X-rays and gamma rays).

[4] It is remarkable that a *microscopic* particle can possess an energy that is typical for *macroscopic* scales. As a reference, 16 J is the kinetic energy of a tennis ball with a mass of 50 g crossing the net at a velocity of 90 km hr^{-1}.

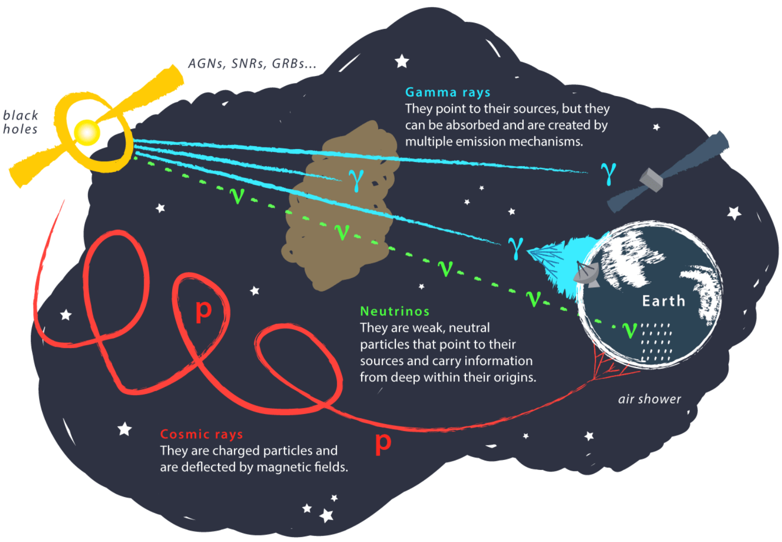

FIGURE 1.1: An illustration of the multimessenger connection between cosmic rays, gamma rays, and neutrinos, taken from [16]. Cosmic rays (in this case a proton) that escape their source are deflected by magnetic fields on their trajectory to Earth, since they possess an electric charge. Some cosmic rays are expected to interact within their source environment before escaping, producing gamma rays and neutrinos, which are not electrically charged. Gamma rays can be attenuated by matter or radiation before reaching Earth, and are not uniquely produced in cosmic-ray interactions. High-energy neutrinos are the ideal smoking-gun signature of cosmic-ray interactions, as they are solely produced in such processes and reach Earth unattenuated.

and they can also be attenuated by matter and radiation on their path to Earth. High-energy neutrinos, on the other hand, are uniquely produced in cosmic-ray interactions, and they propagate through the Universe unhindered. Thus, neutrinos are the ideal smoking-gun signature of cosmic-ray sources, as illustrated in Figure 1.1.

This Chapter provides a brief review of the latest advances in neutrino astronomy, which is the main field in which this work is situated. Section 1.1 gives more details on where neutrinos fit in the overarching multimessenger picture, by discussing their connection with cosmic rays and gamma rays in more detail. Note that gravitational waves will not be considered in the remainder of this thesis. Next, the measurements of diffuse high-energy cosmic neutrinos are presented in Section 1.2, whereas the discussion on their astrophysical sources is reserved for Section 1.3. Finally, to conclude this review, Section 1.4 provides a look into the future prospects for neutrino astronomy and how the field might develop over the coming decades.

For a brief introduction into some of the conventions used in this work regarding astronomy and astroparticle physics, the reader is referred to Appendix A. Furthermore, Appendix B outlines some basic nomenclature of particle physics that is relevant to this thesis.

1.1 The High-Energy Multimessenger Connection

1.1.1 Cosmic Rays and their Origin

Energy Spectrum

At the lowest energies, below about 10 GeV, **cosmic rays** (CRs) originate from within the heliosphere [14], which is the region in space under direct influence of the solar magnetic field. However, the cosmic rays of interest to this work are those with energies (many times) higher than 10 GeV, which find their origin somewhere outside the Solar System. Observations of these extrasolar cosmic rays cover a vast energy range, from 10 GeV up to more than 10^{11} GeV, between which the flux of cosmic rays decreases by more than 30 orders of magnitude. Direct detection of cosmic rays is only feasible up to roughly 100 TeV using satellite experiments such as the Alpha Magnetic Spectrometer (AMS) onboard the International Space Station (ISS) [17]. At energies above 100 TeV, the flux of cosmic rays becomes so low that they can only be detected indirectly using ground-based observatories with large detection areas.[5]

Ground-based experiments exploit the fact that Earth's atmosphere acts as a calorimeter for cosmic rays. When a primary cosmic ray penetrates the atmosphere, it will interact with an air molecule and induce a hadronic particle cascade of up to 10^9 secondary particles, which is known as an **extensive air shower** (see Figure 1.1). By measuring the particle footprint of the air shower, as done in for example IceTop [18] (see also Section 3.1) and the surface detectors of both the Pierre Auger Observatory [19] and the Telescope Array [20], one can infer the direction, energy, and composition of the primary cosmic ray. The latter two experiments also use their surface detectors in hybrid with fluorescence detectors [19, 21]—which observe the air shower's longitudinal development—to obtain refined measurements of the primary cosmic-ray energy and direction. Alternatively, the properties of the primary cosmic ray can be measured through the detection of radio waves emitted by the air shower, as done in e.g. AERA [22] and LOFAR [23].

The observed energy spectrum of cosmic rays above 10 TeV is shown in Figure 1.2, which combines data from various ground-based experiments as reviewed in [14]. Note that we observe a *diffuse* flux of cosmic rays, i.e. they have an isotropic distribution on the sky (except at the highest energies, see below). This diffusion is due to (inter)galactic magnetic fields that deflect cosmic rays on their trajectory to Earth. The observed cosmic-ray flux is well-described by a falling power law as a function of energy, $\Phi_{\mathrm{CR}}(E_{\mathrm{CR}}) \propto E_{\mathrm{CR}}^{-\gamma}$ with a spectral index $\gamma \approx 2.7$, up to $\sim 3 \times 10^{15}$ eV [14]. At this energy, several breaks start to emerge in the spectrum; see [24–27] for more detailed discussions. The first spectral break, called the "knee," is observed at $\sim 3 \times 10^{15}$ eV, where the spectrum steepens ($\gamma \approx 3.1$). A second steepening is observed at $\sim 2 \times 10^{17}$ eV, called the "second knee," where the spectral index takes a value $\gamma \approx 3.3$ until reaching the "ankle" at $\sim 5 \times 10^{18}$ eV. At this point, the spectrum hardens ($\gamma \approx 2.5$) until reaching a cutoff around $\sim 5 \times 10^{19}$ eV, after which statistics rapidly become scarce.[6] Cosmic rays with energies exceeding 10^{18} eV are also

[5] The cosmic-ray particle flux at 100 GeV is roughly 1 particle $\mathrm{m}^{-2}\,\mathrm{s}^{-1}$, which can be targeted by satellite detectors with collection areas of $\mathcal{O}(1\ \mathrm{m}^2)$. At 10^{15} eV, the particle flux decreases to about 1 particle $\mathrm{m}^{-2}\,\mathrm{yr}^{-1}$, such that ground-based experiments targeting these energies have a detection area of $\mathcal{O}(1\ \mathrm{km}^2)$. At 10^{18} eV, the particle flux decreases further to approximately 1 particle $\mathrm{km}^{-2}\,\mathrm{yr}^{-1}$, and ground-based experiments targeting ultra-high energies therefore cover an area of $\mathcal{O}(1000\ \mathrm{km}^2)$.

[6] Recent studies [28–30] have found more detailed structures in the anatomy of the cosmic-ray spectrum. Between the knee and second knee, a "low-energy ankle" is observed around $\sim 3 \times 10^{16}$ eV, where $\gamma \approx 2.9$. Between the ankle and the suppression at the highest energies, an "instep" is observed

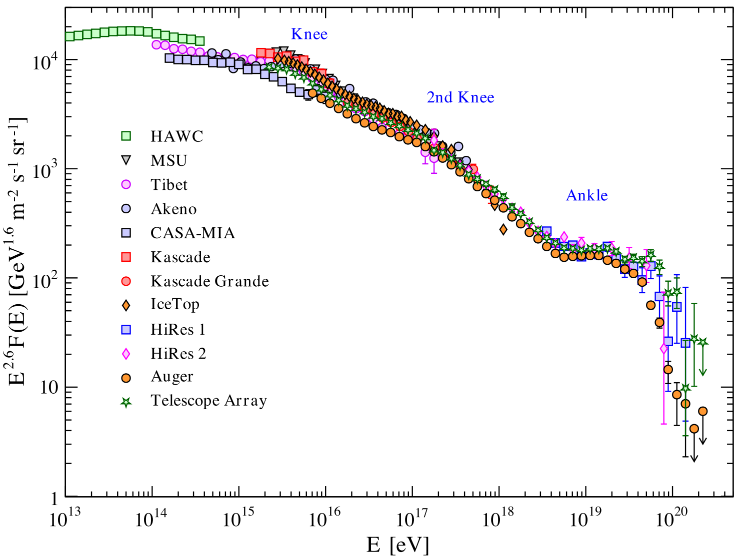

FIGURE 1.2: Cosmic-ray energy spectrum showing data from a variety of ground-based experiments, taken from [14]. The steeply falling particle flux $F(E)$, shown as a function of energy E, is scaled with $E^{2.6}$ in order to highlight the features of the observed broken power-law spectrum, which cuts off at the highest energies. The knee, second knee, and ankle represent the breaks in the spectrum.

known as **ultra-high-energy cosmic rays** (UHECRs; see [31] for a detailed review). To this day, the most energetic UHECR observation dates from 1991, when the Fly's Eye experiment measured the "Oh-My-God particle" at an energy of $(3.2 \pm 0.9) \times 10^{20}$ eV [32].

Source Constraints

Up to the knee, cosmic rays are most likely of galactic origin and thought to be produced in supernova remnants (SNRs) [33, 34]. After they are accelerated, galactic cosmic rays mostly diffuse within the Milky Way, since they are confined by its magnetic field. Furthermore, measurements of the cosmic-ray composition indicate that before the spectral break of the knee, cosmic rays are predominantly protons [35, 36]. Towards the second knee, however, the average cosmic-ray composition shifts more towards iron[7] [35, 36], which can be confined up to higher energies—see also Equation (1.1) later on. A possible interpretation for the knee and second knee is that they correspond to the maximum energies up to which SNRs can accelerate protons and iron nuclei, respectively [33, 34].

The flattening of the cosmic-ray spectrum around the ankle reveals the appearance of a new type of sources capable of accelerating UHECRs. Since UHECRs cannot be contained by the magnetic field of the Milky Way, their sources are most likely extragalactic [33, 34]. This is consistent with an anisotropy study of the observed diffuse UHECR flux above 2×10^{19} eV, which disfavors a fully isotropic UHECR sky [38].

at $\sim 1 \times 10^{19}$ eV, where $\gamma \approx 3.0$. After the suppression, the spectrum can be described with a spectral index $\gamma \approx 5.3$.

[7] Since iron has the largest nuclear binding energy [14], fusing iron nuclei to create heavier elements is not energetically efficient. Consequently, star fusion only produces elements up to iron [37]. After the death of a star, these elements are expelled into the interstellar medium, where they can be accelerated in a cataclysmic event to become the cosmic rays we see on Earth.

Evidence of a 10%-scale anisotropy is presented in [38], which has been associated to the locations of nearby (mostly within 25 Mpc) starburst galaxies.[8] The region between the second knee and the ankle is poorly understood, although it might be interpreted as a transition from galactic to extragalactic sources [41, 42]. Around the ankle, the cosmic-ray composition is again more proton-like, and measurements at the highest energies suggest that the average composition trends towards heavier elements closer to the spectral cutoff [43, 44]. As discussed in [45], this trend in the UHECR composition might indicate that their sources become exhausted, i.e. they have reached their maximum acceleration limit.

Above roughly 6×10^{19} eV, the Universe becomes opaque to UHECRs. At this energy, protons start to interact with cosmic microwave background (CMB) photons—the omnipresent relic radiation of the Big Bang [46]—via the Δ resonance (see Section 1.1.2). This is called the **GZK effect** [47, 48]—named after Greisen, Zatsepin, and Kuzmin—and it reduces the mean free path of the most energetic UHECRs to less than 50 Mpc. Heavier nuclei are also expected to interact with the CMB, causing them to photodisintegrate [49], i.e. their constituent nucleons are torn apart. Whether the cutoff at the end of the cosmic-ray spectrum is influenced by the GZK effect or solely caused by the limiting power of astrophysical sources remains uncertain. The detection of ultra-high-energy neutrinos produced via the GZK effect could resolve this ambiguity, as discussed in Section 1.4.

Although cosmic rays are deflected by magnetic fields and therefore do not point back to their origin, one can impose a general condition on their sources with the following argument. In order to be accelerated, cosmic rays need to be confined to their source environment by a magnetic field with strength B. Under the assumption of a uniform magnetic field, the maximal energy up to which a cosmic ray can be accelerated corresponds to the point where its gyroradius roughly equals the characteristic size R of the accelerator. As such, one obtains the so-called **Hillas criterion** [50, 51],

$$E_{\mathrm{CR,max}} \sim \beta c Z e B R. \tag{1.1}$$

Here, Z is the atomic number of the cosmic ray (Ze is its charge) and $\beta = v/c$ is the bulk velocity of the accelerator medium, discussed below. The Hillas criterion therefore gives an indication of the astrophysical environments that could confine cosmic rays up to a given energy, as shown in Figure 1.3. Furthermore, the maximum confinement energy of heavier nuclei ($Z = 26$ for e.g. iron) is higher than that of protons ($Z = 1$), such that the former can thus be accelerated to higher energies. Note that the Hillas criterion only allows us to identify sources with the right conditions for cosmic-ray acceleration, but it does *not* imply that such acceleration actually takes place in these sources.

[8] Since UHECRs have such high energies, their deflection by magnetic fields can be relatively small, even $\lesssim 1^\circ$ in some cases [39]. Furthermore, only a few bright sources are expected to dominate the UHECR flux above 6×10^{19} eV due to the GZK effect [40]. Hence, with enough statistics, UHECRs are expected to cluster around the locations of their nearby sources on the sky, as discussed in [38].

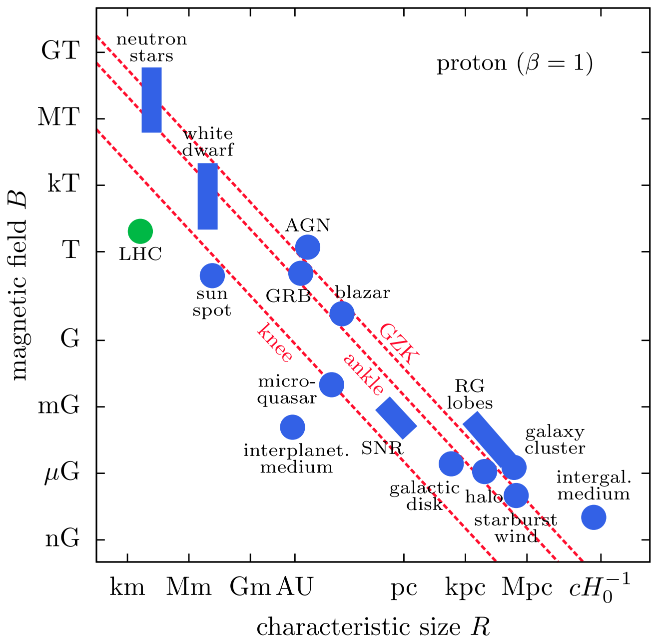

FIGURE 1.3: A rendition of the so-called Hillas plot for a proton ($Z = 1$) and a relativistic shock with velocity $\beta = 1$, adapted from [52]. Note that the scales are logarithmic. The diagonal dashed lines correspond to the Hillas criterion of Equation (1.1) for the characteristic source size R (1 AU = 1.500×10^{11} m; 1 pc = 3.262 ly = 3.086×10^{16} m; $cH_0^{-1} = 1.365 \times 10^{20}$ m) and magnetic field B (1 G = 10^{-4} T) at fixed maximum proton energies corresponding to the knee, ankle, and GZK cutoff (see text and Figure 1.2). The blue circles and squares indicate the typical values of R and B for different astrophysical environments that could host cosmic-ray acceleration sites; the Large Hadron Collider (LHC; green circle) is also shown for reference.

Acceleration Mechanisms

The exact mechanism responsible for the acceleration of cosmic rays is still a matter of active research (see [31] and references therein). The distinct power-law characteristics of the cosmic-ray spectrum indicate that their acceleration cannot occur via purely thermal processes [33]. Moreover, high-energy astrophysical environments are typically ionized plasmas, which cannot sustain electrostatic fields due to the movement of free charges [34]. Instead, it is the bulk motion ($\boldsymbol{\beta}$) of these plasmas and their *magnetic* fields ($\mathbf{B}$) that induce the electric fields ($-\boldsymbol{\beta} \times \mathbf{B}$) required to accelerate charged particles [31]. Such a bulk motion can occur in the form of a shock, i.e. a discontinuity in the plasma that propagates through the interstellar medium at a speed $\beta = v/c$ larger than the ambient speed of sound [53, 54].

Astrophysical shocks are thought to accelerate particles via the **first order Fermi mechanism** [55], in a process known as diffuse shock acceleration. A detailed description of this mechanism falls outside the scope of this work; see e.g. [51, 56–60] for more details. The main idea behind first order Fermi acceleration is that scattering of charged particles allows them to cross the shock front multiple times, thereby gradually gaining energy. In each crossing, the particles have a fixed fractional energy gain proportional to the shock velocity,

$$\frac{\Delta E}{E} \propto \beta. \tag{1.2}$$

Since both the probability for a particle to cross the shock and its fractional energy gain are independent of the particle energy E, i.e. the system is scale-free, diffuse shock acceleration naturally yields a power-law spectrum [61]. For *non-relativistic* shocks ($\beta \ll 1$) [53], the spectrum is given by

$$\frac{\mathrm{d}N}{\mathrm{d}E} \propto E^{-2}. \tag{1.3}$$

Non-relativistic shocks are found to accelerate particles in e.g. supernova remnants (SNRs) [62], which are thought to be the sources of galactic cosmic rays, as mentioned previously.[9] UHECRs, however, are believed to be accelerated in *relativistic* shocks ($\beta \approx 1$) [54], where the first order Fermi mechanism still yields a power law, although the spectral index may vary from $\gamma = 2$ [58]. Examples of sources that could accelerate UHECRs in relativistic shocks are active galactic nuclei (AGN), blazars, gamma-ray bursts (GRBs), and starburst galaxies, as indicated in Figure 1.3 (see also Section 1.3.1).

1.1.2 From Cosmic Rays to Gamma Rays and Neutrinos

To identify the yet unknown sources of cosmic rays and UHECRs in particular, we can exploit the fact that a fraction of cosmic rays will interact within their source environment before being able to escape. One possibility is that the cosmic rays—which for the remainder of this work will implicitly be assumed to be protons (p), as the extrapolation to heavier nuclei is relatively straightforward since they undergo the same interactions—interact with ambient *radiation* via a **photohadronic** ($p\gamma$) **interaction** [63]. This becomes possible once the proton energy E_p exceeds the threshold required to produce a Δ^+ baryon via the Δ-resonance, illustrated in Panel (a) of Figure 1.4. For ultraviolet (UV) photons with an energy $E_\gamma \sim 10$ eV, emitted by e.g. stars, this threshold energy is $E_p \sim 10^{16}$ eV [64], whereas for CMB photons ($E_\gamma \sim 0.6$ meV), the threshold energy is $E_p \sim 6 \times 10^{19}$ eV (i.e. the GZK threshold discussed in Section 1.1.1). Another possibility is that a cosmic ray interacts with ambient *matter*—also assumed to be protons for simplicity—via inelastic **hadronuclear** (pp) **interactions** [65]. In contrast to $p\gamma$-interactions, no high-energy threshold is required for inelastic pp-collisions; in the rest frame of the target matter, inelastic pp-interactions can occur for cosmic-ray energies $E_p \gtrsim 1.2$ GeV. This is illustrated in Panel (b) of Figure 1.4, which also shows that the cross section for pp-interactions is generally a factor 100 larger than the cross section for $p\gamma$-interactions.

The hadronic interactions described above will produce secondary baryons[10] and mesons, which are mostly pions.[11] The decay modes of charged ($\pi^\pm$) and neutral

[9] The fact that the observed cosmic-ray spectrum up to the knee, $E_{\mathrm{CR}}^{-2.7}$, is softer than the expected E_{CR}^{-2} can be understood by considering that cosmic rays have a probability to escape the Milky Way. Such "leaky-box models" find that this leads to an overall softening of the galactic cosmic-ray spectrum consistent with observations [33].

[10] These secondary baryons are typically protons and neutrons. Neutrons will eventually decay via $n \to p\, e^- \,\overline{\nu}_e$, thus producing an antineutrino but with a lower energy compared to those of Equation (1.4). See e.g. [66, 67] for concrete examples.

[11] In pp-interactions, roughly 80% of the mesons are expected to be pions, and most of the remaining 20% are attributed to kaons [68]. In $p\gamma$-interactions, the kaon-to-pion ratio is expected to lie between roughly 0.01–0.1% [63].

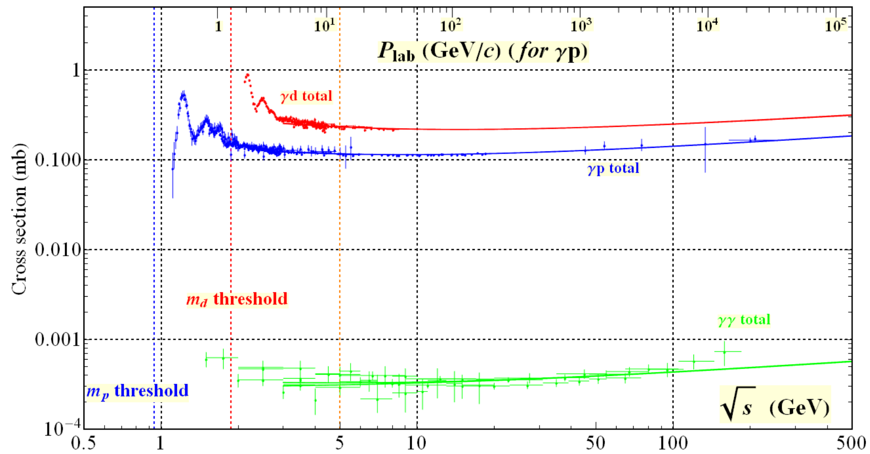

(a) $p\gamma$ and $\gamma\gamma$

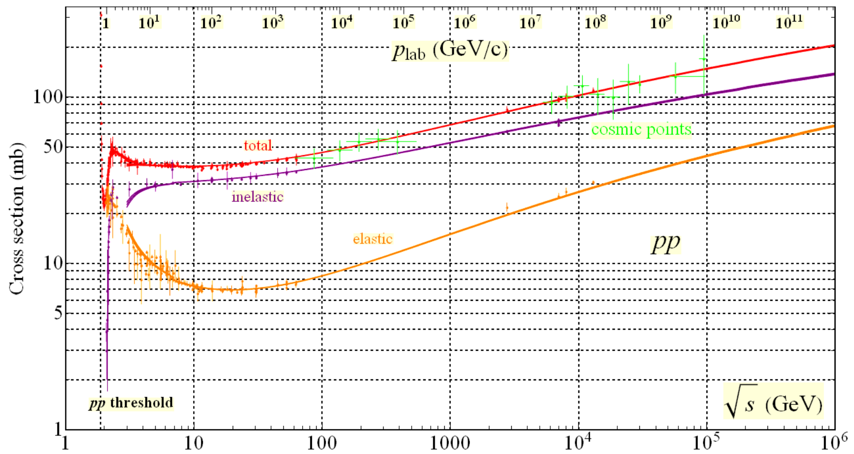

(b) pp

FIGURE 1.4: Total cross sections of proton-proton (pp), proton-photon ($p\gamma$), and photon-photon ($\gamma\gamma$) interactions as a function of the center-of-mass energy $\sqrt{s}$, taken from [14]. Note that 1 mb = 10^{-27} cm^2. Panel (a) shows the total cross sections for $p\gamma$ and $\gamma\gamma$-interactions (γd-processes are not of relevance to this work). The Δ-resonance for $p\gamma$-interactions corresponds to peak at $\sqrt{s} = m_\Delta = 1.23$ GeV. Panel (b) shows the cross section for pp-collisions, indicating both the elastic and inelastic contributions. The $p\gamma$ and pp cross sections are also shown as a function of the momentum p_{lab} of the beam particles—photons ($E_\gamma = p_{\text{lab}}c$) and protons ($E_p \approx p_{\text{lab}}c$ at cosmic-ray energies) in Panels (a) and (b), respectively—shot at a proton target in the lab frame.

pions (π^0) lead to the production of neutrinos and gamma rays, respectively [14]:

$$
\begin{aligned}
&\pi^+ \longrightarrow \mu^+ \nu_\mu \longrightarrow e^+ \nu_e \overline{\nu}_\mu \nu_\mu, \\
&\pi^- \longrightarrow \mu^- \overline{\nu}_\mu \longrightarrow e^- \overline{\nu}_e \nu_\mu \overline{\nu}_\mu, \\
&\pi^0 \longrightarrow \gamma\,\gamma.
\end{aligned}
\tag{1.4}
$$

The electrons and positrons are expected to interact electromagnetically within their source environment and are of no further interest here. However, the gamma rays and neutrinos are capable of escaping the source environments with roughly 10% and 5% of the original cosmic-ray energy, respectively, i.e. $E_\nu \sim E_\gamma/2 \sim E_p/20$ [69,70].

The ratio of charged to neutral pions, $K_\pi \equiv N_{\pi^\pm}/N_{\pi^0}$ with $N_{\pi^\pm} \equiv N_{\pi^+} + N_{\pi^-}$, depends on the type of hadronic interaction. For pp-interactions, $K_\pi \approx 2$ [65], while for $p\gamma$-interactions this ratio lies in the range $1 \lesssim K_\pi \lesssim 3/2$ [63]. This ratio directly influences the relation between the gamma-ray and neutrino fluxes of a source, as well as the neutrino (and antineutrino) flavor composition. In addition, π^+ are created in equal abundance to π^- in pp-interactions [65], whereas $p\gamma$-interactions predominantly produce π^+, i.e. $N_{\pi^\pm} \approx N_{\pi^+}$ [63]. This on its turn affects the ratio of neutrinos to antineutrinos. The flavor ratio and particle-antiparticle ratio at the source influence the corresponding ratios that we observe at Earth, which are subject to neutrino oscillations. More on this topic in Section 1.2.2.

Since neither gamma rays nor neutrinos possess an electric charge, they are not deflected by magnetic fields and thus point back to their source when observed at Earth. However, gamma rays, in contrast to neutrinos, are not uniquely produced in hadronic processes. They can also be produced leptonically via for example inverse Compton scattering.[12] Moreover, gamma rays can be attenuated by matter and radiation on their trajectory, whereas neutrinos travel through the Universe without interacting.[13] Consequently, neutrinos are the ideal smoking-gun signature of cosmic-ray sources, particularly when combined with gamma rays in multimessenger studies. Astrophysical neutrinos are the main cosmic messenger of interest to this work, such that detailed discussions about their observations and candidate sources are reserved for Sections 1.2 and 1.3. In the upcoming Section 1.1.3, the observations of gamma rays will be explored briefly.

1.1.3 Gamma-Ray Observations

Gamma rays refer to all photons with energies $E_\gamma > 100$ keV. Up to several 100 GeV, observations of the gamma-ray sky are performed using direct detection techniques, using satellite experiments such as INTEGRAL [71], AGILE [72], and the Large Area Telescope (LAT) as part of the *Fermi* mission [73].[14] Similarly to cosmic rays, the low flux of very-high-energy (VHE) gamma rays, 100 GeV $\leq E_\gamma <$ 100 TeV, and ultra-high-energy (UHE) gamma rays, $E_\gamma \geq 100$ TeV, require us to resort to indirect detection methods using ground-based observatories. However, in contrast to cosmic-ray air showers, which also have a hadronic component, the particle showers induced

[12] In such a process, a high-energy electron scatters off an ambient low-energy photon, boosting it to gamma-ray energies [34].

[13] Of course, there is a probability that a neutrino interacts with matter, because otherwise we would not be able to observe them. However, as discussed in Section 3.1.1, this probability is *very* small. Hence, astrophysical neutrinos propagate through the Universe quasi unharmed, but it also makes their detection a challenging feat.

[14] The *Fermi* satellite also hosts the Gamma-Ray Burst Monitor (GBM) [74] specifically dedicated to observations of GRBs.

by gamma rays are purely electromagnetic (that is, they consist solely of photons, electrons, and positrons). One possible detection method is to measure the particle footprint of these electromagnetic showers with experiments such as HAWC [75] and LHAASO [76], which recently reported the first ever detection of PeV gamma rays [77]. Alternatively, the optical Cherenkov emission of the shower (see also Section 3.1.1) can be observed using imaging air Cherenkov telescopes (IACTs) such as HESS [78], MAGIC [79], and VERITAS [80].

Above $E_\gamma \gtrsim 1$ TeV, the Universe becomes opaque to gamma rays. At these energies, gamma rays can interact with ambient photons of the CMB or the extragalactic background light (EBL)—the cumulative emission of radiation from galaxies across the complete electromagnetic spectrum—reducing their mean free path to less than 100 Mpc [81, 82]. These $\gamma\gamma$-interactions (see Figure 1.4 for their cross section) induce electromagnetic cascades, from which new gamma rays emerge but with lower energies. Hence, the GeV gamma-ray sky is more adequate to study extragalactic cosmic-ray sources, such that the focus here will lie exclusively on *Fermi*-LAT observations. Recall, however, that gamma rays are not unique signatures of hadronic acceleration, and that they can also be attenuated by matter and radiation at their source (see also Section 1.3.3).

As shown in Figure 1.5, most of the observed gamma-ray emission between 10 GeV and 2 TeV originates from within the Milky Way. In order to obtain the cumulative gamma-ray emission of *extragalactic* sources, known as the **extragalactic gamma-ray background** (EGB), the contribution from galactic foreground needs to be subtracted. Figure 1.6 shows the energy spectrum of the EGB between 100 MeV and 820 GeV obtained in [83], which consists of two major contributions. The first contribution is due to resolved gamma-ray sources. The second contribution to the EGB is called the diffuse isotropic gamma-ray background (IGRB), which on its turn can be split in two components. Firstly, the IGRB consists of the gamma-ray emission of unresolved sources. Secondly, the IGRB includes a truly diffuse component of gamma rays cascading down to lower energies due to the aforementioned interactions with the CMB and EBL.

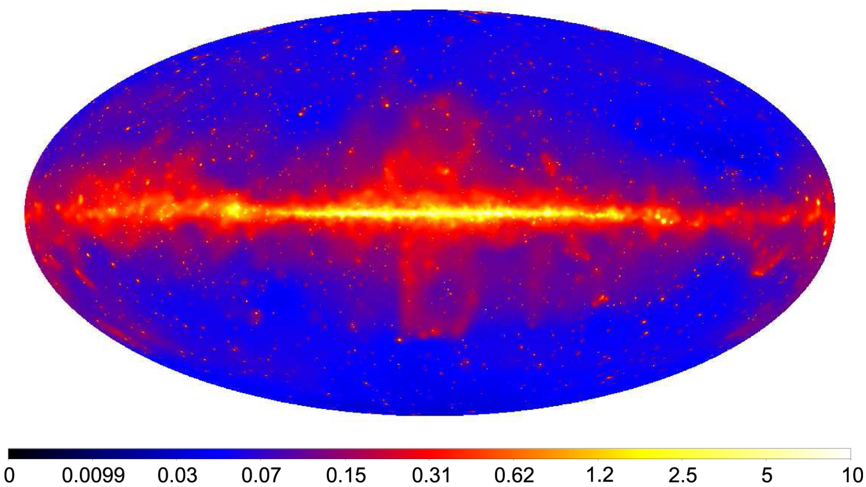

FIGURE 1.5: Gamma-ray skymap observed by *Fermi*-LAT with 7 years of data, taken from [84]. The skymap is presented in galactic coordinates, and the logarithmic color scale is in units of counts per pixel with size $0.1° \times 0.1°$. The structures seemingly emerging from the Galactic Center are also known as the *Fermi* bubbles.

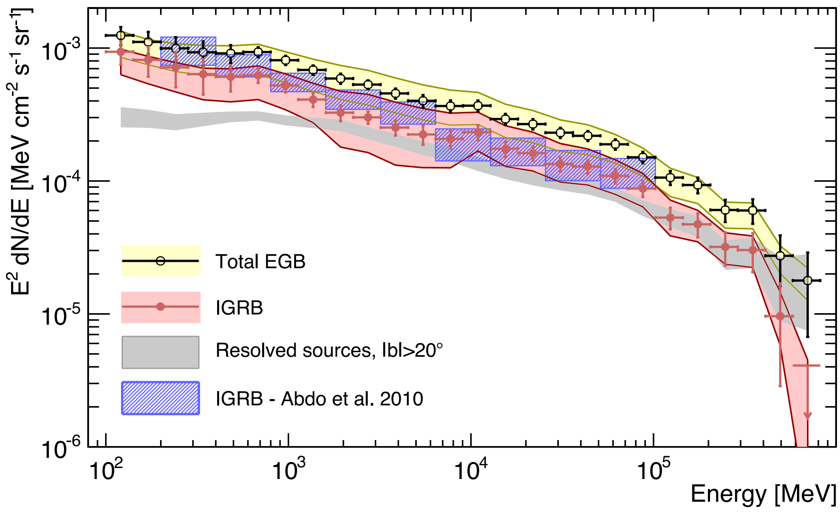

Figure 1.6: The energy spectrum of extragalactic gamma rays as observed with 4.2 years of *Fermi*-LAT data, taken from [83]. Yellow non-filled data points represent the measurements of the total extragalactic gamma-ray background (EGB), whereas the red filled data points are the observations of the isotropic gamma-ray background (IGRB). The corresponding bands indicate the systematic uncertainties due to galactic foreground models. The gray filled band estimates the contribution of resolved gamma-ray sources with a galactic latitude $|b| > 20°$. The blue dashed band indicates IGRB measurements from a previous study [85].

Both the total EGB and IGRB fluxes can be characterized by a power law with an exponential cutoff of the form [83]

$$\Phi_\gamma(E_\gamma) \propto \left(\frac{E_\gamma}{100\ \text{MeV}}\right)^{-\Gamma} \exp\left(-\frac{E_\gamma}{E_\text{cut}}\right). \tag{1.5}$$

As already evident from Figure 1.6, the spectral shapes of the EGB and IGRB are compatible with each other; their respective power-law spectral indices are $\Gamma_\text{EGB} = 2.31 \pm 0.02$ and $\Gamma_\text{IGRB} = 2.32 \pm 0.02$, and their exponential cutoffs are $E_\text{cut,EGB} = (362 \pm 64)$ GeV and $E_\text{cut,IGRB} = (279 \pm 52)$ GeV, respectively. The power-law spectrum reflects the non-thermal origin of the observed gamma-ray emission, while the cutoff corresponds to the point where $\gamma\gamma$-interactions with the CMB and EBL start to significantly attenuate the gamma-ray flux.

Resolved *Fermi*-LAT sources between 50 MeV and 1 TeV can be found in the 4FGL catalog [86,87], whereas the 3FHL catalog [84] specifically targets hard gamma-ray sources with energies between 10 GeV and 2 TeV. In both the 4FGL and 3FHL catalogs, most of the resolved extragalactic sources are **blazars**, which are active galactic nuclei (AGN; see Section 2.1.2) with a relativistic particle jet pointed towards Earth. Blazars therefore dominate the resolved EGB and are also expected to be the main contributors to the IGRB; the estimated blazar contribution to the total EGB is $86^{+16}_{-14}\%$, while secondary contributions are expected from misaligned gamma-ray AGN and star-forming galaxies [83]. Searches for high-energy neutrinos from resolved blazars in the 2LAC catalog [88]—a predecessor of the most recent 4LAC catalog which specifically targets gamma-ray AGN [89]—have constrained the pionic gamma-ray emission from these objects [90] (see Section 1.3.4 for more details). This result suggests that a significant fraction of the extragalactic gamma-ray emission is of leptonic origin. Current observations of gamma rays on their own are therefore not sufficient to pinpoint cosmic-ray sources, although they play an important role in multimessenger studies, as discussed in Section 1.3.

1.2 Diffuse Observations of High-Energy Cosmic Neutrinos

The main cosmic messengers of relevance to this work are **high-energy astrophysical neutrinos**, also known as cosmic neutrinos,[15] in the TeV–PeV range. As mentioned previously, the unique characteristics of the neutrino—chargeless and not attenuated by matter or radiation—make them ideal to study and identify cosmic-ray sources. To this date, high-energy astrophysical neutrinos have only been observed and characterized by the 1-km^3 IceCube Neutrino Observatory at the South Pole. Consequently, the remainder of this review Chapter will primarily be focused on IceCube results.

The IceCube experiment is extensively described in Chapter 3, although some introduction is required here for the upcoming discussions. IceCube is an in-ice optical-Cherenkov telescope sensitive to neutrinos with energies between 100 GeV and 10 PeV. Cherenkov radiation is emitted by secondary particles produced in charged-current (CC) or neutral-current (NC) interactions of neutrinos with the ice or underlying bedrock. The Cherenkov patterns in the detector can be classified into two major topologies, i.e. tracks, which are characteristic for ν_μ interacting via the CC channel, and single cascades, which are produced in CC interactions of ν_e and ν_τ and NC interactions of all flavors. At the highest energies, however, ν_τ can produce double cascades via the CC channel. Since IceCube cannot distinguish astrophysical neutrinos from antineutrinos (except in a very specific case, discussed in Section 1.2.1), the term "neutrino" generally refers to both henceforth.

Tracks have an elongated topology and therefore a good angular resolution ($\lesssim 1°$ above 1 TeV), such that they are most adequate for neutrino-source studies (Section 1.3). However, they are typically not contained within the detector volume, such that the neutrino energy resolution obtained with tracks is poor (roughly a decade in energy). Cascades, on the other hand, have a rather spherical topology, thus resulting in a poor angular resolution ($\gtrsim 8°$). Nevertheless, they are typically contained within the detector volume, resulting in a neutrino energy resolution of $\gtrsim 15\%$. Note that this value corresponds to the resolution of the *deposited* energy in IceCube, a quantity that is also quoted in terms of the equivalent deposited charge, which has units of detected photoelectrons (PE).

Most of the detection rate in IceCube—each individual detection is called an event—is due to atmospheric muons (2.7 kHz) and atmospheric neutrinos (of the order of a few mHz), which are both produced in cosmic-ray air showers. Atmospheric muons only reach IceCube from the Southern Hemisphere, whereas atmospheric neutrinos form a background over the full sky. Note that atmospheric muons traversing the detector are characterized by (downgoing) track signatures. One of the main challenges in the study of astrophysical neutrinos (which have a detection rate of the order of a few μHz) is to reduce the overwhelming atmospheric background, as discussed in the following.

[15] *Cosmic* neutrinos should not be confused with *cosmogenic* neutrinos, which are produced via the GZK effect. See Section 1.4 for more details.

1.2.1 Energy Spectrum of the Diffuse Neutrino Sky

List of Diffuse IceCube Analyses

The **diffuse high-energy astrophysical neutrino flux** has been measured in several independent IceCube studies, which apply different strategies to reduce the overwhelming atmospheric-muon background. Atmospheric neutrinos, however, form an irreducible background, although they have a relatively soft energy spectrum ($E_\nu^{-3.7}$). Consequently, diffuse analyses typically target energies $E_\nu \gtrsim 10$ TeV, where the harder astrophysical neutrino spectrum becomes distinguishable from the atmospheric neutrino background. Below, a short description is given of the different analyses that contribute to the diffuse observations:

- **High-Energy Starting Events (HESE) [91].** The HESE analysis focuses on high-energy events (with a total deposited charge $Q_{\text{tot}} > 6{,}000$ PE) with a neutrino interaction vertex that lies well within the detector volume. To achieve this, the outer parts of IceCube are used as a veto layer, which efficiently rejects atmospheric muons. The resulting event selection (starting tracks and contained cascades) spans 7.5 years of data between 2010–2017, covers the whole sky, and contains astrophysical neutrinos of all flavors with $E_\nu > 60$ TeV. The 7.5-yr HESE measurements are shown in Panel (a) of Figure 1.7. Note that the original HESE analysis using 3 years of data was the one that lead to the discovery of astrophysical neutrinos in 2013, where a background-only scenario was already rejected with a significance of[16] 5.7σ [7, 8].

- **Throughgoing tracks [92].** This analysis focuses exclusively on track-like events in the Northern Sky, where there is no background contamination of atmospheric muons. The benefit of using tracks is that the effective volume of IceCube is larger for this type of events, since the neutrino interaction vertex does not need to be inside the instrumented volume for a track to go through IceCube. Consequently, a relatively large number of events can be collected for the analysis.[17] Panel (b) of Figure 1.7 shows the corresponding astrophysical muon neutrino observations for $E_\nu > 15$ TeV in 9.5 years of data between 2009–2018. This analysis rejects a background-only scenario with a significance of 5.6σ.

- **Cascades [93].** To target astrophysical electron and tau neutrinos, this analysis solely considers cascades recorded over the full sky between 2010–2015. These cascades can also be partially contained in the detector volume, which increases statistics significantly and is also one of the main distinctions compared to other studies. Furthermore, atmospheric muons, which generally produce tracks in IceCube, can be excluded based on their topology. Moreover, machine-learning techniques allow to reduce this background significantly down to energies below 10 TeV. The 6-yr all-sky astrophysical cascade measurements reject a background-only hypothesis at a 9.9σ significance level, and they are shown in Panel (c) of Figure 1.7.

[16] In (astro)particle physics, a $\geq 3\sigma$ significance—corresponding to (one-sided) p-value $p \leq 2.70 \times 10^{-3}$—is regarded as evidence, whereas a $\geq 5\sigma$ significance ($p \leq 5.73 \times 10^{-7}$) is required to claim a discovery. Note that the p-value corresponds to the probability that an observation is consistent with the background hypothesis. More on this topic in Chapter 4.

[17] To compare, the 9.5-yr northern-track sample contains about 650,000 events, whereas the 7.5-yr HESE sample contains 102 events, of which only 60 have an energy exceeding 60 TeV. Note that HESE events are given nicknames based on characters of the *Sesame Street* series.

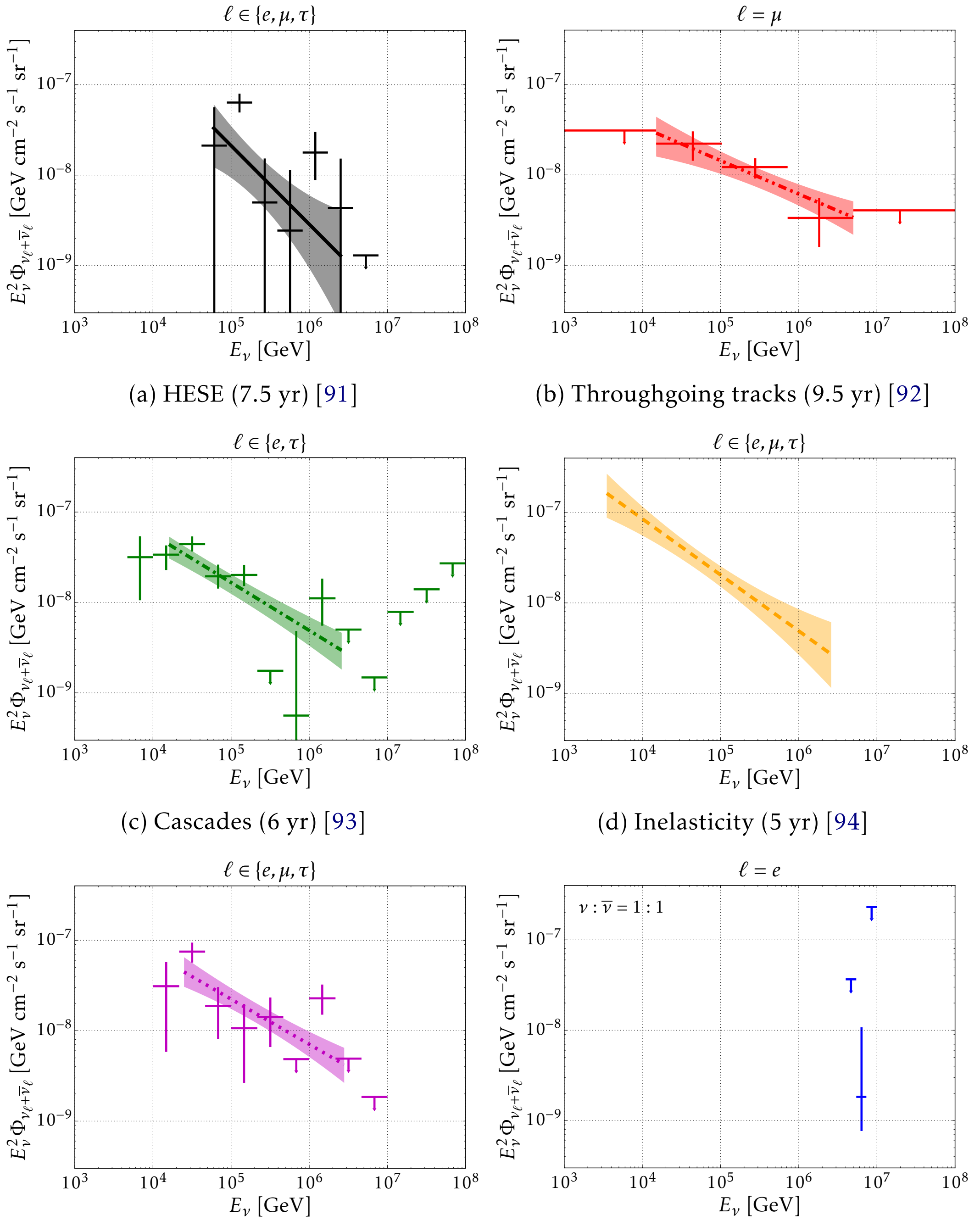

(a) HESE (7.5 yr) [91]

(b) Throughgoing tracks (9.5 yr) [92]

(c) Cascades (6 yr) [93]

(d) Inelasticity (5 yr) [94]

(e) Combined (5 yr) [95]

(f) Glashow (4.6 yr) [96]

FIGURE 1.7: Energy spectra of diffuse high-energy astrophysical neutrinos as measured by IceCube, showing the scaled per-flavor flux $E_\nu^2 \Phi_{\nu_\ell + \overline{\nu}_\ell}$ as a function of neutrino energy E_ν. Each panel corresponds with an independent IceCube analysis (see text for more details). A flavor ratio $(\nu_e : \nu_\mu : \nu_\tau)_E = (1 : 1 : 1)$ at Earth is assumed to compute per-flavor fluxes for all analyses that are sensitive to multiple neutrino flavors $\ell \in \{e, \mu, \tau\}$. The lines indicate the best fits to the IceCube data under an unbroken power-law assumption, and the "butterfly" bands represent the corresponding $\pm 68\%$ confidence regions. Note that the lines do *not* represent fits through the data points, which are differential measurements of the diffuse neutrino flux.

- **Inelasticity [94].** The event selection for this analysis consists of medium-energy starting events (MESE) of all neutrino flavors, and is optimized to study the inelasticity of neutrino interactions with matter (see also Section 3.1.1). The main differences w.r.t. the HESE sample is that more relaxed energy cuts are applied (the total charge cut depends on the charge deposition in the first 3 μs of the event), and that the veto layer is scaled depending on the event energy [97]. As such, this event selection can target cascades and starting tracks down to TeV energies. Panel (d) of Figure 1.7 shows the corresponding astrophysical diffuse-flux measurements using 5 years of all-sky data recorded in the 2011–2016 period.

- **Combined analysis [95].** In this study, the various samples described above are combined between 2008–2013 to perform one global fit to the data including all flavors. The 5-yr combined results of the diffuse astrophysical neutrino flux cover the full sky and are presented in Panel (e) of Figure 1.7.

Diffuse Neutrino Spectra

Practically, in order to obtain diffuse measurements, the above analyses test different hypotheses of the astrophysical neutrino spectrum by fitting several flux models to the IceCube data. These models range from (un)broken power laws with(out) a high-energy exponential cutoff to more elaborate spectral shapes motivated by theoretical predictions (see e.g. [91] for an overview). However, to this date, no model is favored w.r.t. the most simple scenario, i.e. an **unbroken power law** without an exponential cutoff. Consequently, the following discussion will mostly focus on these unbroken power-law fits.

The unbroken power-law parameterization of a per-flavor diffuse astrophysical neutrino flux is given by (see Appendix A for the implied notation)

$$\Phi_{\nu_\ell+\overline{\nu}_\ell} = \phi_0 \left(\frac{E_\nu}{100\ \mathrm{TeV}}\right)^{-\gamma} \times 10^{-18}\ \mathrm{GeV}^{-1}\ \mathrm{cm}^{-2}\ \mathrm{s}^{-1}\ \mathrm{sr}^{-1}, \tag{1.6}$$

where the flux normalization ϕ_0 and spectral index γ are fit parameters, and the flavor is denoted by $\ell \in \{e, \mu, \tau\}$. A per-flavor flux is related to the all-flavor neutrino flux as $\Phi_{\mathrm{all}} \equiv \sum_\ell f_\ell \Phi_{\nu_\ell+\overline{\nu}_\ell}$, where f_ℓ represents the corresponding flavor ratio, with $\sum_\ell f_\ell \equiv 1$. As discussed in Section 1.2.2, current IceCube observations are consistent with flavor equipartition, such that diffuse fits generally set $f_\ell = 1/3$ for all ℓ. This is of particular relevance for analyses sensitive to multiple flavors, since they in fact measure the combined contribution of these flavors. Table 1.1 summarizes the fit parameters of the unbroken power-law measurements performed with the different IceCube analyses described above, which are also shown in Figure 1.8 (with the exception of the combined fit). The corresponding spectra are visualized in Figure 1.7.

As shown in Figure 1.8, the various unbroken power-law measurements are consistent with each other within 2σ (95% confidence level). It is worth noting, however, that there is a rather large spread in spectral-index observations. The throughgoing track analysis yields the hardest spectral index ($\gamma \approx 2.37$), while the HESE analysis measures the softest value ($\gamma \approx 2.87$). At this point in time, it is not completely clear whether this is due to some underlying physics, or a consequence of the distinct methods applied by the different analyses (also in e.g. the treatment of systematic uncertainties). In any case, the most complete measurement is the combined

IceCube analysis	Sky coverage	Flavor	E_ν-range [TeV]	ϕ_0	γ
HESE (7.5 yr) [91]	N + S	e, μ, τ	60–2,500	$2.12^{+0.49}_{-0.54}$	$2.87^{+0.20}_{-0.19}$
TT (9.5 yr) [92]	N	μ	40–3,500	$1.44^{+0.25}_{-0.26}$	$2.37^{+0.09}_{-0.09}$
C (6 yr) [93]	N + S	e, τ	16–2,600	$1.66^{+0.25}_{-0.27}$	$2.53^{+0.07}_{-0.07}$
Inelasticity (5 yr) [94]	N + S	e, μ, τ	3.5–2,600	$2.04^{+0.23}_{-0.21}$	$2.62^{+0.07}_{-0.07}$
Combined (5 yr) [95]	N + S	e, μ, τ	25–2,800	$2.23^{+0.37}_{-0.40}$	$2.50^{+0.09}_{-0.09}$

TABLE 1.1: Summary of the diffuse IceCube analyses, where TT and C stand for throughgoing tracks and cascades, respectively. The respective sky coverage is indicated—where N is Northern Sky and S is Southern Sky—as well as the neutrino flavors to which an analysis is sensitive. The three rightmost columns correspond to the unbroken power-law fits of the astrophysical neutrino flux. The sensitive energy range of the fit is specified, while ϕ_0 and γ are defined in Equation (1.6) as the flux normalization at E_ν = 100 TeV and the power-law spectral index, respectively.

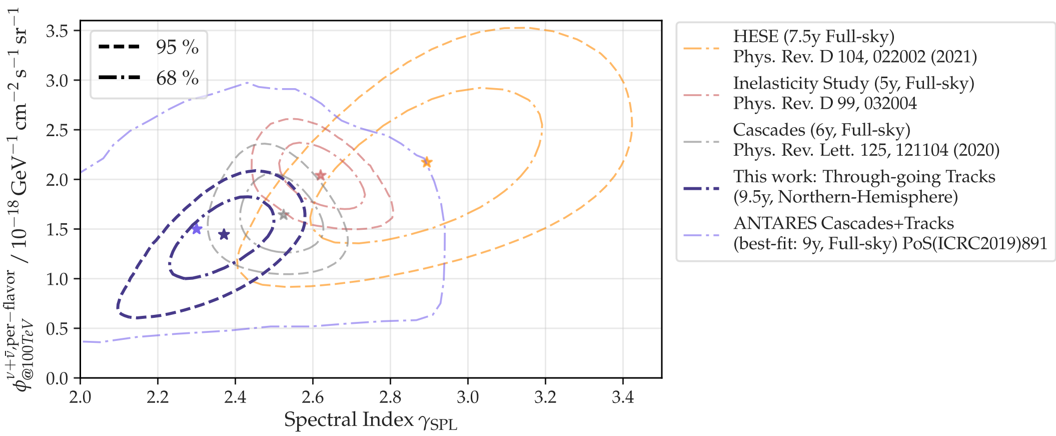

FIGURE 1.8: Parameter space of the fitted single power-law (SPL) models to the diffuse astrophysical neutrino flux, taken from [92]. The fit parameters are the neutrino flux at 100 TeV and the spectral index of the power law. The stars indicate the best-fit values, while the dash-dotted and dashed lines are the contours at 68% and 95% confidence level, respectively. The IceCube measurements correspond to those in Table 1.1. The fit by ANTARES—a 0.01-km^3 neutrino telescope in the Mediterranean Sea—is shown for reference, although it only corresponds to a mild 1.8σ excess above the atmospheric background [98].

global fit, which takes into account all events selections and yields $\gamma \approx 2.5$. However, this global measurement is becoming outdated; efforts are currently underway to perform an updated combined fit in the near future [99].

In addition to unbroken power-law fits, one can also perform **differential flux measurements**[18] of diffuse astrophysical neutrinos, which are the least dependent on a spectral model compared to other fits. Such analyses apply a segmented-fit technique, by splitting their sensitive energy range into bins with a width that depends on the typical energy resolution of the events, which is better for cascades than for tracks. In each bin, Equation (1.6) is fit but with the spectral index fixed to $\gamma = 2.0$, yielding a measurement (or upper limit) of the neutrino flux in that specific bin. Figure 1.7 shows the differential measurements of the diffuse analyses described above.

HESE Skymap of Astrophysical Neutrinos

The diffuse neutrino observations are consistent with an **isotropic flux**. A simple point-source search was performed using the HESE sample, which has a high purity of astrophysical events. This search used similar techniques to those described in Chapter 4, by essentially testing if the HESE events cluster in some position on the sky. The corresponding HESE skymap, which can be regarded as our current picture of the neutrino sky above 60 TeV, is shown in Figure 1.9. No evidence is found for event clustering, and the HESE data is thus consistent with an isotropic measurement of the diffuse astrophysical neutrino flux.

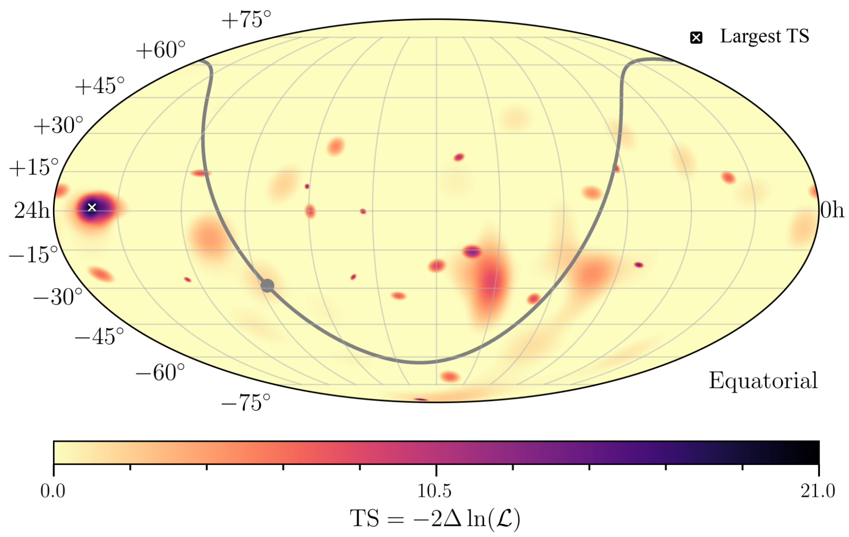

FIGURE 1.9: High-energy neutrino sky observed with the IceCube HESE sample, taken from [91]. The skymap is shown in equatorial coordinates, and the gray line (resp. dot) indicates the Galactic Plane (resp. Galactic Center). The color scale represents a test statistic (TS) that tests for clustering of HESE events on the sky compatible with a point source. No significant TS excesses are observed, and the skymap is consistent with an isotropic neutrino sky.

[18] Note that the diffuse cosmic-ray and gamma-ray fluxes of Figures 1.2 and 1.6 are also differential measurements. See Section 5.1.3 for a more elaborate discussion on the computation of differential fluxes in the context of an IceCube analysis.

First Event at the Glashow Resonance

At an energy of 6.3 PeV, a $\overline{\nu}_e$ becomes capable of producing an on-shell W^- boson via a CC interaction with an atomic electron, which is called the **Glashow resonance**. This process is expected to dominate the overall (anti)neutrino cross section at 6.3 PeV (Section 3.1.1), and thus allows for a measurement of the astrophyscial neutrino-to-antineutrino ratio. A recent study presented the first detection of a cascade, informally known as Gargantua, at the Glashow resonance in 4.6 years of IceCube data[19] [96]. With a *deposited* energy of 6.05 ± 0.72 PeV, Gargantua is the most energetic event observed in IceCube, with a $\sim 5\sigma$ significance for being of astrophysical origin. Moreover, the event is compatible with $E_\nu = 6.3$ PeV after taking into account the expected energy of shower particles that do not radiate Cherenkov emission. For an $E_\nu^{-2.49}$ astrophysical neutrino flux, the significance of Gargantua being a Glashow event is 2.3σ. In any case, under the assumption that neutrinos and antineutrinos are observed in equal amounts, the Gargantua event allows us to extend the spectrum of the astrophysical neutrinos up to 6.3 PeV. This result is shown in Panel (f) of Figure 1.7.

1.2.2 Flavor Composition of High-Energy Astrophysical Neutrinos

Neutrino Oscillations over Astrophysical Scales

The existence of **neutrino oscillations** was confirmed in 1998 using atmospheric-neutrino observations with the Super-Kamiokande experiment [100]. It provides incontrovertible evidence that they have a non-zero (albeit small) mass, which cannot be explained by the Standard Model of particle physics [14]. IceCube provides a unique opportunity to study neutrino oscillations at TeV–PeV energies over astronomical distances by observing the flavor ratios of high-energy astrophysical neutrinos. For the following discussion, only a very brief outline is given on neutrino oscillations, as a detailed description falls beyond the scope of this thesis. Moreover, only the case of the three Standard-Model flavors $\ell \in \{e, \mu, \tau\}$ will be considered. For a review of neutrino oscillations and non-standard neutrino interactions, see [101].

Neutrinos are observed in so-called flavor eigenstates $|\nu_\ell\rangle$ which at a given point in time are related to the mass eigenstates $|\nu_j\rangle$, $j \in \{1,2,3\}$, via

$$|\nu_\ell\rangle = \sum_{j=1}^{3} \mathcal{U}_{\ell j}\, |\nu_j\rangle. \tag{1.7}$$

Here, the so-called PMNS (Pontecorvo–Maki–Nakagawa–Sakata) matrix is given by

$$\mathcal{U} = \begin{pmatrix} c_{12}\,c_{13} & s_{12}\,c_{13} & s_{13}\,e^{-i\delta_{\mathrm{CP}}} \\ -s_{12}\,c_{23} - c_{12}\,s_{23}\,s_{13}\,e^{i\delta_{\mathrm{CP}}} & c_{12}\,c_{23} - s_{12}\,s_{23}\,s_{13}\,e^{i\delta_{\mathrm{CP}}} & s_{23}\,c_{13} \\ s_{12}\,s_{23} - c_{12}\,c_{23}\,s_{13}\,e^{i\delta_{\mathrm{CP}}} & -c_{12}\,s_{23} - s_{12}\,c_{23}\,s_{13}\,e^{i\delta_{\mathrm{CP}}} & c_{23}\,c_{13} \end{pmatrix}, \tag{1.8}$$

where δ_{CP} is a complex phase related to charge-parity (CP) violation,[20] and where terms including the neutrino mixing angles θ_{jk} ($j \neq k \in \{1,2,3\}$) are given by $c_{jk} \equiv$

[19] A dedicated event selection was used for this analysis, which is called the PeV-energy partially contained event (PEPE) sample [96].

[20] CP violation would manifest itself as a difference between the oscillation patterns of neutrinos and antineutrinos [101]. Although currently not observed in the neutrino sector, CP violation does occur in quark mixing [14].

$\cos\theta_{jk}$ and $s_{jk} \equiv \sin\theta_{jk}$. Since there is no evidence for CP violation in the neutrino sector, the CP phase is set to $\delta_{\rm CP} = 0$ in this discussion.

For neutrinos propagating through vacuum, the probability that a neutrino of flavor ℓ and energy E_ν oscillates into a neutrino with flavor $\ell' \in \{e, \mu, \tau\}$ over a baseline length scale L is then given by

$$\mathcal{P}(\nu_\ell \to \nu_{\ell'}) = \delta_{\ell\ell'} - 4 \sum_{j<k} \mathcal{U}_{\ell j} \mathcal{U}^*_{\ell' j} \mathcal{U}^*_{\ell k} \mathcal{U}_{\ell' k} \sin^2\left(\frac{\Delta m^2_{jk} L}{4\hbar c^3 E_\nu}\right). \tag{1.9}$$

Here, $\Delta m^2_{jk} \equiv m_j^2 - m_k^2$ is the squared neutrino mass difference of the mass eigenstates $|\nu_j\rangle$ and $|\nu_k\rangle$, $\delta_{\ell\ell'}$ is a Kronecker delta,[21] and the sum in the second term is negative (resp. positive) if $\ell \neq \ell'$ (resp. $\ell = \ell'$).

Precise measurements of the neutrino mixing angles—see [102, 103] for a recent overview—have been performed with experiments focused on solar neutrinos (θ_{12}), atmospheric neutrinos (θ_{23}), and nuclear-reactor neutrinos (θ_{13}). These observations restrict neutrino masses to[22] $m_j \lesssim 120$ meV/c^2. Thus, given these measurements, the oscillation probability of Equation (1.9) is completely described by the ratio L/E_ν. For astrophysical scales relevant to IceCube, which is sensitive to TeV–PeV astrophysical neutrinos, L lies in the kpc–Gpc range. Since L is therefore much larger than the typical oscillation length,[23] the $\sin^2 x$ term averages out to 1/2 in observations with neutrino telescopes [104]. This is a consequence of the limited energy resolution of these experiments, which cannot discern the energy-dependent oscillation patterns at these scales.

Hints for Astrophysical Tau Neutrinos

A recent analysis of the 7.5-yr HESE sample reported the first evidence of the presence of ν_τ in the astrophysical neutrino flux [105]. This analysis exploits the fact that at the highest energies, the unique double-cascade signature of ν_τ interacting via the CC channel starts to become detectable in IceCube (see Section 3.1.1). The first cascade is due to the CC interaction of the ν_τ within the detector volume. This interaction produces a tau lepton, which travels a distance of roughly 50 m $\times (E_\nu/\text{PeV})$ before decaying [105], thereby producing a second cascade. The two cascades can be distinguished in IceCube if $E_\nu \gtrsim 100$ TeV.

The first-ever candidate ν_τ event observed in [105], nicknamed Double Double, is a double cascade with a vertex separation of 17 ± 2 m. The reconstructed energy of the first and second cascades are ∼9 TeV and ∼80 TeV, respectively. This energy asymmetry provides additional evidence that Double Double is indeed a ν_τ event [106]; the "tauness" of this event—an a posteriori probability of the event to originate from a ν_τ—is found to be ∼98%. Moreover, the study of [105] disfavors a diffuse astrophysical neutrino flux without ν_τ at a significance level of 2.8σ.

[21] The Kronecker delta is defined as $\delta_{ab} = 1$ if $a = b$ and $\delta_{ab} = 0$ if $a \neq b$.

[22] A global fit of neutrino-oscillation experiments yields $|\Delta m^2_{12}| \approx 7.4 \times 10^{-5}$ eV$^2/c^4$ (solar neutrinos) and $|\Delta m^2_{k3}| \approx 2.5 \times 10^{-3}$ eV$^2/c^4$ with $k \neq 3$ (atmospheric neutrinos) [102, 103]. However, the exact ordering of the masses remains unknown. One of the major aims for neutrino experiments in the coming decade is to solve this so-called mass hierarchy problem. The two possibilities are a "normal" ordering, where $k = 1$ and $m_1 < m_2 < m_3$, or an "inverted" ordering with $k = 2$ and $m_3 < m_1 < m_2$.

[23] The oscillation length is given by $L_\pi \equiv 4\pi\hbar c^3 E_\nu / |\Delta m^2_{ij}|$. For $E_\nu = 1$ PeV and $|\Delta m^2_{12}| = 7.4 \times 10^{-5}$ eV$^2/c^4$, one finds $L_\pi \approx 1.1 \times 10^{-3}$ pc.

Flavor Ratio of Astrophysical Neutrino Fluxes

The **flavor ratio** of high-energy neutrinos at an astrophysical source depends on the neutrino production environment, which influences the flavor ratio observed at Earth. However, as shown in [107], for $L/E_\nu \gtrsim 10^{-10}$ pc GeV^{-1} the flavor ratios of the astrophysical neutrino fluxes tend to average out to a single value. In the most generic pp-scenario discussed in Section 1.1.2, where the expected flavor ratio at the source is $(\nu_e : \nu_\mu : \nu_\tau)_S = (1 : 2 : 0)$, neutrino oscillations during propagation change the flavor composition to an average $(\nu_e : \nu_\mu : \nu_\tau)_E \approx (1 : 1 : 1)$ at Earth [107, 108]. This prediction is shown in Figure 1.10, as well as other predictions on the flavor ratio at Earth corresponding to different flavor ratios at the source.[24] In addition, Figure 1.10 indicates the 3σ contour of allowed flavor ratios according to the mixing-angle measurements mentioned above.

Finally, Figure 1.10 shows the measurements of the high-energy astrophysical flavor ratio found in three diffuse IceCube analyses. The HESE measurement, which includes the first candidate ν_τ event, breaks the degeneracy between ν_e and ν_τ observed in the global-fit and inelasticity studies (which contain less years of data).

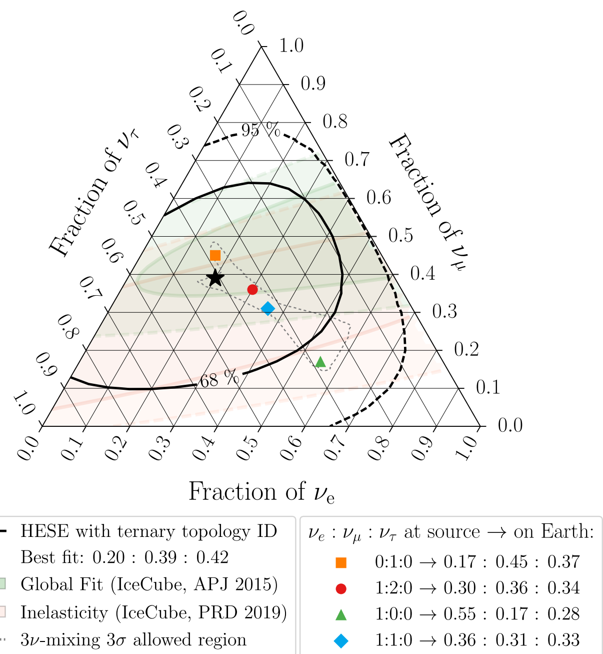

FIGURE 1.10: Flavor triangle of the astrophysical neutrino fluxes observed by IceCube, taken from [105]. Solid and dashed lines correspond to 68% and 95% confidence level contours, respectively. The non-filled black contours correspond to the 7.5-yr HESE analysis—of which the best-fit point is indicated with the black star—whereas filled red and green contours represent the 5-yr global-fit and 5-yr inelasticity measurements, respectively. The dotted line is the 3σ (99.7% confidence level) contour allowed by measurements of the three standard neutrino mixing angles [102, 103]. The remaining symbols show the neutrino-oscillation predictions of the flavor ratio at Earth given different flavor ratios at an astrophysical source.

[24]For example, if the muons in Equation (1.4) interact within their environment before decaying, one finds $(\nu_e : \nu_\mu : \nu_\tau)_S = (1 : 0 : 0)$. This is also known as the damped-muon scenario; see e.g. [109]. In any case, recall that the flavor ratio at the source depends on the charged-to-neutral pion ratio K_π, as discussed in Section 1.1.2

The best-fit HESE flavor ratio falls within the 3σ allowed region of the mixing-angle observations. However, due to a lack of data, the uncertainties on the IceCube measurements are large, such that they remain consistent with all flavor-ratio models within 95% confidence level. Consequently, IceCube analyses generally assume the most generic scenario of $(\nu_e : \nu_\mu : \nu_\tau)_E = (1:1:1)$, as done in the remainder of this work.

1.2.3 High-Energy Neutrinos in the Multimessenger Picture

Before moving towards candidate astrophysical sources of high-energy neutrinos, let us inspect Figure 1.11, which combines the diffuse observations of GeV–TeV gamma rays, TeV–PeV neutrinos, and EeV–ZeV UHECRs. As covered in Appendix A, a diffuse flux scaled with the particle energy squared is a measure for the overall energy density of the sources producing this flux. A remarkable finding of Figure 1.11 is that the energy densities for each of the aforementioned messengers lie within the same ballpark. This hints towards a common origin of these messengers, as exemplified in Figure 1.1. However, one has to be cautious with such an interpretation. Based on energy arguments alone (recall from Section 1.1.2 that $E_\nu \sim E_\gamma/2 \sim E_p/20$), the observed gamma rays and high-energy neutrinos do not necessarily coincide with the sources of UHECRs.[25] Future studies targeting UHE astrophysical neutrinos ($E_\nu > 100$ PeV) will play a key role in unraveling the mystery of the UHECR origin, as briefly covered in Section 1.4.

If the sources of TeV–PeV astrophysical neutrinos and UHECRs are indeed the same, it is worth noting that the diffuse IceCube measurements do not violate the **Waxman-Bahcall upper bound** [69]. This bound is estimated directly from the differential energy density[26] of UHECRs between 10^{19} eV and 10^{21} eV, which is of the order of 10^{44} erg yr^{-1} Mpc^{-3}. Waxman & Bahcall assume that the differential energy density of cosmic rays (assumed to be protons) follows an E_p^{-2} spectrum between 10 PeV and 1 ZeV, such that it is constant per decade of energy (see Appendix A). As such, the corresponding differential energy density of neutrinos—which will also follow an E_ν^{-2} power law and thus be constant per energy decade—can be estimated in the TeV–PeV range ($E_\nu \sim E_p/20$). It can then be translated to a diffuse neutrino flux by taking into account the contribution of sources over cosmic history,[27] which are assumed to evolve with redshift like the star-formation rate (see also Section 5.2.1). In addition, a maximum neutrino-production efficiency is assumed at the sources, as well as a $(\nu_e : \nu_\mu : \nu_\tau)_S = (1:2:0)$ flavor ratio at the source yielding a $(\nu_e : \nu_\mu : \nu_\tau)_E = (1:1:1)$ flavor ratio at Earth. With these assumptions, the Waxman-Bahcall per-flavor upper bound is given by [69]

$$E_\nu^2 \Phi_{\nu_\ell + \overline{\nu}_\ell} \sim 2 \times 10^{-8} \text{ GeV cm}^{-2} \text{ s}^{-1} \text{ sr}^{-1}. \tag{1.10}$$

[25] The high-energy neutrinos observed by IceCube between 0.5–5 PeV are namely produced by cosmic rays with energies between about 10–100 PeV, whereas UHECRs have energies exceeding 1,000 PeV. Note that a spatial correlation study has recently been performed between the observed directions of UHECRs and high-energy neutrinos, yielding null results [110].

[26] As elaborated in Appendix A, the energy density or luminosity density of a cosmic messenger typically refers to the total energy output of that messenger per volume of space.

[27] An example of such a computation can be found in Appendix E.

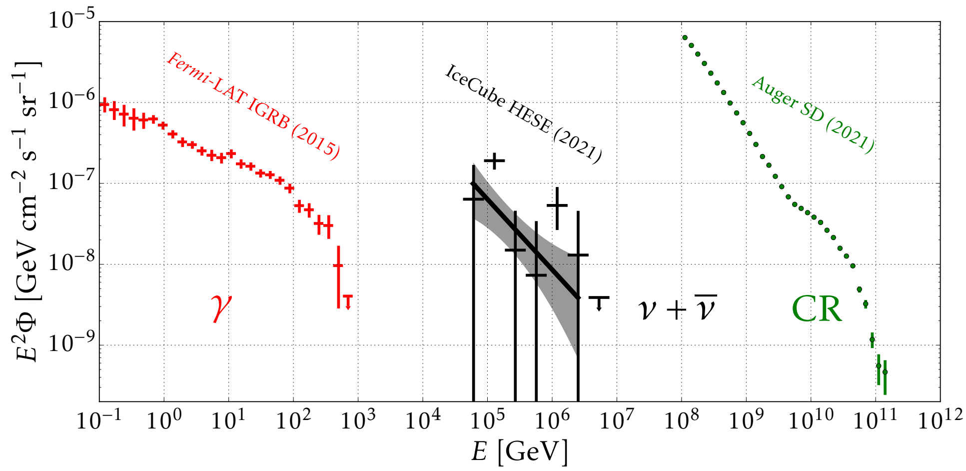

FIGURE 1.11: Diffuse observations of the three high-energy messengers, which are a measure for their respective energy densities as explained in the text. Gamma-ray observations of the IGRB by *Fermi*-LAT (4.2 yr) [83] are indicated by the red data points. The all-flavor neutrino flux ($\nu + \overline{\nu}$) measured in the IceCube HESE analysis (7.5 yr) [91] is represented by the black data points and the corresponding band (cf. Figure 1.7). The green data points correspond to the cosmic-ray spectrum observed by the surface detectors SD-750 and SD-1500 of the Pierre Auger Observatory using 15 years of data [27].

This predicted flux is of the same order as the diffuse neutrino observations presented in Figures 1.7 and 1.11. Note, however, that Equation (1.10) should be regarded more as an optimistic order-of-magnitude prediction under the above interpretation rather than a strict upper bound on the diffuse neutrino flux.

1.3 Astrophysical Sources of High-Energy Neutrinos

The diffuse IceCube observations of astrophysical neutrinos have opened up a new window to the Universe. However, to this date, their origin remains largely unknown. Over the past decade, a wide variety of studies have been performed searching for the sources of these IceCube neutrinos. Most of these studies use IceCube datasets consisting of high-quality tracks (see Section 3.3.1) because of their superior angular resolution ($\lesssim 1°$ above $E_\nu \gtrsim 1$ TeV) w.r.t. cascades. Note that these track event selections are performed separately for the Northern Sky (declination $\delta \geq -5°$) and Southern Sky ($\delta < -5°$). This is necessary to deal with the fact that the background in the Southern Hemisphere, dominated by atmospheric muons, is much larger than the background in the Northern Hemisphere, which solely consists of atmospheric neutrinos.

In the following, a short review is presented regarding the observational status of TeV–PeV neutrino sources.[28] First, Section 1.3.1 describes a chosen number of IceCube searches for point-like sources of neutrinos.[29] This discussion is focused

[28] See [111,112] for IceCube studies of GeV neutrinos from solar flares and compact binary mergers.
[29] For a study of extended neutrino sources with IceCube, see [113].

towards IceCube analyses of extragalactic astrophysical objects,[30] which are of main interest to this work. Section 1.3.2 then covers the first searches that found evidence for neutrinos originating from such astrophysical sources. Finally, current constraints on sources that could be responsible for the diffuse neutrino observations are discussed in Section 1.3.3.

1.3.1 IceCube Searches for Point Sources of Neutrinos

The techniques applied in **IceCube point-source analyses** are presented in Chapter 4, such that they will not be described in detail here. The main idea is that one searches for a spatial clustering of track[31] events on the sky, typically at the location of some astrophysical source of interest. Such a clustering would stand out against the overwhelming background of atmospheric muons and atmospheric neutrinos, which is isotropic in a given band of declination δ. Furthermore, more energetic events are given a higher weight in the analysis, since they are more likely to be of astrophysical origin, as discussed in Section 1.2.1. Lastly, a distinction is made between time-integrated and time-dependent analyses. The former search for steady neutrino emission while the latter search for transient neutrino emission in a certain time window, which can be motivated by transient electromagnetic (or gravitational-wave) emission.

Steady Sources

The most generic time-integrated point-source analysis to date is a scan of the full sky[32] using 10 years of IceCube data[33] [118] collected between 2008–2018. This study does not consider any predefined locations of interesting astrophysical sources; instead, it looks for sources emerging from the isotropic atmospheric background after integrating the data over sufficiently long time spans. To do so, the sky is divided into pixels of roughly $0.1° \times 0.1°$ (smaller than the detector resolution), and an unbinned point-source analysis is performed in each of these pixels. As such, a local (i.e. pre-trial) p-value is obtained in each pixel, yielding the skymap shown in Figure 1.12.

Due to their differing event selections, a hotspot—the location on the sky with the smallest local p-value—is reported for each of the hemispheres. The pre-trial p-values of the northern and southern hotspots are $p_{\mathrm{local}} = 3.5 \times 10^{-7}$ and $p_{\mathrm{local}} = 4.3 \times 10^{-6}$, respectively. After taking into account the look-elsewhere effect—i.e. the fact that by performing $\mathcal{O}(10^7)$ trials, one expects on average one statistical fluctuation at the 5σ level with a local p-value $p_{\mathrm{local}} \leq 10^{-7}$—the corresponding post-trial p-values are $p = 9.9 \times 10^{-2}$ (1.6σ; North) and $p = 0.75$ (0.3σ; South). Both hotspots are thus consistent with statistical fluctuations of the background. However, in [118], an additional search was performed for neutrinos from sources in a pre-defined

[30] Here, "astrophysical source" generally refers to astronomical objects that have been characterized by some form of electromagnetic emission. More exotic scenarios, such as high-energy neutrinos originating from dark-matter decays in astrophysical environments, will not be discussed. See [114, 115] for an overview of the latest IceCube searches for dark matter and physics beyond the Standard Model.

[31] Since neutrino-source searches tend to use tracks, they predominantly probe the $\nu_\mu + \overline{\nu}_\mu$ emission from these sources. Note that due to neutrino oscillations, the astrophysical neutrino fluxes per flavor are different at Earth compared to the flavor ratio at the source, although they are generally assumed to average out between flavors (see Section 1.2.2).

[32] See [116] for a complementary point-source analysis exclusively focusing on the Northern Hemisphere.

[33] This dataset has recently been published in [117].

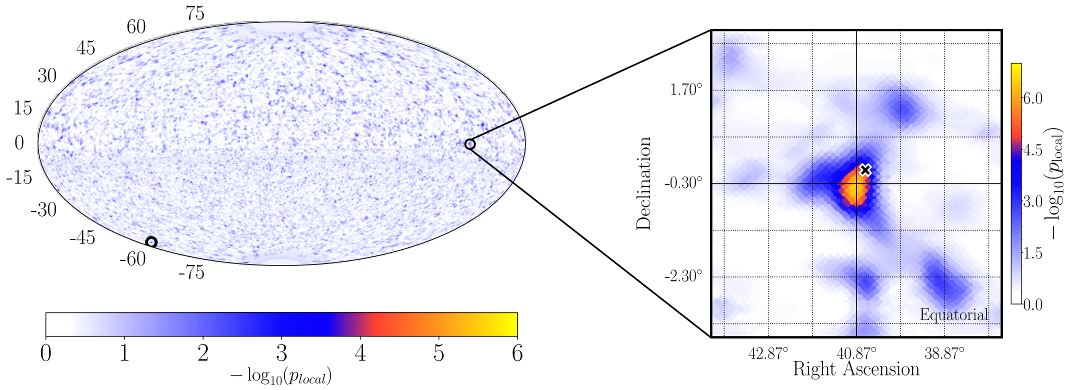

FIGURE 1.12: Results of the all-sky search for point sources using 10 years of IceCube track data, adapted from [118]. *Left*: Skymap of local p-values in equatorial coordinates, where the numbers represent the declination δ in units of degrees. The apparent discontinuity at $\delta = -5°$ is due to the different event selections in the Northern and Southern Sky. The corresponding hotspots, i.e. the smallest local p-values per hemisphere, are indicated with the black circles. *Right*: A zoomed-in map of the hotspot in the Northern Sky, where the black cross represents the location of NGC 1068. Note that the color scale is slightly offset from that of the complete skymap.

source list. The most significant source, corresponding to an excess of 2.9σ (post trial correction), was found to be NGC 1068, whose coordinates are at the location of the northern hotspot on the sky (see Figure 1.12). The interpretation of this result is reserved for Section 1.3.2.

Figure 1.13 shows the 10-yr point-source sensitivity of IceCube obtained with the all-sky scan as a function of the declination δ. The sensitivity for sources emitting neutrinos according to a harder E_ν^{-2} spectrum is more competitive w.r.t. to the sensitivity for neutrino sources with a softer E_ν^{-3} spectrum. This is a consequence of the fact that sources with harder spectra are easier to distinguish from the $E^{-3.7}$ atmospheric background, which mostly affects the sensitivity in the Southern Sky where atmospheric muons dominate the event selection. In fact, the E_ν^{-3} sensitivity of ANTARES—a 0.01-km^3 sized neutrino telescope in the Mediterranean Sea [119]—in the Southern Sky is more competitive [120], since it does not suffer from the atmospheric background of the Southern Hemisphere. Nevertheless, it should be noted that the IceCube point-source sensitivity in the Southern Sky can outperform the ANTARES sensitivity by using *cascades* instead of tracks, most notably in searches for neutrino emission from the Galactic Plane [121, 122].

Apart from the above point-source scan, many IceCube studies have been performed searching for neutrino emission from astrophysical sources of interest, based on their electromagnetic emission. They will not all be reviewed here, but an overview of the latest searches can be found in [114, 115]. Below, some source classes are highlighted which will be the subject of further discussions:

- **Active galactic nuclei (AGN).** These supermassive black holes, typically located in the center of galaxies, are in the process of accreting large quantities of matter (see also Section 2.1.2). Some AGN expel radio jets that exceed the size of the host galaxy, which are therefore also known as **radio AGN**. On the other hand, objects hosting an AGN without visible jets are typically referred to as **Seyfert galaxies**. In any case, both the core and jets of AGN are possible sources of high-energy neutrino emission (note that AGN are also candidate

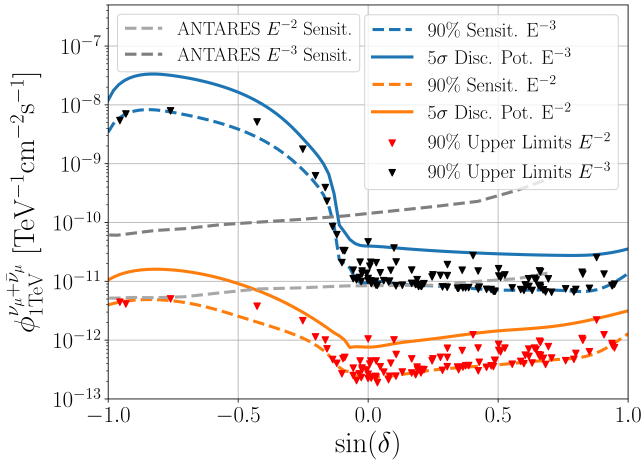

FIGURE 1.13: Time-integrated point-source sensitivity at 90% confidence level (dashed lines) and 5σ discovery potential (solid lines) with 10 years of IceCube track data, taken from [118] (see Section 4.3.3 for the exact definition of these quantities). Both are shown in terms of the muon-neutrino flux at $E_\nu = 1$ TeV as a function of declination. Orange and blue curves correspond to the sensitivities and discovery potentials for sources emitting neutrinos according to unbroken E_ν^{-2} and E_ν^{-3} power-law spectra, respectively. The dashed gray lines correspond to the 11-yr ANTARES point-source sensitivities for E_ν^{-2} (light gray) and E_ν^{-3} (dark gray) spectra [120]. The triangles represent upper limits at 90% confidence level on the E_ν^{-2} (red) and E_ν^{-3} (black) neutrino emission for targeted astrophysical sources in the study of [118].

UHECR sources). See [123] for a recent IceCube search for neutrinos from AGN cores with a post-trial significance of 2.6σ, and [114] for other ongoing AGN studies.

- **Blazars.** AGN with a jet pointed towards Earth are also known as blazars.[34] This subclass of AGN is of particular interest since blazars are the main sources of the extragalactic gamma-ray background (EGB) observed by *Fermi*-LAT. The latest null results of a time-integrated search for neutrinos from *Fermi*-3FHL blazars has been reported in [124]; see also [114] for ongoing IceCube analyses of blazars. It should be remarked that the 2017 study of [90] finds that blazars in the *Fermi*-2LAC catalog can only account for a fraction of the diffuse neutrino flux, as discussed in Section 1.3.4.

- **Starburst galaxies.** These stellar factories produce an equivalent of more than 10 suns per year. They are thought to be so-called cosmic-ray reservoirs, which can result in a steady neutrino flux over time (see Section 2.2.1). Some starburst galaxies are monitored by the standard time-integrated point-source analysis in IceCube [118], although the latest dedicated (stacking) search for these objects was performed before the detector was fully constructed [125], yielding a null result. Also recall that the observed UHECR anisotropy shows evidence for a correlation with the locations of nearby starburst galaxies, as discussed in Section 1.1.1.

[34] Blazars can on their turn be classified into two categories: BL Lacartae (BL Lac), characterized by a relatively smooth non-thermal spectrum over all electromagnetic wavelengths, and flat-spectrum radio quasars (FSRQs), which typically have more pronounced spectral lines compared to BL Lac.

- **Ultra-luminous infrared galaxies (ULIRGs).** The most extreme starburst galaxies, producing over 100 solar masses per year, are known as ULIRGs. With more than 10^{12} solar luminosities between 8–1000 μm, ULIRGs are the most luminous objects in the infrared sky. In addition to starburst activity, ULIRGs can also host AGN, making these objects a prime class of neutrino source candidates. Since this thesis presents the first search for high-energy neutrinos from ULIRGs, a detailed overview of these objects is reserved for Chapter 2.

Transient Sources

An all-sky scan such as the one described above has also been performed searching for transient point sources of neutrinos (note that the atmospheric background can be considered steady over time). Using the same 10 years of IceCube data, the analysis of [126] searches multiple Gaussian-like flares with a characteristic width[35] σ_T in each pixel on the sky. The corresponding sensitivity for single flares is shown in Figure 1.14. The hotspots of the scan were found to be consistent with background, with post-trial p-values $p = 4.3 \times 10^{-2}$ in the Northern Sky and $p = 0.72$ in the Southern Sky. Additionally, a binomial test was performed to search for neutrino flares from the same list of astrophysical sources used in the time-integrated analysis. Whereas the result in the Southern Sky yields a null result ($p = 0.89$ post-trial), a 3.0σ post-trial significance was found for neutrino flare emission in four northern objects over a period of 10 years.[36] A single flare is fitted for three objects, including NGC 1068, while two flares are fitted for the source TXS 0506+056. The latter result is consistent with flaring neutrino emission observed from TXS 0506+056 in previous studies, which are discussed in Section 1.3.2.

Various time-dependent searches for neutrinos coincident with transient electromagnetic emission[37] have been conducted over the past decade. As in the discussion of steady sources, not all of these analyses will be described here—see again [114,115] for the most recent IceCube studies—and only some transient sources are highlighted below:

- **Gamma-ray bursts (GRBs).** Generally associated with the mergers of neutron stars (short GRBs; $\lesssim$2 s) or extreme hypernova explosions (long GRBs; $\gtrsim$2 s), these flashes are the brightest gamma-ray sources ever to be observed. GRBs[38] are one of the candidate sources that could accelerate UHECRs (see also Figure 1.3). However, the neutrino emission associated with GRBs has been strongly constrained with several IceCube searches; see [129] for the most recent results.

- **Blazar flares.** AGN are generally variable sources of electromagnetic radiation, and blazars in particular can have periods of enhanced gamma-ray emission that can last several days. A dedicated IceCube search for neutrinos from these so-called blazar flares can be found in [130], which reports a null result. However, separate analyses did find some evidence for neutrino flares from the blazar TXS 0605+056 (see Section 1.3.2).

[35]Note that for $\sigma_T \gtrsim 200$ days, the time-integrated analysis becomes more sensitive than the transient one.

[36]Note that this 3σ excess is *not* a significance *per* source, but rather the overall significance for neutrino flares occurring in these four sources.

[37]For recent IceCube searches for neutrinos coincident with gravitational waves, see [112,127].

[38]For an excellent review of GRBs, see [128].

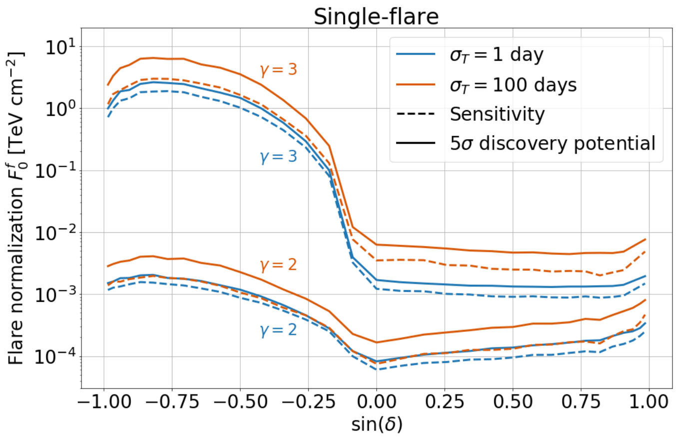

FIGURE 1.14: Time-dependent equivalent of Figure 1.13, taken from [126]. More specifically, sensitivities (dashed lines) and 5σ discovery potentials (solid lines) are shown for single-flare point-source emission in 10 years of IceCube data with Gaussian time windows of $\sigma_T = 1$ day (blue lines) and $\sigma_T = 100$ days (orange lines). These quantities are given in terms of the fluence, i.e. the time-dependent flux integrated over 10 years, at a normalization energy $E_\nu = 1$ TeV (note that F_0^f represents the fluence scaled with E_ν^2). The upper and lower curves correspond to the sensitivities and discovery potentials for sources emitting neutrinos according to unbroken E_ν^{-2} and E_ν^{-3} power-law spectra, respectively.

- **Tidal disruption events (TDEs).** When a star passes near a supermassive black hole, it will undergo strong tidal forces due the gravitational pull of the latter. Since this pull is significantly stronger on the side of the star nearest to the black hole, its shape will become distorted. In a TDE, the tidal forces are so large that the star is torn apart, yielding a (non-thermal) electromagnetic transient that can last several weeks. Null results have been reported in a dedicated IceCube analysis of TDEs [131], although a follow-up study of a neutrino alert did find hints for neutrino emission from AT2019dsg, as discussed in Section 1.3.2.

1.3.2 First Hints for Astrophysical Neutrino Sources

TXS 0506+056

On 22 September 2017, IceCube issued an alert (via its realtime alert system [132]) to the multimessenger community reporting the observation of a well-localized track event, named IC-170922A [12]. Not only was this event found to have a 56.5% probability of being of astrophysical origin—based on its direction and energy ($E_\nu \sim 270$ TeV)—but its localization pointed back to the known *Fermi* blazar TXS 0506+056, as shown in Figure 1.15. Furthermore, follow-up observations by *Fermi*-LAT and MAGIC observed an excess in (VHE) gamma-ray emission from this blazar during the time of the alert, indicating that it was in a flaring state. A post-trial significance of $\sim 3\sigma$ was inferred for the coincident observation of a high-energy neutrino and a gamma-ray flare from the blazar TXS 0506+056.

Apart from a broad multimessenger campaign ensuing the alert, an archival IceCube study was performed searching for previous instances of neutrino emission

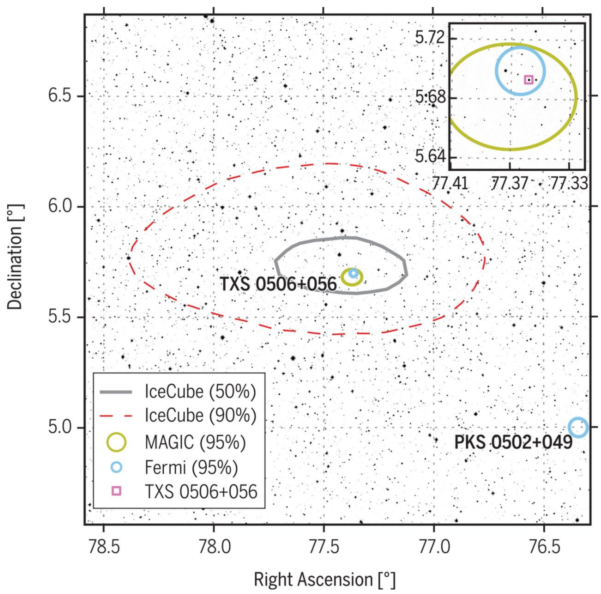

FIGURE 1.15: Optical skymap that is roughly centered around the location of the blazar TXS 0506+056, taken from [12]. The optical position of the blazar is marked in the inlay with the pink square. The solid gray and dashed red lines represent the IceCube localization of the IC-170922A alert at 50% and 90% confidence level, respectively. In addition yellow and blue circles correspond to the position of TXS 0506+056 at 95% confidence level as determined by gamma-ray observations of *Fermi*-LAT and MAGIC, respectively (note that the *Fermi* source known as PKS 0502+049 is also indicated).

from TXS 0506+056 [13]. The time-dependent analysis of this study found a neutrino flare of 13±5 events from the blazar in the period between September 2014 and March 2015, with a post-trial significance of 3.5σ. In contrast to the IC-170922A excess, no increase in gamma-ray emission was observed from TXS 0506+056 during this period. Note that both the 2014–2015 and 2017 neutrino flares were recovered in the time-dependent point-source analysis of [126], discussed in Section 1.3.1.

The two independent observations of neutrino emission from TXS 0506+056 at the 3σ level suggest that this blazar could be the first high-energy neutrino source ever to be identified. However, the neutrino emission of TXS 0506+056 would only be able to account for ~1% of the diffuse astrophysical neutrino flux [12, 13], such that the origin of the latter remains largely unknown. Moreover, the fact that the 2014–2015 excess was solely observed in neutrinos suggests that blazars can experience significant variability that is obscured in gamma rays. Such gamma-ray obscuration in sources of neutrino emission is further explored in Section 1.3.4.

NGC 1068

Complementary to the time-integrated point-source scan discussed in Section 1.3.1, the study in [118] also performed an IceCube search for neutrinos from a selection of sources in the *Fermi* 4FGL catalog [86] (as well as some galactic sources). Apart from all eight starburst galaxies, this selection contains 5% of the gamma-ray AGN in the 4FGL catalog for which the best IceCube sensitivity is expected based on their gamma-ray flux. The most significant source in this catalog search is NGC 1068, with a post-trial significance of 2.9σ.

NGC 1068 is classified as a starburst galaxy in the 4FGL catalog, although it has also been classified as a Seyfert galaxy[39] in other works (see [118] for more details). In addition, NGC 1068 is a luminous infrared galaxy (LIRG, $L_{\rm IR} \geq 10^{11} L_{\odot}$), i.e. a less luminous counterpart of ULIRGs [133]. Its location on the sky, which is near the horizon where IceCube has the best sensitivity, is shown in Figure 1.12. Remarkably, by taking into account the typical subdegree resolution of IceCube above 1 TeV, the location of NGC 1068 is consistent with the hotspot of the all-sky scan in the Northern Sky. If NGC 1068 is indeed a steady neutrino source, an upcoming point-source study in the Northern Hemisphere [134] should see its significance increase in both the all-sky scan and the catalog search.

AT2019dsg

The work of [135] found that the radio-emitting TDE with identification AT2019dsg occurred in spatial and temporal coincidence with the IceCube alert IC-191001A. Similar to IC-170922A, this alert has a probability of 59% to be of astrophysical origin, with an estimated neutrino energy $E_\nu \sim 200$ TeV. The probability of finding a TDE with the properties of AT2019dsg in coincidence with such a high-energy neutrino was estimated to be 0.2% ($\sim 3\sigma$). Therefore, the authors of [135] suggest that AT2019dsg and other TDEs could be sources of high-energy neutrinos. However, as mentioned previously, a dedicated IceCube search for neutrinos from TDEs reported a null result [131], such that one should be cautious with this interpretation.

Radio-Bright AGN

Using publicly available IceCube data, the study of [136] performed a spatial correlation study of neutrinos with energies $E_\nu \geq 200$ TeV and radio-bright AGN with radio flux densities exceeding 150 mJy at a frequency of 8 GHz. The latter were obtained from a catalog of sources based on very-long-baseline interferometry (VLBI) data. They found that the average VLBI flux density of these radio-bright AGN was higher at the locations of the IceCube events. The post-trial p-value for such an occurrence was estimated to be $p = 0.2\%$, which is at the 3σ level. Furthermore, for the radio-bright AGN located within the error regions of the IceCube events on the sky, a time-dependent analysis was also performed. The authors of [136] claim a suggestive indication of an increased VLBI flux during the times of the IceCube events; the corresponding post-trial p-value is $p = 5\%$ ($\sim 2\sigma$). Overall, the authors state that their results represent observational evidence for neutrinos with $E_\nu \geq 200$ TeV from radio-bright AGN, although such a strong claim should be treated with a grain of salt. A dedicated IceCube search for radio AGN and their variability could provide further insights into the possible neutrino emission of these objects.

1.3.3 Constraints on Source Populations of Astrophysical Neutrinos

A population of sources, or source class, is typically characterized by some properties of their electromagnetic spectrum. However, not only do these properties manifest themselves differently over cosmological distances, but the number of sources in the population also varies over cosmic history. This dependence, known as a **source**

[39] In fact, NGC 1068 is a luminous infrared galaxy (LIRG)—10^{11} solar luminosities between 8–1000 μm—and thus a less luminous sibling of ULIRGs, the main objects of interest to this thesis. Hybrid starburst and AGN environments are typical for LIRGs and ULIRGs, as discussed in Chapter 2, making NGC 1068 an interesting "prototype" for possible neutrino emission from such objects.

evolution, describes how the differential luminosity density (see Appendix A) of the sources, $E\mathcal{Q}_E(E,z)$, evolves with cosmological redshift, z. Note that the luminosity density of neutrinos is generally calibrated with an electromagnetic counterpart; see Section 2.2 for an example.

The redshift evolution of an astrophysical source class can be categorized qualitatively as follows:

- **Strong positive evolution.** These are sources that were much more abundant at high redshifts compared to the local Universe. Examples are sources that tend to follow the universal star-formation rate (SFR), such as starburst galaxies and ULIRGs (see Section 2.1.3), and most types of AGN. Blazars of the type FSRQ have a particularly strong evolution [137].
- **Weak positive evolution.** For example, blazars of the type BL Lac have a relatively weak evolution [137].
- **Negative evolution.** Some sources, such as TDEs [138], are becoming more common compared to earlier cosmological times. This type of source evolution will not be relevant to further discussions.

It is common to parameterize the redshift evolution as $(1+z)^m$, where $m > 0$ (resp. $m < 0$) represents a positive (resp. negative) source evolution. In particular, $3 \lesssim m \lesssim 4$ is a reasonable approximation for the evolution of the SFR and AGN [139]. The case of $m = 0$ corresponds to a so-called flat evolution, i.e. a more hypothetical scenario where sources do not evolve with redshift, which is generally used for comparative purposes.

The upcoming discussion is mainly based on the work of [139], where the neutrino luminosity density of steady[40] sources is factorized as $E_\nu \mathcal{Q}_{E_\nu}(E_\nu, z) = E_\nu L^{\text{eff}}_{E_\nu}(E_\nu) \times n(z)$. Here, $E_\nu L^{\text{eff}}_{E_\nu}$ is an effective differential neutrino luminosity (all-flavor) that is assumed to be redshift-independent. The number density of sources is given by $n(z) = n_0^{\text{eff}} \mathcal{H}(z)$, where n_0^{eff} is the effective local source density, and $\mathcal{H}(z)$ describes their redshift evolution. By integrating the contribution of all sources in the population over cosmic history, and assuming that each source emits neutrinos according to an E_ν^{-2} spectrum, the cumulative diffuse neutrino flux (per-flavor; assuming equipartition) of the full population is given by

$$E_\nu^2 \Phi^{\text{diff}}_{\nu_\ell+\bar{\nu}_\ell} = \frac{1}{3} \frac{c\, n_0^{\text{eff}}}{4\pi H_0} \xi_z E_\nu L^{\text{eff}}_{E_\nu}. \tag{1.11}$$

Here, the parameter ξ_z encodes the redshift evolution of the sources. For an evolution following the star-formation rate, $\xi_z = 2.4$, while flat and FSRQ evolutions yield $\xi_z = 0.53$ and $\xi_z = 8.4$, respectively [139]. A more detailed description of this estimation and its underlying assumptions is given in Section 5.2.1.

Let us now focus on the IceCube diffuse neutrino observations of northern throughgoing tracks ($\ell = \mu$) above 100 TeV, shown in Panel (b) of Figure 1.7, where $E_\nu^2 \Phi^{\text{diff}}_{\nu_\mu+\bar{\nu}_\mu} \sim 10^{-8}$ GeV cm^{-2} s^{-1} sr^{-1}. From Equation (1.11), one can directly determine the condition for the product $n_0^{\text{eff}} \times E_\nu L^{\text{eff}}_{E_\nu}$ that is required to fully supply the diffuse neutrino observations. This condition is indicated by the orange band in Figure 1.16, where the bandwidth is determined by considering flat to strong (FSRQ) source evolutions. In addition, Figure 1.16 shows the values of n_0^{eff} and $E_\nu L^{\text{eff}}_{E_\nu}$ for

[40] Transient sources are not covered in detail here, but a similar argument can be given based on an effective bolometric energy output of the sources and their effective local rate density [140].

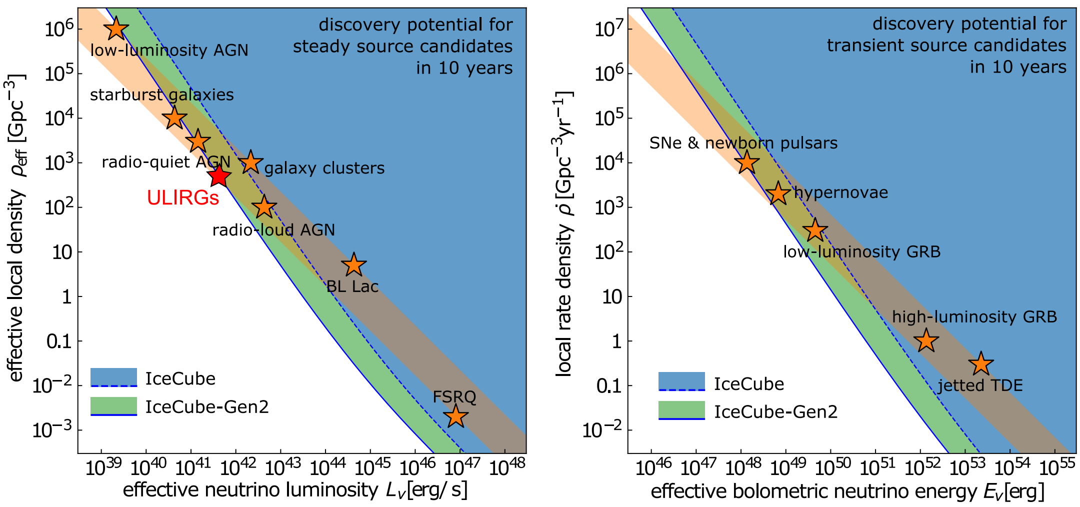

FIGURE 1.16: Constraints on source populations that could be fully responsible for the diffuse IceCube observations, adapted from [141]. *Left*: The effective local number density as a function effective neutrino luminosity for steady sources of neutrinos (corresponding to the notations $n_0^{\rm eff}$ and $E_\nu L_{E_\nu}^{\rm eff}$ in the main text, respectively), as defined by [139]. The orange band corresponds to the requirement for a source population to supply the complete diffuse neutrino flux. The upper and lower edges of the band represent flat and strong (FSRQ) source evolutions, respectively. Stars indicate source populations that can supply these diffuse-flux requirements; the outstanding red star marks the ULIRG source class, which is of main interest to this work. The dashed line corresponds to the limits inferred from the non-discovery of point sources in 10 years of IceCube data, which exclude the parameter space to the right of this dashed line (blue region). Analogously, the parameter space to the right of the full line (green region) corresponds to the region that could be probed with IceCube-Gen2 after 10 years of data. *Right*: Similar to the left panel, but showing the constraints on transient source populations. These are shown for completeness and not described in the main text; see [140] for more details.

some source populations that could produce high-energy neutrinos. While the local source density can be measured, the neutrino luminosity is estimated from electromagnetic observations, as described in [139].

An additional constraint can be obtained from the non-discovery of point sources in 10 years of IceCube data, which can be interpreted as a non-detection of muon-neutrino multiplets[41] above 100 TeV [139]. In this context, the upper limit on the flux from a point source is given by the E_ν^{-2} discovery potential (5σ) in the Northern Sky, i.e. $E_\nu^2 \Phi^{\rm PS,5\sigma}_{\nu_\mu+\bar\nu_\mu} \sim 10^{-9}$ GeV cm^{-2} s^{-1}. Combined with the requirement that the sources in the population should supply the whole diffuse neutrino flux, one can independently compute a lower limit on the effective local source density and an upper limit on the effective neutrino luminosity. These limits are obtained numerically in [139], and allow to restrict the allowed parameter space of Figure 1.16.

The main result of Figure 1.16 is that if a source population is fully responsible for the diffuse observations, it has to be relatively numerous and consist of relatively dim sources. Otherwise, more luminous sources would have started to appear in the all-sky point-source scan. From Figure 1.16, we can conclude that the point-source constraints disfavor blazars (BL Lac and FSRQs) as sources fully responsible for the

[41] A multiplet refers to multiple astrophysical neutrinos being detected from the same source.

diffuse neutrino observations,[42] which is consistent with result in [90]. ULIRGs, which are the main sources of interest to this work, are not disfavored, although Figure 1.16 implies that the all-sky point-source scan is not sensitive enough to probe *individual* sources in this population. Nevertheless, a point-source *stacking* analysis, like the one developed in Chapter 4 for ULIRGs, *is* sensitive to the cumulative emission of the weaker, individual sources that constitute this population.

To conclude, it should be noted that the above interpretation is only valid for source populations that would be *fully* responsible for the diffuse neutrino observations. It is not unlikely that the diffuse flux is comprised of contributions from a variety of source classes. In any case, the future IceCube-Gen2 facility, which is planned to be roughly 10 times larger and 10 times more sensitive than IceCube (Sections 1.4 and 3.1), could be able to identify multiple sources of fainter, more numerous populations at the 5σ level, as illustrated in Figure 1.16.

1.3.4 Multimessenger Indications of Obscured Neutrino Sources

Since blazars are thought to be possible UHECR accelerators, they have been the topic of various neutrino studies, as mentioned previously. In [90], an IceCube stacking search was performed for neutrino emission from blazars in the *Fermi*-2LAC catalog. However, no neutrinos were identified in this analysis, yielding constraints on the contribution of *Fermi*-2LAC blazars to the diffuse IceCube observations between 10 TeV and 2 PeV. More specifically, for unbroken $E_\nu^{-\gamma}$ power-law spectra, the diffuse neutrino emission from blazars has been restricted to $\lesssim$27% for $\gamma = 2.5$, and $\lesssim$50% for $\gamma \leq 2.2$.

The above result poses limitations on possible source populations that could be responsible for the diffuse neutrino observations. Recall from Section 1.1.3 that blazars constitute about 86% of the EGB observed by *Fermi*-LAT above 50 GeV. Thus, if a source population is to supply the diffuse neutrino flux, it cannot exceed the remaining non-blazar contribution to the EGB. This constraint particularly affects neutrino sources that are transparent to gamma rays, as they tend to violate the non-blazar EGB bound [143].

To illustrate this tension, consider the work of [144], which models the hadronic gamma-ray and neutrino emission produced via *pp*-interactions in hadronic calorimeters (also known as cosmic-ray reservoirs), such as e.g. starburst galaxies. By fitting the diffuse pionic gamma-ray emission to the non-blazar EGB between 50 GeV and 1 TeV, the corresponding diffuse neutrino flux—which is directly related to the pionic gamma-ray flux, as discussed in Section 1.1.2—predicted by this model undershoots the IceCube observations, as shown in Figure 1.17. Inversely, if the neutrino flux is fit to the diffuse observations of the combined fit between 25 TeV and 2.8 PeV (Section 1.2.1), the predicted gamma-ray flux overshoots the non-blazar EGB bound.

As argued in [143], the above tension can be relieved if the sources of neutrinos are gamma-ray opaque. In such hidden or **obscured neutrino sources**, the gamma rays are attenuated before escaping their source environment. For $p\gamma$-sources, the gamma rays could be attenuated via $\gamma\gamma$-interactions with the strong ambient radiation fields [143]. On the other hand, for *pp*-sources of neutrinos, the gamma rays could be attenuated by dense clouds of matter near the source in cosmic-ray

[42] Although galaxy clusters also seem to be constrained by Figure 1.16, their prediction assumes a flat evolution, which is not fully realistic [139]. A recent IceCube stacking analysis of massive galaxy clusters observed by *Planck* has constrained their contribution to the diffuse neutrino flux [142].

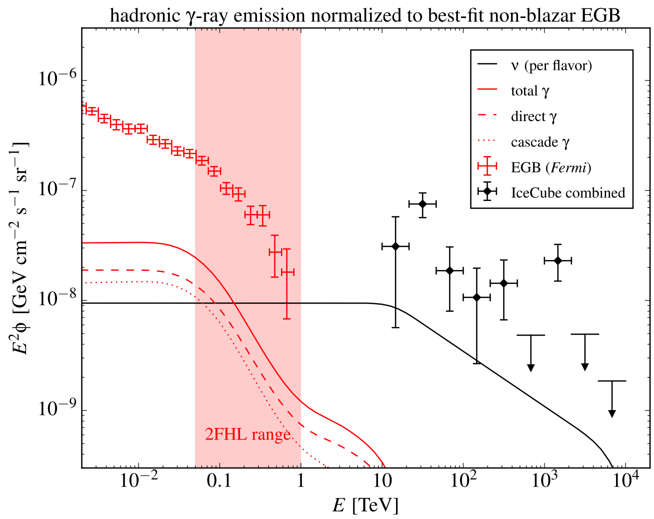

FIGURE 1.17: Prediction by [144] for gamma-ray transparent calorimeters, illustrating the tension between the observed EGB (red data points) and diffuse neutrino flux (combined fit; black data points) measured by *Fermi*-LAT and IceCube, respectively. The solid red line is the total gamma-ray flux predicted by [144], which is fit to the non-blazar EGB between 50 GeV and 1 TeV (i.e. the 2FHL range marked with the red band), and consists of a direct gamma-ray component (dashed red line) and a component of gamma rays that cascaded down to lower energies after interactions with the EBL (dotted red line). The corresponding neutrino flux prediction, indicated by the solid black line, undershoots the diffuse IceCube measurements.

beam-dump scenarios [145, 146]. In contrast, gamma-ray-transparent calorimetric *pp*-scenarios have been proposed that can explain a large fraction of the diffuse neutrino flux without violating the EGB bound; see e.g. [147–150]. Such calorimetric and obscured beam-dump models are of particular relevance to ULIRGs—the candidate neutrino sources investigated in this thesis—and will be covered extensively in Section 2.2.

1.4 Future Prospects for Neutrino Astronomy

To conclude this Chapter, it is worth spending some words on current plans for the future of the field, which are extensively reviewed in [151]. One of the major goals in neutrino astronomy is to identify the sources of high-energy astrophysical neutrinos with optical Cherenkov telescopes such as IceCube. For that purpose, several 1-km^3 under-water experiments are currently under construction (KM3NeT and Baikal-GVD [152, 153]) or development (P-ONE [154]) in the Northern Hemisphere, which will complement IceCube searches for point sources, particularly in the Southern Sky.[43] Furthermore, the optical component of IceCube-Gen2 [141] (see Section 3.1) is planned to instrument a volume of 8 km^3, which will not only allow for diffuse-flux measurements up to 10 PeV, but will also improve the current IceCube point-source sensitivity roughly by a factor of 10, as shown in Figure 1.16.

[43] Recall that, from the perspective of an optical water-Cherenkov telescope, the overwhelming background of atmospheric muons is only a contributing factor above the horizon. Hence, experiments in the Northern Hemisphere will not suffer from atmospheric muons in (most of) the Southern Sky.

A second major objective in neutrino astronomy is to discover **ultra-high-energy neutrinos** (UHE neutrinos; $E_\nu \geq 100$ PeV). Since $E_\nu \sim E_p/20$, detecting UHE neutrinos would allow us to directly probe the sources of UHECRs. Moreover, UHE neutrinos would reveal the reason behind the observed cutoff of the UHECR spectrum, i.e. if it is due to the exhaustion of hadronic accelerators or due to the GZK effect (Section 1.1.1). The latter is expected to yield so-called **cosmogenic neutrinos** via the photohadronic cosmic-ray interactions with the CMB, which could dominate the diffuse neutrino flux above 1 EeV [155, 156], as illustrated in Figure 1.18. To target UHE energies, most proposed projects focus on radio techniques to detect the particle showers induced by neutrinos. For example, in-ice detectors such as RNO-G, ARA, ARIANNA, and the radio array of IceCube-Gen2 [141,157–159] aim to directly detect the Askaryan emission[44] of such neutrino-induced showers. Another in-ice proposal, RET-N [161], applies an indirect radar technique to detect radio waves as they reflect off a neutrino-induced particle shower. In contrast to these in-ice techniques, the radio pulse of UHE neutrino interactions near the surface of the ice sheet can also be measured with airborne balloon experiments such as ANITA and PUEO [162, 163].

While the above detectors are sensitive to all neutrino flavors, other experiments specifically target UHE tau neutrinos that skim Earth's surface. Tau leptons produced in UHE neutrino interactions can emerge from the surface before decaying into the air, thereby inducing a horizontal extensive air shower [164]. Radio emission from this shower can be observed using surface arrays located in mountainous terrains, such as GRAND, TAROGE, and BEACON [165–167]. Non-radio surface arrays—also in mountainous terrains—include Trinity [168], which is a future imaging air Cherenkov telescope (IACT; similar to those used for VHE gamma rays), and particle detectors (water-Cherenkov tanks) such as the Pierre Auger Observatory and TAMBO [19,169], although the latter targets ν_τ between 1–100 PeV. Finally, POEMMA [170] is a satellite mission planned to observe the optical Cherenkov emission of skimming ν_τ showers as they develop through Earth's atmosphere.

Figure 1.18 summarizes the above experiments and their expected sensitivities to the diffuse neutrino spectrum from TeV up to UHE energies. The leading upper limits of neutrino emission between 10^{16} eV and 10^{21} eV are currently set by IceCube, the Pierre Auger Observatory, and ANITA at the highest energies [171–173]. Less stringent upper limits have been obtained with ARIANNA and ARA [174, 175]. Note that these limits are still consistent with expectations of diffuse UHE neutrinos. Future experiments are expected to improve current sensitivities by up to two orders of magnitude, which would make the detection of UHE neutrinos, and cosmogenic neutrinos in particular, feasible over the coming decades. As a final remark, it is worth pointing out that a study for neutrinos with energies exceeding 10^{21} eV (i.e. exceeding the highest UHECR energies observed to date) is being performed by searching for neutrinos that skim off the surface of the *moon* [176]. In this case, the neutrino interaction itself is expected to produce radio emission, which can be detected with observatories such as LOFAR.

[44] When a particle shower develops through a medium, it will produce a net charge excess of electrons being stripped off their host atoms. This so-called Askaryan effect thus yields a moving charge on macroscopic scales, which results in the emission of electromagnetic radiation at radio wavelengths. However, in *air*, the particle density is lower than in e.g. ice, such that the drift current induced by the geomagnetic field dominates the radio emission of the shower. See [160] and references therein for more details.

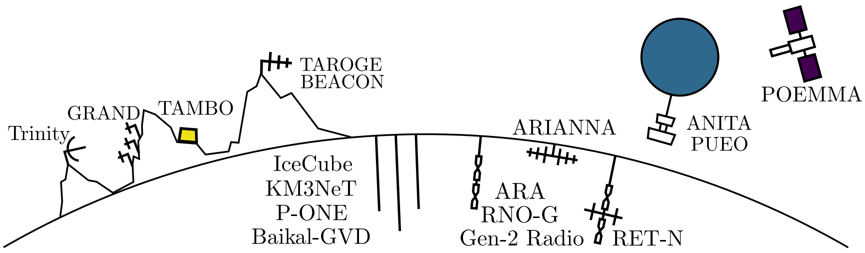

(a) Schematic of current and future neutrino experiments [177]

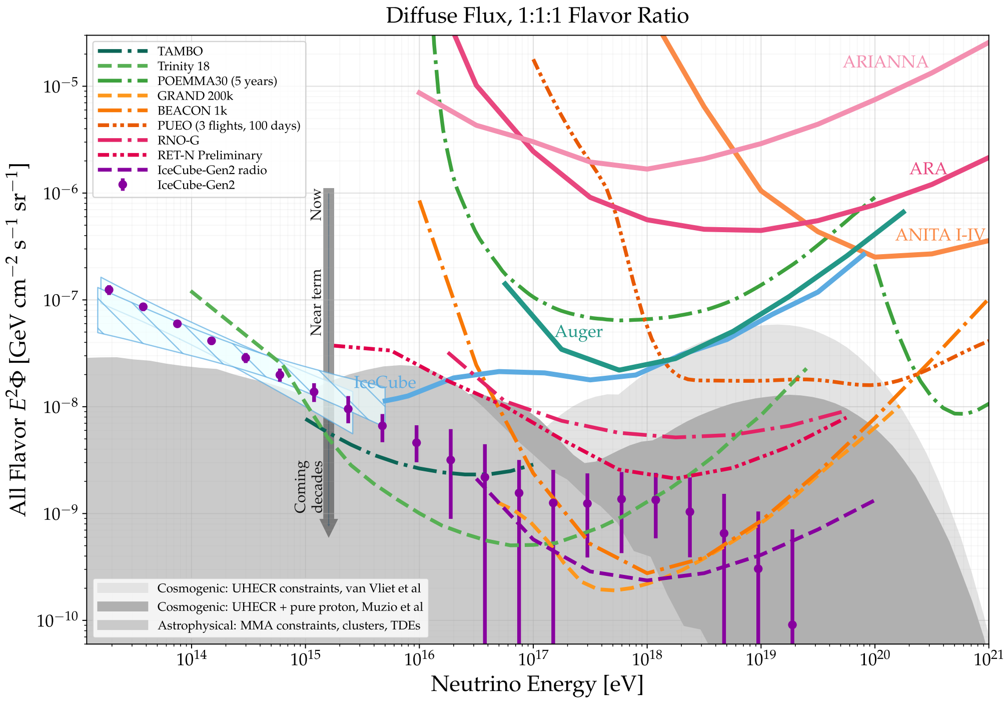

(b) Future prospects for diffuse neutrino observations [151]

FIGURE 1.18: Summary of the various experiments that are planned to cover the diffuse extraterrestrial neutrino spectrum between 10^{13}–10^{21} eV. Panel (a) illustrates the different types of neutrino experiments, as described in the text. Panel (b) shows the expected sensitivities of these experiments (non-solid lines and data points)—excluding optical water-Cherenkov telescopes apart form IceCube—as well as predicted contributions of neutrinos from astrophysical sources and cosmogenic neutrinos (gray regions). Solid lines correspond to upper limits from existing experiments, while the blue bands correspond to IceCube observations of TeV–PeV neutrinos. A qualitative timeline of the expected developments is also indicated.

Chapter 2
Ultra-Luminous Infrared Galaxies

> *Now the world has gone to bed,*
> *Darkness won't engulf my head,*
> *I can see in infrared,*
> *How I hate the night.*
>
> **— Marvin the Paranoid Android (Douglas Adams)**

Introduction

The first infrared (IR) sky surveys were performed throughout the 1960s and 1970s using ground-based observatories, balloon experiments, and suborbital rockets [178, 179]. As shown in e.g. [180], these surveys already revealed the existence of galaxies with an IR output many times stronger than the total bolometric[1] luminosity of the Milky Way, which is of the order of $10^{10} L_\odot$ [181]. Here, $L_\odot = 3.828 \times 10^{26}$ W represents the bolometric luminosity of the Sun.

A turning point in IR astronomy was reached with the mission of the Infrared Astronomical Satellite (IRAS) in 1983 [182]. IRAS was the first space-based telescope to make an extensive all-sky survey covering a large part of the thermal IR spectrum (12–100 μm). Not only did IRAS observe a large number of **luminous infrared galaxies** (LIRGs), defined as objects with a total rest-frame IR luminosity $L_{\mathrm{IR}} \geq 10^{11} L_\odot$ between[2] 8–1000 μm, but it also discovered the existence of **ultra-luminous infrared galaxies** (ULIRGs), for which $L_{\mathrm{IR}} \geq 10^{12} L_\odot$ [183]. Furthermore, the first hyper-luminous infrared galaxy (HyLIRG; $L_{\mathrm{IR}} \geq 10^{13} L_\odot$) was identified soon after, in 1988 [184].

During the 1990s, studies of the IR sky were performed using observations of IRAS and the Infrared Space Observatory (ISO) [185]. The turn of the millennium saw the launch of various IR satellites, such as the *Spitzer* Space Telescope [186], the *AKARI* mission [187], the *Herschel* Space Observatory [188], and the Wide-field Infrared Survey Explorer (WISE) [189]. These satellites allowed to perform detailed spectroscopic observations and deep-redshift surveys of the IR universe. Remarkably, in 2015 WISE discovered the existence of 20 distant extremely luminous infrared galaxies (ELIRGs; $L_{\mathrm{IR}} \geq 10^{14} L_\odot$) [190], which are the most luminous IR objects observed to this date. In any case, a new dawn of IR astronomy is upon us thanks to the successful launch of the *James Webb* Space Telescope [191] on Christmas Day of 2021.

[1] The *bolometric* luminosity of an object refers to its total luminosity integrated over all possible frequencies (see also Appendix A).

[2] The 8–1000 μm range covers the thermal part of the electromagnetic spectrum. It contains a large part of mid-IR wavelengths (8–40 μm) as well as the complete far-IR (40–200 μm) and submillimeter (200–1000 μm) regimes. In this work, the 8–1000 μm waveband is referred to as the total IR waveband.

In this Chapter, the focus will mostly be laid on ULIRGs, which are extensively reviewed in [183]. Since HyLIRGs and ELIRGs are rare and located at much higher redshifts[3] compared to ULIRGs, they will not be distinguished from the ULIRG source class in the following. Section 2.1 covers the main properties of ULIRGs, such as their electromagnetic spectrum, the mechanisms powering these objects, and their evolution over cosmic history. Subsequently, Section 2.2 elaborates on ULIRGs forming a promising class of neutrino-source candidates, which could also be responsible for a significant fraction of the diffuse astrophysical neutrino flux measured with IceCube. This motivates the IceCube stacking search presented in this work, for which a dedicated selection of ULIRGs is obtained based on IRAS observations, as presented in Section 2.3.

2.1 General Properties of ULIRGs

2.1.1 Morphology

Let us start our exploration of ULIRGs by taking a look at their appearance.[4] Figure 2.1 displays high-resolution optical images of two nearby ULIRGs, which are both **interacting galaxies**. As elaborated in [183] and references therein, ULIRGs are merging systems of spiral galaxies that are typically going through an advanced, coalescing phase of the merger (see e.g. [196] for more images), both in the local

(a) Arp 220 (b) Mrk 273

FIGURE 2.1: Optical images captured by the *Hubble* Space Telescope of the ULIRGs Arp 220 and Mrk 273, shown in Panels (a) and (b), respectively. Arp 220 is the closest ULIRG to Earth, and Mrk 273 is also known as the “Toothbrush Galaxy.” Both objects have morphological features of galaxy mergers. The bright spot in the top left of Panel (b) is a foreground star from the Milky Way. Taken from [194, 195].

[3]The closest HyLIRG (IRAS P07380-2342) is located at a redshift $z = 0.292$ [192] and the closest ELIRG (WISE J024008.10-230915.0) is located at $z = 2.225$ [190]. For comparison, the closest ULIRG (Arp 220) is located at $z = 0.018$ [193].

[4]Although it is generally not the best idea to judge a book by its cover, or in this case, an astrophysical object by its optical image, we can safely say that the quasi-unpronounceable acronym for ULIRGs is more than compensated for by their magnificent looks.

Universe and at high redshifts ($z \sim 1$) [197]. On the other hand, the less luminous LIRGs are largely identified with earlier, pre-coalescence phases of such spiral-galaxy mergers [198].

These morphological observations lead to the idea, first proposed in 1988 [199], that LIRGs and ULIRGs correspond with particular stages in the evolution of such merging systems. The corresponding evolutionary scenario is illustrated in Figure 2.2; see Section 2.1.2 for more details concerning the power mechanisms. In this scenario, the early phases of the merger trigger nuclear activity in the interacting galaxies, resulting in typical LIRG luminosities. During coalescence, the nuclear activity further increases, forming an ULIRG. In the final stages of the merger, the ULIRG becomes a quasar, defined as an object in which an active supermassive black hole (SMBH; mass $\gtrsim 10^6 M_\odot$) outshines the host galaxy. The final remnant left behind once all nuclear activity dies out is an elliptical galaxy.

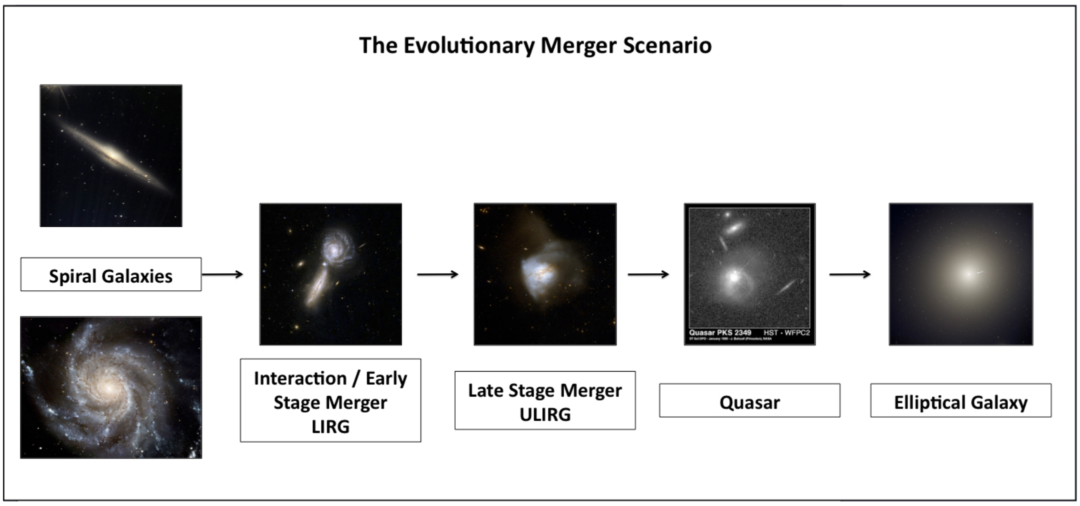

FIGURE 2.2: A schematic overview of the evolution of spiral-galaxy mergers, taken from [200]. In particular, the merger phases corresponding with LIRGs and ULIRGs are indicated.

2.1.2 Electromagnetic Spectrum and Power Mechanisms

Thermal Spectrum: Infrared

A representative broadband **spectral energy distribution** (SED) of ULIRGs is shown in Figure 2.3. The most characteristic feature of the SED is the dominant black-body spectrum between 8–1000 μm, which is the reason why ULIRGs are defined as objects with $L_{\mathrm{IR}} \geq 10^{12} L_\odot$ in that waveband.[5] Not only does their extreme IR luminosity imply that ULIRGs host energetic environments, but it also indicates that these environments are among the most **dust-obscured objects** in the Universe, as the IR radiation is emitted by dense dust clouds. This dust absorbs and reprocesses higher-energy radiation from the central engines powering the ULIRGs. The temperatures inferred for the dust clouds in ULIRGs have typical values between 30–60

[5] Note that the less luminous LIRGs have similar broadband SEDs.

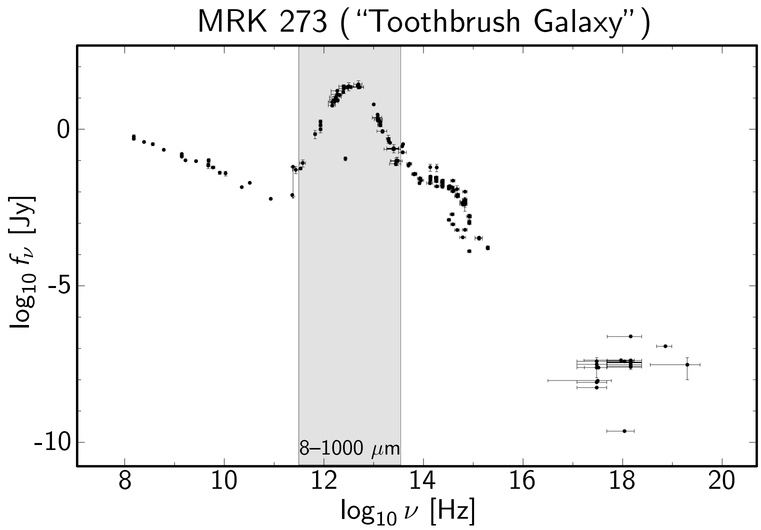

FIGURE 2.3: The SED of the ULIRG named Mrk 273, showing the flux density f_ν as a function of frequency ν using data from [193], which covers the entirety of the electromagnetic spectrum. The gray band highlights the thermal 8–1000 μm range. An optical image of Mrk 273 can be found in Panel (b) of Figure 2.1.

K, which are significantly hotter than dust temperatures (typically 10–30 K) found for non-IR-luminous galaxies ($L_{\mathrm{IR}} < 10^{11} L_\odot$) [201].

The intense luminosity of ULIRGs is mainly driven by **starbursts**, which are compact environments (of the order of 10–100 pc, see also Figure 2.4) of enhanced star-forming activity. These stellar factories are typically found in the nuclear regions of ULIRGs, and exhibit a typical star-formation rate[6] (SFR) that exceeds 100 $M_\odot$ yr^{-1} and can go up to 1000 $M_\odot$ yr^{-1} [183, 203–205]. The starburst activity is thought to be incited by the spiral-galaxy merger (see Section 2.1.1), which triggers the funneling of gas and dust towards the nuclear regions of the interacting galaxies. N-body simulations show that this funneling can occur both before and during coalescence, due to tidal forces and galactic-scale shocks, respectively (see [183] and references therein). It is the accumulation of matter combined with pressure waves that results in the birth of many young, bright stars. These young stars mostly emit optical and ultraviolet (UV) radiation, which heats up the dense and dusty interstellar medium (ISM) of the starburst nucleus, giving rise to enhanced IR luminosities. Consequently, the total IR luminosity can serve as a measure for the SFR. For starbursts, a rough estimation is given by [206]

$$\frac{\mathrm{SFR}}{1\ M_\odot\ \mathrm{yr}^{-1}} = \frac{L_{\mathrm{IR}}}{5.8 \times 10^9 L_\odot}. \tag{2.1}$$

The SFR is also commonly estimated with the Kennicutt-Schmidt law [207, 208], which links the gas surface density, Σ_{gas}, of a star-forming region to its SFR surface density,[7] Σ_{SFR}, as $\Sigma_{\mathrm{SFR}} \propto \Sigma_{\mathrm{gas}}^n$. For star-forming galaxies, the power-law index is

[6] As a reference, the SFR of the Milky Way lies between 0.68–1.45 $M_\odot$ yr^{-1} [202].

[7] The surface density, or column density, of a gas is generally the integral of its *mass* density ρ_{gas} along the line of sight, $\Sigma_{\mathrm{gas}} = \int \rho_{\mathrm{gas}}\, \mathrm{d}\ell$, typically in units of g cm^{-2}. In other words, it is the mass of the gas cloud per unit of area encountered along the line of sight, which is closely related to the definition of the so-called slant depth used in (astro)particle physics. Similarly, integrating the SFR

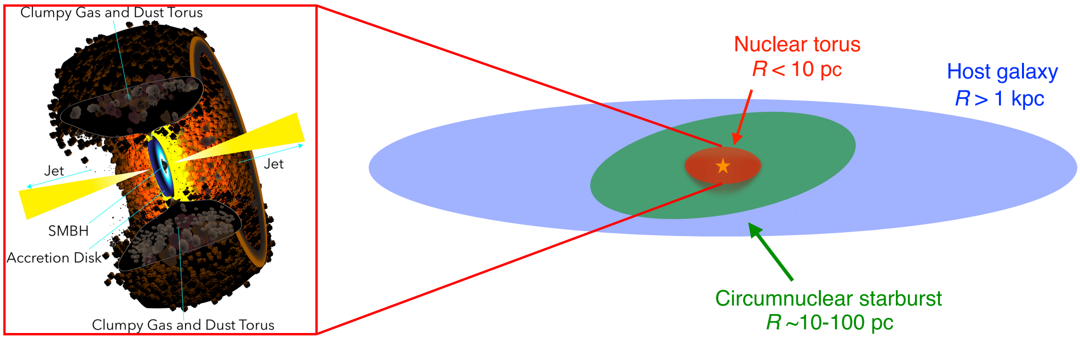

FIGURE 2.4: Typical sizes (not to scale) of the starburst and AGN environments found in ULIRGs compared to the host galaxy. The inset shows an artist interpretation of the unified AGN model, consisting of a supermassive black hole (SMBH) fed by an accretion disk, which is surrounded by a dense torus of gas and dust. Some AGN emit one or two jets along the axis of the accretion disk, but this is generally not observed in ULIRGs. Adapted from [216, 217].

estimated to be $n \approx 1.4$ [206]. A detailed description of the Kennicutt-Schmidt law falls outside the scope of this thesis.

ULIRGs can also manifest nuclear activity in the form of an **active galactic nucleus** (AGN) [183, 209–211], a SMBH that is actively accreting matter. SMBHs are commonly present in the nuclear regions of spiral galaxies, although they are typically in a quiescent state.[8] However, since ULIRGs are merging systems, the inflow of matter to the nuclear regions of the interacting galaxies can activate one or multiple SMBHs. A detailed description of AGN lies beyond the scope of this work, but an extensive review can be found in e.g. [214]. Here, a short description is given of the **unified AGN model**, illustrated in Figure 2.4, in which the SMBH is fed by a hot accretion disk, emitting optical through X-ray wavelengths. These central regions are surrounded by a cloud of dust and gas extending several pc, which is heated by the accretion disk and consequently emits IR radiation. In some cases, radio jets exceeding the size of the host galaxy emerge from the AGN, although this is generally not the case for ULIRGs, which are typically associated with Seyfert galaxies.[9] Nevertheless, as shown in Figure 2.4, an AGN hosted by an ULIRG is thought to be surrounded by a circumnuclear starburst, suggesting an intricate relationship between the enhanced star formation and SMBH activity [183, 216].

The number of ULIRGs hosting an AGN is generally found to be $\gtrsim$40%, although reported values can differ significantly between studies [218–223]. In any case, the general observed trend is that this fraction increases with IR luminosity, as shown in Figure 2.5. The contribution of the AGN to the total IR luminosity is typically of the order of $\sim$10% [224–228], and this number tends to increase with IR luminosity as well, which is also shown in Figure 2.5. However, in [183] it is noted that the AGN

---

per unit volume over the line of sight yields the SFR surface density, $\Sigma_{\text{SFR}} = \int \rho_{\text{SFR}}\, d\ell$, typically in units of $M_\odot$ yr^{-1} cm^{-2}.

[8]The most straightforward example of a quiescent SMBH is the one present in the center of the Milky Way, Sagittarius A*, of which the first image was recently captured by the Event Horizon Telescope [212]. However, extended gamma-ray structures originating from the Galactic Center have been observed by *Fermi*-LAT (Figure 1.5). These structures are known as the *Fermi* Bubbles, and suggest that Sagittarius A* might have been active in a not too distant past [213].

[9]In Seyfert galaxies, both the AGN and the host galaxy are resolvable. On the other hand, if the AGN outshines the host galaxy, the object is called a quasar. Note that Mrk 231, the most luminous local ($z < 0.1$) ULIRG with $\log_{10}(L_{\text{IR}}/L_\odot) = 12.51$, is also the nearest observed quasar ($z = 0.042$) [215].

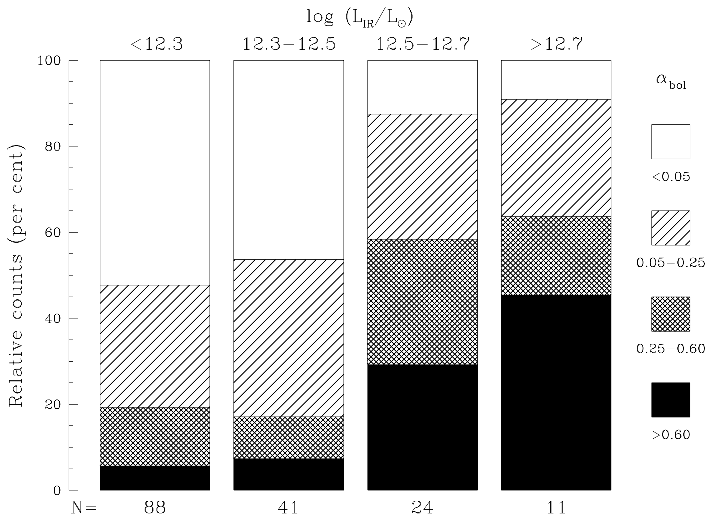

FIGURE 2.5: Results from the work presented in [227] studying the starburst (SB) versus AGN contribution in a local sample of 164 ULIRGs. Objects are classified in four regions according to the AGN contribution to the bolometric IR luminosity, α_{bol}: negligible ($\alpha_{\mathrm{bol}} < 0.05$), minor ($0.05 \leq \alpha_{\mathrm{bol}} < 0.25$), significant ($0.25 \leq \alpha_{\mathrm{bol}} < 0.60$), and dominant ($\alpha_{\mathrm{bol}} \geq 0.60$). The relative number of ULIRGs with a non-negligible AGN contribution increases with IR luminosity, as well as the bolometric contribution of the AGN.

power can be underestimated if the AGN is strongly obscured by its surrounding dust clouds (see [216] for a review on obscured AGN). In particular, the work presented in [229] finds that the AGN in a local sample of ULIRGs are **Compton thick**, i.e. the dust clouds obscuring the AGN have a column density[10] $N_H \gtrsim 1.5{\times}10^{24}$ cm^{-2} [230]. This is consistent with observations of Arp 220 presented in [231], which indicate that a possible AGN in this ULIRG should be obscured by a dust column with $N_H \gtrsim 10^{25}$ cm^{-2}.

Nevertheless, the large energy budgets and dense regions of matter in both the starburst and AGN components of ULIRGs make these environments suitable for hadronic acceleration and high-energy neutrino production. The discussion of ULIRGs as candidate neutrino sources is reserved for Section 2.2.

Thermal Spectrum: X-Rays

Figure 2.3 shows that ULIRGs are also sources of X-ray emission, which has been the topic of the study in [232]. This work finds that below 1 keV, the X-ray emission of ULIRGs originates from a hot plasma associated with a starburst nucleus. Between 2–10 keV, the X-ray spectrum is well-described by a mixture of this hot plasma and X-ray binary emission, which is also associated with starburst activity. Some ULIRG spectra display a characteristic Fe-K emission line at 6.4 keV, which is an indicator of obscured-AGN activity. Although the X-ray radiation from the accretion disk is attenuated, the emission from the AGN core can be reprocessed by a relatively cold surrounding medium. This reprocessing gives rise to the Fe-K emission line [233]. However, it should be noted that this method might not be able to identify the

[10] In contrast to a *mass* column density, N_H represents the equivalent *number* of hydrogen atoms per unit of area along the line of sight. In other words, $N_H = \int n_H \, \mathrm{d}\ell$, where n_H is the effective hydrogen number density of the dust cloud.

complete AGN content of ULIRGs, since these are objects with extreme obscuration that can also attenuate the Fe-K lines [229].

Intermezzo: ULIRGs versus Star-Forming Galaxies and Starburst Galaxies

Now that we have touched upon star formation in ULIRGs, let us clarify some of the sometimes confusing nomenclature used in the literature. **Star-forming galaxies** (SFGs) refer to all galaxies that exhibit star formation, including "normal" galaxies like the Milky Way, which have a typical SFR between 1–5 $M_\odot$ yr^{-1}. A subset of SFGs are the **starburst galaxies**, where enhanced star formation (SFR $\gtrsim 10$ $M_\odot$ yr^{-1}) typically occurs in compact short-lived ($\lesssim 10^8$ yr) nuclear starburst regions, known as starburst nuclei. Starbursts are generally associated with merging systems, as touched upon in Section 2.1.2. Since the IR luminosity of galaxies is a direct tracer of star-forming activity, starburst galaxies are characterized by an enhanced IR luminosity. At the highest IR luminosities, starburst galaxies are also known as—you guessed it—LIRGs ($L_{\mathrm{IR}} \geq 10^{11} L_\odot$) and ULIRGs ($L_{\mathrm{IR}} \geq 10^{12} L_\odot$), which have the most extreme SFRs ($\gtrsim 100$ $M_\odot$ yr^{-1}).

Non-Thermal Spectrum: Radio

Apart from being the most luminous IR objects in the sky, ULIRGs are also sources of non-thermal electromagnetic emission associated with particle acceleration. Such accelerated particles will interact with ambient matter, radiation, or magnetic fields, producing different sorts of emission. Since particle acceleration is characterized by power laws (see Section 1.1.1), the cumulative non-thermal emission of all particles will inherit the power-law characteristic, which can manifest itself at both the longest and shortest wavelengths in ULIRGs.

As illustrated in Figure 2.3, a typical SED of ULIRGs shows the characteristic power-law behavior, $f_\nu \propto \nu^{-\alpha}$, of non-thermal synchrotron emission at radio frequencies between 0.1–100 GHz, where typically $\alpha \sim 0.5$ [234]. Synchrotron emission serves as evidence for the presence of accelerated electrons and strong magnetic fields that can efficiently cool these electrons. In ULIRGs, the synchrotron emission generally originates from a starburst nucleus[11] [235], which contains magnetic fields with typical strengths $B \sim 10^2$–10^4 μG [236]. Below ~100 MHz, the synchrotron radiation falls off due to free-free absorption,[12] while above ~100 GHz, the thermal IR peak becomes the dominant source of emission.

AGN are also sources of synchrotron emission at radio frequencies. In Seyfert galaxies such as ULIRGs, the typical magnetic-field strength of an AGN is $B \sim 10$–100 mG [237]. Furthermore, the effect of synchrotron self-absorption[13] can lead to a

[11] Starburst nuclei are also expected to be sources of thermal free-free emission—or Brehmsstrahlung ("braking radiation")—at radio wavelengths, which is emitted by an electron that is decelerated by the electric field of an ion in the thermal plasma. However, it is challenging to observe this thermal component, since it is overwhelmed by non-thermal synchrotron emission [235].

[12] Free-free *absorption*, in contrast to free-free *emission*, is the thermal process where an electron *gains* energy by absorbing an ambient photon when trespassing the electric field of an ion. This process is more likely to occur for low-energy electrons, which spend more time under the influence of the ion's electric field. Hence, there is a cutoff in the number of free electrons at lower energies. Since synchrotron emission is proportional to the electron energy, this cutoff becomes visible at the low-frequency end of the synchrotron spectrum of ULIRGs [235].

[13] This effect occurs when synchrotron radiation re-interacts with the electrons that produced them via inverse Compton scattering. In such a process, the electron scatters off the synchrotron photon, thereby boosting its energy and leading to an overall hardening of the synchrotron spectrum.

flat or rising spectral shape of the AGN radio emission between 0.1–100 GHz, which is also expected to show significant variability [238]. The work of [238] studies the radio spectra of 10 local ULIRGs containing an obscured AGN. Although the majority of spectral shapes can be explained by starburst activity alone, some sources show evidence for an AGN contribution to the radio spectrum.

Non-Thermal Spectrum: Gamma Rays

At the other extreme of the electromagnetic spectrum, so far only one ULIRG has been observed in gamma rays between 0.2–100 GeV, namely Arp 220 [239]. The gamma-ray spectrum of Arp 220 is well-described a power law, $\Phi_\gamma \propto E_\gamma^{-\Gamma}$, with a spectral index $\Gamma = 2.35 \pm 0.16$. As discussed below, the gamma-ray emission of Arp 220 is compatible with observations of less luminous SFGs, where gamma rays are thought to be produced in hadronic[14] interactions within the star-forming regions of the galaxy. The authors of [239] also investigate the possibility that the gamma rays might originate from the AGN possibly hosted by Arp 220. They find no significant variability in the data, such that they conclude that the observed gamma-ray emission is probably not associated with an AGN. Since this AGN would likely be Compton-thick with a column density $N_H \gtrsim 10^{25}$ cm^{-2} [231], it should be remarked that the gamma-ray emission from the AGN would be attenuated significantly by its surrounding dust columns (see Section 2.2.2).

Multiwavelength Relations: Thermal and Non-Thermal Connection

As discussed above, the IR and X-ray emissions of ULIRGs both originate from related thermal processes, and it is therefore not surprising that a strong log-linear correlation is observed between the total IR and 2-10 keV luminosities of these objects [232]. However, in this section we will focus more on the relationship between thermal and non-thermal emission in ULIRGs.

The existence of a tight log-linear correlation between the IR and radio luminosities of IR-bright galaxies was established with the first IRAS surveys [240]. This property is characterized by the logarithmic IR-to-radio luminosity ratio,

$$q_{\mathrm{IR}} = \log\left(\frac{L_{\mathrm{IR}}}{3.75\times 10^{12}\ \mathrm{W}}\right) - \log\left(\frac{L_{1.4\ \mathrm{GHz}}}{\mathrm{W\ Hz^{-1}}}\right), \tag{2.2}$$

with L_{IR} the total IR luminosity and $L_{1.4\ \mathrm{GHz}}$ the radio luminosity at $\nu = 1.4$ GHz. The study of [241] finds a local average IR-to-radio luminosity ratio $\langle q_{\mathrm{IR}}\rangle \approx 2.6$ for ULIRGs, which does not evolve up to a redshift $z \sim 2$. On the other hand, a slightly negative evolution of $\langle q_{\mathrm{IR}}\rangle$ is observed in the study of [242]. In any case, the **radio-IR correlation** of ULIRGs indicates a strong coupling between the non-thermal acceleration processes and the thermal emission mechanisms. Moreover, this correlation does not appear to change drastically during the course of cosmic history.

It would also be interesting to investigate the relation between the IR emission of ULIRGs and their gamma-ray emission. Unfortunately, Arp 220 is the sole ULIRG that has currently been resolved in gamma rays [239]. Nevertheless, it is enlightening to take a look at the work of [243], which is a study of the gamma-ray emission of SFGs in general. This study separately performs a point source analysis of SFGs resolved in gamma rays and a stacking analysis of SFGs unresolved in gamma rays, and also combines both analyses. In all three analyses, they find a clear log-linear

[14] Recall that generally, gamma rays can also be produced in leptonic processes; see Section 1.1.3.

correlation between the total IR and gamma-ray (0.1–800 GeV) luminosities of SFGs, as shown in Figure 2.6. Note that the observations of Arp 220 are consistent with the **gamma-IR relation** of SFGs. This correlation supports the previous claim that an intricate relationship exists between non-thermal acceleration processes and thermal emission mechanisms in ULIRGs. It is also worth mentioning that the work of [235] explicitly studies the complete radio-IR-gamma connection for gamma-ray resolved SFGs, yielding similar conclusions.

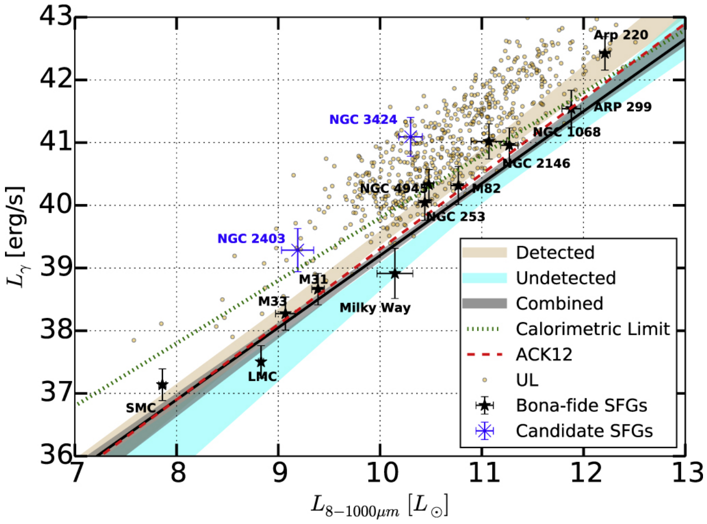

Figure 2.6: Observed correlation between the total IR luminosity, $L_{\rm IR} = L_{8-1000\ \mu{\rm m}}$, and the total gamma-ray luminosity between 0.1–800 GeV, L_γ, of SFGs [243]. Both axes are scaled with $\log_{10}$. The data points represent gamma-ray resolved sources, both well-known SFGs (bona-fide SFGs; black stars) and candidate SFGs (blue crosses), as well as the gamma-ray upper limits for unresolved sources (brown circles). Log-linear fits with 1σ bands are shown for the bona-fide SFGs alone (brown band), unresolved SFGs (cyan band), and the combination of these two (gray band).

2.1.3 Redshift Evolution and Infrared Luminosity Function

The evolution of the ULIRG source class over cosmic history has been a topic of numerous works[15] [183, 210, 246–259]. Since the observation of sources at high redshifts is limited by the sensitivity of our telescopes, these studies rely heavily on simulations to correct for source completeness, introducing large uncertainties. Nevertheless, a general trend is observed in the **redshift evolution** of ULIRGs, which is that their **comoving IR luminosity density**[16] increases strongly up to a redshift $z \sim 1$, after which it flattens out. This trend can be observed in Figure 2.7,

[15]ULIRGs at low redshifts are thought to be the local counterparts of submillimeter galaxies (SMGs), which form a population of high-redshift objects mainly observed in submillimeter (200–1000 μm) wavelengths [210]. The most luminous SMGs, or the HyLIRGs, are also sometimes referred to as hot DOGs (dust-obscured galaxies) [244, 245].

[16]The luminosity *density* represents the total luminosity per unit of volume. See Appendix A for more details.

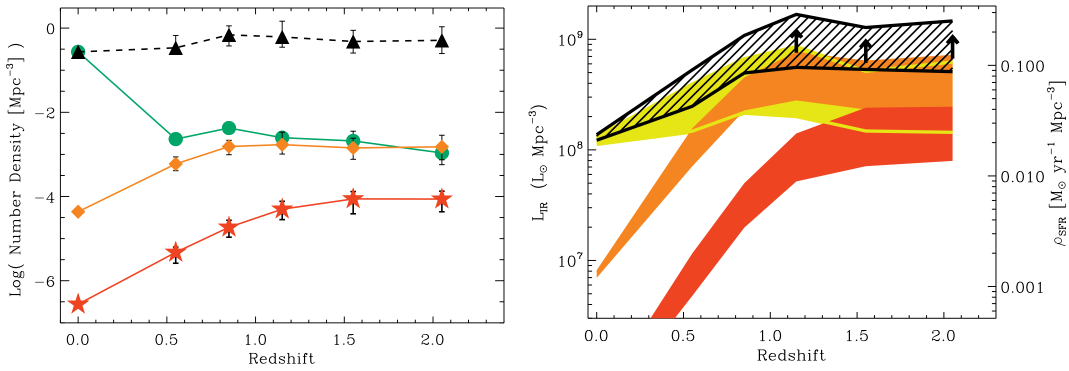

(a) Number density evolution

(b) Luminosity density evolution

FIGURE 2.7: The redshift evolution of the IR luminosity function up to a redshift $z = 2.3$, taken from [258]. Panel (a) shows the redshift evolution of the comoving number density of "normal" IR galaxies ($10^7 L_\odot \leq L_{IR} < 10^{11} L_\odot$; black triangles), LIRGs ($10^{11} L_\odot \leq L_{IR} < 10^{12} L_\odot$; orange diamonds), and ULIRGs ($L_{IR} \geq 10^{12} L_\odot$; red stars). The green circles indicate the total number density of galaxies that pass the flux detection threshold in the conducted survey. Panel (b) shows the redshift evolution of the comoving IR luminosity density (denoted here as L_{IR}) of "normal" IR galaxies (filled yellow band), LIRGs (filled orange band), and ULIRGs (filled red band). The cumulative contribution of these three components yields the total comoving IR luminosity in the Universe (dashed black band). Each band corresponds to an estimated $\pm 1\sigma$ uncertainty interval. The black arrows are estimates of the total IR luminosity density from a separate stacking analysis. The IR luminosity density is also related to the SFR density, denoted here as ρ_{SFR}, via Equation (2.1).

which displays the redshift evolution of the IR luminosity function.[17] Here, the luminosity function is integrated over three separate luminosity intervals, namely $10^7 L_\odot \leq L_{IR} < 10^{11} L_\odot$ ("normal" IR galaxies), $10^{11} L_\odot \leq L_{IR} < 10^{12} L_\odot$ (LIRGs), and $L_{IR} \geq 10^{12} L_\odot$ (ULIRGs). Panels (a) and (b) of Figure 2.7 show the redshift evolution of the **comoving number density** and IR luminosity density of these three source classes, respectively, which accumulate to the total IR luminosity density in the Universe.

From Figure 2.7 we can conclude that "normal" IR galaxies greatly outnumber LIRGs and ULIRGs over cosmic history. However, the redshift evolution of "normal" IR galaxies remains relatively flat between $0 \leq z \leq 2.3$, while the number density of LIRGs and ULIRGs increases rapidly between $0 \leq z \lesssim 1$. Consequently, although "normal" IR galaxies are responsible for the bulk of the total IR luminosity locally, LIRGs and ULIRGs become more important contributors to the IR luminosity density at higher redshifts. This observation is consistent with other works, where it is generally found that LIRGs are the main contributors to the total IR luminosity density between $z \sim 2$–3 [248–250]. It is also worth noting that for $z \lesssim 1$, studies report an IR luminosity density of LIRGs that is ~10–50 times larger than the luminosity density of ULIRGs [253–257], as in Figure 2.7.

The IR luminosity density is typically factorized as $\mathcal{Q}_{IR}(z) = \mathcal{Q}_{IR}(z = 0)\mathcal{H}(z)$, where $\mathcal{H}(z)$ is a parameterization of the redshift evolution. This thesis will mostly

[17] A luminosity function $\rho(L, z) \equiv \mathrm{d}n/\mathrm{d}\log L(z)$ describes the number of sources per comoving volume, $\mathrm{d}n$, typically per logarithmic bin of the source luminosity, $\mathrm{d}\log L$. Due to the logarithmic binning, ρ usually has the explicit units Mpc^{-3} dex^{-1}, where "dex" stands for decade in source luminosity.

utilize the parameterization of [145, 146] for the redshift evolution of ULIRGs,

$$\mathcal{H}_{\mathrm{ULIRG}}(z) \propto \begin{cases} (1+z)^4 & \text{for } 0 \leq z < 1, \\ \text{flat} & \text{for } 1 \leq z < 4. \end{cases} \tag{2.3}$$

Figure 2.7 also relates the total IR luminosity density in the Universe to the corresponding SFR density,[18] $\mathcal{Q}_{\mathrm{SFR}}$, using Equation (2.1). Here, the results of [260, 261] will be used to parameterize the redshift evolution of the SFR as

$$\mathcal{H}_{\mathrm{SFR}}(z) \propto \begin{cases} (1+z)^{3.4} & \text{for } 0 \leq z < 1, \\ (1+z)^{-0.3} & \text{for } 1 \leq z < 4, \\ (1+z)^{-3.5} & \text{for } z \geq 4. \end{cases} \tag{2.4}$$

It is not remarkable that ULIRGs, which are extreme SFGs, have a similar evolution to the global SFR over cosmic history. The redshift evolution of the SFR, which is closely related to the evolution of galaxies, remains a topic of active study that falls outside the scope of this work. As e.g. reviewed in [262], current interpretations argue that shortly after the Big Bang, young galaxies experienced a "boom" in star formation. Between $1 \lesssim z \lesssim 4$, the SFR was then dominated by extreme starburst galaxies (LIRGs and ULIRGs), resulting in the relatively flat evolution around this period in cosmic history. Since $z \sim 1$, however, "normal" galaxies with much more moderate SFRs have become the main contributors to the overall SFR in the Universe, which consequently started to decay exponentially over time. This generic picture is consistent with Figure 2.7 and the discussions above.

2.2 ULIRGs as Candidate Neutrino Sources

As discussed extensively in Section 1.3.3, previous IceCube point-source studies have constrained the source populations that could be fully responsible for the diffuse neutrino observations. In fact, such a source population should be numerous but consist of relatively dim neutrino sources, as expected for e.g. starburst galaxies. In [139], the gamma-IR relation of Figure 2.6 is applied to estimate the total gamma-ray luminosity of starburst galaxies between 0.1–800 GeV. This gamma-ray luminosity is then directly related to the differential neutrino luminosity via a calorimetric pp-scenario (Section 2.2.1), yielding $E_\nu L_{E_\nu}^{\mathrm{eff}} \sim 0.2 L_\gamma$. The results of this estimation are shown in Figure 1.16.

Since ULIRGs are extreme starburst galaxies, one can expand this method to estimate their effective neutrino luminosity. Assuming $L_\gamma \sim 3 \times 10^{42}$ erg s^{-1} as measured for Arp 220 (Figure 2.6), one finds $E_\nu L_{E_\nu}^{\mathrm{eff}} \sim 6 \times 10^{41}$ erg s^{-1}. Using an effective local source density $n_0^{\mathrm{eff}} \sim 5 \times 10^{-7}$ Mpc^{-3} [145, 146], ULIRGs are found to be capable of supplying the diffuse neutrino observations, as shown in Figure 1.16. Moreover, ULIRGs are not constrained by the current point-source limits. Consequently, ULIRGs form a promising class of neutrino-source candidates, and the following discussions cover the different neutrino production mechanisms that could occur in these sources.

[18] The SFR density is the rate of star formation per comoving volume element, typically given in units of $M_\odot$ yr^{-1} Mpc^{-3}.

2.2.1 Starburst Reservoirs

A first environment in which high-energy neutrino production can occur in ULIRGs is a **starburst nucleus** (see [263] for a detailed overview). As a consequence of the enhanced star-formation rate, more short-lived massive stars are produced in these starburst regions, which also leads to an enhancement of the supernova rate. These supernovae can act as hadronic accelerators, in which protons can reach energies up to $\sim 10^{18}$ eV in the most extreme cases[19] [264, 265]. The strong magnetic fields ($B \sim 10^2$–10^4 μG) within a starburst nucleus are able to confine the accelerated cosmic rays within this region [236]. The confinement is strong enough such that the typical timescale for a cosmic ray to escape[20] the region is larger than the timescale for inelastic energy loss of the cosmic ray through interactions with the dense interstellar medium ($n_{\mathrm{ISM}} \gtrsim 100$ cm^{-3}) of the starburst nucleus [266]. Hence, starburst nuclei act as **calorimetric reservoirs** in which cosmic rays lose most of their energy through pp-interactions, resulting in the production of neutrinos and pionic gamma rays (Section 1.1.2). Various studies have investigated starburst galaxies as a source population that could explain a significant fraction of the diffuse astrophysical neutrino flux measured by IceCube [147, 148, 150, 267–270].

ULIRGs form the most extreme of the starburst galaxies, containing starburst nuclei with averaged ISM densities that can be as large as $n_{\mathrm{ISM}} \sim 10^4$ cm^{-3} [271]. Combined with their huge star-formation rates ($\gtrsim 100\ M_\odot$ yr^{-1}), this makes ULIRGs an exceptional set of starburst galaxies which could on their own account for a significant fraction of the diffuse IceCube neutrino flux up to PeV energies. Here, two reservoir models are considered that predict such a diffuse neutrino flux originating from the ULIRG source population.

The first model, by He et al. [272], considers **hypernovae**[21] as engines that can accelerate cosmic rays up to energies of $\sim$100 PeV. According to He et al. these will on their turn produce neutrinos according to an $E^{-2.0}$ power-law spectrum with an exponential cutoff at several PeV. In addition, due to the enhanced star-formation rate in ULIRGs, He et al. argue that the hypernova rate will be significantly enhanced as well. This motivates them to predict a diffuse neutrino flux from the population of ULIRGs up to a redshift $z_{\mathrm{max}} = 2.3$, as shown in Figure 2.8, for which they use the ULIRG redshift evolution found in [258] (Figure 2.7). The prediction can only explain a fraction of the diffuse IceCube observations discussed in Section 1.2.1. However, the validity of this model can still be tested with the dedicated ULIRG stacking analysis performed in this work.

The second reservoir model considered here is that of Palladino et al. [149], illustrated in Figure 2.9. They construct a framework to compute the diffuse gamma-ray and neutrino emission of a generic population of **hadronically-powered gamma-ray galaxies** (HAGS). Palladino et al. propose starburst galaxies with $L_{\mathrm{IR}} < 10^{12} L_\odot$ and ULIRGs as two candidate HAGS populations, based on prototype sources NGC 253

[19] These more extreme cases, such as hypernovae and trans-relativistic supernovae, are much more rare than regular supernovae, which are typically only associated with cosmic-ray energies up to $\sim 10^{15}$ eV (Section 1.1.1). See [264, 265] and references therein for more detailed discussions.

[20] The escape time of cosmic rays depends on diffusion by magnetic fields and advection by turbulent stellar winds. However, in starburst nuclei the escape time is dominated by the advection timescale, which is of the order of 10^5–10^6 yr [266].

[21] Hypernova outflows have kinetic energies and velocities that can be larger by several orders of magnitude compared to those of regular supernovae. Hypernovae have also been associated with long gamma-ray bursts. See [273] and references therein for more details.

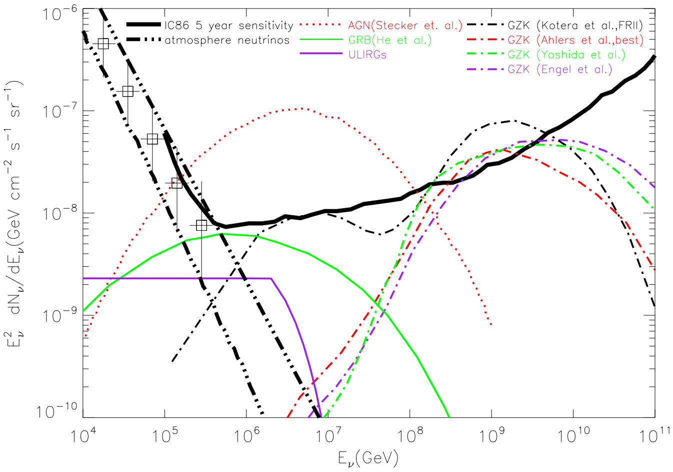

FIGURE 2.8: Prediction by He et al. [272] of a diffuse neutrino flux from the population of ULIRGs up to a redshift $z_{\mathrm{max}} = 2.3$ (magenta solid line). Note that this model was constructed before the observation of the diffuse astrophysical neutrino flux with IceCube, which is of the order of 10^{-8} GeV cm^{-2} s^{-1} sr^{-1} at 100 TeV. Therefore, this plot shows the anticipated sensitivity of the full IceCube configuration using 5 years of data (black solid line), together with measurements and predictions of the atmospheric neutrino flux (data points and black dash-triple-dotted lines). The remaining lines are other model predictions of astrophysical and cosmogenic neutrinos which are not relevant to this work.

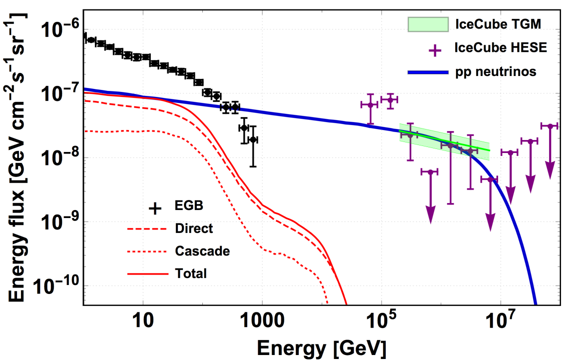

FIGURE 2.9: Prediction by Palladino et al. [149] of a diffuse neutrino flux from a population of HAGS up to a redshift $z_{\mathrm{max}} = 4.0$. This is shown for an $E^{-2.12}$ spectrum with a cutoff around 10 PeV (blue solid line), which was fit to the IceCube 8-year diffuse muon-neutrino flux [274] (green band). The corresponding diffuse gamma-ray flux of the model (red solid line), which consists of direct and cascaded gamma rays (red dashed and dotted lines, respectively), does not exceed the non-blazar EGB bound (not shown on this plot). Black and magenta data points represent the measurements of the total EGB by *Fermi* [83] and the diffuse neutrino flux from the 6-year HESE analysis by IceCube [275], respectively. Note that the y-axis has been erroneously scaled with an extra factor of π.

and Arp 220, respectively. The neutrino emission from HAGS is modeled according to an $E^{-\gamma}$ power-law spectrum with an exponential cutoff, which is integrated over the full source population up to $z_{\max} = 4$ following the redshift evolution of the SFR—see Equation (2.4). This neutrino flux is then fitted to the 8-year diffuse muon-neutrino observations [274] between 100 TeV–1 PeV. Palladino et al. find that for $\gamma \leq 2.12$ their model can fit a fraction of the IceCube observations without violating the non-blazar EGB bounds of [83, 276, 277] above 50 GeV (Section 1.3.4). Their most optimistic scenario, with $\gamma = 2.12$ and an exponential cutoff at $\sim$10 PeV, is shown in Figure 2.9. A population of HAGS, such as ULIRGs, could therefore be responsible for the bulk of the diffuse IceCube neutrino flux.

2.2.2 AGN Beam Dumps

As mentioned in Section 2.1.2, it is plausible that ULIRGs host an AGN which not only contributes significantly to the total energy output of the galaxy, but is also highly obscured by columns of gas that are Compton thick ($N_H \geq 10^{24}$ cm^{-2}). AGN are prime candidates for hadronic acceleration, and a vast number of studies have modeled the production of neutrinos in non-blazar AGN (see [278] for a review). Most notably, the cores of AGN are promising neutrino source candidates [279, 280]. A dedicated IceCube stacking analysis has found suggestive indications of neutrino emission from AGN cores [123], although the results are not significant enough to be conclusive.

In this work, we will focus on the **AGN beam-dump** model constructed by Vereecken & de Vries [145, 146]. They consider a Compton-thick AGN in which the beamed outflow of accelerated particles from the central engine is dumped into the surrounding columns of matter. As such, neutrinos can be produced in *pp*-interactions of cosmic rays with the ambient gas and dust. Moreover, Vereecken & de Vries argue that for column densities $N_H \gtrsim 10^{25}$ cm^{-2}, the gamma rays produced in such *pp*-interactions will on their turn be attenuated before escaping these dense clouds. This idea of a **dust-obscured AGN** as a neutrino source was already proposed in a previous study [281], although in this case the corresponding gamma rays are attenuated by the columns of matter surrounding the AGN [281]. Furthermore, a dedicated IceCube analysis was conducted searching for neutrinos from obscured flat-spectrum radio AGN [282], but no significant excess of neutrinos was found.

Since radio emission is a signature of particle acceleration, the model of Vereecken & de Vries normalizes the proton energy generation rate[22] $\mathcal{Q}_p$ of a source to its radio luminosity density $\mathcal{Q}_R$, which can be inferred from electromagnetic observations. The normalization is given by

$$\mathcal{Q}_p = \frac{\chi}{f_e} \mathcal{Q}_R. \tag{2.5}$$

The first parameter in this relation is the electron-to-radio luminosity ratio χ, which is related to the synchrotron emission of electrons moving in the magnetic fields of the accelerator [283]. The authors find that this value can be roughly approximated by $\chi = 100$. The second parameter is the **electron-to-proton luminosity ratio** f_e,

[22]This quantity has the dimensions of a luminosity density (see Appendix A), and is a measure for the energy output of the AGN that goes into accelerated protons. These protons will on their turn interact with surround dust columns, thereby producing neutrinos. Thus, $\mathcal{Q}_p$ should not be interpreted as the contribution of ULIRGs to the overall cosmic-ray energy density in the Universe.

which relates the leptonic and hadronic components of the acceleration process[23] [284]. This is the most uncertain parameter of the model, since the interplay between leptons and hadrons in cosmic accelerators is poorly understood. Vereecken & de Vries opt for a conservative value $f_e = 0.1$ in their model predictions.

This beam-dump model is used to obtain a neutrino flux from the population of ULIRGs up to a redshift $z_{\mathrm{max}} = 4.0$. In a first prediction, the proton luminosity associated to an ULIRG is obtained using Equation (2.5), where $\mathcal{Q}_R$ is determined using the IR-radio relation[24] of ULIRGs given in Equation (2.2). Using the value $L_{\mathrm{IR}} = 10^{12} L_{\odot}$ for all ULIRGs, and assuming that all ULIRGs host an AGN that is responsible for the bulk of the IR energy output, Vereecken & de Vries find that ULIRGs can only account for a rather small fraction of the observed diffuse neutrino flux. However, this method relies on the usage of $f_e = 0.1$, which is a conservative value and also has large uncertainties. A second prediction is found by normalizing the proton luminosity directly to the differential neutrino observations of the 6-year IceCube HESE analysis [275]. Figure 2.10 shows the corresponding diffuse neutrino and gamma-ray fluxes of the ULIRG population for an $E^{-2.0}$ spectrum and a column density $N_H = 10^{26}$ cm^{-2}. Most notably, Vereecken & de Vries find that for $N_H \gtrsim 5 \times 10^{25}$ cm^{-2}, ULIRGs could fit the diffuse IceCube observations without violating the non-blazar EGB bound above 50 GeV [83] (Section 1.3.4).

Later in this work both Equation (2.5) and the results of the ULIRG stacking analysis will be used to combine these two methods that normalize the proton luminosity. This will allow us to get insights in the electron-to-proton luminosity ratio f_e of ULIRGs. More details on the computations behind this AGN beam-dump model, which will also be relevant in further discussions, are given in Appendix E.

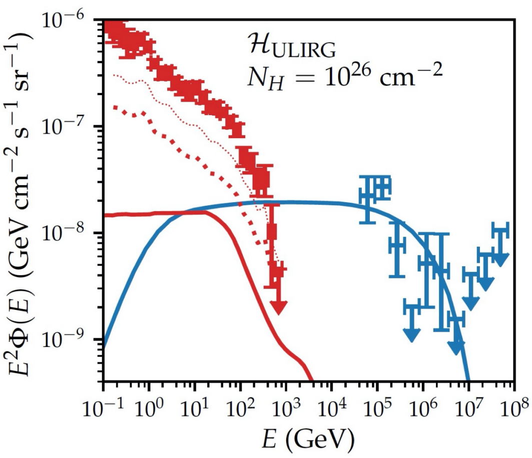

FIGURE 2.10: Prediction by Vereecken & de Vries [146] of a diffuse neutrino flux from the population of ULIRGs up to a redshift $z_{\mathrm{max}} = 4.0$. This is shown for an $E^{-2.0}$ spectrum and a column density $N_H = 10^{26}$ cm^{-2} (blue solid line). The red solid line shows the corresponding diffuse gamma-ray flux, which is well below the constraints of the non-blazar EGB (red dotted lines). The red and blue data points represent the measurements of the total EGB by *Fermi* [83] and the diffuse neutrino flux from the 6-year HESE analysis by IceCube [275], respectively.

[23] The electron-to-proton luminosity ratio f_e can also be referred to as the inverse baryonic loading.

[24] The radio luminosity of Equation (2.2) is converted to a luminosity density using the local ULIRG source density, which Vereecken & de Vries set to $n_0 = 5 \times 10^{-7}$ Mpc^{-3}.

2.3 Selection of ULIRGs

2.3.1 Catalog Description and Initial Selection

With the motivation of ULIRGs being promising neutrino-source candidates, a selection of ULIRGs is required for the IceCube search presented in this work. For this, three different IR catalogs are considered that are primarily based on IRAS data. These catalogs follow the method presented in [285] to estimate the total IR luminosity as[25]

$$\begin{aligned} L_{\mathrm{IR}} &= 4\pi d_L^2 \times F_{\mathrm{IR}}, \\ F_{\mathrm{IR}} &= \left(13.48\,\frac{f_{12}}{\mathrm{Jy}} + 5.16\,\frac{f_{25}}{\mathrm{Jy}} + 2.58\,\frac{f_{60}}{\mathrm{Jy}} + \frac{f_{100}}{\mathrm{Jy}}\right) \times 1.8 \times 10^{-14}\ \mathrm{W\,m^{-2}}. \end{aligned} \tag{2.6}$$

Here, d_L is the luminosity distance, and each $f_{\lambda/\mu\mathrm{m}}$ represents the IRAS flux density at $\lambda/\mu\mathrm{m} \in \{12, 25, 60, 100\}$. A description of the three catalogs is given below:

1. The **IRAS Revised Bright Galaxy Sample** (RBGS) [215]. This catalog contains the brightest extragalactic sources observed by IRAS. These are sources with a 60-μm infrared flux $f_{60} > 5.24$ Jy and a galactic latitude $|b| > 5°$ to exclude the Galactic Plane. The RBGS provides the total infrared luminosity between 8–1000 μm for all objects in the sample, containing 21 ULIRGs.

2. The **IRAS 1 Jy Survey of ULIRGs** [246] selected from the IRAS Faint Source Catalog (FSC) [286] contains sources with $f_{60} > 1$ Jy. The survey required the ULIRGs to have a galactic latitude $|b| > 30°$ to avoid strong contamination from the Galactic Plane. Furthermore, in order to have accessible redshift information from observatories located at Mauna Kea, Hawaii, this survey is restricted to declinations $\delta > -40°$. The resulting selection is a set of 118 ULIRGs.

3. The ULIRG sample used in [227]. The ULIRG selection is primarily based on the redshift survey [287] of the **IRAS Point Source Catalog** (PSC; the redshift survey is abbreviated as PSCz) [288]. This catalog contains objects with $f_{60} \gtrsim 0.6$ Jy and covers 84% of the sky. In addition, the authors require the ULIRGs to be observed by the Infrared Spectograph (IRS) [289] onboard *Spitzer*. As such, they obtain a sample of 164 ULIRGs.

There exists some overlap between the ULIRGs of the above three catalogs, as shown in Figure 2.11 (see also Section 2.3.2). Therefore, the NASA/IPAC Extragalactic Database (NED) [193] is used to cross-identify these sources. The result is an **initial selection** of 189 unique ULIRGs, of which a complete list can be found in Appendix C. For uniformity, NED is also used to obtain the equatorial coordinates and redshift for each object. Since L_{IR} values depend on IRAS flux measurements, which are optimized separately for the different IRAS surveys, they are taken in the following order:

- From Catalog 1 if available;
- From Catalog 2 if not available in Catalog 1;

[25] Equation (2.6) is obtained by fitting a single-temperature dust-emissivity model to the IRAS flux measurements [285]. The total IR flux F_{IR} is expected to be accurate within ±5% for dust temperatures between 25–65 K.

- From Catalog 3 if not available in Catalog 1 or 2.

Note that Catalog 3 is the only catalog that provides uncertainties on these values. Therefore, from this catalog, all objects are included that are consistent with $L_{IR} = 10^{12} L_\odot$ within one standard deviation, selecting three objects[26] with a best-fit $L_{IR} < 10^{12} L_\odot$. The distributions of the redshifts and total IR luminosities of this initial selection of ULIRGs are shown in Figure 2.12.

The main physical quantities of relevance in further discussions are the luminosity distance d_L (or redshift z), flux at 60 μm f_{60}, total IR luminosity L_{IR}, and total IR flux $F_{IR} = L_{IR}/(4\pi d_L^2)$. Figure 2.13 visualizes the correlations between these quantities for the initial selection of 189 ULIRGs. A completeness cut at $z = 0.13$, which will be motivated in Section 2.3.4, is also indicated in the appropriate panels. Note that after this redshift cut, a bias is observed towards more luminous objects (top left panel), which is expected due to the limited completeness of the three ULIRG catalogs.

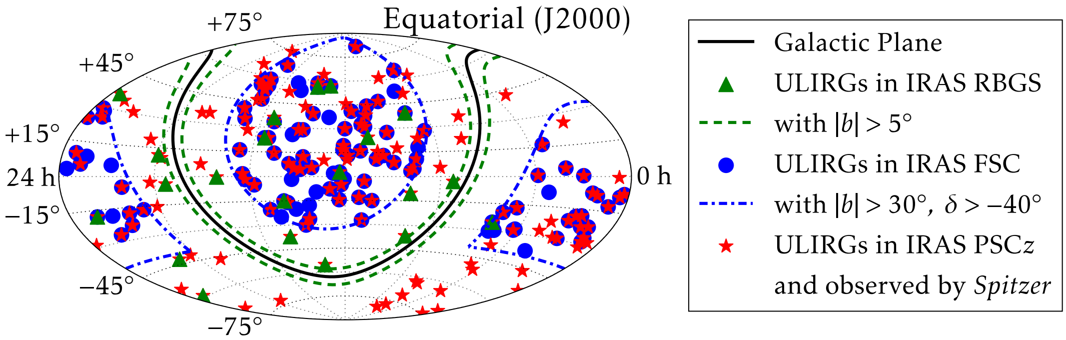

Figure 2.11: Skymap of the 189 unique ULIRGs identified in the IRAS Revised Bright Galaxy Sample (RBGS; green triangles), the IRAS Faint Source Catalog (FSC; blue circles), and the catalog of ULIRGs (red stars) in the redshift survey of the IRAS Point Source Catalog (PSCz) that have been observed by *Spitzer*. Spatial restrictions of the RBGS (green dashed line) and the FSC (blue dash-dotted line) are also indicated. Note that the same object can be identified in more than one of these catalogs.

[26] The NED identifications (with $\log_{10}(L_{IR}/L_\odot)$ values) of these objects are UGC 05101 (11.99±0.02), IRAS 18588+3517 (11.97 ± 0.04), and 2MASX J23042114+3421477 (11.99 ± 0.04).

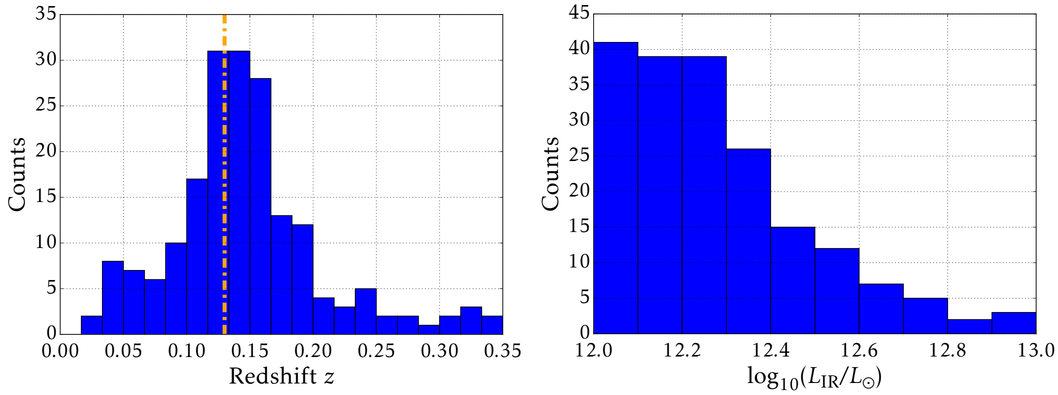

(a) Redshift z (b) Total IR luminosity L_{IR}

FIGURE 2.12: The distributions of redshift and total IR luminosity for the initial selection of 189 ULIRGs, shown in Panels (a) and (b), respectively. The orange dash-dotted line in Panel (a) indicates the redshift cut at $z = 0.13$ that results in the final representative ULIRG sample. Note that the three ULIRGs with a best-fit $L_{\mathrm{IR}} < 10^{12} L_{\odot}$ are included in the first bin of the histogram in Panel (b).

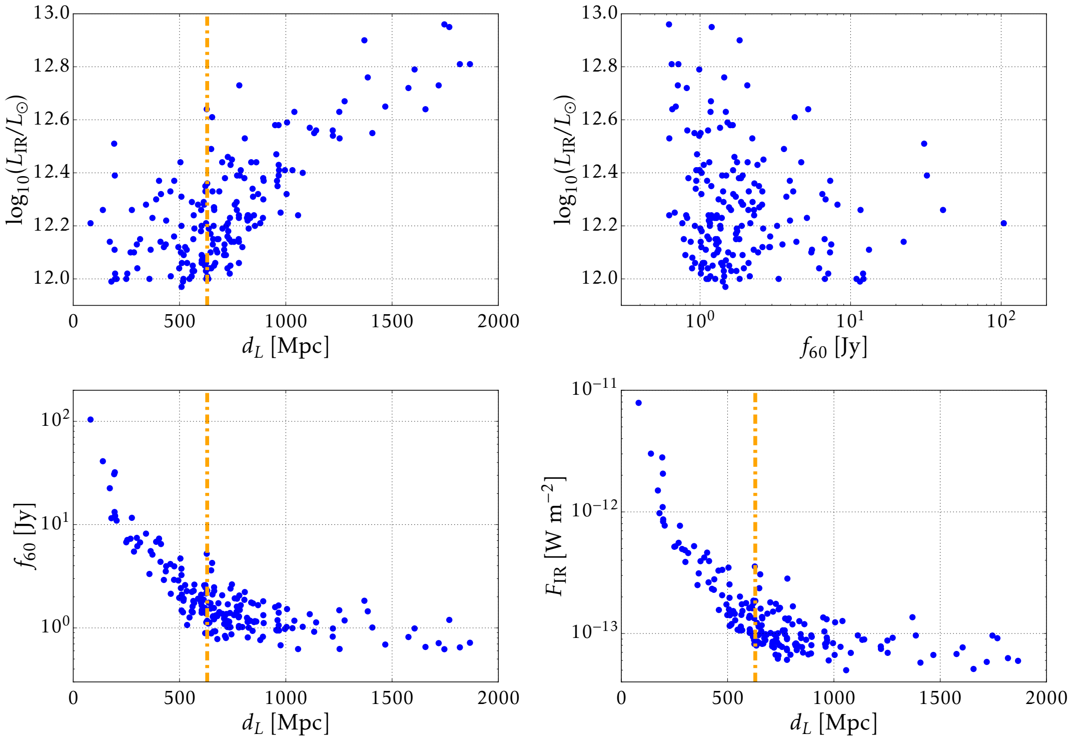

FIGURE 2.13: Correlations of some quantities of the initial selection of 189 ULIRGs, indicated by the blue dots. These include the luminosity distance d_L, flux at 60 μm f_{60}, total IR luminosity L_{IR}, and total IR flux $F_{\mathrm{IR}} = L_{\mathrm{IR}}/(4\pi d_L^2)$. The orange dash-dotted line indicates the redshift cut at $z = 0.13$ of the representative ULIRG sample used in the IceCube stacking analysis.

2.3.2 Catalog Overlaps

As a consistency check of the initial selection of 189 ULIRGs, the overlap is studied between the three ULIRG catalogs. A summary of the cuts on galactic latitude, equatorial declination, and flux at 60 μm is presented in Table 2.1 for the three catalogs. From these cuts, one expects that Catalogs 2 and 3 contain all sources of Catalog 1 within their respective coverage of the sky. Analogously, one expects that all sources in Catalog 3 have a counterpart in Catalog 2 within the spatial and flux cuts of the latter. Table 2.2 compares these expected overlaps with their observations.

The observed numbers of overlapping ULIRGs correspond well with the expectations. However, some minor inconsistencies can be noticed, which are discussed in more detail below:

- One additional source is observed in Catalog 3 compared to the number expected from Catalog 1. The object is named Superantennae, and has a flux density $f_{60} = 5.48 \pm 0.22$ Jy reported in the IRAS FSC [286]. However, in the more recent IRAS RBGS (i.e. Catalog 1), this object is omitted since it has a value $f_{60} = 5.16 \pm 0.03$ Jy [215], which falls below the RBGS threshold of $f_{60} > 5.24$ Jy. Since this object was selected from Catalog 3, the former value for f_{60} is used in this work.

- One additional source is observed in Catalog 3 compared to the expected number within the cuts of Catalog 2. This object, 2MASX J08380365+5055090, has a total IR luminosity $\log_{10}(L_{\mathrm{IR}}/L_\odot) = 12.01 \pm 0.03$ reported in Catalog 3. From this value, it can be suspected that this object would likely be classified as a LIRG ($10^{11} L_\odot \leq L_{\mathrm{IR}} < 10^{12} L_\odot$) using the criteria of Catalog 2.

Quantity	Catalog 1	Catalog 2	Catalog 3
Galactic latitude	$\lvert b\rvert > 5°$	$\lvert b\rvert > 30°$	see [287]
Equatorial declination	—	$\delta > -40°$	see [287]
Flux at 60 μm	$f_{60} > 5.24$ Jy	$f_{60} > 1$ Jy	$f_{60} \gtrsim 0.6$ Jy

Table 2.1: Spatial cuts and flux density cuts reported by the three ULIRG catalogs.

Number of overlapping ULIRGs	Observed	Expected
in Catalog 2 within cuts of Catalog 1	8	8
in Catalog 3 within cuts of Catalog 1	22	21
in Catalog 3 within cuts of Catalog 2	95	94

Table 2.2: Comparison of the observed and expected number of overlaps between the three ULIRG catalogs. Each row is a comparison of the first named catalog with the second named catalog within the cuts of the latter (see also Table 2.1).

2.3.3 ULIRG Selection Bias

Consider a generic standard-candle source population with a characteristic luminosity L_0 and a uniform source density n that does *not* evolve with redshift. The total number of sources within a certain luminosity distance d_L^{thresh} is then given by

$$N\left(d_L < d_L^{\mathrm{thresh}}\right) = \frac{4\pi n}{3}\left(d_L^{\mathrm{thresh}}\right)^3. \tag{2.7}$$

If we define a flux threshold as

$$f_{60}^{\mathrm{thresh}} = \frac{L_0}{4\pi\left(d_L^{\mathrm{thresh}}\right)^2}, \tag{2.8}$$

our assumptions imply that the number of sources with a flux larger than this threshold is equal to the number of sources within the corresponding threshold distance, $N\left(f_{60} > f_{60}^{\mathrm{thresh}}\right) = N\left(d_L < d_L^{\mathrm{thresh}}\right)$. Thus, by combining Equations (2.7) and (2.8) we find the power-law relation

$$N\left(f_{60} > f_{60}^{\mathrm{thresh}}\right) \propto \left(f_{60}^{\mathrm{thresh}}\right)^{-3/2}. \tag{2.9}$$

An unbiased selection of homogeneous, standard-candle sources is therefore expected to be compatible with Equation (2.9).

The ULIRGs selected for this work are limited to redshifts $z \leq 0.35$, as shown in Panel (a) of Figure 2.12, within which redshift-evolution effects are expected to be relatively small (Figure 2.7). Furthermore, the IR luminosities of the selection, shown in Panel (b) of Figure 2.12, are constrained within $\log_{10}(L_{\mathrm{IR}}/L_\odot) \in [12, 13]$. Hence, for the purpose of the following discussion, we can approximate the ULIRG source class as a homogeneous standard-candle population within $z \leq 0.35$.

Figure 2.14 shows the observed relation between $N\left(f_{60} > f_{60}^{\mathrm{thresh}}\right)$ and f_{60}^{thresh} for the initial selection of 189 ULIRGs (blue circles). The observed flattening at the lowest flux thresholds is consistent with an IRAS sensitivity $f_{60} \approx 1$ Jy. However, the kink at $f_{60}^{\mathrm{thresh}} \sim 2.5$ Jy indicates that the initial ULIRG selection likely misses objects with 1 Jy $\leq f_{60} <$ 5.24 Jy, called "1-Jy sources" hereafter. This is due the fact that Catalog 2, although complete, only covers 40% of the sky. In addition, the required *Spitzer* observations limit the coverage of Catalog 3.

The number of selected 1-Jy sources $N_{\mathrm{sel}} = 135$ can be corrected in order to account for this selection bias. As explained in Section 2.3.2, the selection is consistent with the statement of [246] that Catalog 2 is complete within its sky coverage. In particular, effectively all 1-Jy sources of Catalog 3 are also listed in Catalog 2. Hence, the number of 1-Jy sources is corrected as $N_{\mathrm{corr}} = 0.4N_{\mathrm{FSC}} = 0.4N_{\mathrm{sel}} \times N_{\mathrm{FSC}}/N_{\mathrm{sel}} \approx 0.49N_{\mathrm{sel}}$, where $N_{\mathrm{FSC}} = 111$ is the total number of ULIRGs in the 40% of the sky covered by Catalog 2.

The above correction is applied to each data point within 1 Jy $\leq f_{60}^{\mathrm{thresh}} <$ 5.24 Jy in Figure 2.14 (green triangles). Note that a different correction is required for ULIRGs with $f_{60} < 1$ Jy, but these will be of no further relevance for this work (see Section 2.3.4). After the correction, the artifacts of the selection bias have been relatively smoothed out. Moreover, a log-linear fit through the corrected data points yields a best-fit slope -1.498 ± 0.020, which is in agreement with the $-3/2$ value expected from Equation (2.9). This enforces the previous statement that the selection bias of the initial ULIRG selection is indeed a consequence of limited sky coverage.

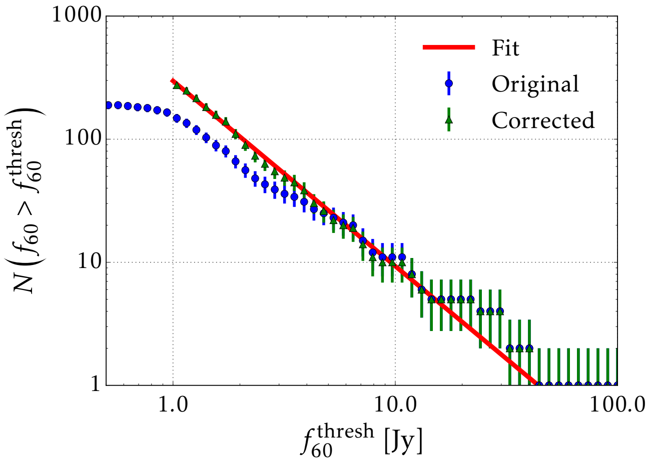

FIGURE 2.14: Number of ULIRGs with a 60-μm flux f_{60} larger than a certain threshold f_{60}^{thresh} as a function of that threshold. The blue circles indicate the direct observations of the initial ULIRG selection, while the green triangles correct these observations for the limited sky coverage of the selection for sources with 1 Jy $\leq f_{60} <$ 5.24 Jy. The log-linear fit to the corrected data points is also shown.

2.3.4 The Representative ULIRG Sample

The purpose of the ULIRG selection is to perform an IceCube stacking analysis on these objects, and to relate its results to the neutrino emission originating from the full population of ULIRGs stretching over cosmic history. The latter can be achieved by obtaining a representative sample of the local ULIRG population. Thus, a **completeness cut** is made on the initial ULIRG selection. The completeness is determined by finding the redshift up to which the least luminous ULIRGs (i.e. $L_{\mathrm{IR}} = 10^{12} L_{\odot}$) can be observed, given a conservative IRAS sensitivity of $f_{60} = 1$ Jy. To do so, the observed correlation between f_{60} and the total IR flux F_{IR} (8–1000 μm) of the ULIRG sample is used. Since the f_{60} measurements are optimized separately for the different IRAS surveys, these are taken in the following order:

- From the RBGS if available;
- From the FSC if not available in the RBGS;
- From the PSC if not available in the RBGS or FSC.

Note that the data from the FSC and PSC are obtained from NED. The total IR flux[27] $F_{\mathrm{IR}} = L_{\mathrm{IR}}/(4\pi d_L^2)$ is calculated using the L_{IR} values provided by the catalogs, and using the luminosity distance d_L computed from the redshift measurements.

To determine the F_{IR} value corresponding with $f_{60} = 1$ Jy, a log-linear fit is performed,

$$\log_{10}\left(\frac{f_{60}}{\mathrm{Jy}}\right) = a \log_{10}\left(\frac{F_{\mathrm{IR}}}{\mathrm{W\ m^{-2}}}\right) + b. \tag{2.10}$$

This is illustrated in Figure 2.15, and the resulting best-fit parameters are $a = (95.85 \pm 0.81) \times 10^{-2}$ and $b = 12.645 \pm 0.094$. Subsequently, the luminosity distance $d_L = \sqrt{L_{\mathrm{IR}}/(4\pi F_{\mathrm{IR}})}$ is determined for which $L_{\mathrm{IR}} = 10^{12} L_{\odot}$, given $f_{60} = 1$ Jy or $F_{\mathrm{IR}} \approx 6.4 \times$

[27] Although the three ULIRG catalogs use Equation (2.6) to estimate the total IR luminosity, they do not directly provide values of the total IR flux.

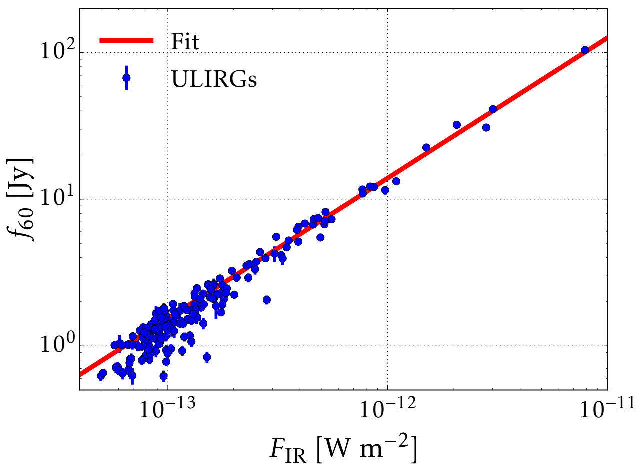

FIGURE 2.15: Correlation between the IRAS flux density at 60 μm, f_{60}, and the total IR flux between 8–1000 μm, F_{IR}, for the initial selection of 189 ULIRGs. The log-linear fit to these observations is also shown.

10^{-14} W m^{-2} using Equation (2.10). The result is $d_L \sim 700$ Mpc, which corresponds to a redshift $z \sim 0.143$. However, the uncertainties on L_{IR} were not taken into account, since they are not provided by Catalogs 1 & 2. Therefore, a conservative cut at $z = 0.13$ is performed, as indicated in Panel (a) of Figure 2.12. This results in a final sample of 75 ULIRGs, which is shown in Figure 2.16. See Appendix C for a detailed list of these 75 objects.

The redshift cut at $z = 0.13$ effectively corresponds with a flux constraint $f_{60} \gtrsim 1$ Jy (bottom left panel of Figure 2.13). However, the final sample of 75 ULIRGs likely misses a number of 1-Jy sources (1 Jy $\leq f_{60} <$ 5.24 Jy) due to the limited sky coverage of both Catalogs 2 and 3 (see Section 2.3.3). The final ULIRG sample contains 37 1-Jy sources from Catalog 2, covering 40% of the sky, and 15 1-Jy sources from Catalog 3 which are located in the complementary 60%. Hence, the final ULIRG selection likely misses ~40 1-Jy sources, assuming that Catalog 2 is indeed complete over its coverage. Note that the remaining 23 sources of the final ULIRG sample, for which $f_{60} \geq 5.24$ Jy, are taken from Catalog 1 which has a sky coverage that exceeds 99%. No missing sources are therefore expected in this high-flux regime.

The effect of these missing 1-Jy sources to the stacking analysis of Chapter 4 can be estimated using simulations. The stacking analysis searches for the cumulative ULIRG neutrino flux, where each source k is given a stacking weight $w_k \propto t_k r_k$, as discussed in Section 4.2.2. The stacking weight depends on a theoretical term, which is set to the total IR flux, $t_k = L_{\mathrm{IR}}/(4\pi d_L^2)$. In addition, the stacking weight depends on a detector-response term, r_k, which depends on the source declination and spectrum (Section 3.3.2). By testing how much the missing 1-Jy sources influence the cumulative stacking weight, one can determine their expected contribution to the combined neutrino flux of all sources.

For the simulations, 40 1-Jy sources are simulated evenly over the 60% of the sky not covered by Catalog 2. The detector weight r_k is computed for each source, while the theoretical weight t_k is fixed to the median value of the total IR flux of the 37 ULIRGs taken from Catalog 2. This simulation is repeated 10^4 times for both

$E_\nu^{-2.0}$ and $E_\nu^{-3.0}$ spectra, as shown in Figure 2.17. The resulting median contribution of 40 missing 1-Jy sources to the cumulative stacking weight is roughly 10% for both spectra. The final selection of 75 ULIRGs can therefore still be regarded as a representative sample of the local ULIRG population within $z \leq 0.13$.

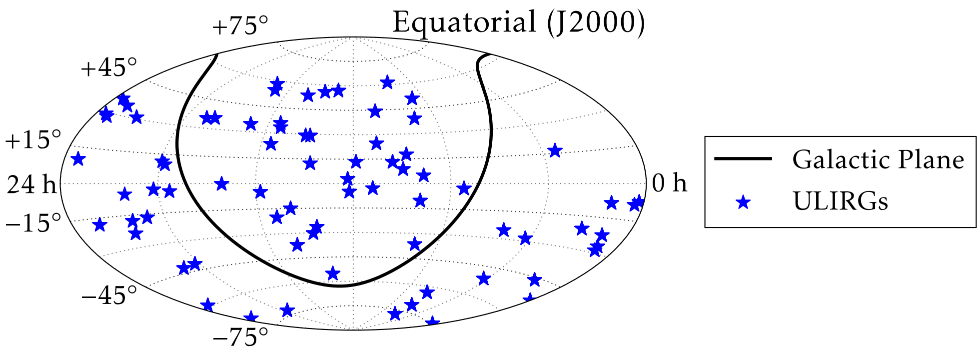

FIGURE 2.16: Skymap of the 75 ULIRGs selected for an IceCube search, which forms a representative sample of the local ULIRG population within a redshift $z \leq 0.13$.

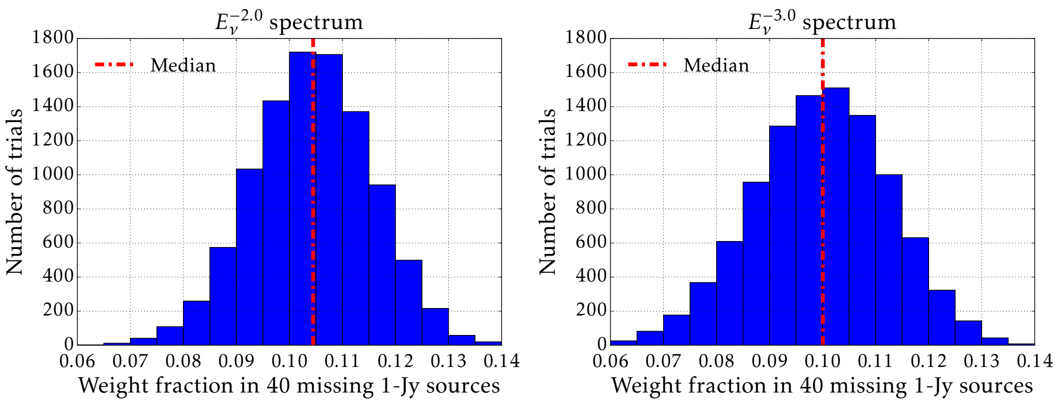

(a) $E_\nu^{-2.0}$ spectrum (b) $E_\nu^{-3.0}$ spectrum

FIGURE 2.17: Contributions of 40 missing 1-Jy sources with $z \leq 0.13$ to the total weight of the ULIRG stacking analysis. These are shown for both $E_\nu^{-2.0}$ and $E_\nu^{-3.0}$ spectra in Panels (a) and (b), respectively. Each distribution is constructed by performing 10^4 simulations of 40 1-Jy sources over the part of the sky that is not completely covered by the ULIRG catalogs.

Chapter 3

Detecting Astrophysical Neutrinos with IceCube

> *I have done a terrible thing: I have postulated a particle that cannot be detected.*
>
> — **Wolfgang Pauli**

> *How hard can it be?*
>
> — **Paul Coppin**

Introduction

When Pauli postulated the existence of the neutrino[1] back in 1930 [292], he stated his infamous quote given above. Nevertheless, only 26 years[2] after their postulation, Cowan & Reines [296] unambiguously proved the existence of these ghost particles originating from nuclear reactors at MeV energies. Almost a decade later, in 1965, two independent observations discovered MeV–GeV neutrinos produced in our atmosphere [297,298]. Shortly thereafter, the first extraterrestrial keV–MeV neutrinos from the Sun were discovered with the Homestake experiment [299]. Almost two decades later, Kamiokande-II, IMB, and Baksan simultaneously observed the first MeV neutrinos from outside our Solar System, i.e. from the now well-known supernova SN1987A [300].

Fortunately, contrary to Pauli's statement, it was thus proven that neutrinos *can* be detected—but that it is very hard to do so. Because their interactions with matter are very rare, neutrino experiments are generally forced to have a large detection volume. This volume is filled with some adequate target that can not only capture a neutrino from time to time, but also produce a distinguishable signal in the detector. To open the window for high-energy (TeV–PeV) neutrino astronomy, Markov proposed the idea of instrumenting large volumes of water or ice with optical sensors [301]. These sensors would then detect the optical Cherenkov radiation emitted by secondary particles produced in neutrino interactions. They would also have to be deployed at large depths to maximally avoid the contamination by cosmic rays.

DUMAND was the first concrete project of such an optical Cherenkov telescope, initiated during the 1980s [302]. It was started near the coast of Hawaii, although it

[1] Originally, Pauli proposed the name "neutron" for his ghost particle, which was taken in 1932 by Chadwick when he discovered the heavy, electrically-neutral nucleon we know today by that name [290]. To distinguish Pauli's particle from the neutron, it was Amaldi who named it the "little neutral one," or "neutrino" in Italian [291].

[2] It is quite remarkable that neutrinos, the *ghost* particles, were discovered so soon after their proposal. To put this into context, it took nearly 50 years to discover the Brout-Englert-Higgs particle at the LHC [293,294], and almost a century to detect gravitational waves with LIGO-Virgo after Einstein predicted them in his theory of relativity [295]. Luckily, neutrinos are stable, and most importantly, *abundant*, which was vital for their eventual discovery.

had to be abandoned during the 1990s due to technical failures [303]. Nevertheless, DUMAND served as a pioneer for several detectors at the 0.01-km^3 scale. One of these was the Baikal Neutrino Telescope, located in Lake Baikal, Russia. Over the course of the 1990s, the Baikal experiment instrumented 200 metric tons of water with 192 optical sensors. As such, the Baikal Neutrino Telescope provided the first underwater measurements of atmospheric neutrinos [304]. Between 2004–2005, the detector was expanded with a course array of 36 additional sensors, in order to obtain a 0.01-km^3 detection volume [305]. However, this volume proved to be insufficient for the detection of astrophysical neutrinos. Consequently, since 2016, the experiment is being upgraded to the Baikal Gigaton Volume Detector (GVD) [153], which is planned to instrument 1 km^3 of deep-lake water with roughly 2,300 optical sensors.

A second 0.01-km^3 scaled detector inspired by the DUMAND project was AMANDA [306], located in the glacial ice of the geographic South Pole. AMANDA operated from 1997 through 2004, during which it was upgraded to AMANDA-II [307], instrumenting 0.15 km^3 of ice with 677 optical modules in total. After its decommission, it was succeeded by the current IceCube Neutrino Observatory. The third and last 0.01-km^3 successor[3] of DUMAND was ANTARES [119], deploying 900 sensors in the Mediterranean Sea. ANTARES was completed in 2008, after it was decommissioned in early 2022 to make way for KM3NeT [152], which is planned to be a cubic-kilometer telescope[4] in the coming decade.

IceCube, the main experiment relevant to this thesis, is currently the most advanced and only fully operational optical neutrino telescope with a volume $\geq$1 km^3. With over 5,000 optical sensors, it is the sole observatory that has been able to detect astrophysical TeV–PeV neutrinos to date, as discussed in Chapter 1. Section 3.1 gives an overview of the IceCube experiment, including the detection principle, instrumentation, online systems, and the various detection signatures that are called events. The distinction between background and astrophysical-signal events, and how they can be simulated, will also be discussed. Subsequently, the reconstruction of physical quantities such as the direction and energy will be described in Section 3.2 for the event signatures of interest to this work. Finally, Section 3.3 gives a description of the GFU event selection, which is the IceCube data used in the ULIRG stacking analysis outlined in Chapter 4.

3.1 The IceCube Neutrino Telescope

The **IceCube Neutrino Observatory** [310], depicted in Figure 3.1, is a 1-km^3 neutrino telescope buried deep within the glacial ice at the geographic South Pole. The goal of IceCube is to measure the Cherenkov emission of secondary particles produced in neutrino-ice interactions (Section 3.1.1). The detector is instrumented with 5,160 **digital optical modules** (DOMs; see Section 3.1.2) distributed over 86 vertical strings containing 60 DOMs each, deployed between 1450–2450 m below the surface. The typical vertical and horizontal DOM spacings are 17 m and 125 m,

[3]DUMAND also served as a precursor to NEMO [308] and NESTOR [309], which are on their turn prototypes for the novel KM3NeT project.

[4]KM3NeT is planned to comprise two major building blocks of 4,140 optical sensors each [152]. ARCA, under construction near the coast of Sicily, Italy, will instrument 1 km^3 of water to perform TeV–PeV neutrino astronomy. On the other hand, near the coast of Toulon, France, the compact 0.01-km^3 ORCA is being built to target neutrino physics down to GeV energies.

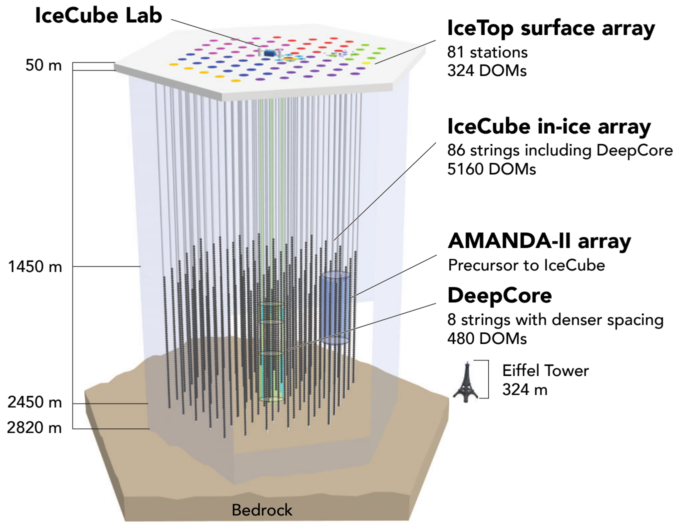

(a) IceCube array

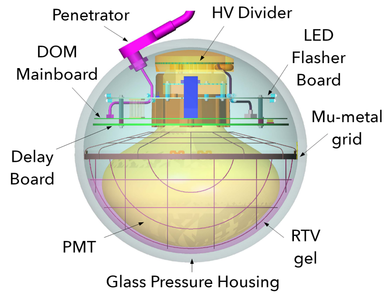

(b) DOM

FIGURE 3.1: Illustration of the IceCube Neutrino Observatory, adapted from [310]. Panel (a) depicts the complete in-ice array including DeepCore, as well as the IceTop surface array. The location of AMANDA-II, the precursor to IceCube, is also indicated. Raw IceCube and IceTop data is sent to the IceCube Lab (ICL) at the surface, which contains the online systems for data acquisition, triggering, and filtering. Panel (b) shows a schematic of the digital optical module (DOM) that lies at the heart of both IceCube and IceTop. Its main components are described in Section 3.1.2.

respectively, in order to detect neutrinos with energies between 100 GeV and 10 PeV.

The central **DeepCore** component of IceCube, which is designed to detect neutrinos down to energies of several GeV, comprises a denser subarray of 8 strings with 7-m vertical spacing and 70-m horizontal spacing. Complementary to IceCube, the **IceTop** surface array consists of 162 ice tanks with two DOMs each—one with a low gain and the other with a high gain to obtain a large dynamic range—and is used for the detection of cosmic-ray air showers. Since DeepCore and IceTop are not directly relevant to the study presented in this work, the reader is referred to [18, 311] for more details on these instruments.

In the next couple of years, around 700 additional optical modules will be deployed over 7 strings between the existing DeepCore strings of IceCube, as shown in Figure 3.2. This so-called **IceCube Upgrade** [312] will thus yield a denser array with a vertical spacing of 3 m and a horizontal spacing of 20 m. As such, the IceCube Upgrade will allow us to probe neutrino physics down to GeV energies and perform detailed calibrations of the ice. The latter is also expected to improve the reconstruction accuracies of the already existing IceCube data samples. Furthermore, several novel designs for the optical modules [313–316] will be tested.

The IceCube Upgrade will lay the foundations for the future **IceCube-Gen2** [141], illustrated in Figure 3.2. The optical component of IceCube-Gen2 is planned to encompass a volume of 8 km^3 around the existing IceCube array in the next decade. With its current baseline design, a total of 9,600 optical modules will be deployed between depths of 1325–2575 m over 120 strings, with average horizontal and vertical spacings of 240 m and 16 m, respectively. While this optical in-ice component will target astrophysical neutrinos with energies up to 10 PeV and aim

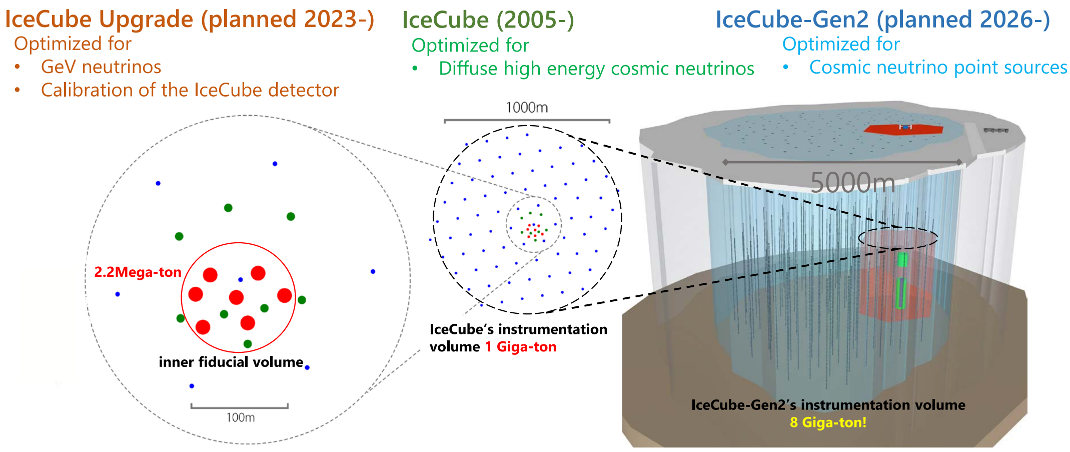

FIGURE 3.2: Schematic illustration of the future expansions of IceCube, taken from [314]. The IceCube Upgrade, a dense subarray of 7 strings, will be built over the next years. The current design of IceCube-Gen2 consists of an optical in-ice array with a volume of 8 km^3, and above that, a radio surface array covering an area of 500 km^2.

to identify their sources, the radio component of IceCube-Gen2 will search for neutrinos in the PeV–EeV regime (Figure 1.18). The current baseline design plans to construct an array of 200 radio stations—covering an area of 500 km^2—consisting of both surface and 200-m deep radio antennas. Combining the optical and radio components of IceCube-Gen2 will thus yield an unprecedented coverage of the astrophysical neutrino spectrum in the GeV–EeV range.

From this point onward, the focus lies exclusively on the current IceCube detector, and its usage for the study of high-energy astrophysical neutrinos and their sources.[5] Data recorded by the DOMs is sent via cables on the strings (or tanks) to the surface, where they are collected in the **IceCube Lab** (ICL). The ICL contains all online systems (Section 3.1.3) responsible for the data acquisition (DAQ) as well as data processing and filtering (PnF). These systems construct physics events from the data, which correspond to different detection patterns in IceCube (Section 3.1.4). These events form the foundation of all IceCube analyses, which typically search for a small astrophysical signal in data dominated by atmospheric backgrounds (Section 3.1.5). To assess the performance of such analyses, dedicated simulations are required (Section 3.1.6). In the following, a more detailed overview is given of these different topics.

3.1.1 Detection Principle

When a high-energy ($E_\nu \gtrsim 100$ GeV) neutrino ν_ℓ or antineutrino $\overline{\nu}_\ell$ of any leptonic flavor $\ell \in \{e, \mu, \tau\}$ traverses the South Pole ice, it can interact weakly with an ice

[5]It is worth pointing out that IceCube is also used to search for indirect signatures of dark matter in astrophysical objects. Furthermore, observations of atmospheric neutrinos allow to perform detailed studies of fundamental neutrino physics (beyond the Standard Model). On top of that, IceCube's unique location allows to perform geological studies of the South Pole. See [114, 115] for an overview of the most recent IceCube studies.

nucleus N via two possible deep-inelastic-scattering[6] (DIS) channels,

$$\underbrace{\begin{aligned} \nu_\ell + N &\xrightarrow{W^+} \ell^- + X, \\ \overline{\nu}_\ell + N &\xrightarrow{W^-} \ell^+ + X, \end{aligned}}_{\text{charged current}} \qquad \underbrace{\begin{aligned} \nu_\ell + N &\xrightarrow{Z^0} \nu_\ell + X, \\ \overline{\nu}_\ell + N &\xrightarrow{Z^0} \overline{\nu}_\ell + X. \end{aligned}}_{\text{neutral current}} \tag{3.1}$$

On the one hand, the (anti)neutrino can interact via the **charged-current** (CC) channel through the exchange of an electrically charged $W^\pm$ boson. In this process, the (anti)neutrino is converted to a relativistic charged lepton $\ell^\mp$ of the same flavor, which carries $\gtrsim$50% of the original (anti)neutrino energy[7] [94]. On the other hand, in a **neutral-current** (NC) interaction, the (anti)neutrino scatters off the nucleus through the exchange of an electrically neutral Z^0 boson. In both CC and NC interactions, the ice nucleus is shattered, and its fragments X result in the production of a relativistic hadronic shower[8] in the surrounding ice. For CC interactions, this shower carries the remaining (anti)neutrino energy that was not transferred to the charged lepton, while for NC interactions, the (anti)neutrino transfers roughly between 20–30% of its energy to the shower [317].

Figure 3.3 shows the **cross section** of (anti)neutrino interactions with oxygen[9] nuclei over the energy range relevant to IceCube, as predicted by the Standard Model [318] (see also Appendix B). For all flavors, the CC cross section exceeds that of NC DIS by a factor ~3. For each interaction, the cross section for neutrinos slightly exceeds that of antineutrinos, although they become identical above ~1 PeV. IceCube observations of the (anti)neutrino-nucleon cross section are consistent with these Standard-Model predictions [319, 320]. Figure 3.3 also shows the subdominant contributions of (anti)neutrino CC DIS in which an on-shell[10] $W^\pm$ boson is produced. However, around 6.3 PeV, $\overline{\nu}_e$ become capable of producing an on-shell W^- boson through the CC interaction with atomic *electrons*. This process is known as the Glashow resonance[11] [322], which dominates the $\overline{\nu}_e$-ice cross section at 6.3 PeV. Nevertheless, it should be noted that the overall (anti)neutrino-ice cross section discussed here is small. It is roughly a factor 10^7–10^8 smaller compared to the total cross section of pp-interactions, which is $\mathcal{O}(100 \text{ mb} = 10^{-25} \text{ cm}^2)$ for the energies relevant here (see Figure 1.4). The low expected flux of high-energy astrophysical (anti)neutrinos (Section 1.2.1) combined with their small interaction cross sections is the main motivation behind the 1-km^3 size of IceCube.

---

[6] At the energies relevant to IceCube, the neutrino is capable of probing the inner structure of the ice nucleus. It therefore interacts with a quark within one of the nucleons that compose the nucleus. In particle physics, this is referred to as deep inelastic scattering.

[7] The exact amount depends on the inelasiticity of the deep inelastic scattering, i.e. the fraction of neutrino energy that is deposited into the hadronic component X.

[8] These hadronic showers contain a plethora of relativistic particles, both charged and neutral. They are analogous to the cosmic-ray showers described in Section 1.1.1; the difference here is that the shower propagates through ice instead of air.

[9] Recall that ice molecules consist of two hydrogen nuclei, i.e. two protons, and one oxygen nucleus formed by eight protons and eight neutrons.

[10] In quantum field theory [321], on-shell force mediators are real particles with fields that obey the equations of motion. Off-shell mediators, on the other hand, are described as "virtual" particles that do not satisfy this condition.

[11] Indications of the first ever Glashow event in IceCube were recently reported in [96], as discussed in Section 1.2.1.

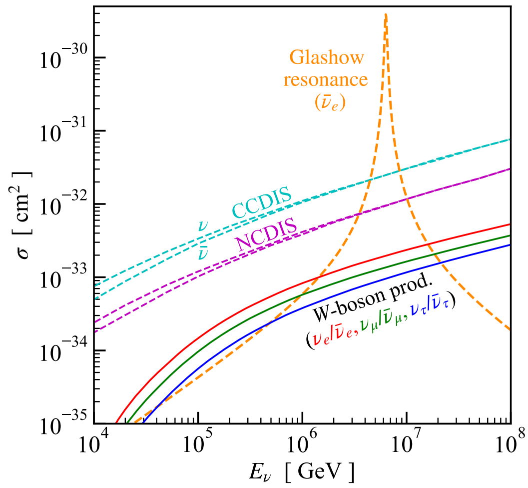

FIGURE 3.3: Cross section σ of (anti)neutrino-ice interactions as a function of the (anti)neutrino energy E_ν, taken from [318]. Charged-current (CC) and neutral-current (NC) deep inelastic scatterings (DIS) are denoted by the cyan and magenta dashed lines, respectively. In each case, the upper line corresponds with $\nu_\ell \equiv \nu$ interactions, and the lower line corresponds with $\overline{\nu}_\ell \equiv \overline{\nu}$ interactions. Solid lines represent the cross section for CC DIS that results in the production of an on-shell $W^\pm$ boson. The orange dashed line indicates the Glashow resonance, which yields a peak in the $\overline{\nu}_e$-ice cross section around 6.3 PeV.

Neutrino-ice DIS interactions such as those described above produce highly relativistic charged particles that travel through the medium with a speed v higher than the speed of light in that medium—$c/n(\lambda)$ with $n(\lambda)$ the wavelength-dependent refractive index. This creates a shock front[12] of electromagnetic radiation, also known as **Cherenkov emission**[13] [324, 325]. Cherenkov radiation is emitted in a cone around the charged particle (see also Figure 3.5), which is characterized by the opening angle

$$\cos\theta_c = \frac{1}{n(\lambda)\beta}, \tag{3.2}$$

where $\beta = v/c$. This angle is also known as the Cherenkov angle, and for highly relativistic particles ($\beta \approx 1$) traveling through ice ($n \approx 1.32$ between 300–600 nm) it has a value $\theta_c \approx 41°$ [326, 327]. The number of Cherenkov photons $\mathrm{d}N_\gamma$ emitted by a particle with charge Ze, per unit of wavelength $\mathrm{d}\lambda$ and distance $\mathrm{d}x$, is given by the Frank-Tamm relation [14, 325],

$$\begin{aligned}\frac{\mathrm{d}N_\gamma}{\mathrm{d}\lambda\,\mathrm{d}x} &= \frac{2\pi\alpha Z^2}{\lambda^2}\sin^2\theta_c \\ &= \frac{2\pi\alpha Z^2}{\lambda^2}\left(1 - \frac{1}{n^2(\lambda)\beta^2}\right),\end{aligned} \tag{3.3}$$

with $\alpha \approx 1/137$ the fine-structure constant. The Cherenkov spectrum is therefore

[12] This effect is analogous to a fighter jet creating a shock wave of sound when traveling faster than the speed of sound in air, resulting in a loud “bang” when the shock front reaches an external observer.

[13] Although named after Pavel Cherenkov, who discovered the properties of this radiation in the 1930s, the phenomenon itself was originally recorded by Marie Curie in 1910 [323].

continuous and its intensity increases for shorter wavelengths.[14] It typically peaks in the UV regime, since at shorter wavelengths a cutoff is encountered where Equation (3.3) is no longer satisfied.

As we shall discuss in Section 3.1.2, IceCube DOMs are designed to observe the Cherenkov radiation emitted by the charged particles produced in (anti)neutrino-ice interactions. The remote location of the detector is chosen due to the fact that **glacial ice** is one of the most transparent solids for photons with wavelengths between 300–500 nm [329, 330]. Furthermore, at the depths of IceCube, photon scattering becomes minimal, since air bubbles trapped in the ice—the major source of scattering at relatively shallow depths—succumb under the pressure of the glacier [331]. Figure 3.4 shows the scattering and absorption coefficients[15] of the South Pole ice reported in [330], as a function of both depth and wavelength. Below ~1400 m, the depth-dependent structure of both coefficients originates from insoluble dust impurities[16] and volcanic ashes [332]. One particularly large concentration of dust and ashes is observed at ~2000 m depth,[17] which is colloquially referred to as the "dust layer."

Even though the South Pole ice is an ideal medium for a Cherenkov telescope, a detailed understanding of the ice properties is imperative for the reconstruction of detected events in IceCube. Using light-emitting diode (LED) flashers on the DOMs (Figure 3.1), in-situ measurements have not only probed the transparency of the

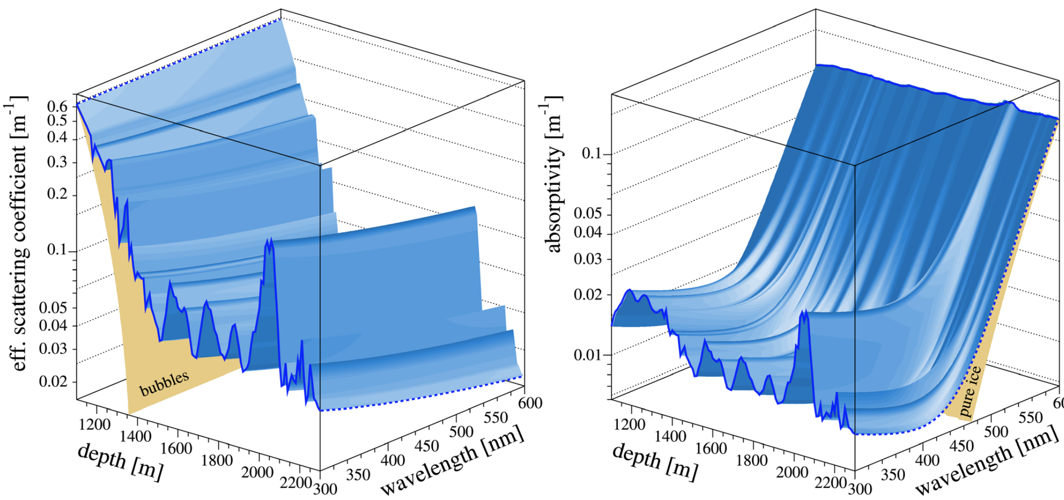

Figure 3.4: Optical/UV properties of the glacial ice at the South Pole as a function of depth and photon wavelength [330]. The left panel shows the effective scattering coefficient, also indicating the contribution of air bubbles which becomes negligible below 1300 m. The right panel shows the absorptivity, which is compared to that expected for pure ice. Depth-dependent impurities in the form of dust and ashes are the main causes of absorption and scattering in the South Pole ice. The prominent impurity around a depth of 2000 m is called the dust layer.

[14] This is why Cherenkov light has a characteristic blue glow which can be observed with the naked eye in e.g. open-pool nuclear reactors [328].

[15] These coefficients are the inverse of the mean free path of photons w.r.t. scattering and absorption. Hence, they give a measure for the amount of scattering and absorption that occurs in the ice.

[16] The dust is comprised of mineral grains, sea-salt crystals, acids, and soot [330].

[17] This layer accumulated some ~6.5×10^4 yr ago in the midst of the Last Glacial Period [333], and is associated with major volcanic activity [332].

surrounding ice [334], but also found evidence for anisotropies in the photon attenuation correlated with the flow[18] of the glacial ice sheet [335, 336]. Such studies of the ice properties allow us to continuously improve the ice models used in event reconstructions. However, current uncertainties in these ice models remain one of the main systematic effects in IceCube searches (see also Section 5.1.4).

3.1.2 Digital Optical Modules

Panel (b) of Figure 3.1 displays the various hardware components that comprise an IceCube DOM. The most prominent component is the **photon-multiplier tube** (PMT), which is designed to detect individual Cherenkov photons with wavelengths between 300–650 nm. When a photon reaches the PMT, it will create a photoelectron (PE) through the photoelectric effect, which serves as a measure for the charge deposited at the DOM. A high-voltage (HV) gain multiplies the original electron to 10^7 electrons, which on their turn yield an analog electric signal. The **charge** deposited by these electrons is typically measured in terms of $1\text{ PE} \equiv 10^7 e = 1.602$ pC. The optimal quantum efficiency—i.e. the ratio of detected photoelectrons w.r.t. the number of incident photons—of most PMTs is 25% at 390 nm, whereas DeepCore PMTs have a higher quantum efficiency of up to 34% [337]. In order to shield the PMT from the geomagnetic field, which affects the electron collection efficiency, it is encased in a mu-metal grid. Finally, the PMT is secured within the glass housing of the DOM by an optically clear RTV-silicon gel.

Whenever a charge threshold of 0.25 PE is reached, a so-called **hit** is recorded, and the analog waveform of the PMT is captured and digitized by the DOM Main Board. To record the waveform down to about 75 ns before the start of the threshold excess, the PMT signal is first routed through the delay board, which essentially consists of a 10-m wound-up copper wire. The **waveform digitization** is performed by both a custom-built Analog Transient Waveform Digitizer (ATWD, see also [338]) and a fast analog-to-digital converter (fADC), which is made of switched capacitor arrays. The ATWD records 427 ns of the waveform at a high sampling rate of 3×10^8 samplings per second (sps), and it utilizes three different channels with varying amplifier gains to avoid saturation during readout. In order to include the weaker contribution of photons that traveled longer distances in the ice, the fADC covers a longer time window of 6.4 μs at a lower sampling rate of 4×10^7 sps.

The DOM Main Board is also responsible for controlling and supplying power to all electronic components inside the module, as well as communicating with neighboring DOMs and the DAQ system at the surface. In addition, it takes care of the **DOM calibration**. Due to their excellent stability, calibration of the PMT waveforms is only required once per year in IceCube (monthly for IceTop to account for changes in temperature). This calibration is performed using DOMCal [310], a software package which utilizes inputs from dedicated electronic components on the DOM Main Board with known references for single photoelectrons, electric charges, voltages, and timing. Furthermore, calibration of the internal DOM clocks is performed continuously during data taking using the Reciprocal Active Pulsing Calibration (RAPCal) software [338]. RAPCal translates timestamps from each DOM clock to synchronized clocks in the ICL, and its calibration is occasionally verified between neighboring DOMs using the LEDs on the Flasher Board. Apart from time

[18] Just like water in a river, ice in a glacier is not static but flows downstream at a rate of $\mathcal{O}(10\text{ m yr}^{-1})$ [335, 336].

calibration, LED flashing is also used to accurately determine the relative DOM positions in the ice, as well as measuring local ice properties.

All DOM electronics have been designed to last for a couple of decades, while their glass housing protects them from the surrounding pressures of the glacial ice. **DOM reliability** is imperative for detector operations, since direct access to the DOMs has become impossible since their deployment.[19] In 2016—5 years after the completion of IceCube—98.4% of all DOMs (including IceTop) were operating smoothly, with most DOM failures occurring during deployment. By 2030, the overall DOM survival fraction is expected to be $97.4 \pm 0.3\%$ [310].

3.1.3 Data Acquisition & Online Processing and Filtering

Every second, the central DAQ system [338] collects the hit data that is stored on the Main Board of each DOM. The amount of information sent to the surface depends on whether the hit was recording in **hard local coincidence** (HLC), i.e. within a time window of ± 1 μs, with another hit in at least one of the neighboring or next-to-neighboring DOMs. For HLC hits the complete waveform is sent to the surface, since they are expected to be causally connected to the Cherenkov emission of high-energy particles. On the other hand, soft-local-coincidence (SLC) hits—those that do not satisfy the HLC condition—are mainly caused by dark noise. Effects that contribute to the overall dark-noise rate include electronic noise, radioactive decays, and luminescence in the glass components of the DOM. Since SLC hits are unlikely[20] to be caused by high-energy physics events of interest, only a time signature and brief charge summary are transmitted to the central DAQ.

Subsequently, in order to select hits induced by high-energy particles while avoiding contamination of stray noise, the data is required to pass a certain trigger threshold for it to be read out. The main trigger in IceCube is the **simple multiplicity trigger** (SMT), which searches for causally connected HLC hits in the data stream. The SMT or SMT-8 requires a minimum[21] of 8 HLC hits within a sliding time window of 5 μs. The complete data-readout window of the SMT-8 covers 4 μs before and 6 μs after the trigger conditions are satisfied. Other triggers (see [310] for an overview) combine similar hit-multiplicity requirements with some additional topological criteria. Since multiple trigger conditions can be satisfied simultaneously, all trigger windows are combined into one Global Trigger. A readout of Global-Trigger data is called a DAQ event, which is written to disk and prepared for further processing. The median[22] trigger rate of DAQ events in IceCube is 2.7 kHz, which corresponds to a data-storage consumption of 1 TB day^{-1} [310]. The storage disks are collected and transferred to Madison, Wisconsin on a yearly basis.

Next, the DAQ sends its recorded events to the online PnF system. Here, the DAQ events are first split into multiple **physics events** corresponding to the different triggers that were launched during the Global-Trigger window. In this work, only

[19] The deployment of the IceCube strings was performed over several austral-summer seasons between 2005–2011 using a dedicated hot-water drill designed to melt the glacial ice [339]. Once the holes were drilled, the strings were lowered into them, after which the water inside the holes refroze. As such, the DOMs are now permanently frozen inside the South Pole glacier.

[20] The per-DOM dark-noise rate is 560 Hz (780 Hz for DeepCore DOMs). For comparison, the HLC hit rate associated with cosmic-ray muons ranges between 5–25 Hz [310].

[21] Since the causality argument fundamentally depends on the inter-DOM spacing, the SMT requires at least 3 (resp. 6) hits in a sliding time window of 2.5 μs (resp. 5 μs) for DeepCore (resp. IceTop).

[22] The majority of triggered events are cosmic-ray muons, whose rate varies seasonally between 2.5 kHz and 2.9 kHz [18].

physics events passing the SMT-8 are considered, which are subsequently cleaned to further remove hits that are caused by noise and low-energy particles. More details on the event-splitting and hit-cleaning procedures can be found in [340]. At this stage, the data needs to be **filtered** in order to:

- Select physics events of interest for IceCube analyses. The filters that are applied depend on the analysis in question; a detailed description of the event selection and the corresponding filters relevant to this thesis will be given in Section 3.3.1.

- Reduce the global event rate to a level that can be accommodated by the available satellite bandwidth of 100 GB day^{-1} for data transmission. Hence, the online filters are gauged in such a way that the rate of events which pass at least one filter comprises roughly 15% of the total DAQ event rate [310].

Finally, it is worth mentioning that the continuously-operating online systems of IceCube achieve an excellent **data-taking performance** [310]. The average uptime of IceCube, i.e. the fraction of time that the detector is actively taking data, exceeds 99%. This uptime can largely be attributed to the IceCube winterovers,[23] who can swiftly repair software or hardware failures on site. Moreover, the time fraction that the detector operates with its full 86-string configuration, the so-called clean uptime, lies between 97–98% on average. The remaining 2–3% are data-taking periods where only a part of the detector configuration is active, or where maintenance or calibration is taking place.

3.1.4 Event Signatures

The waveform of each DOM hit that forms part of an event yields a measure for the deposited charge in that DOM. Since the Cherenkov light yield is directly proportional to the energy loss of the radiating particles [341], the total deposited energy of an event is found by combining the recorded charges of all DOMs. The overall **deposited-energy resolution** of IceCube is ~10–15% [317]. In addition, the $\mathcal{O}$(ns) time resolution of the array allows us to accurately separate DOM hits in time [310]. Combined with the event geometry, the timing is used to obtain directional information of the high-energy particles that caused the event, as discussed below.

Event signatures in IceCube are broadly classified in terms of their **topology**. For neutrino-induced events, this topology depends on the type of neutrino interaction in the ice—see Equation (3.1) and also Appendix B for related particle decays. A summary of the event topologies corresponding with the different neutrino-ice interactions is presented in Table 3.1; a more detailed description on these event signatures follows in the upcoming paragraphs. Note that neutrinos and antineutrinos of the same flavor $\ell \in \{e, \mu, \tau\}$ yield the same event signatures in the detector. As a consequence, they cannot be distinguished with IceCube on an event-by-event basis. From this point onward they will both be referred to as neutrinos, $\nu_\ell \equiv \nu_\ell + \overline{\nu}_\ell$, and no explicit distinction will be made between other particles and their antiparticle counterparts.

[23] Two IceCube winterovers spend a complete year at the South Pole, including 9 months of isolation from the rest of the world, to actively maintain the online systems of the detector. In addition, remote monitoring of the detector is performed by all members of the IceCube collaboration using a dedicated website called IceCube Live, available at https://live.icecube.wisc.edu/.

	$\nu_e + \overline{\nu}_e$	$\nu_\mu + \overline{\nu}_\mu$	$\nu_\tau + \overline{\nu}_\tau$
CC interaction	Cascade	Track (+ cascade)	Cascade / Double Bang [83%] Track (+ cascade) [17%]
NC interaction	Cascade	Cascade	Cascade

Table 3.1: Overview of the event signatures in IceCube for all neutrino flavors and interaction channels given in Equation (3.1). Neutrinos and antineutrinos can generally not be distinguished. The double-bang signature for tau neutrinos can only be discerned from a single cascade at the highest energies. Tracks are only accompanied by a cascade if the neutrino-interaction vertex is located within the detector volume.

Tracks

Muons are relatively long-lived particles which are capable of traversing several kilometers of ice at energies above 100 GeV [317]. Therefore, a muon is capable of crossing the entire IceCube array, leaving behind a track-like signature in the detector. An example of such a track is shown in the left panel of Figure 3.5. Hence, tracks form a golden channel to probe ν_μ through the CC interaction. A minor contribution of tracks is expected to come from CC interactions of ν_τ, since the secondary tau decays into a muon 17% of the time [14]. Tracks observed in IceCube are mostly produced by atmospheric muons and atmospheric muon neutrinos produced in cosmic-ray air showers, which form the main background for astrophysical-neutrino searches (Section 3.1.5).

The track geometry allows for an excellent directional reconstruction of the muon trajectory, which is directly linked to the arrival direction of the original neutrino. As will be shown in Section 3.2.1, a **subdegree angular resolution** is achieved on the muon direction in IceCube for muon energies $E_\mu \gtrsim 1$ TeV, making tracks ideal for neutrino astronomy. Furthermore, most tracks have a neutrino-interaction vertex that lies outside of the instrumented volume. This increases the effective volume of IceCube for this type of events, resulting in a larger ν_μ detection rate compared to other flavors. However, this same effect means that we typically cannot determine the muon energy at the vertex, which is required to obtain an estimate of the original neutrino energy. A proxy for the muon energy can be inferred from its radiative energy-loss pattern in IceCube (Section 3.2.3), which serves as a rough lower limit on the neutrino energy.

Cascades

All neutrino interactions result in the fragmentation of an ice nucleus, producing a hadronic shower in the ice. Since such a shower develops at scales much smaller than the inter-DOM spacing of IceCube—the typical shower size is roughly 10 m [317]—only the collective Cherenkov emission of the particles is observed. Due to the scattering of the photons, the resulting event signature from such a shower has a relatively spherical morphology, called a cascade, which is illustrated in the right panel of Figure 3.5. Hence, NC interactions of all neutrino flavors yield such a cascade signature.

In addition, electrons produced in CC interactions of ν_e produce an electromagnetic shower due to their radiative energy losses, which blends in with the hadronic shower. The collective Cherenkov emission of both showers is observed as a single

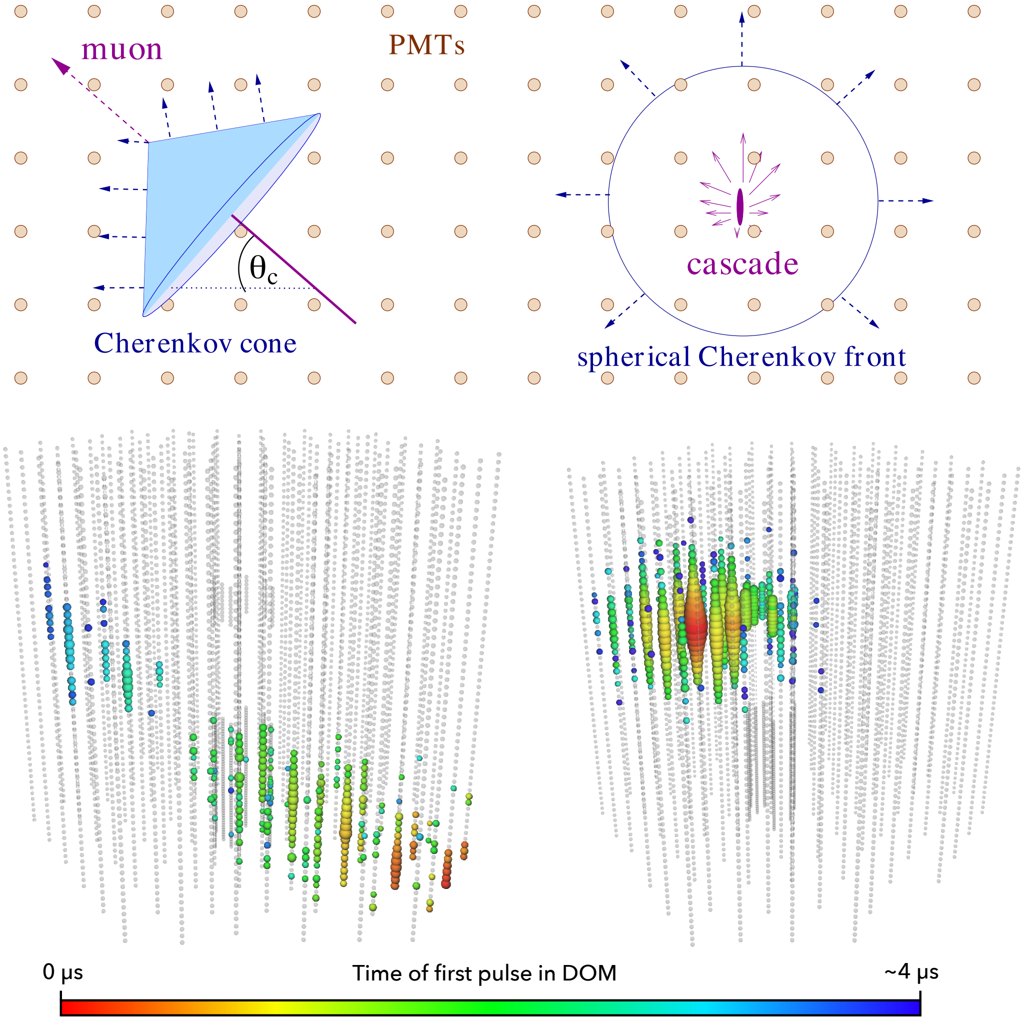

FIGURE 3.5: *Top*: Schematic of the two major event topologies in IceCube, adapted from [327]. On the left, a muon is shown traversing the detector in an upgoing direction. Its Cherenkov emission is characterized by the angle θ_c. On the right, a particle cascade is shown, whose physical size is smaller than the inter-DOM spacing of IceCube. This results in a somewhat spherical Cherenkov front. Note that the relative PMT spacing is not to scale. *Bottom*: Event displays, adapted from [340], of a 75-TeV muon track (left) and an $\mathcal{O}$(PeV) cascade (right). DOMs that recorded a hit are represented by colored spheres, where the size of a sphere is proportional to the measured charge. The color scale indicates when the DOM hits were recorded relative to the first hit. The track in this display is upgoing, and a region is visible where no track hits were recorded. This region corresponds to the dust layer (Figure 3.4), thus illustrating the impact of dust impurities to IceCube signals.

cascade. Finally, most CC interactions of ν_τ are also observed as single cascades, since the secondary tau decays hadronically or to an electron with branching ratios of 65% and 18%, respectively [14]. Both of these decays result in the production of a secondary particle shower whose emission cannot be distinguished from the original hadronic shower, except at the highest energies, as will be discussed below.

Due to the spherical geometry of cascades, the shower direction can only be inferred from the time profile of DOM hits. Consequently, the angular resolution of cascades is limited to $\gtrsim 8°$ [121]. On the other hand, since particle showers develop completely within the detector volume, IceCube acts as a calorimeter for this type of events. Hence, within the sensitive energy range of IceCube, all the energy deposited by the neutrino is measured, which is a good approximation for the neutrino energy in ν_e or ν_τ CC-induced cascades. However, for NC-induced cascades, only a fraction of the neutrino energy is deposited in the detector. Since ν_e or ν_τ CC and all NC-induced cascades cannot be distinguished on an event-by-event basis, the deposited energy is always considered to be a lower limit on the true neutrino energy.

Double Bangs

The tau produced in a CC interaction of a ν_τ has a decay length of roughly $50\ \mathrm{m} \times (E_\tau/\mathrm{PeV})$ [105]. Hence, for $E_\tau \gtrsim 1$ PeV, the distance traveled by the tau exceeds the vertical inter-DOM spacing of IceCube, yielding an observable displacement in the detector. When the tau eventually decays, the secondary shower produced in 83% of its decays will be observed as a second cascade that is clearly separated from the neutrino-interaction vertex. This second cascade can have a higher energy deposition than the first cascade—which has 25% of the original ν_τ energy on average [106]—allowing for additional discriminating power w.r.t. other neutrino flavors [105]. Thus, such a double-cascade signature, known as a "double bang," is a golden channel to probe ν_τ at the highest energies. However, due to the low neutrino flux at these energies, only one candidate astrophysical ν_τ has been identified with a double-bang signature to this date[24] [105], as mentioned in Section 1.2.2.

3.1.5 Astrophysical Signal versus Atmospheric Background

The main background for astrophysical-neutrino searches with IceCube consists of atmospheric muons and atmospheric neutrinos produced in cosmic-ray air showers, as shown in Figure 3.6. Both originate from the decay of mesons—mainly pions and kaons—like those described in Section 1.1.2. **Atmospheric muons** [343] dominate the observed DAQ event rate of 2.7 kHz at trigger level. However, due to the location of IceCube, these atmospheric muons only form a background in the Southern Sky, since they are only capable of traversing a handful of kilometers through the Earth [14]. Thus, for declinations $\delta \gtrsim -5°$, the background in IceCube is reduced drastically to the atmospheric-neutrino level. **Atmospheric neutrinos** [344,345] are capable of traversing the entire Earth, and therefore form an irreducible background over the full sky with a detection rate of $\mathcal{O}(\mathrm{mHz})$. Note that this is still several orders of magnitude higher than the astrophysical event rate of $\mathcal{O}(\mu\mathrm{Hz})$ (see Section 3.3 for more details). Nevertheless, the atmospheric background rates are only dominant

[24] The double-bang signature of this candidate ν_τ event is subtle, since the vertices of the two cascades are only separated by 17 ± 2 m [105]—a "double bangetje" in Anglo-Dutch lingo. It is worth noting that a complementary IceCube study [342] searched for double pulses in the waveform of a single DOM, which would indicate the presence of two distinct cascades induced by a ν_τ. This independent analysis also identified the same candidate astrophysical ν_τ event.

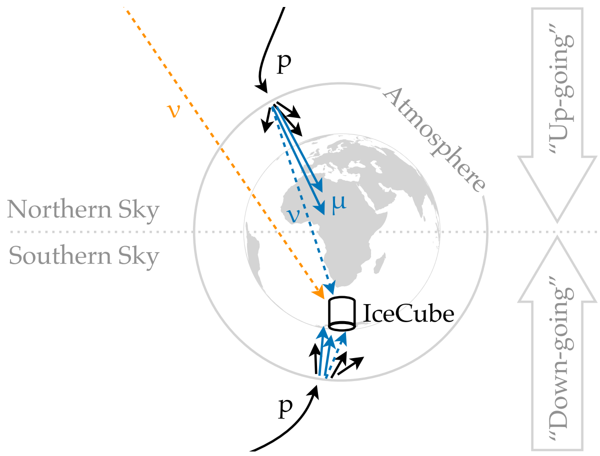

FIGURE 3.6: Illustration of the atmospheric backgrounds in the searches for astrophysical neutrinos (dashed orange arrow) in IceCube, adapted from [340]. Cosmic rays (in this case protons) create air showers, producing atmospheric muons (solid blue arrows) and atmospheric neutrinos (dashed blue arrows). Atmospheric muons dominate the observed event rate in IceCube, but only form a background in the Southern Sky since they cannot reach the detector from the Northern Hemisphere. Atmospheric neutrinos, on the other hand, form an isotropic background over the full sky. Events (usually tracks) from the Southern and Northern Hemispheres are labeled as downgoing and upgoing events, respectively.

at relatively low energies, i.e. below $\mathcal{O}(100\text{ TeV})$, since the energy spectrum of atmospheric muons and atmospheric neutrinos is relatively soft and well-described by an $E^{-3.7}$ power law[25] [343–345]. This is steeper than the $E_{\mathrm{CR}}^{-2.7}$ spectrum of the parent cosmic rays (see Section 1.1.1), due to the energy losses suffered by the propagating air-shower mesons before decaying.

To discern astrophysical neutrinos from the atmospheric background above several tens of TeV, diffuse analyses exploit the fact that astrophysical neutrinos have a comparatively harder spectrum ($\sim E^{-2.5}$; see Section 1.2.1). In addition, different techniques are applied to mitigate the overwhelming detection rate of atmospheric muons. For example, one can focus on cascade signatures [93], since atmospheric muons solely yield tracks in the detector. Moreover, the high-energy starting event sample (HESE) [91] uses the edges of the detector as a veto layer, since atmospheric muons cannot produce events that start in the detector. Combined with a total deposited-charge requirement of $Q_{\mathrm{tot}} \geq 6{,}000$ PE in the detector, the HESE method resulted in the discovery of the diffuse astrophysical-neutrino flux in 2013 [7, 8]. Another approach is to only consider events in the Northern Sky, where the atmospheric-muon component is absent. The diffuse IceCube analysis in the Northern Sky focuses on ν_μ only [92], exploiting the increased effective detection volume of IceCube compared to other flavors (Section 3.1.4).

Searches for neutrinos from astrophysical sources, like the ULIRG stacking analysis presented in Chapter 4, apply different strategies to identify a signal component in the background-dominated data. Since atmospheric events are distributed

[25] Above 100 TeV, a second, harder contribution is expected to arise in the atmospheric-neutrino spectrum due to the decay of charmed hadrons in air showers. This so-called "prompt" component is yet to be observed. The low flux of atmospheric neutrinos and the dominant contribution of the astrophysical component at these energies are the major challenges for the detection of the prompt atmospheric background [344, 345].

isotropically over a celestial hemisphere, such analyses search for a clustering of events on the sky, typically around the locations of interesting astrophysical sources (e.g. ULIRGs). As a consequence, neutrino-source analyses generally use event selections that solely consist of tracks, because of their superior angular resolution. Furthermore, events with higher energies are given a larger weight in the analysis, since they are more likely to be of astrophysical origin. In any case, the event selections for such searches are typically performed separately over the Northern and Southern Sky to take into account the different background characteristics of both hemispheres. The event selection used in this work will be discussed in Section 3.3.

3.1.6 Event Simulation

Monte-Carlo (MC) simulations of events form a key element in testing the performance of reconstructions, event selections, and IceCube analyses in general. Neutrino-induced events are simulated using the `ANIS` (All Neutrino Interaction Simulation) framework [346]. Here, neutrinos with a chosen power-law spectrum—typically a hard E_ν^{-1} or E_ν^{-2} spectrum to obtain enough statistics at the highest energies—are generated uniformly over the full surface of the Earth. They are then propagated towards IceCube and forced to interact within or near the detector volume.

Each simulated neutrino event is given a weight that is proportional to its **interaction probability** with which the secondary particles can be observed in IceCube. This probability compensates for the forced interaction and depends on the neutrino-ice DIS cross section (Figure 3.3). However, for neutrinos coming from the Northern Hemisphere, one also has to take into account that neutrinos can interact with the Earth before reaching IceCube. As shown in Figure 3.7, the Earth becomes opaque to neutrinos with energies[26] $E_\nu \gtrsim 100$ TeV. The simulated-event weight therefore includes the Earth transmission probability of the neutrino. The final weight used for the analysis of the simulated data includes a term that scales the neutrino-generation spectrum to any arbitrary neutrino spectrum of interest.

The atmospheric-muon background is generated using a cosmic-ray air-shower simulator called `CORSIKA` (Cosmic Ray Simulations for Kascade) [347]. The cosmic-ray primaries of the showers are generated according to a user-defined spectral model [347]. The muonic component of the shower that reaches the surface is then further propagated through the ice [348]. Muons that reach IceCube are subsequently stored, and they can be rescaled to any arbitrary spectrum analogous to simulated neutrino events.

The final step is to simulate the propagation of charged particles inside or near the detection volume, as well as the corresponding Cherenkov-light yields. In this work, muon tracks are the main events of interest. For both atmospheric and astrophysical track events, the muon propagation and light yield is simulated using the `MMC` (Muon Monte Carlo) framework [349, 350]. The `MMC` also propagates the Cherenkov photons through the ice. Finally, for photons that reach a DOM, specific IceCube software simulates the response of the PMT and other relevant DOM electronics. The resulting waveforms are subsequently stored and passed through the DAQ and PnF software. For a certain event selection of interest, one can therefore obtain a corresponding MC sample that attempts to reflect the observed data.

[26]Consequently, the field of view of IceCube is limited to the Southern Sky at the highest energies.

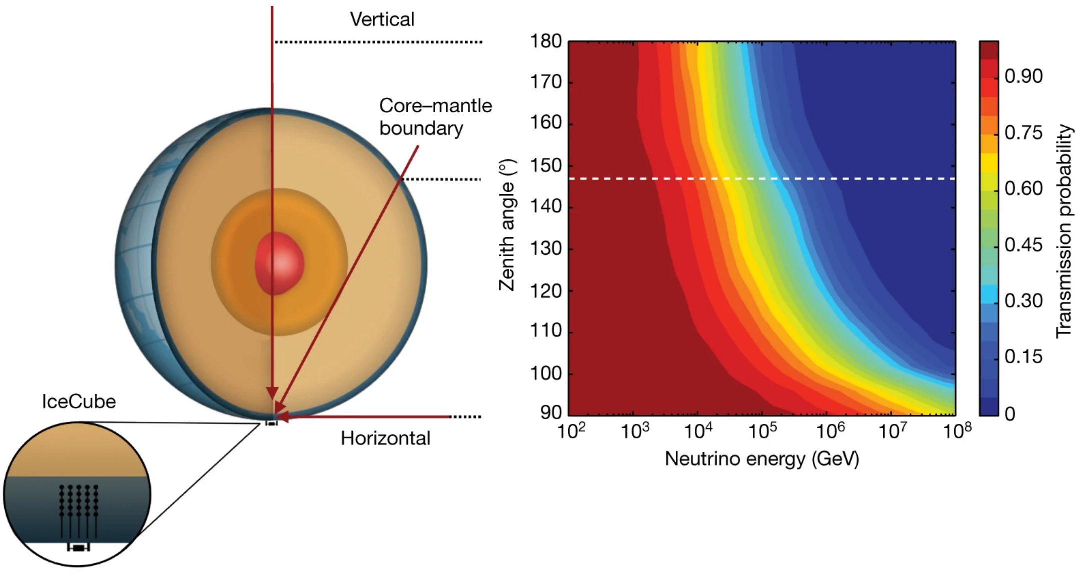

FIGURE 3.7: Transmission probability of neutrinos traversing the Earth, taken from [319]. The left panel illustrates the Earth, consisting of a core and mantle, as well as the location of IceCube. The right panel presents the transmission probability as a function of both zenith angle and neutrino energy.

3.2 Reconstruction of Track Events

As will be motivated in Section 3.3, the event selection for the IceCube search presented in this work is solely focused on tracks. In the following, a description is given of the various **track-reconstruction algorithms** that are used in the event selection. For each individual event, these algorithms allow us to obtain estimates for the track direction, its angular uncertainty, and the muon energy at the detector. These quantities form the key ingredients for the ULIRG stacking analysis presented in Chapter 4. Note that the reconstruction of the track direction is performed in **detector coordinates**, i.e. in terms of the zenith θ and azimuth ϕ, which are subsequently translated to equatorial coordinates. Due to IceCube's location at the South Pole, the zenith, θ, is simply related to the declination, δ, as $\theta = \delta + \pi/2$, while the azimuth at the time of observation directly yields the corresponding right ascension.

3.2.1 Angular Reconstruction

LineFit

The most primitive angular-reconstruction method is one which attempts to minimize the distance between the N DOMs that recorded a hit and the muon track hypothesis. The muon is assumed to travel in a straight line with a constant velocity $\mathbf{v}$, such that the track—the muon position as a function of time—is parameterized as

$$\mathbf{r}(t) = \mathbf{r}_0 + \mathbf{v}(t - t_0), \tag{3.4}$$

where $\mathbf{r}_0 \equiv \mathbf{r}(t_0)$ is the position at some time t_0. Let $\mathbf{x}_i$ be the position of the i^{th} DOM that recorded a hit at a time t_i, for $i \in \{1, 2, ..., N\}$. The LineFit method [351] then searches for

$$\underset{(t_0,\mathbf{r}_0,\mathbf{v})}{\arg\min} \sum_{i=1}^{N} \varphi\left(|\mathbf{r}(t_i) - \mathbf{x}_i|\right), \tag{3.5}$$

where the **Huber cost function** [352] is defined as

$$\varphi(\Delta x) = \begin{cases} (\Delta x)^2 & \text{for } \Delta x < \mu, \\ \mu(2\Delta x - \mu) & \text{for } \Delta x \geq \mu. \end{cases} \tag{3.6}$$

For small DOM-track distances $\Delta x < \mu$, LineFit is reduced to a least-squares optimization problem. In this regime, hits are given a quadratic weight since they are assumed to be strongly correlated with the track. On the other hand, the Huber cost function for $\Delta x \geq \mu$ penalizes hits that occurred far away from the track by giving them a linear weight, since these hits are more likely to be caused by noise. The choice for the parameter μ is optimized by calibration to IceCube data [351].

The optimization problem given above can be solved analytically [351]. As such, the LineFit reconstruction allows for a coarse estimate of the track parameters $(t_0, \mathbf{r}_0, \mathbf{v})$ without the need for a time-consuming numerical minimization. Photon-scattering effects are mitigated by excluding DOM hits that were likely caused by such scattered photons. However, since LineFit does not take into account any Cherenkov effects—it simply assumes that the muon emits a plane wave perpendicular to its direction of motion—the reconstruction is only a crude approximation of the track. Nevertheless, due to its fast performance, LineFit is used as the first track-reconstruction method in the data-processing chain. Its results are then used as a seed that is required for subsequent reconstruction algorithms.

SPE Fit

The next angular-reconstruction method considers a relativistic muon with constant velocity $\mathbf{v} = c\hat{\mathbf{e}}_{\mathbf{v}}$ that emits Cherenkov radiation, where $\hat{\mathbf{e}}_{\mathbf{v}}$ is described by a zenith angle θ and azimuth angle ϕ in detector coordinates. As discussed in Section 3.1.1, this emission is characterized by the Cherenkov cone $\theta_c \approx 41°$. Using the geometry and quantities defined in Figure 3.8, and neglecting photon scattering, the expected arrival time of a Cherenkov photon in DOM i can be expressed as

$$t_{\mathrm{geo},i} = t_0 + \frac{1}{c}\left[\hat{\mathbf{e}}_{\mathbf{v}} \cdot (\mathbf{x}_i - \mathbf{r}_0) + d \tan\theta_c\right]. \tag{3.7}$$

The difference between the time of the recorded hit time and the expected arrival time defines the **time residual**

$$t_{\mathrm{res},i} \equiv t_{\mathrm{hit},i} - t_{\mathrm{geo},i}. \tag{3.8}$$

Let $\mathcal{P}_1(t_{\mathrm{res}})$ denote the probability density function (PDF) for time residuals corresponding to the detection of a single photon. Through the definition of t_{res}, this PDF is a function of the track parameters $\boldsymbol{\theta} = (\mathbf{r}_0, \theta, \phi)$. We can then define the **single-photoelectron (SPE) likelihood** as

$$\mathcal{L}_{\mathrm{SPE}}(\boldsymbol{\theta}) = \prod_{i=1}^{N} \mathcal{P}_1(t_{\mathrm{res},i}|\boldsymbol{\theta}), \tag{3.9}$$

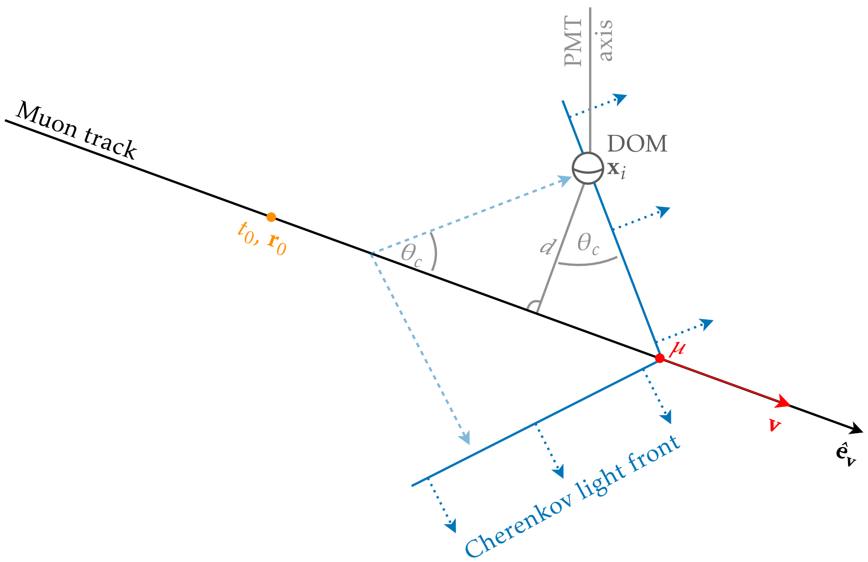

FIGURE 3.8: Geometry used for SPE track-reconstruction method, adapted from [327, 340]. A muon μ with velocity $\mathbf{v} = c\hat{\mathbf{e}}_\mathbf{v}$ emits Cherenkov radiation at the Cherenkov cone θ_c. At some time t_0, the muon was located at $\mathbf{r}_0$ along the track. Its emission reaches DOM i located at $\mathbf{x}_i$, which is separated by a distance d from the track.

with N the total number of DOMs that recorded a hit. The SPE-fit method [327] then searches for

$$\hat{\boldsymbol{\theta}} = \underset{\boldsymbol{\theta}}{\arg\max}\, \mathcal{L}_{\mathrm{SPE}}(\boldsymbol{\theta}), \tag{3.10}$$

i.e. those track parameters that maximize the SPE likelihood. See Section 4.1 for the statistical formalism behind this likelihood concept.

The SPE-likelihood maximization requires a seed, which is provided by the Line-Fit reconstruction. In addition, it uses an analytical expression for the PDF called the **Pandel function** [353], which describes the time-residual profile for a single photon propagating through the South Pole ice. The Pandel function takes the form

$$P(t_{\mathrm{res}}) = \frac{1}{N(d)} \frac{\tau^{-d/\lambda}\, t_{\mathrm{res}}^{d/\lambda-1}}{\Gamma(d/\lambda)} \exp\left[-t_{\mathrm{res}}\left(\frac{1}{\tau} + \frac{c_n}{\lambda_a}\right) - \frac{d}{\lambda_a}\right], \tag{3.11}$$

and is normalized by

$$N(d) = e^{-d/\lambda_a}\left(1 + \frac{\tau c_n}{\lambda_a}\right)^{d/\lambda}. \tag{3.12}$$

Here, λ_a and c_n represent the photon-absorption length and the speed of light in ice, respectively. The parameters λ and τ were determined empirically by fitting the Pandel function PDF to a South-Pole ice model [327]. Apart from t_{res} itself, the DOM-track distance d is the only quantity that depends on the track parameters (Figure 3.8).

Note that the Pandel function is only defined for positive t_{res}, which makes sense from a purely geometrical standpoint. However, the occurrence of negative time residuals is possible due to the non-zero time resolution of the PMTs, σ_t. To mitigate these PMT effects,[27] the Pandel function is convoluted with a Gaussian PDF centered around zero with a width σ_t [354],

$$\mathcal{P}_1(t_{\text{res}}) = \int_0^\infty \frac{P(t')}{\sqrt{2\pi}\sigma_t} \exp\left[-\frac{(t_{\text{res}} - t')^2}{2\sigma_t^2}\right] \mathrm{d}t'. \tag{3.13}$$

This convolution can be solved analytically, yielding the PDF that enters the SPE likelihood of Equation (3.9).

The analytic formulation of the Gaussian-convoluted Pandel PDF allows for a fast evaluation of the SPE likelihood. Furthermore, its integral can be solved analytically [327], which is convenient for a more elaborate track reconstruction (see below). Hence, the SPE fit yields a more precise reconstruction compared to LineFit (Figure 3.9), without introducing a large cost in terms of computation time [340]. In addition, the SPE likelihood provides a quality parameter to judge whether an event actually corresponds with a track-like signature.

MPE Fit

It is possible to detect $n_i \geq 1$ hits in a single DOM i, especially in the case of highly energetic muon tracks. To take this into account, it is shown in [327] that the SPE likelihood in the maximization of Equation (3.10) can be expanded to the **multiple-photoelectron (MPE) likelihood**,

$$\mathcal{L}_{\text{MPE}}(\boldsymbol{\theta}) = \prod_{i=1}^{N} \left[n_i \mathcal{P}_1(t_{\text{res},i}|\boldsymbol{\theta}) \left(\int_{t_{\text{res},i}}^{\infty} \mathcal{P}_1(t'|\boldsymbol{\theta})\, \mathrm{d}t' \right)^{n_i - 1} \right]. \tag{3.14}$$

Note that $\mathcal{L}_{\text{MPE}} \xrightarrow{n_i=1} \mathcal{L}_{\text{SPE}}$. The MPE likelihood therefore yields a more refined reconstruction compared to the SPE scenario at higher energies (Figure 3.9). Since the integration in Equation (3.14) can be performed analytically and the MPE fit is seeded by the SPE-fit results, the median computation time of the MPE-likelihood maximization is at the level of its SPE counterpart [340].

SplineMPE Fit

The final angular-reconstruction method used for tracks in IceCube uses the same likelihood of Equation (3.14), but considers a more precise description of the single-photon PDF $\mathcal{P}_1$. This description is obtained by performing detailed simulations of photon propagation in ice for various track-DOM configurations. The results of these simulations are then stored in lookup tables and subsequently interpolated with **multidimensional splines** [355, 356]—hence the name SplineMPE. As such, a continuous description of the PDF is obtained (see Section 4.2.1 for examples of spline smoothing in a different context).

Compared to the analytic MPE fit, the SplineMPE approach allows us to introduce the following improvements to either the angular resolution, the computing time, or both [340, 357]:

- By construction, a more detailed description of the glacial ice is achieved compared to the homogeneous model used in the Pandel function, by including

[27] Concretely, effects that may cause negative time residuals are PMT timing jitter, and time delays due to backwards illumination of the PMT (recall that the PMTs inside the IceCube DOMs face downwards in the ice) [340].

depth-dependent scattering and absorption effects as in Figure 3.4. Note that anisotropies due to the flow of the glacier have not yet been taken into account in SplineMPE.[28]

- Additional pulse cleaning takes place to take into account late DOM hits caused by stochastic energy losses of the muon (Section 3.2.3). Recent efforts have been able to model these stochastic losses directly into the PDF $\mathcal{P}_1$, yielding moderate improvements to the angular resolution [358]. However, these latest implementations are not included in the data used in this work.
- The overall PDF that enters the SplineMPE likelihood includes an accurate model of the PMT noise. In particular, it takes into account the shape of the noise distribution after pulse cleaning.
- To obtain a better description in the transition region between the SPE and MPE regimes, both likelihoods are combined as $\mathcal{L}_{\mathrm{SPE}}^{1-m} \times \mathcal{L}_{\mathrm{MPE}}^{m}$ in the maximization. The parameter $m \in [0.4, 1]$ is a function of the muon energy. Its minimum value yields optimal results for muon energies below 1 TeV, while its maximum value gives the best description for muons with energies above 300 TeV.
- PMT-related timing uncertainties were taken into account in Equation (3.13) on a hit-by-hit basis. However, additional timing uncertainties on e.g. the relative clock synchronization of the DOMs and the signal transmission times to the DAQ affect all PMTs in the same manner. Therefore, a second Gaussian convolution is applied to the final likelihood in order to mitigate these uncertainties.

Performance Overview

The four angular-reconstruction methods described above are performed in the following order during the data-processing chain:

$$\text{LineFit} \xrightarrow{\text{seed}} \text{SPE Fit} \xrightarrow{\text{seed}} \text{MPE Fit} \xrightarrow{\text{seed}} \text{SplineMPE Fit.}$$

This procedure has an overall per-event computation time of $\mathcal{O}(100\text{ ms})$, which can be handled by the online PnF system [340]. Note that for this reason, the SplineMPE settings are configured in such a way that a fast online reconstruction can be achieved, which comes at the cost of angular resolution. Subsequent offline data processing applies the full potential of the SplineMPE reconstruction using the fast SplineMPE results as a seed. The offline SplineMPE fit currently yields the best angular resolution, although its computation time is roughly 10 times larger compared to the online SplineMPE.

Figure 3.9 shows the median angular error of each reconstruction method for simulated muon tracks, both as a function of muon energy and declination δ, at the final level of the GFU event selection (see Section 3.3.1). Clear improvements in angular resolution are obtained with each subsequent reconstruction algorithm. Most notably, the MPE algorithms yield better results at higher energies compared to the LineFit and SPE methods. This improvement particularly affects downgoing events ($\sin\delta < 0$), for which higher energy-threshold criteria are applied in the selection. For upgoing events ($\sin\delta > 0$), Earth-absorption effects limit the rate of high-energy

[28] For cascades, however, some progress has been made to include these particular ice anisotropies in the reconstructions [347].

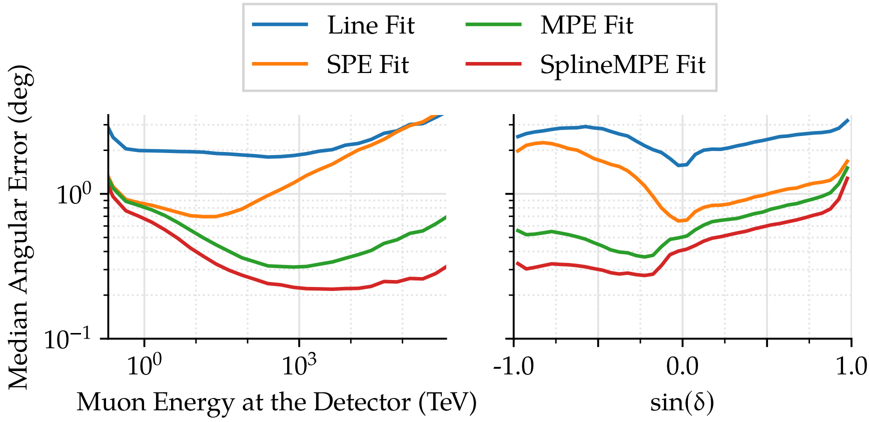

FIGURE 3.9: Performance of the various angular-reconstruction algorithms for tracks as described in the text [340]. The left and right panels show the median angular error as a function of muon energy in IceCube and declination δ, respectively.

tracks. Combined with the fact that the IceCube geometry is most suited to observe horizontal tracks[29] ($\sin\delta \approx 0$), the median angular error increases with declination in the Northern Sky.

3.2.2 Estimation of Angular Error

Cramér Rao

Let $\boldsymbol{\theta} = (\theta_1, \theta_2, ..., \theta_M) = (\mathbf{r}_0, \theta, \phi)$ represent the tracks parameters using the notations of Section 3.2.1. We can define the elements of the $M \times M$ **Fisher-information matrix** $I(\boldsymbol{\theta})$ as [359]

$$I_{ij} = -\left\langle \frac{\partial^2}{\partial\theta_i\,\partial\theta_j} \log \mathcal{L}_{\mathrm{MPE}}(\boldsymbol{\theta}) \right\rangle, \tag{3.15}$$

where the MPE likelihood of Equation (3.14) is defined using the single-photon PDF $\mathcal{P}_1$ of the SplineMPE reconstruction. Assuming that the maximum-likelihood estimators $\hat{\boldsymbol{\theta}}$ are unbiased, the **Cramér-Rao bound** [360, 361] states that the covariance matrix of these estimators is bound by

$$\underset{\boldsymbol{\theta}}{\mathrm{cov}}(\hat{\boldsymbol{\theta}}) \geq I(\boldsymbol{\theta})^{-1}. \tag{3.16}$$

Hence, the diagonal elements of the inverse Fisher-information matrix allow us to obtain lower bounds for the variances σ_θ^2 and σ_ϕ^2 of both the zenith angle and the azimuth angle, respectively. These bounds can then be used to estimate the circularized angular error on the track direction as [362]

$$\sigma = \sqrt{\frac{\sigma_\theta^2 + \sigma_\phi^2 \sin^2\hat{\theta}}{2}}, \tag{3.17}$$

where $\hat{\theta}$ is the SplineMPE fit of the zenith angle.

[29] The reason why is because the vertical inter-DOM spacing (17 m) is smaller than the horizontal spacing of IceCube (125 m). Consequently, the Cherenkov cone of horizontal muons is able to hit more DOMs compared to vertical muons of the same energy.

Analytic expressions for the covariance matrix have been obtained in [363]. Since no additional minimization is required, the Cramér-Rao method yields a very fast and stable estimation of the angular error of the track reconstruction. This estimation can therefore be performed for all events during online data processing. However, its performance is not at the level of the other estimators described below (see Figure 3.11).

Paraboloid

Another approach to estimate the angular error of a track is to construct a **confidence ellipse** of the directional parameters θ and ϕ in the likelihood space of the SplineMPE track reconstruction. As elaborated in [364], the MPE likelihood of Equation (3.14) can be approximated by a 5D Gaussian PDF centered around the best-fit $\hat{\boldsymbol{\theta}}$ as long as the number of DOMs that recorded a hit, N, is large enough. Since the supporting vector $\mathbf{r}_0$ is not of interest here, the dimensionality of the problem can be reduced to the (θ, ϕ)-plane [365]. In this plane, the likelihood is described by a 2D Gaussian PDF—also known as a paraboloid—centered around the best-fit angular reconstruction $(\hat{\theta}, \hat{\phi})$ with standard deviations $(\sigma_\theta, \sigma_\phi)$. This Gaussian approximation implies that[30]

$$\log \mathcal{L}_{\mathrm{MPE}}\left(\hat{\theta} \pm \sigma_\theta, \hat{\phi} \pm \sigma_\phi\right) = \log \mathcal{L}_{\mathrm{MPE}}\left(\hat{\theta}, \hat{\phi}\right) - \frac{1}{2}, \tag{3.18}$$

which defines an ellipse in the (θ, ϕ)-plane as shown in Figure 3.10.

In practice, the MPE-likelihood space is sampled in a 3×8 grid around the best-fit point $(\hat{\theta}, \hat{\phi})$ in the (θ, ϕ)-plane [340]. In each of these 24 points, the likelihood is fixed in zenith and azimuth, and maximized with respect to the supporting vector $\mathbf{r}_0$. Subsequently, a paraboloid is fitted through the sampled points, and a confidence ellipse is determined using Equation (3.18). Finally, an estimate for the circularized

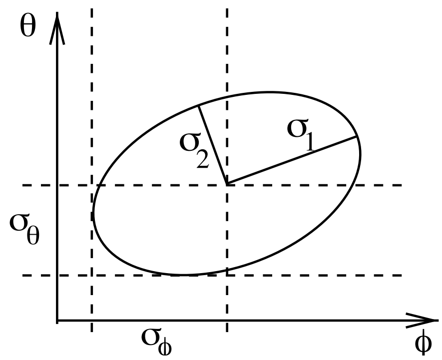

Figure 3.10: Illustration, adapted from [365], of the confidence ellipse obtained with the paraboloid method. The ellipse contour is defined using Equation (3.18), and it is centered around the reconstructed direction in zenith θ and azimuth ϕ. The ellipse is described in terms of the uncertainties σ_θ and σ_ϕ on the directional parameters, which can be related to the semi-major and semi-minor axes σ_1 and σ_2.

[30] In one dimension, a Gaussian PDF of x with mean μ and standard deviation σ_x takes the form $f(x) = A \exp\left[-(x-\mu)^2/2\sigma_x^2\right]$ with $A = (2\pi\sigma_x^2)^{-1/2}$. Hence, $\log f(\mu) = \log A$ and $\log f(\mu \pm \sigma_x) = \log A - 1/2$, such that $\log f(\mu \pm \sigma_x) = \log f(\mu) - 1/2$. In two dimensions this translates to Equation (3.18).

angular error of the track direction is found as [365]

$$\sigma = \sqrt{\frac{\sigma_1^2 + \sigma_2^2}{2}}, \tag{3.19}$$

where σ_1 and σ_2 are the semi-major and semi-minor axes of the confidence ellipse, respectively (see Figure 3.10). This paraboloid method results in the best estimation of the angular uncertainty of tracks (Figure 3.11), although the various likelihood maximizations make this approach computationally expensive [340].

Bootstrapping

The final method for estimating the angular error attempts to empirically model the unknown theoretical distribution $\mathcal{F}_{\text{true}}$ of the track direction using a technique called **bootstrapping** [366]. Let a track event be described by the observables $\mathbf{x}_{\text{obs}} = (x^1_{\text{obs}}, x^2_{\text{obs}}, ..., x^N_{\text{obs}})$, where each element represents one of the measured pulses in IceCube. From this sample, an empirical distribution $\hat{\mathcal{F}}$ can be obtained, which serves as an estimate for the true distribution $\mathcal{F}_{\text{true}}$. Next, a so-called bootstrapped event $\mathbf{x}_{\text{boot}} = (x^1_{\text{boot}}, x^2_{\text{boot}}, ..., x^M_{\text{boot}})$ is obtained by randomly sampling pulses from $\hat{\mathcal{F}}$ until the total charge in the $\mathbf{x}_{\text{boot}}$ equals that of $\mathbf{x}_{\text{obs}}$.

In practice, 6 bootstrapped events are sampled[31] from $\hat{\mathcal{F}}$, which are then reconstructed using the SplineMPE algorithm. The average direction and mean angular difference of the bootstrapped events can be combined to obtain a measure for the angular uncertainty of the original $\mathbf{x}_{\text{obs}}$. In online systems, Bootstrapping serves as a compromise between the fast but less accurate Cramér-Rao method and the slow but more accurate Paraboloid estimation (see also Figure 3.11).

Performance Overview

As will be discussed in Section 3.3.1, the online event selection of the GFU sample uses a different estimator depending on the muon energy and number of hit DOMs. In this online selection, the median runtimes for Cramér Rao, Paraboloid, and Bootstrapping are 10 ms, 430 ms, and 210 ms respectively [340]. Afterwards, the Paraboloid method is used in offline data processing to estimate the angular uncertainty for all selected events. In this offline estimation, the median runtime of Paraboloid is 6.15 s [340].

The accuracy of an uncertainty estimator is quantized by defining the so-called **pull** as $\Delta\Psi/\sigma$. Here, $\Delta\Psi$ is the true angular error of the simulated event, while σ represents the estimated angular error. Figure 3.11 shows the pull for each of the angular-error estimators described above as a function of reconstructed muon energy (Section 3.2.3) at the final level of the GFU event selection (Section 3.3.1). Note that the shown values include pull corrections, which will be described in Section 3.3.1. Because of these corrections, the median pull of all methods is consistently equal to $\Delta\Psi/\sigma = 1.177$ for all energies. However, the spread in pull of the Cramér-Rao estimator is significantly larger compared to the Paraboloid and Bootstrapping methods over the complete energy range. Of these last two methods, Paraboloid yields a mildly smaller spread compared to Bootstrapping between

[31] This is only the case for online systems, which is the only time in the data-processing chain were bootstrapping is relevant to this work. Offline systems typically sample 8 bootstrapped events [340].

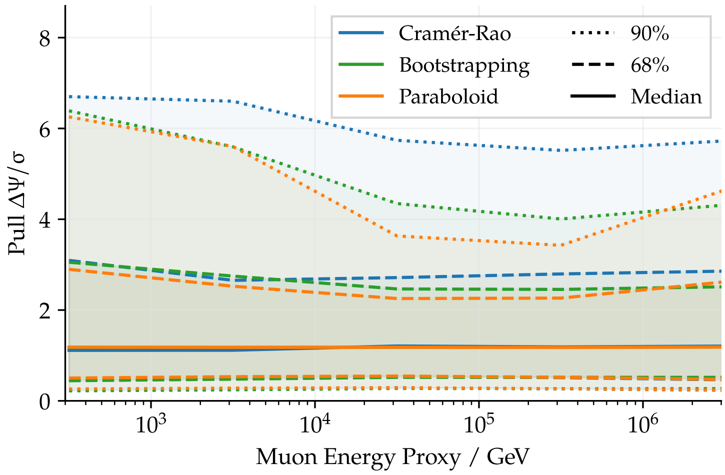

FIGURE 3.11: Distribution of the corrected pull (see Figure 3.14) as a function of muon-energy proxy for the different angular-error estimators described in the text. The pull is defined as the ratio between the true angular error $\Delta\Psi$ and the estimated angular error σ. For each method, the solid line represents the median of the pull, while the dashed (resp. dotted) lines indicate the 68% (resp. 90%) contours. Taken from [340].

roughly 10 TeV and 1 PeV. In conclusion, the Paraboloid method yields the most accurate angular-error estimator for track reconstructions.

3.2.3 Energy Reconstruction

As discussed in Section 3.1.4, muons with energies E_μ larger than several 100 GeV are capable of traversing the whole detector and only deposit a fraction of their energy in IceCube. Above $E_\mu \gtrsim 1$ TeV, the muon energy loss along its track x is dominated by **stochastic processes** such as ionization, bremsstrahlung, pair production, and photonuclear interactions [14]. Each of these processes will produce secondary particle showers, which can be approximated as point-like sources of spherical Cherenkov emission [317]. The mean stochastic energy loss, which is directly proportional to the Cherenkov-photon yield [341], scales roughly linearly with energy, $-\langle \mathrm{d}E_\mu/\mathrm{d}x \rangle \propto E_\mu$ [14]. Hence, the muon energy at the detector can be estimated from the observed number of track photons.

The likelihood of observing k photons in IceCube from a muon with energy E_μ is described by a Poisson distribution [317],

$$\mathcal{L}_{\mathrm{loss}}(E_\mu) = \frac{\lambda^k}{k!} e^{-\lambda}. \tag{3.20}$$

Here, $\lambda = \Lambda E_\mu + \rho$ is the mean number of photons, which includes a contribution from noise through the term ρ. The parameter Λ represents a template for the mean number of track photons per unit of energy, typically calibrated at 1 GeV [367]. The exact calibration depends on the energy-reconstruction method, which eventually searches for the energy that maximizes the above likelihood,

$$\hat{E}_\mu = \arg\max_{E_\mu} \mathcal{L}_{\mathrm{loss}}(E_\mu). \tag{3.21}$$

In this work, only the MuEX energy reconstruction is of relevance [317, 368]. For this method, the template Λ is obtained using an analytical model[32] of uniform Cherenkov-cone emission along the muon track. For a given PMT with an effective photon-collection area A, the light yield from a track at a distance d from the sensor (Figure 3.8) is given by the empirical formula

$$\mu(d) = \frac{\ell_0 A}{2\pi \sin\theta_c} \frac{e^{-d/\lambda_p}}{\sqrt{\lambda_\mu d}\,\tanh\sqrt{\lambda_\mu d}}, \tag{3.22}$$

where

$$\lambda_\mu = \frac{2}{\pi\lambda_p}\left(\frac{\lambda_e}{3\,e^{-\lambda_a/\lambda_e}\sin\theta_c}\right)^2. \tag{3.23}$$

Here, ℓ_0 is the number of photons per unit of length of the uniform track, while λ_a and λ_e represent the effective absorption and scattering lengths, respectively, averaged over the track and PMT positions in the ice (see also Figure 3.4). Near the track ($d \ll \lambda_p$), the light yield scales as $1/d$, as expected for a uniform cylindrical source. Moving further away ($d \gg \lambda_p$), scattering and absorption effects cause photons to diffuse, such that the light yield becomes proportional to $e^{-d/\lambda_p}/\sqrt{d}$. The characteristic diffusion length of the photon is found to be $\lambda_p = \sqrt{\lambda_a\lambda_e/3}$ [317].

The above formulation yields a valid approximation for Λ in the case of minimum ionizing muons (100 GeV $\lesssim E_\mu \lesssim$ 1 TeV), which exhibit continuous energy losses. To take into account the stochastic effects of more energetic muons [317], the MuEX reconstruction reformulates the likelihood of Equation (3.20) as

$$\mathcal{L}_\text{loss} = \int_0^\infty \frac{\lambda^k}{k!} e^{-\lambda}\, G_\mu(\lambda - x')\,\mathrm{d}x', \tag{3.24}$$

where the Poisson distribution is convoluted with the empirical function

$$G_\mu(x) = \frac{B}{x\left[e^{-w\log(x/\mu)} + \log(x/\mu)^2/\sigma^2\right]}. \tag{3.25}$$

The parameters w, σ, and B are determined empirically to describe the wider tails of the likelihood function caused by the stochastic energy losses.

The median energy resolution of the MuEX estimator is shown in Figure 3.12 using simulated muon tracks at the final level of the GFU event selection (Section 3.3.1). Since the likelihood description inherently assumes that the number of photons is proportional to the energy loss, MuEX achieves a better resolution with increasing energy. However, the stochastic nature of the muon energy loss limits the resolution to $\sigma_{\log_{10}(\hat{E}_\mu/\text{GeV})} \gtrsim 0.25$ for $E_\mu \gtrsim 100$ TeV. This resolution is comparable to the one obtained with a more elaborate—and computationally expensive—method using interpolated splines in the template Λ (similar to those used in the SplineMPE angular reconstruction) [317, 340].

Finally, note that $\hat{E}_\mu$ represents the reconstructed *muon* energy at the detector. For neutrino-induced events, this value represents a lower limit on the muon energy at the neutrino-interaction vertex, which is required to estimate the energy of the original neutrino. The ***neutrino* energy resolution** of tracks is thus poor, and typically quoted as a decade in neutrino energy.

[32] This model was verified using Monte-Carlo simulations [369].

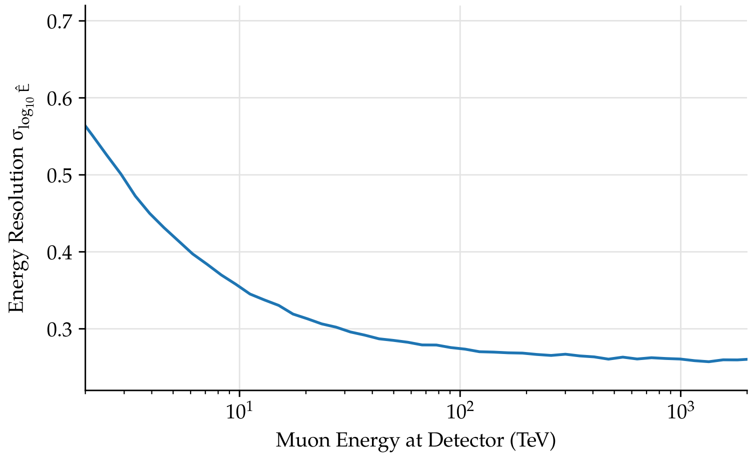

FIGURE 3.12: Median energy resolution of the MuEX reconstruction method described in the text, adapted from [340]. The resolution is given in terms of the estimated logarithmic muon energy at the detector, $\log_{10}(\hat{E}/\mathrm{GeV})$, and plotted as a function of the true muon energy at the detector.

3.3 The Gamma-Ray Follow-Up Data Sample

The IceCube analysis presented in this work aims to search for astrophysical neutrinos that are spatially correlated with the ULIRG selection obtained in Section 2.3, which covers the complete sky. Since tracks yield the best angular resolution in IceCube, they are the ideal events for such a neutrino-source search. Hence, a data sample of events is required that

- consists of well-reconstructed tracks;
- covers the full sky;
- has an optimal selection efficiency for astrophysical events while retaining a good rejection efficiency for atmospheric-background events.

These conditions are met by the **gamma-ray follow-up (GFU) dataset**[33] [340], which is an all-sky sample of high-quality, through-going, and isolated tracks. The GFU sample is an **online event selection** performed by the PnF system, since its original purpose is to serve as a data sample for issuing and following up multimessenger realtime alerts [132]. Subsequent **offline reprocessing** of the GFU data with optimal track-reconstruction algorithms yields a sample adequate for time-integrated searches.

An overview of the online data stream from trigger level up to the GFU selection is given in Figure 3.13, which will be described in detail below. To quantify the performance of the event selection, a dedicated **GFU MC sample** [340] is generated using the techniques described in Section 3.1.6. This MC sample is subsequently passed through the same filters as the actual GFU data to obtain a complementary simulated dataset. Note that this MC sample is the one used for the performance plots in Section 3.2.

[33]The GFU data sample is historically named after the GFU filter (Section 3.3.1), which was originally designed for the IceCube gamma-ray follow-up program [370].

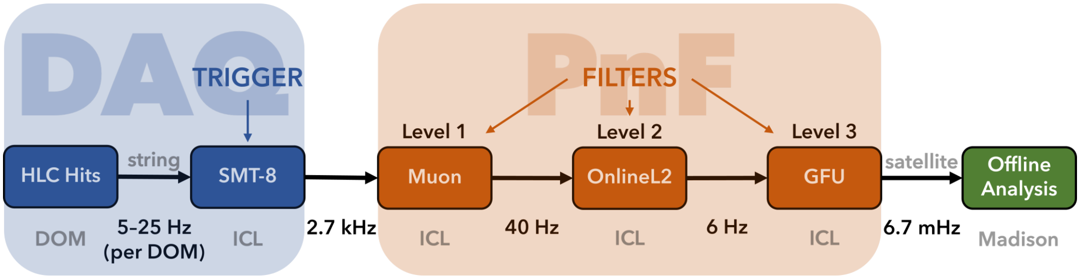

FIGURE 3.13: Schematic of the IceCube data flow for events in the GFU sample. The stream of events triggered by the DAQ (Section 3.1.3) is passed through a set of PnF filters (Section 3.3.1) to reduce the overall event rate and obtain a data sample adequate for neutrino-source studies.

3.3.1 Event Selection

Muon Filter

The purpose of the **muon filter** [310, 340] is to reduce the DAQ triggered event rate to a level that can be handled by more elaborate online and offline reconstructions. Hence, for each DAQ triggered event, a course track reconstruction is performed with the LineFit method, and subsequently the SPE method. For tracks arriving from the Northern Hemisphere, the SPE likelihood of Equation (3.9) is used as a quality parameter to reject cascade events. For tracks arriving from the Southern Hemisphere, however, a zenith-dependent charge cut is imposed to reduce the overwhelming rate of atmospheric muons. This cut is designed to filter out low-energy muons that are more likely to be of atmospheric origin (Section 3.1.5). Concretely, the muon filter can be expressed as [310]

$$\begin{cases} \log \mathcal{L}_{\mathrm{SPE}}/(N-3) \leq 8.7 & \text{for } -1.0 < \cos\theta \leq 0.2; \\ \log(Q_{\mathrm{tot}}/\mathrm{PE}) > 3.9\cos\theta + 0.65 & \text{for } \quad 0.2 < \cos\theta \leq 0.5; \\ \log(Q_{\mathrm{tot}}/\mathrm{PE}) > 0.6\cos\theta + 2.3 & \text{for } \quad 0.5 < \cos\theta \leq 1.0. \end{cases} \tag{3.26}$$

Here, N denotes the number of hit DOMs, Q_{tot} is the total deposited charge in the detector, $\mathcal{L}_{\mathrm{SPE}}$ is the maximized SPE likelihood, and θ is the reconstructed zenith angle from the SPE fit. As such, the muon filter reduces the overall event rate to about 40 Hz.

OnlineL2 Filter

When flagged by the muon filter, events are subsequently passed through the **online level 2 (OnlineL2) filter** [371]. This filter is designed to form a starting point for online and realtime analyses. First, the angular reconstruction is refined by seeding the SPE fit with two random directions that have a separation angle of 120° w.r.t. the original fit. This allows to mitigate the effect of local extrema being misinterpreted as the global maximum of the SPE likelihood. Next, the MPE reconstruction is performed using the refined SPE fit as a seed. Since it takes into account the deposited charge in each of N hit DOMs, the MPE fit significantly improves the angular reconstruction at high energies (Figure 3.9), which allows for a better identification of such high-energy events.

The MPE reconstruction and the total deposited charge of the events are then used to define the main cut of the OnlineL2 filter. Similar to Equation (3.26), four (instead of three) regions on the sky are defined where different cut criteria are applied (see [371] for the detailed expressions). As such, the OnlineL2 filter reduces the overall event rate to roughly 6 Hz. Events that pass the OnlineL2 cut are then subject to further reconstructions. The angular reconstruction is optimized with the SplineMPE method (with fast settings) using the MPE fit as a seed, while the muon energy E_μ is reconstructed using MuEX. Lastly, the angular error of the tracks is estimated with [340]:

- Paraboloid if $E_\mu < 4$ TeV.
- Bootstrapping if $E_\mu \geq 4$ TeV and $N < 300$.
- Cramér Rao if $E_\mu \geq 4$ TeV and $N \geq 300$.

Although Paraboloid yields the best angular-uncertainty estimation (Figure 3.11), it becomes too computationally expensive for online systems at high energies. Consequently, faster but lower-quality uncertainty estimators are used for high-energy events in the OnlineL2 filter.

Pull Corrections

The pull of an angular-uncertainty estimator was defined in Section 3.2.2 as the ratio between the true error, $\Delta\Psi$, and the estimated error, σ, of a track reconstruction. Panel (a) of Figure 3.14 shows the pull as a function of the MuEX energy reconstruction, after the application of the OnlineL2 filter. This pull is significantly affected by two effects. First, stochastic energy losses are not taken into account in the angular reconstruction of tracks, as mentioned in Section 3.2.1. Consequently, the true angular error is typically underestimated at higher energies. Second, for neutrino-induced events, the **kinematic angle**[34] between the muon and the original neutrino is approximately given by $\sigma_{\text{kin}} \approx 1.8° \times (E_\nu/\text{TeV})^{-1/2}$ [33]. Since the kinematic angle is not taken into account by the uncertainty estimators, the true angular error is also typically underestimated at lower energies. Note that the discontinuities in Figure 3.14 are a consequence of the energy-dependent choice of the applied estimation method [340].

To mitigate the above biases, so-called **pull corrections** are performed to calibrate the estimated angular error to its true value. This calibration is performed under the specific interpretation of the angular error used in point-source analyses. Here, the distribution of astrophysical events around a candidate source is modeled according to a two-dimensional circularized Gaussian (see Section 4.2.1). For each event, the standard deviation of the Gaussian is defined as the estimated angular uncertainty of the event, σ. In this situation, the median containment of this Gaussian lies within 1.177σ. Therefore, to correctly describe this median containment, the pull correction calibrates the median pull to $\Delta\Psi/\sigma = 1.177$. The result is shown in Panel (b) of Figure 3.14. In the remainder of this work, all estimated event uncertainties are implicitly assumed to be pull corrected.

[34] For a detailed study of the kinematic angle and its effect on IceCube reconstructions, see [128].

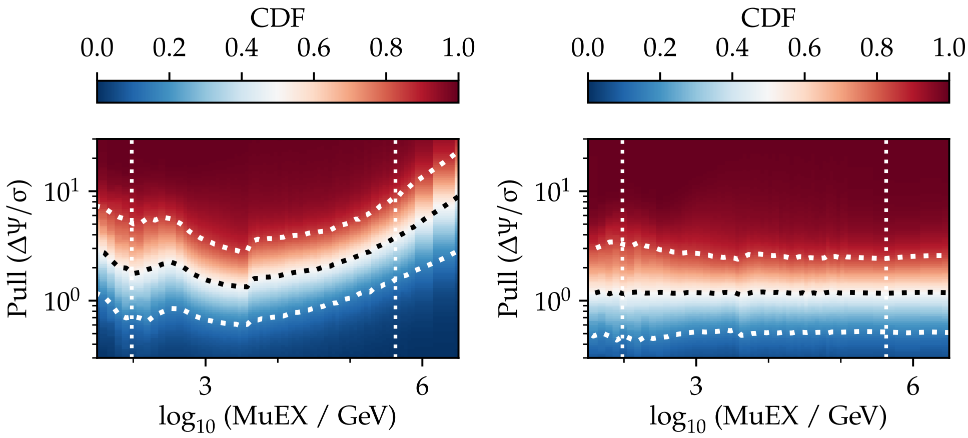

(a) Non-corrected pull

(b) Corrected pull

FIGURE 3.14: Illustration of the energy-dependent pull correction. The pull is shown in Panels (a) and (b) as a function of the reconstructed muon energy MuEX before and after the correction, respectively. In each plot, the color scale represents the cumulative distribution function (CDF) of the pull per energy bin. The thick black dotted line is the median of the CDF, while the thick white dotted lines indicate the central 68% containment. The vertical thin white dotted lines define the central 99% energy range found in the observed data. Taken from [340].

GFU Filter

At the final stage of the data-filtering process, the GFU filter aims to maximally reject background events while retaining an optimal signal-selection efficiency. This filter is based on a machine-learning approach which classifies events using **boosted decision trees** (BDTs) [340, 372]. Such a BDT consists of N layers of so-called nodes, where $N = 5$ for the GFU selection. Each node applies a binary classification of the events by defining a cut on one of the reconstruction variables—see [340] for complete listing—computed after the OnlineL2 cut. This classification is optimized to separate background and signal events form each other. Starting from a single node, a BDT branches out and ends up with 2^{N-1} nodes at its final layer. These final nodes are also referred to as the leaves of the tree.

To optimize the cut of a reconstruction variable for each node, a dedicated set of MC data is generated which contains both simulated background and signal events. This simulated dataset is called the BDT **training sample**. Each simulated event is assigned a certain weight, which is proportional to the expected rate of events with the same energy and declination. Let $w = w_s + w_b$ represent the cumulative weight of the events at a node, where w_s and w_b denote the contribution of signal and background, respectively. The purity at the node is then defined as $p = w_s/w$. The cut applied to the data separates events into two categories—those that pass the cut (child node 1), and those that do not pass the cut (child node 2). Each of the children nodes $i \in \{1, 2\}$ has its own cumulative weight w_i and purity p_i. The optimal choice for the cut at the parent node is the one which maximizes the **separation gain**

$$\Delta S = w\,S(p) - w_1 S(p_1) - w_2 S(p_2), \tag{3.27}$$

where $S(x) = x(1-x)$ with $x \in [0, 1]$ represents the Gini separation criterion [372]. The cut variable at a node is chosen from one of three randomly-picked reconstruction quantities. For each of these three variables, Equation (3.27) is optimized. The quantity that yields the best separation power is then used as the cut variable. This process is repeated until the final layer of the BDT is reached, where the GFU filter requires at least 1,000 events in a leaf.

In order to mitigate the effect of signal being erroneously classified as background and vice versa, the weight of misclassfied events is increased by 10% in a process called **boosting**. The boosted training sample is then used to create a second BDT via the procedure described above, after which another round of boosting takes place, etc. In total, 300 (resp. 400) BDTs are trained for the event selection in the Northern Hemisphere (resp. Southern Hemisphere). Such an ensemble of BDTs is also known as a **random forest**.

The size of a random forest is typically limited by the available statistics, since too many BDTs will eventually cause **overtraining**. This effect occurs when the BDTs start to become sensitive to statistical fluctuations in the data rather than actual physical variations. To ensure no overtraining occurs in the GFU filter, a test sample of MC data was simulated analogous to the training sample. This test sample was then passed through the previously trained BDTs. As shown in [340], a good agreement was found between the two samples after the BDT classification.

The eventual GFU data selection is performed by only selecting events that exceed a BDT-score threshold. The BDT **score** of an event is proportional to the combined purity of all the random-forest leaves—one for each BDT—in which the event is classified. The score criterion was set separately for each hemisphere, since they correspond to independent random forests. Both score criteria were chosen to optimize the point-source discovery potential (Section 4.3.3), while ensuring a smooth transition between the selections in the Northern and Southern Sky. They were also fixed to reduce the all-sky rate of events passing the GFU filter to 6.7 mHz, in order to be suitable for realtime analyses. For astrophysical neutrinos following an E_ν^{-2} spectrum, the GFU signal-selection efficiency [340] in the Northern Hemisphere is $\sim$50% at $E_\nu \sim 100$ GeV and reaches $\sim$95% for $E_\nu \gtrsim 100$ TeV. In the Southern Hemisphere, the signal-selection efficiency is $\sim$5% at $E_\nu \sim 10$ TeV and exceeds 70% for $E_\nu \gtrsim 1$ PeV.

Figure 3.15 shows the resulting event rate of GFU-selected data as a function of declination, which is compared to the results of the GFU MC sample.[35] A diffuse astrophysical neutrino spectrum was simulated according to the $E_\nu^{-2.19}$ spectrum observed in [274]. Excellent data-MC agreement is found in the Northern Sky, where simulations benefit from fits to the measured atmospheric-neutrino background [274]. In the Southern Sky, such fits are unavailable for atmospheric muons, resulting in worse data-MC agreement. Despite the significant background reduction, the GFU sample remains dominated by atmospheric muons (South) and atmospheric neutrinos (North). For the diffuse $E_\nu^{-2.19}$ spectrum discussed here, the average all-sky contribution of astrophysical events to the GFU sample is estimated to be $\sim$0.1% [340]. Nevertheless, as we shall discuss in Chapter 4, competitive sensitivities can be achieved for point-source analyses even with such small astrophysical signals buried in the background-dominated data.

[35] Note that the so-called GFU MC sample is distinct from the training sample and the test sample. The former is used as to mirror the GFU event selection using simulations. The latter are solely used for the optimization of the GFU filter algorithm, and are of no further usage after the development of the filter.

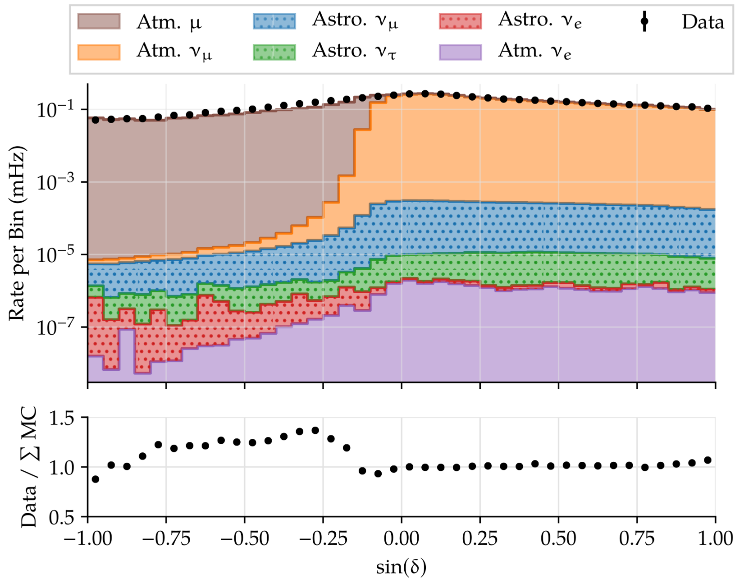

FIGURE 3.15: Event rate as a function of declination δ at the final level of the GFU track selection, taken from [340]. *Top*: Filled histograms represent different atmospheric and astrophysical components obtained with MC simulations. Astrophysical-neutrino events are simulated assuming a diffuse $E_\nu^{-2.19}$ spectrum as measured in [274]. The actual observed IceCube data is indicated by the black points. *Bottom*: Ratio between the rate of observed data and the sum of all MC components.

Final GFU Sample

Data that passes the GFU event selection is sent via satellite to Madison, USA for storage and further offline analysis. Compared to online systems, computational time constraints are much more relaxed for offline data processing. As such, the complete GFU sample is reprocessed using the optimal reconstruction methods which would otherwise be too time consuming for the online selection. Concretely, the following **offline reconstructions** are applied to all GFU events:

- SplineMPE with offline settings for the angular reconstruction;
- Paraboloid for the angular-error estimation;
- MuEX for the energy reconstruction.

This reprocessed offline GFU sample forms the main dataset used in the remainder of this work. The stacking analysis of Chapter 4 uses 7.2 years of GFU data recorded with the full 86-string detector (IC86) between May 2011 and October 2018. An overview of the GFU dataset is given in Table 3.2.

Number of Events	Livetime [days]	Time Period
1,501,394	2,615.97	IC86 2011–2018

TABLE 3.2: Properties of the GFU track-event selection used in the ULIRG stacking analysis.

3.3.2 Effective Area & Angular Resolution

Consider an astrophysical source with right ascension α and declination δ in equatorial coordinates. Assume that this source yields a high-energy neutrino flux $\Phi_\nu(E_\nu)$ at Earth. This flux will result in a certain detected event rate in IceCube. The **effective area** is defined as the quantity that links the neutrino flux arriving at Earth to the event rate, $\dot{N}_\nu$, observed in the detector,

$$\dot{N}_\nu = \int_0^\infty A_{\mathrm{eff}}(E_\nu|\alpha,\delta)\,\Phi_\nu(E_\nu)\,\mathrm{d}E_\nu. \tag{3.28}$$

By definition, the effective area takes into account the interaction probability of an astrophysical neutrino in or near IceCube. This probability includes the neutrino-ice interaction cross section (Figure 3.3) and the transmission probability of neutrinos through the Earth (Figure 3.7). Furthermore, the effective area takes into account the detector response for astrophysical neutrinos with a certain flavor, energy, and arrival direction. Since this response depends on the event selection, each dataset has its own unique effective area. Note that in this work, only time-integrated searches are of relevance. Since IceCube rotates with Earth's axis, and due to its geometry, the right-ascension dependence of the detector response is averaged out.

Panel (a) of Figure 3.16 shows the GFU effective area for muon neutrinos, determined using the dedicated GFU MC sample, as a function of the neutrino energy for different declination bands. In the Northern Sky, the effective area decreases above ~1 PeV as a result of neutrino absorption by the Earth. Below ~1 PeV, the effective area in the Southern Sky is significantly smaller than for the Northern Hemisphere. This is a consequence of the event selection in the Southern Hemisphere, which targets high-energy events (Section 3.3.1). It should be noted that the GFU sample is also expected to have a secondary contribution of tau neutrinos (~17%, see Table 3.1 and Figure 3.15), although these are not taken into account in the effective area used in this work. See [340] for GFU effective areas of other neutrino flavors.

Apart from the GFU effective area, a key ingredient for the ULIRG stacking analysis of Chapter 4 is the typical **angular resolution** of the GFU sample. Figure 3.17 shows the median GFU angular resolution—defined as the angular separation between the true neutrino direction and reconstructed track direction—for simulated neutrinos as a function of neutrino energy E_ν. For $E_\nu \gtrsim 2$ TeV, a subdegree median angular resolution is obtained. At lower energies, low Cherenkov-light yields and the kinematic angle between the neutrino and secondary muon limit the quality of the track reconstruction. The median angular resolution plateaus around ~0.3° above $E_\nu \gtrsim 1$ PeV, where stochastic energy losses dominate the reconstruction uncertainties.

3.3.3 Comparison with the IceCube Point-Source Dataset

To put the performance of the GFU sample into context, it is compared to the so-called **point-source (PS) event selection** [118]. The PS sample is a dedicated all-sky selection of tracks for time-integrated point-source analyses with IceCube (see also Section 1.3.1). Whereas the GFU selection is fully performed online to obtain a data stream for realtime searches, the sole online component of the PS selection is the muon filter. All subsequent filtering algorithms are performed offline, where reconstructions and selections can benefit from effectively unlimited computation times.

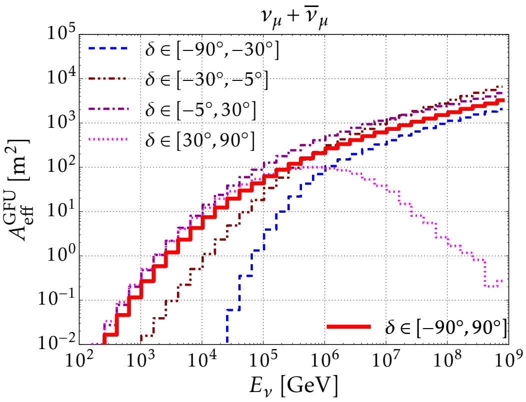

(a) GFU

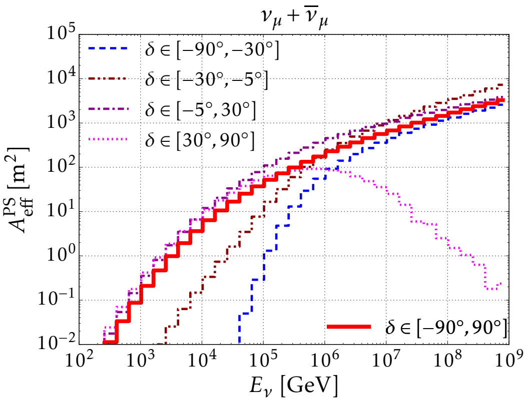

(b) PS

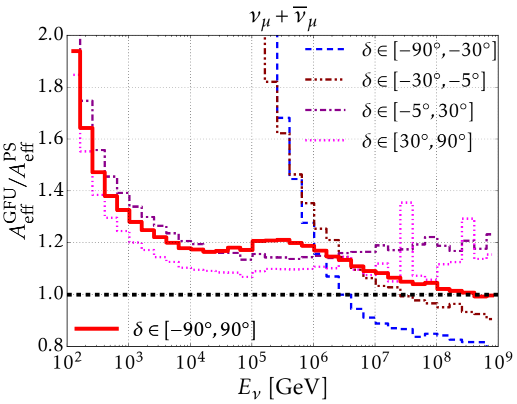

(c) Ratio

FIGURE 3.16: Effective area, A_{eff}, for muon neutrinos as a function of neutrino energy, E_ν, for various bands in declination δ. Thick solid red lines represent the effective area averaged over the full sky. Panels (a) and (b) show the effective area for the GFU and PS samples, respectively. Panels (c) shows the ratio between the GFU and PS effective areas, where the black dotted line in indicates a ratio of unity. The structures observed for $\delta \in [30°, 90°]$ for $E_\nu > 10$ PeV are a consequence of low statistics, since neutrinos with these energies become incapable of traversing the Earth (Figure 3.7).

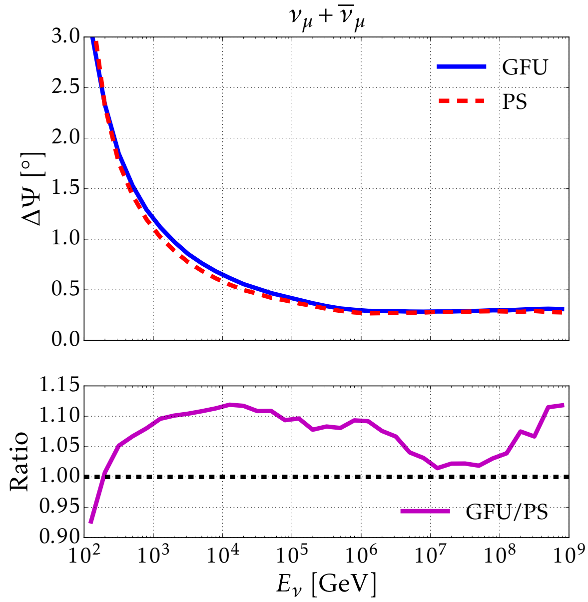

FIGURE 3.17: Median angular resolution, $\Delta\Psi$, as a function of neutrino energy, E_ν, for muon neutrinos. *Top*: Median angular resolution of the GFU and PS samples, represented by the solid blue and dashed red lines, respectively. *Bottom*: The GFU-to-PS ratio of the angular resolution.

Consequently, the median PS angular resolution is up to ∼10% better compared to that of the GFU sample for neutrino energies $E_\nu \gtrsim 1$ TeV, as shown in Figure 3.17.

Since the ULIRG stacking analysis of Chapter 4 is a time-integrated point-source search, it is worth motivating the choice of using the GFU sample in this work. Panel (b) of Figure 3.16 shows the muon-neutrino effective area of the PS sample, which exhibits similar behaviors compared to the GFU sample. The differences between the two selections are more apparent when considering the GFU-to-PS effective-area ratio, shown in Panel (c) of Figure 3.16. The GFU effective area is generally $\mathcal{O}(10\%)$ higher than the PS effective area for $E_\nu \gtrsim 1$ TeV. The only exception is for events in the Southern Sky with $E_\nu \gtrsim 3$ PeV. Here, the PS selection obtains a slightly better astrophysical-event purity by not only including well-reconstructed through-going tracks, like in the GFU sample, but also events that start in the detector (similar to the HESE criterion described in Section 3.1.5) [118].

In conclusion, although the PS sample has a better median angular resolution, the GFU sample typically has the upper hand in terms of effective area. Nevertheless, what eventually matters for a point-source analysis, is which sample results in the best sensitivity and discovery potential (Section 4.3.3). The work in [340] shows that the relative differences in angular resolution and effective area between the samples essentially cancel each other out, with statistically equivalent sensitivities obtained for both samples. However, during the time when the ULIRG stacking analysis was conducted, the GFU selection—in contrast to the PS sample—included improvements to the MuEX reconstruction algorithm used by both selections [373]. Since this affects the energy distribution of selected events, which is used in the analysis method of Chapter 4, the ULIRG stacking analysis exclusively uses the GFU sample, which is the only relevant IceCube dataset in the remainder of this thesis.

Chapter 4

Stacking Analysis of ULIRGs

All models are wrong, but some are useful.

— George E. P. Box

Introduction

Data analysis is one of the major pillars of experimental (astro)particle physics, for which we can generally rely on two major statistical formalisms. The most frequently[1] used formalism is called frequentist inference, where one relates probability to the frequency of observing a specific realization of the data. The other formalism is called Bayesian inference, where probability is related to the so-called degree of belief in the data being described by a certain model, which can be based on prior information about the experiment. In this work, exclusively frequentist methods will be applied (see e.g. [374, 375] for more details), which will briefly be outlined in Section 4.1. Examples of Bayesian inference in neutrino astronomy can e.g. be found in [64, 376].

The aim of this thesis is to analyze the IceCube GFU data (Section 3.3) in search for an astrophysical neutrino flux from the representative selection of ULIRGs (Section 2.3). Section 4.2 presents the point-source stacking method that will be applied to this IceCube analysis, which will rely on the SkyLab[2] software framework. The performance of the stacking analysis is subsequently discussed in Section 4.3. Here, an investigation is made on how well the analysis can recover an astrophysical flux from ULIRGs, and how sensitive we are to such a flux. As will be explained later on, in this Chapter we blind ourselves from the real GFU data in order to avoid any biases in the final results. The revelation of the final results using the unblinded data is reserved for Chapter 5.

4.1 Statistical Formalism

Each time an event $i \in \{1, 2, ..., N\}$ is observed with IceCube, we determine various quantities such as the reconstructed energy and arrival direction of the event. Let us denote our set of measurable physical quantities as $\mathbf{x} = (x^1, x^2, ..., x^p)$, which for event i take on the values $\mathbf{x}_i = (x_i^1, x_i^2, ..., x_i^p)$. There exists a **probability density function** (PDF), $\mathcal{P}(\mathbf{x}|\boldsymbol{\theta})$, that describes the probability to obtain these measured values, $\mathcal{P}_i(\boldsymbol{\theta}) \equiv \mathcal{P}(\mathbf{x} = \mathbf{x}_i|\boldsymbol{\theta})$. This PDF depends on a set of parameters $\boldsymbol{\theta} = (\theta^1, \theta^2, ..., \theta^q)$ which describe the underlying physics that give rise to the observed data, such as the possible contribution of an astrophysical neutrino flux.

Typically, the goal of an empirical analysis is to obtain estimates of the true values of these physical parameters, $\boldsymbol{\theta}_{\text{true}}$, given the dataset $\{\mathbf{x}_i\}$. For that purpose, we

[1] Pun absolutely intended.

[2] Available at https://github.com/icecube/skylab.

can define the following **likelihood function**,

$$\mathcal{L}(\boldsymbol{\theta}) = \prod_{i=1}^{N} \mathcal{P}_i(\boldsymbol{\theta}), \tag{4.1}$$

which describes the probability[3] that a set of parameters $\boldsymbol{\theta}$ is compatible with the measurements $\{\mathbf{x}_i\}$. Therefore, the parameters that best fit the data are those that maximize the likelihood over the full parameter space Θ,

$$\hat{\boldsymbol{\theta}} = \arg\max_{\boldsymbol{\theta}\in\Theta} \mathcal{L}(\boldsymbol{\theta}). \tag{4.2}$$

In order to compute these **maximum-likelihood estimators**, we require an expression for the PDF $\mathcal{P}(\mathbf{x}|\boldsymbol{\theta})$. In practical applications this PDF has to be modeled,[4] since its exact expression is generally unknown.

Experimental searches generally look for signatures in the dataset $\{\mathbf{x}_i\}$ that are caused by a specific physical process. This signature, or signal, is typically a small component of the data, which mainly consists of background. In a maximum-likelihood analysis for example, one would like to test whether the best-fit parameters $\hat{\boldsymbol{\theta}}$ are consistent with the presence of such a signal component in the data. For this purpose, one can perform a **hypothesis test**, where the null hypothesis, $\mathcal{H}_0$, states that the data consists of background only, while the alternative hypothesis, $\mathcal{H}_s$, states that the data consists of both background and a signal component. Given the result of the analysis, the null hypothesis will either be accepted or rejected, resulting in four possible outcomes that are listed in Table 4.1.

	$\mathcal{H}_0$ is true	$\mathcal{H}_s$ is true
$\mathcal{H}_0$ is accepted	Correct decision: True negative $1-\alpha$	Type II error: False negative β
$\mathcal{H}_0$ is rejected	Type I error: False positive α	Correct decision: True positive $1-\beta$

TABLE 4.1: Possible outcomes of a hypothesis test, each with an assigned probability. The probability α is the significance level of the test, while the probability $1-\beta$ is the power of the test.

[3]This statement is true since each event i is observed independently, and all measurements $\{\mathbf{x}_i\}$ follow the same PDF, $\mathcal{P}(\mathbf{x}|\boldsymbol{\theta})$.

[4]Ideally, the maximum-likelihood estimators should be consistent, i.e. $\hat{\boldsymbol{\theta}} \to \boldsymbol{\theta}_{\text{true}}$ as $N \to \infty$. However, a consequence of the PDF modeling is that this consistency cannot be achieved perfectly, since "all models are wrong." Nevertheless, simulations can be used to infer the consistency of the parameters under the assumptions of the PDF model. We can therefore expand the aphorism to the one quoted at the beginning of this Chapter.

To perform such a hypothesis test, one can construct the following **likelihood-ratio test statistic**,

$$\mathrm{TS} = 2\log\left[\frac{\max_{\boldsymbol{\theta}\in\Theta}\mathcal{L}(\boldsymbol{\theta})}{\max_{\boldsymbol{\theta}\in\Theta_0}\mathcal{L}(\boldsymbol{\theta})}\right] = 2\log\left[\frac{\mathcal{L}(\boldsymbol{\theta}=\hat{\boldsymbol{\theta}})}{\mathcal{L}(\boldsymbol{\theta}=\boldsymbol{\theta}_0)}\right]. \tag{4.3}$$

Here, $\boldsymbol{\theta}_0 \in \Theta_0$ is the set of parameters that maximizes the likelihood under the assumption that $\mathcal{H}_0$ is true. The TS will follow differing PDFs under the null and alternative hypotheses, denoted by $\mathcal{T}_0$ and $\mathcal{T}_s$, respectively. The factor of 2 in the TS ensures that **Wilks' theorem** holds, which states that as $N \to \infty$, $\mathcal{T}_0$ converges to a χ^2_ν distribution with $\nu = \dim\Theta - \dim\Theta_0$ degrees of freedom [377].

The data is most consistent with the null hypothesis when $\hat{\boldsymbol{\theta}} = \boldsymbol{\theta}_0$, i.e. when $\mathrm{TS} = 0$. All other $\hat{\boldsymbol{\theta}} \neq \boldsymbol{\theta}_0$ will result in a $\mathrm{TS} > 0$. As such, the likelihood-ratio method provides a one-tailed hypothesis test, in which each TS has the following associated **p-value**,

$$p = \int_{\mathrm{TS}}^{\infty} \mathcal{T}_0(\mathrm{TS}')\,\mathrm{d}(\mathrm{TS}'). \tag{4.4}$$

The p-value is the probability that one can obtain a test-statistic value $\geq$ TS under the null hypothesis, reflecting the compatibility of TS with $\mathcal{H}_0$. We can now define a certain TS threshold according to

$$\alpha = \int_{\mathrm{TS_{thresh}}}^{\infty} \mathcal{T}_0(\mathrm{TS}')\,\mathrm{d}(\mathrm{TS}'), \tag{4.5}$$

which is the **significance level** of the analysis. If $\mathrm{TS} \geq \mathrm{TS_{thresh}}$ or equivalently $p \leq \alpha$, the null hypothesis is rejected. Thus, α describes the probability of committing a Type I error (see Table 4.1). In particle physics, the rule of thumb is that a 5σ significance level is required in order to reject the null hypothesis, which corresponds to[5] $\alpha = 5.73\times10^{-7}$. Under the alternative hypothesis $\mathcal{H}_s$, one can also compute the probability that a Type II error is committed,

$$\beta = \int_0^{\mathrm{TS_{thresh}}} \mathcal{T}_s(\mathrm{TS}')\,\mathrm{d}(\mathrm{TS}'). \tag{4.6}$$

The **power** of the hypothesis test is then defined as the complementary probability $1-\beta$. Since the power is proportional to the strength of the signal relative to the background, one aims to achieve the largest possible power[6] down to the smallest possible signal strengths. In other words, one aims to optimize the sensitivity of the search.

To study its overall performance, the analysis is typically performed blindly in order to avoid biases in the final decision of the hypothesis test. In a **blind analysis**, the truly observed data remains undisclosed. Instead, data scrambles and Monte Carlo simulations are used to perform so-called pseudo-experiments with "fake" renditions of the data. Once the analysis method is optimized, the observed data is unblinded, resulting in a certain observed test statistic $\mathrm{TS_{obs}}$ and its corresponding

[5] The $n\sigma$ significance level of a one-tailed test corresponds with the p-value $p = \int_{n\sigma}^{\infty}\mathcal{N}_{\mathrm{half}}(x|\sigma)\,\mathrm{d}x$, where $\mathcal{N}_{\mathrm{half}}(x|\sigma)$ is a half-normal distribution with standard deviation σ.

[6] In the specific case where each hypothesis corresponds with a discrete parameter value, i.e. $\mathcal{H}_0$: $\boldsymbol{\theta} = \boldsymbol{\theta}_0$ and $\mathcal{H}_s$: $\boldsymbol{\theta} = \boldsymbol{\theta}_s$, the Neyman-Pearson lemma states that the likelihood ratio of Equation (4.3) is the most powerful α-level test [378].

p-value. Depending on the result of this $\mathrm{TS}_{\mathrm{obs}}$ the null hypothesis will either be accepted or rejected.

4.2 Methods for an IceCube Stacking Analysis of ULIRGs

In the IceCube analysis presented here, the GFU track data $\{\mathbf{x}_i\}$ will be searched for an astrophysical signal originating from the selection of ULIRGs. A general assumption made in the following is that a muon-neutrino flux from ULIRGs can be described by an unbroken power-law spectrum, $\Phi_{\nu_\mu+\overline{\nu}_\mu} = \Phi_0(E_\nu/E_0)^{-\gamma}$. This assumption is motivated both from modeling (Section 2.2) and observational perspectives, since the diffuse IceCube neutrino flux show no evidence for more elaborate spectral features (Section 1.2.1). The ULIRG neutrino flux $\Phi_{\nu_\mu+\overline{\nu}_\mu}$ would give rise to certain number of astrophysical signal events in the data, n_s. Consequently, the parameters of interest here are $\boldsymbol{\theta} = (n_s, \gamma)$, which are directly related to the flux normalization Φ_0. The goal of this analysis will be to find the maximum-likelihood estimators $\hat{\boldsymbol{\theta}} = (\hat{n}_s, \hat{\gamma})$ that best fit the GFU data $\{\mathbf{x}_i\}$, and to test whether these best-fit parameters are consistent with the contribution of an astrophysical neutrino flux from ULIRGs—under a specific likelihood model, as discussed in the following.

4.2.1 Time-Integrated Unbinned Point-Source Likelihood

Since the spatial extension of ULIRGs (arcseconds to arcminutes [193]) is well below the angular resolution of IceCube (Section 3.3.2), they will appear as point sources in an IceCube analysis. In addition, ULIRGs are modeled as steady sources of neutrinos, as discussed in Section 2.2. As such, the full 7.2 years of GFU data are integrated over in search of an astrophysical signal. Let us for the moment consider a single candidate source k. The method of [379] is followed to construct the following **time-integrated unbinned point-source likelihood**,

$$\mathcal{L}(n_s,\gamma) = \prod_{i=1}^{N} \mathcal{P}_i(n_s,\gamma) = \prod_{i=1}^{N} \Bigg[\underbrace{\frac{n_s}{N}\mathcal{S}_i^k(\gamma)}_{\text{signal}} + \underbrace{\left(1-\frac{n_s}{N}\right)\mathcal{B}_i}_{\text{background}} \Bigg]. \tag{4.7}$$

The PDF that enters the likelihood is modeled with a background term, $\mathcal{B}_i$, and a signal term, $\mathcal{S}_i^k$. The background and signal terms are both unbinned PDFs,[7] with a relative contribution that depends on the number of signal events, n_s. For each event $i \in \{1,2,...,N\}$, the observables $\mathbf{x}_i = (\alpha_i, \delta_i, \sigma_i, E_i)$ are used in the PDF evaluation, which are described in Table 4.2.

In order to utilize both the spatial and energy information of the data in the likelihood, each PDF is separated into two components,

$$\mathcal{B}_i = \underbrace{\frac{B_\delta(\delta_i)}{2\pi}}_{\text{spatial}} \times \underbrace{\mathcal{E}_{\mathcal{B}}(E_i|\delta_i)}_{\text{energy}}, \tag{4.8}$$

$$\mathcal{S}_i^k(\gamma) = \underbrace{S(\alpha_k,\delta_k,\alpha_i,\delta_i,\sigma_i)}_{\text{spatial}} \times \underbrace{\mathcal{E}_{\mathcal{S}}(E_i|\delta_i,\gamma)}_{\text{energy}}. \tag{4.9}$$

[7] In an unbinned likelihood method, the PDFs are assumed to be continuous, yielding a better sensitivity compared to binned likelihood methods [379].

Parameters		Description
Event i	(α_i, δ_i)	SplineMPE right ascension & declination
	σ_i	Paraboloid uncertainty on reconstructed direction
	E_i	MuEX muon energy proxy
Source k	(α_k, δ_k)	Right ascension & declination
	w_k	Stacking weight
To be fitted	n_s	Number of astrophysical signal events
	γ	Spectral index of astrophysical signal flux

TABLE 4.2: A list of all the parameters that are used to formulate the time-integrated point-source stacking likelihood of Equation (4.11).

As discussed in the following, the background PDF components are constructed directly from the GFU data, whereas the signal PDF components are constructed using analytic expressions and simulations.

Spatial Signal PDF

Spatially, astrophysical signal events are expected to be clustered around the location of source k on the sky. The spatial signal PDF is therefore modeled as a **circularized bivariate Gaussian** centered around this source, which for event i takes the form

$$S(\alpha_k, \delta_k, \alpha_i, \delta_i, \sigma_i) = \frac{1}{2\pi\sigma_i^2} \exp\left(-\frac{|(\alpha_k, \delta_k) - (\alpha_i, \delta_i)|^2}{2\sigma_i^2} \right). \tag{4.10}$$

This PDF describes the probability that the event i is spatially correlated with source k, where $|(\alpha_k, \delta_k) - (\alpha_i, \delta_i)|$ represents the opening angle between the event and the source. The width of the Gaussian is fully determined by the estimated angular uncertainty of the event, σ_i. Since the source location is generally inferred from optical measurements with resolutions smaller than an arcsecond [193], the uncertainty on the source position can safely be neglected.

As discussed in Section 3.3.1, the estimated event uncertainty does not take into account systematic effects such as the kinematic angle between the detected muon and the original neutrino. In order to partially mitigate underestimated uncertainties, a **floor** $\sigma_i \geq 0.2°$ is imposed for all events following the work of [118]. However, it should be noted that the work in [134] shows that the signal PDF becomes highly non-Gaussian at relatively low energies and small angular uncertainties. This effect is mostly due to the larger kinematic angle at these scales. In order to successfully take this effect into account, the authors of [134] have developed a novel method that constructs the signal PDF from simulations using kernel density estimators (KDEs) [380]. Overall, this KDE method yields a better PDF description; for an E_ν^{-2} spectrum, it yields an improvement of 20–30% to the 5σ discovery potential (see Section 4.3.3). However, the implementation of such KDEs to the ULIRG stacking analysis falls beyond the scope of this thesis.

Spatial Background PDF

Atmospheric background events, on the other hand, will not be clustered around a certain location on the sky. Since a time-integrated search is conducted in this work, the spatial background PDF, $B_\delta(\delta)/2\pi$, is uniform in right ascension,[8] yielding the factor $1/2\pi$. The latitudinal dependence of the PDF is modeled by scrambling (see Section 4.3.1) and binning the GFU data in $\sin\delta$, where δ is the reconstructed declination. This $\sin\delta$ distribution is then interpolated with a **spline** in order to obtain an unbinned spatial background PDF, as shown in Figure 4.1.

Note that in the Southern Hemisphere, the PDF is rather bumpy. This is a consequence of the BDT-score cut applied in the GFU filter (Section 3.3.1), which has a discrete declination dependency in the Southern Sky to target events with higher energies [340] (recall the relatively poor data/MC agreement found in Figure 3.15). Efforts within the IceCube collaboration [381] are currently working on a smoothing of this BDT cut, which would on its turn yield a smoother spatial background PDF (and better data/MC agreement). Nevertheless, the PDF of Figure 4.1 provides a sufficiently accurate description of the background for the purposes of this work; the PDF smoothing generally affects the sensitivity of Section 4.3.3 by $\lesssim$10% [381].

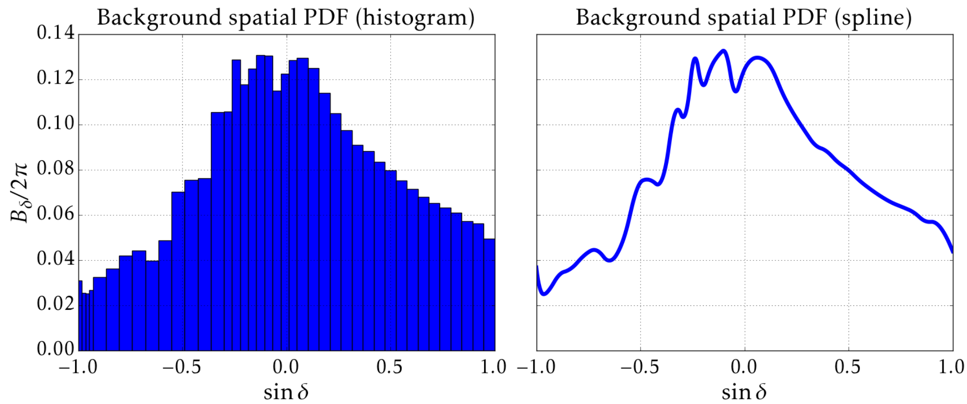

FIGURE 4.1: The spatial background PDF, $B_\delta(\delta)/2\pi$, as a function of the reconstructed declination δ. The left panel shows the PDF which is constructed by binning the scrambled GFU data in $\sin\delta$. The right panel shows the unbinned PDF which is found by interpolating a spline through the binned PDF.

Energy PDFs

By construction, the probability that a GFU event has a certain reconstructed energy E depends on the reconstructed declination δ of that event. Hence, the background energy PDF $\mathcal{E}_\mathcal{B}(E|\delta)$ is obtained by binning the scrambled GFU data in both $\sin\delta$ and $\log_{10} E$, as shown in Figure 4.2. The signal energy PDF $\mathcal{E}_\mathcal{S}(E|\delta,\gamma)$ is constructed analogously using simulated events from the GFU MC sample (Sections 3.1.6 and 3.3). These MC events are generated by simulating a source at $\sin\delta$ that emits neutrinos with energy E_ν according to an unbroken $E_\nu^{-\gamma}$ power-law spectrum. The resulting PDFs for signal spectra with spectral indices $\gamma \in \{2.0, 3.0\}$ are shown in Figure 4.3. Note that both the background and signal energy PDFs are normalized over $\log_{10} E$ in each bin of $\sin\delta$. Given a certain $\sin\delta$ (and γ), these PDFs therefore describe the probability that an event with reconstructed energy E corresponds with signal or background.

[8]The uniformity in right ascension stems from the fact that IceCube has an azimuthal symmetry and is located at the geographic South Pole, such that it rotates with the axis of the Earth.

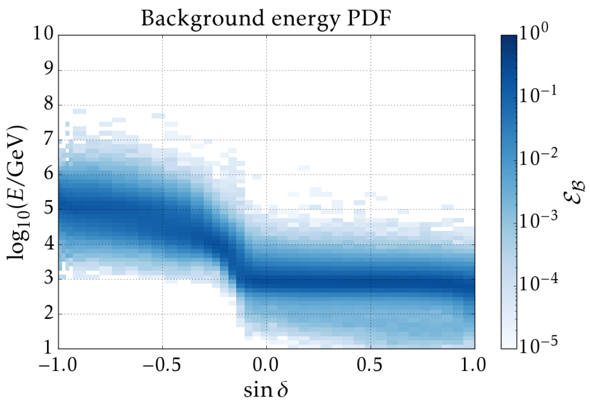

Figure 4.2: The background energy PDF, $\mathcal{E}_{\mathcal{B}}(E|\delta)$, constructed by binning the scrambled GFU data in $\sin\delta$ and $\log_{10} E$, with δ and E the reconstructed declination and energy, respectively. The higher energies for the background in the Southern Hemisphere is a consequence of the GFU selection criteria (Section 3.3.1).

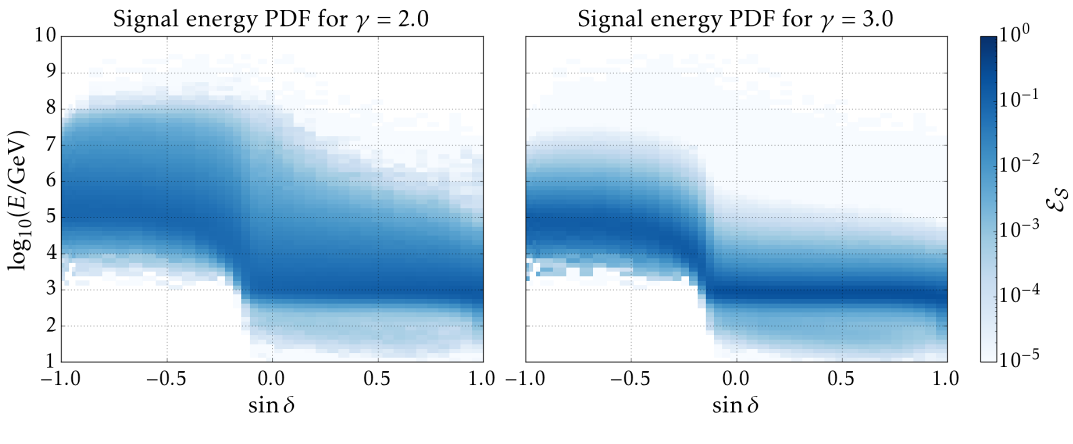

Figure 4.3: The signal energy PDF, $\mathcal{E}_{\mathcal{S}}(E|\delta,\gamma)$, constructed by binning simulated astrophysical events in $\sin\delta$ and $\log_{10} E$, with δ and E the reconstructed declination and energy, respectively. The left and right panels show the PDFs for power-law spectra with spectral indices $\gamma = 2.0$ and $\gamma = 3.0$, respectively.

As will be discussed in Section 4.2.3, the practical goal of the analysis method is to evaluate the *ratio* of the signal and background PDFs. As such, the ratio of the energy PDFs, $\mathcal{E}_{\mathcal{S}}/\mathcal{E}_{\mathcal{B}}$, is computed by simply dividing the corresponding histograms. In bins for which there is a signal entry but no background entry, the background PDF $\mathcal{E}_{\mathcal{B}}$ is given its smallest non-zero value in order to obtain a well-defined PDF ratio. Subsequently, an unbinned PDF ratio is obtained by interpolating a **spline** through these histograms. The signal-over-background histograms and corresponding splines are shown in Figure 4.4 for $\gamma \in \{2.0, 3.0\}$.

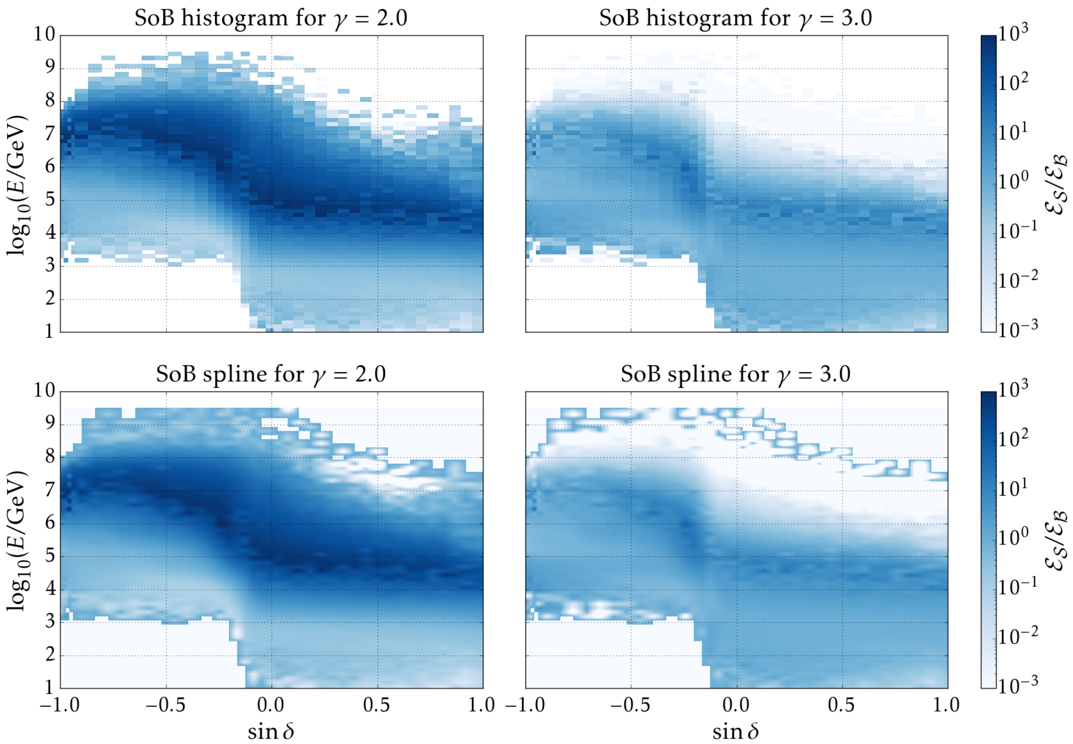

FIGURE 4.4: The signal-over-background (SoB) ratio of the energy PDFs, $\mathcal{E}_{\mathcal{S}}/\mathcal{E}_{\mathcal{B}}$. The top row shows the SoB ratios obtained by dividing the histograms of Figure 4.3 by the histogram of Figure 4.2. The bottom row shows the unbinned SoB ratios, which are found by interpolating a spline through the respective binned SoB ratios of the top row.

4.2.2 Stacking Likelihood and Stacking Weights

Up to this point, the IceCube analysis method has been described for a single point source $k \in \{1, 2, ..., M\}$. If we now want to perform a search for neutrinos from all $M = 75$ ULIRGs, there are two options:

1. Analyze each source **separately**.

   + Can study the neutrino emission of each individual source.
   – Need to take into account a trial factor of the order $\mathcal{O}(M)$ in the final p-value (see e.g. [118]).

2. Perform a **stacking analysis** [382] and consider the contribution of all M sources simultaneously.

   + If the sources are too faint to be observed individually, this method could still be sensitive to their cumulative flux.
   – Cannot discern the individual source fluxes a priori.

The aim of this work is to study the neutrino emission from the ULIRG source population as a whole. Moreover, apart from first hints emerging from NGC 1068 (Section 1.3.2), no point sources have been identified in time-integrated IceCube searches so far. Hence, the stacking-analysis method is opted in this search for neutrinos from ULIRGs.

We can now convert the point-source likelihood of Equation (4.7) to the following **stacking likelihood**,

$$\mathcal{L}(n_s, \gamma) = \prod_{i=1}^{N} \Bigg[\underbrace{\frac{n_s}{N} \sum_{k=1}^{M} w_k(\gamma)\, \mathcal{S}_i^k(\gamma)}_{\text{stacked signal}} + \underbrace{\left(1 - \frac{n_s}{N}\right) \mathcal{B}_i}_{\text{background}} \Bigg]. \tag{4.11}$$

The stacking takes place in the signal term of the likelihood, which is now a weighted sum over the signal PDFs $\mathcal{S}_i^k(\gamma)$ off all point sources, with w_k the corresponding stacking weights. The fit parameter n_s therefore describes the total number of signal events from all sources combined. Regarding the energy component of the signal, the most realistic description is one where each source $k \in \{1, 2, ..., M\}$ is modeled with their own independent spectral index γ_k. However, since fitting separate spectral indices for $M = 75$ ULIRGs would be computationally unfeasible, a single global spectral index γ is assumed in the stacking likelihood. The effects of this assumption are discussed in Section 4.3.3. For completeness, Table 4.2 summarizes all the parameters that are used to compute the stacking likelihood.

To illustrate the benefits of a stacking search, Figure 4.5 shows the IceCube 40-string (IC40) discovery potential (Section 4.3.3) for an increasing set of simulated sources at the same declination $\delta = 45°$ [125]. The sources are also assumed to yield the same E_ν^{-2} neutrino flux at Earth, meaning that $w_k = 1$ in this example (see below). The total flux, or stacked flux—which is proportional to n_s—required for a discovery (Section 4.3) *increases* as more sources are added to the stacking analysis. This is a consequence of the fact that more background events are evaluated by the stacked-signal term in Equation (4.11). However, the average flux *per source* required for a discovery *decreases*, indicating that the stacking analysis can pick up fainter individual source signals compared to a single point-source search. Nevertheless, this decrease eventually saturates, because as more and more sources are added, more background enters the signal term. Consequently, the cumulative signal contribution of all sources becomes harder to distinguish from the overall background. In a more realistic scenario, the relative contribution of the different signal strengths of the various sources is taken into account by the stacking weight w_k.

The **stacking weight** of source k is computed as[9]

$$w_k(\gamma) = \frac{r_k(\gamma)\, t_k}{\sum_{j=1}^{M} r_j(\gamma)\, t_j}. \tag{4.12}$$

[9] By construction, the stacking weight is a relative weight between the sources that are analyzed. As such, when $M = 1$, Equation (4.11) is reduced to the single point-source likelihood of Equation (4.7).

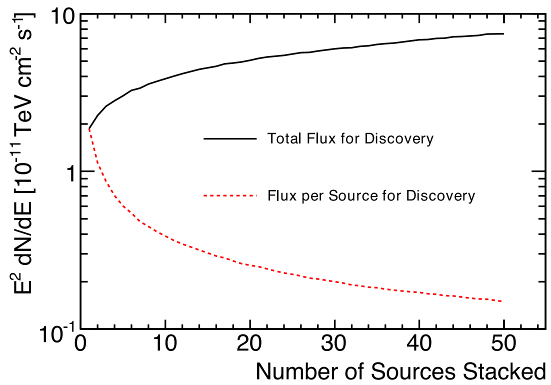

FIGURE 4.5: IC40 discovery potential (5σ) for a stacking analysis of an increasing number of sources. The sources are simulated with the same E_ν^{-2} neutrino flux at Earth, and at the same declination $\delta = 45°$. The black solid line indicates the total stacked flux required for a discovery, whereas the red dashed line shows the corresponding per-source flux. When stacking a single source, the two lines merge to the discovery potential of a single point-source analysis. Note that this plot is simply meant to illustrate the idea behind a stacking analysis; it is not representative of the ULIRG stacking search presented in this work. Taken from [125].

On the one hand, the stacking weight depends on the detector response $r_k(\gamma)$ for an astrophysical signal from this source. This **detector weight** is obtained by convolving the effective area of the detector at the source declination δ_k (see Section 3.3.2) with the assumed power-law spectrum of the signal,

$$r_k(\gamma) = \int_0^\infty A_{\text{eff}}(E_\nu|\delta_k)\, E_\nu^{-\gamma}\, \mathrm{d}E_\nu. \tag{4.13}$$

On the other hand, the stacking weight depends on a **theoretical weight** t_k, which is modeled according to some assumptions about the physics of the candidate neutrino source. In this work case, the total IR luminosity L_{IR} is assumed to be representative for the neutrino output of ULIRGs. This assumption is motivated by the fact that L_{IR} is a measure for the SFR—see Equation (2.1)—and that a possible AGN contribution to the IR luminosity increases with L_{IR} (Figure 2.5). Since both starbursts and AGN are plausible hadronic accelerators that can produce neutrinos in ULIRGs (Section 2.2), L_{IR} can serve as a proxy for the neutrino luminosity. The theoretical weight is therefore set as

$$t_k = F_{\text{IR},k} = \frac{L_{\text{IR},k}}{4\pi d_{L,k}^2}, \tag{4.14}$$

where $F_{\text{IR},k}$ is the total infrared flux of source k. This flux is computed using the total IR luminosity, $L_{\text{IR},k}$, and the luminosity distance, $d_{L,k}$, of the source, as explained in Section 2.3.4.

Panels (a) and (b) of Figure 4.6 show the distributions of the ULIRG stacking weights $w_k(\gamma)$, with subcomponents $r_k(\gamma)$ and t_k, for both $\gamma = 2.0$ and $\gamma = 3.0$, respectively. In general, nearby sources in the Northern Sky are found to contribute most to the stacking analysis. This simply reflects the fact that IceCube is mostly sensitive in the Northern Hemisphere—where there is no contamination from atmospheric muons (Section 3.1.5)—and that the total IR flux of ULIRGs was chosen as a proxy for their neutrino flux.

It is common in IceCube stacking analyses (see e.g. [383]) to investigate different

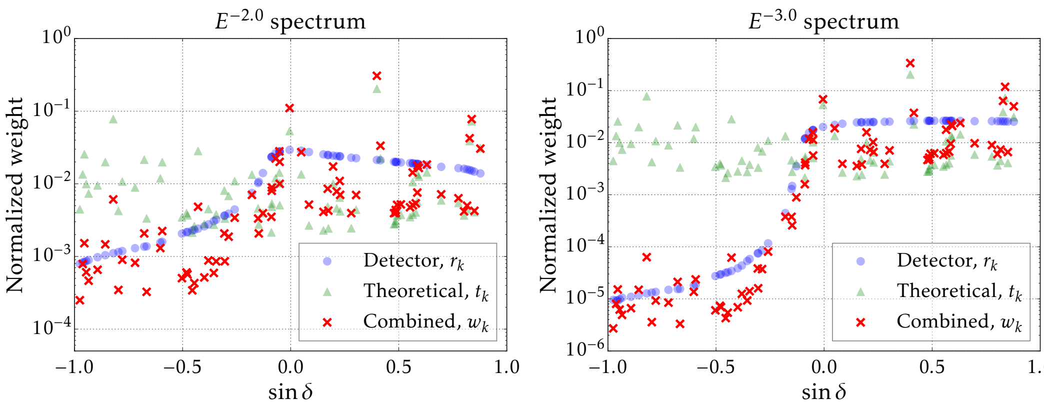

(a) $\gamma = 2.0$ (b) $\gamma = 3.0$

FIGURE 4.6: Normalized stacking weight $w_k(\gamma) \propto r_k(\gamma)\,t_k$ for each ULIRG k, shown as a function of the source declination δ. The normalized detector weights, $r_k(\gamma)$, and normalized theoretical weights, $t_k = F_{\mathrm{IR},k}$, are also shown. To illustrate the effect of the assumed source spectrum on the the final stacking weight, Panels (a) and (b) show the weights for spectral-index values $\gamma = 2.0$ and $\gamma = 3.0$, respectively.

weighting schemes. In particular, an equal-weighting scenario is often considered, where $t_k = 1$. Equal weights do not make any assumptions on source models in the analysis, and are therefore used to perform a more unbiased search. However, this weighting is rather unrealistic, since a neutrino flux observed at Earth will naturally scale inversely with the square of the distance to that source. Distance weights, $t_k = d_{L,k}^{-2}$, thus provide a model-independent way to take this effect into account. In the case of the ULIRG stacking analysis, the distance weights are highly correlated with the total IR flux weights, as shown in Figure 4.7. This correlation is a

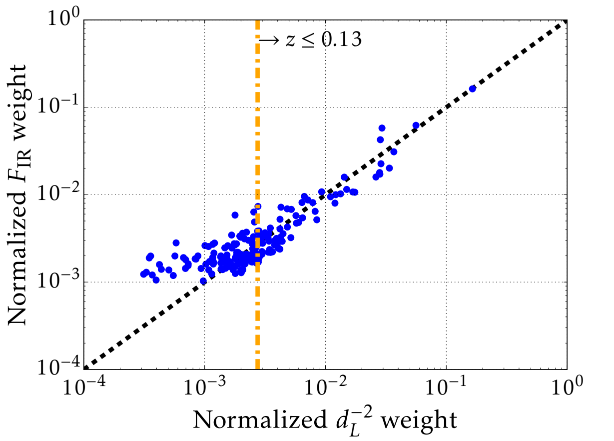

FIGURE 4.7: Correlation between two theoretical weighting schemes for the ULIRG stacking analysis, where d_L is the luminosity distance, and F_{IR} is the total IR flux. The weights are normalized for all 189 objects in the initial ULIRG selection. The orange dash-dotted line indicates the redshift cut at $z = 0.13$ used to obtain the representative sample of 75 ULIRGs. The black dotted line represents an ideal one-to-one correspondence.

consequence of the limited spread of L_{IR} values, which lie within the same order of magnitude (see Figure 2.12). Hence, only the total IR flux weights are considered in the final analysis, since distance weights would not provide any novel information to our search. In Sections 4.3.4 and 4.3.5 some intermediate results of the analysis performance will be presented using distance weights, confirming this statement.

4.2.3 Likelihood-Ratio Test Statistic

The goal of this analysis is to determine the parameters $(\hat{n}_s, \hat{\gamma})$ that maximize the stacking likelihood of Equation (4.11). Furthermore, we aim to test whether these best-fit parameters are compatible with a background-only scenario (null hypothesis $\mathcal{H}_0$) or with the additional presence of an astrophysical signal from ULIRGs in the data (alternative hypothesis $\mathcal{H}_s$). According to the formalism outlined in Section 4.1, the following likelihood-ratio **test statistic** is constructed,

$$\begin{aligned} \mathrm{TS} &= 2\log\left[\frac{\mathcal{L}(n_s = \hat{n}_s, \gamma = \hat{\gamma})}{\mathcal{L}(n_s = 0)}\right] \\ &= 2\sum_{i=1}^{N}\log\left[\frac{\hat{n}_s}{N}\left(\sum_{k=1}^{M} w_k(\hat{\gamma})\frac{\mathcal{S}_i^k(\hat{\gamma})}{\mathcal{B}_i} - 1\right) + 1\right]. \end{aligned} \tag{4.15}$$

Here, $\mathcal{L}(n_s = 0) = \prod_{i=1}^{N}\mathcal{B}_i$ is the likelihood evaluated under the null hypothesis.

In the maximization of the likelihood ratio, the physical bound[10] $\hat{n}_s \geq 0$ is imposed, and the spectral index is constrained to $\hat{\gamma} \in [1, 4]$. Although the latter constraint is rather arbitrary, it is well-motivated. From a theoretical standpoint, a value $\gamma \sim 2$ is expected at the source from first-order Fermi acceleration (Section 1.1.1; see also the model predictions in Section 2.2), while observationally, IceCube measurements of the diffuse neutrino flux yield values $2 < \gamma < 3$ (Section 1.2.1). Hence, the bounds on the spectral index can be seen as conservative.

Furthermore, in order to reduce computation time, only events within a box centered around any source k are used in the evaluation of Equation (4.15) in `SkyLab`.[11] The idea is that events outside any of these M boxes can safely be discarded, since they have a negligible contribution to the spatial signal PDF of Equation (4.10). An event i is located within a box with dimensions $2\Delta_\alpha \times 2\Delta_\delta$ around source k if

$$\delta_{\mathrm{min}} \equiv \max\{-\pi/2, \delta_k - \Delta_\delta\} < \delta_i < \min\{\delta_k + \Delta_\delta, \pi/2\} \equiv \delta_{\mathrm{max}}, \tag{4.16}$$

and

$$|\alpha_i - \alpha_k| < \min\left\{\frac{\Delta_\delta}{\min\{\cos\delta_{\mathrm{min}}, \cos\delta_{\mathrm{max}}\}}, \pi\right\} \equiv \Delta_\alpha. \tag{4.17}$$

Here, a value $\Delta_\delta \equiv 10°$ is chosen. For a source located at the equator, $\Delta_\alpha \approx \Delta_\delta$, yielding a box of roughly $20° \times 20°$ around source k. The more the source is located towards one of the poles, the more Δ_α increases in order to take into account the solid-angle effect. As such, we ensure that there are always sufficient events with which to evaluate the PDF ratio $\mathcal{S}_i^k/\mathcal{B}_i$ for each source k.

[10] Numerically, it is perfectly possible to fit $\hat{n}_s < 0$, which would correspond to an underfluctuation in the data. In case one would desire to distinguish such underfluctuations in the analysis, a factor $\operatorname{sgn}\hat{n}_s$ has to be taken into account in Equation (4.15).

[11] In `Csky` (Section 4.3.5), instead of defining a box, only the events for which $|(\alpha_k, \delta_k) - (\alpha_i, \delta_i)| < 5\sigma_i$ are evaluated in the likelihood.

As a final note, it is worth mentioning that in a previous work [384], a comparison of various statistical methods was performed in the context of a time-integrated point-source analysis with IceCube. It was found that in general, the likelihood-ratio method described here yields the best analysis performance in terms of sensitivity. See also [385] for a comparison of statistical methods used in transient analyses.

4.3 Performance of the ULIRG Stacking Analysis

4.3.1 Description of the Background

As discussed in Section 4.1, the PDF of the above TS under the background-only hypothesis has to be determined to be able to compute a p-value for the analysis. This background-only PDF is determined by performing many **pseudo-experiments**, where the GFU data is scrambled in right ascension. In such a **scramble**, each GFU event is assigned a random right-ascension value drawn from a uniform distribution between $[0, 2\pi)$, since the atmospheric background is uniform in right ascension (Section 4.2.1). The TS is then evaluated using Equation (4.15), yielding a "fake" rendition of our experiment in a background-only scenario. Each data scramble and corresponding TS evaluation is called a **trial**.

The background-only PDF is now obtained by performing 10^5 background-only trials, resulting in the distribution shown in Figure 4.8, against which the GFU data will eventually be tested to obtain a certain p-value (Chapter 5). However, $\sim 10^8$ trials would be required in order to obtain a background-only TS distribution that is accurate up to the 5σ significance level, which is computationally unfeasible. Fortunately, we can apply Wilks' theorem (Section 4.1) and fit a χ^2_ν PDF through our

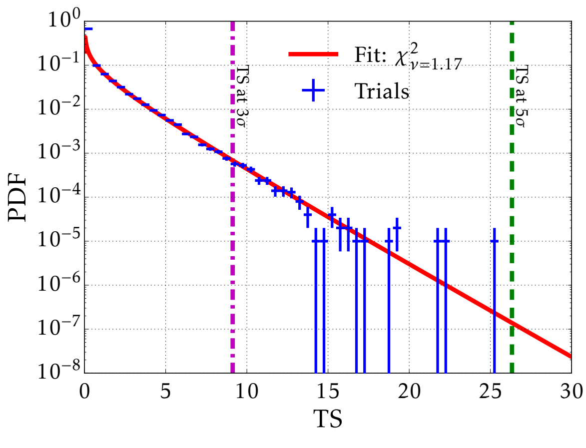

FIGURE 4.8: The background-only PDF of the likelihood-ratio test statistic (TS). The blue crosses represent the histogram obtained by performing 10^5 trials, while the red solid line is the best-fit χ^2_ν PDF with $\nu = 1.17$ degrees of freedom fit through these trials. The TS threshold values corresponding with a 3σ significance level ($\alpha = 2.70\times10^{-3}$) and 5σ significance level ($\alpha = 5.73\times10^{-7}$) are indicated with the magenta dash-dotted line and the green dashed line, respectively.

10^5 background-only trials. The degrees of freedom ν are left as a free parameter in the fit, resulting in a best-fit value[12] $\nu = 1.17$. As shown in Figure 4.8, the $\chi^2_{\nu=1.17}$ PDF fits the trials very well, such that the background-only TS distribution can confidently be described up to an arbitrary significance level.

4.3.2 Recovery of Injected Pseudosignal

To test the performance of the ULIRG stacking analysis when recovering an astrophysical signal, **pseudosignal** muon neutrinos are generated with MC simulations analogous to those described in Sections 3.1.6 and 3.3. These pseudosignal neutrinos are assumed to follow an unbroken power-law spectrum for each source k,

$$\Phi_k(E_\nu) = \Phi_{0,k} \left(\frac{E_\nu}{E_0}\right)^{-\gamma_k}, \tag{4.18}$$

with a normalization energy chosen[13] at $E_0 = 10$ TeV. The **stacked flux** of all $M = 75$ sources is then given by

$$\Phi_{\text{stack}} \equiv \Phi_{\nu_\mu+\bar{\nu}_\mu} = \sum_{k=1}^{M} \Phi_k. \tag{4.19}$$

The flux normalization of the individual sources is related to the **stacked flux normalization**, $\Phi_0 \equiv \Phi_{\nu_\mu+\bar{\nu}_\mu}(E_0)$, via

$$\Phi_{0,k} = \frac{t_k}{\sum_{j=1}^{M} t_j} \Phi_0, \tag{4.20}$$

where t_k is the theoretical stacking weight discussed in Section 4.2.2. Next, all ULIRGs are assumed to have identical properties of hadronic acceleration and neutrino production, such that we can describe their spectra with the same spectral index, $\gamma_k = \gamma$. The implications of this assumption are discussed in Section 4.3.3. The stacked neutrino flux of Equation (4.19) can then be simplified to

$$\Phi_{\nu_\mu+\bar{\nu}_\mu}(E_\nu) = \Phi_0 \left(\frac{E_\nu}{E_0}\right)^{-\gamma}. \tag{4.21}$$

A pseudosignal neutrino is simulated according to Equation (4.21), with a true energy $100 \text{ GeV} = E_{\text{min}} < E_\nu < E_{\text{max}} = 100 \text{ PeV}$, and a true direction exactly at the location of one of the 75 ULIRGs. It is then forced to interact within or near the detector, resulting in a track with a certain reconstructed direction and reconstructed energy, which is called a pseudosignal event. Pseudo-experiments are then expanded by injecting such pseudosignal events to the scrambled data. In such a signal-plus-background pseudo-experiment, the number of **injected events**[14] is drawn from a

---

[12] Ideally, one would expect a value $\nu = 2$. The fact that the best-fit $\nu < 2$ is a consequence of the fact that the atmospheric background is itself well-described by a power-law spectrum with $\gamma = 3.7$ [344]. Consequently, the freedom of $\hat{\gamma}$ in the likelihood fit is effectively reduced, as shown in Appendix D.

[13] The choice of the normalization energy is rather arbitrary. Here, the final choice is motivated by the fact that the ULIRG stacking analysis is sensitive to neutrinos with $E_0 = 10$ TeV for all spectra considered in this work.

[14] Note that in this work, the number of injected pseudosignal events is generally very small compared to the number of evaluated background events. When the injected signal becomes too large compared to the background, the point-source likelihood has to be modified to subtract such a signal

Poisson distribution with a certain specified mean, μ_{inj}. This mean number of injected pseudosignal events is related to the stacked flux normalization as

$$\mu_{\text{inj}} = \Phi_0 T \int_{E_{\min}}^{E_{\max}} A_{\text{eff}}(E_\nu) \left(\frac{E_\nu}{E_0}\right)^{-\gamma_{\text{inj}}} \mathrm{d}E_\nu, \tag{4.22}$$

where T is the GFU livetime (Section 3.3.1), and A_{eff} is the GFU effective area for muon neutrinos[15] (Section 3.3.2). The latter is convoluted with the assumed power law of the injected pseudosignal, which has a spectral index $\gamma = \gamma_{\text{inj}}$. The relative number of events injected per source location is proportional to the theoretical stacking weight of that source.

To test whether the likelihood fit parameters $(\hat{n}_s, \hat{\gamma})$ can correctly recover the injection parameters $(\mu_{\text{inj}}, \gamma_{\text{inj}})$, 10^3 signal-plus-background trials are performed for each combination of $\mu_{\text{inj}} \in \{5, 10, ..., 500\}$ and $\gamma_{\text{inj}} \in \{2.0, 3.0\}$. Other values of γ_{inj} are explored in Appendix D. The so-called **bias plots** for $\hat{n}_s$ and $\hat{\gamma}$ are shown in Figures 4.9 and 4.10, respectively. For $\gamma_{\text{inj}} = 2.0$, the value of $\hat{n}_s$ systematically overestimates μ_{inj}, and this overestimation increases with μ_{inj}. For $\gamma_{\text{inj}} = 3.0$ a similar bias is observed, although in this case $\hat{n}_s$ systematically underestimates μ_{inj}. In both cases, the spread in $\hat{n}_s$ values remains relatively constant. For the fitted spectral index, $\hat{\gamma}$ converges towards γ_{inj} as μ_{inj} increases. For low values of μ_{inj}, γ_{inj} is slightly biased towards the typical value found for the atmospheric background (see Appendix D). In addition, the spread[16] in $\hat{\gamma}$ decreases with increasing μ_{inj}. This trend is expected since the spectral features of the pseudosignal become more prominent as more pseudosignal events are injected.

The observed fit bias for $\hat{n}_s$ is a consequence of the fact that the background energy PDF (Figure 4.2) is constructed from data. Since the data has limited statistics, this PDF is not well-described for e.g. reconstructed energies larger than several 10 TeV in the Northern Hemisphere. Consequently, for harder (resp. softer) spectra such as e.g. $\gamma_{\text{inj}} = 2.0$ (resp. $\gamma_{\text{inj}} = 3.0$), the value of $\hat{n}_s$ is generally overestimated (resp. underestimated). A recent IceCube stacking analysis of AGN cores—which only considers the Northern Sky where there is a good data/MC agreement (Figure 3.15)—has opted for the construction of the background energy PDF using MC simulations [123, 386]. Thanks to the larger statistics of these MC simulations compared to the data, the AGN-core analysis yields unbiased fit parameters. Nevertheless, the $\hat{n}_s$ bias observed in our ULIRG analysis is not of major concern. If we were to observe a significant astrophysical signal when unblinding the data, then we would simply have to correct[17] $\hat{n}_s$ for this bias in order to obtain the true number of astrophysical ULIRG neutrinos.

component from the background PDF $\mathcal{B}_i$. An example of an IceCube analysis using such a signal-subtraction method can be found in [113].

[15] Note that a secondary contribution of $\nu_\tau + \overline{\nu}_\tau$ to the GFU track selection is not taken into account in the analysis. Assuming equipartition, this contribution is expected to be ~17% (Table 3.1). Consequently, the $\Phi_{\nu_\mu + \overline{\nu}_\mu}$ sensitivities and discovery potentials presented in Section 4.3.3 can be seen as conservative.

[16] The harder the injected spectrum, the more efficient the pseudosignal can be distinguished from the background. Consequently, the spread in $\hat{\gamma}$ is larger for $\gamma_{\text{inj}} = 3.0$ than for $\gamma_{\text{inj}} = 2.0$.

[17] Of course, this correction would depend on the observed spectral index $\hat{\gamma}$.

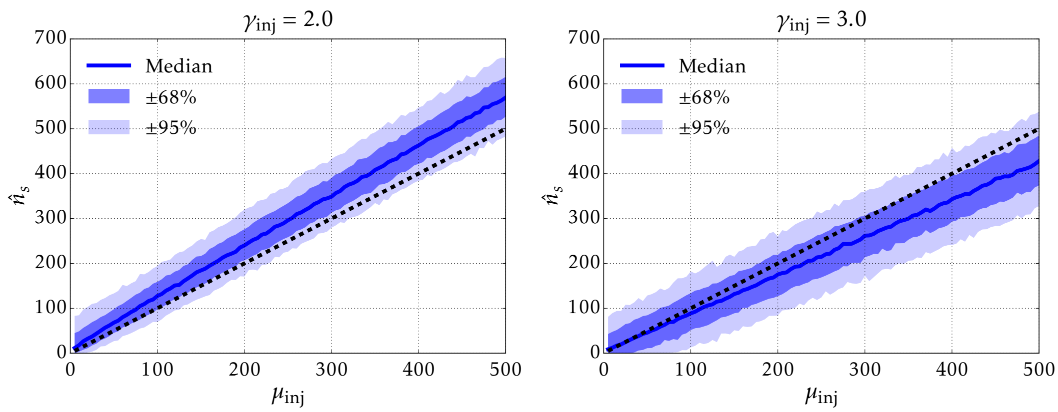

(a) $\gamma = 2.0$ (b) $\gamma = 3.0$

FIGURE 4.9: Bias plots for the fitted number of signal events, $\hat{n}_s$, as a function of the mean number of injected signal events, μ_{inj}. Panels (a) and (b) show these plots for injected spectral indices $\gamma_{\mathrm{inj}} = 2.0$ and $\gamma_{\mathrm{inj}} = 3.0$, respectively. In each plot, the median of the fit parameter is indicated (blue solid line), as well as the ±68% and 95% contours (dark blue and light blue bands, respectively), while the black dashed line represents the ideal non-bias scenario.

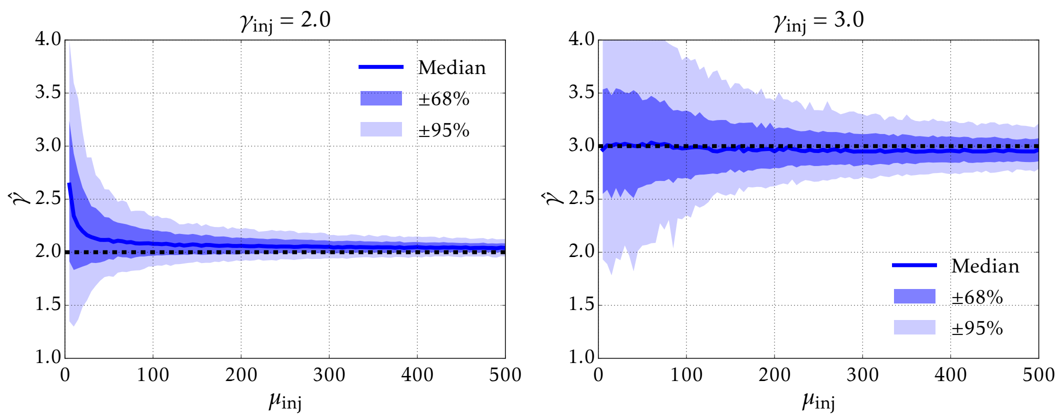

(a) $\gamma = 2.0$ (b) $\gamma = 3.0$

FIGURE 4.10: Bias plots for the fitted spectral index, $\hat{\gamma}$, as a function of the mean number of injected signal events, μ_{inj}. Panels (a) and (b) show these plots for injected spectral indices $\gamma_{\mathrm{inj}} = 2.0$ and $\gamma_{\mathrm{inj}} = 3.0$, respectively. In each plot, the median of the fit parameter is indicated (blue solid line), as well as the ±68% and 95% contours (dark blue and light blue bands, respectively), while the black dashed line represents the ideal non-bias scenario.

4.3.3 Sensitivities and Discovery Potentials

Definition

Now that we have discussed the recovery of injected pseudosignal in our analysis, we can ask ourselves the following questions: How sensitive is our analysis to an astrophysical signal from our selection of ULIRGs? And how strong should this signal be in order to reject the background-only hypothesis with a certain significance level α and power $1-\beta$ (Section 4.1)? To answer these questions, the following quantities are defined in IceCube analyses:

- **Sensitivity.** The amount of pseudosignal required such that in 90% of the signal-plus-background trials, the obtained TS exceeds the median of the background-only TS distribution,[18] as illustrated in Figure 4.11. This parameterization of the alternative hypothesis corresponds with a significance level $\alpha = 0.5$ and power $1-\beta = 0.9$. This 90% sensitivity is also the most stringent upper limit at 90% confidence level that can be placed in case no signal is observed in the unblinded data (see Section 5.1.2).

- **Discovery potential.** The amount of pseudosignal required such that in 50% of the signal-plus-background trials, the obtained TS exceeds the $n\sigma$ significance threshold of the background-only TS distribution. In particular, the parameterizations of the 3σ and 5σ discovery potentials[19] correspond with a power $1-\beta = 0.5$ of the alternative hypothesis for the significance levels $\alpha = 2.70 \times 10^{-3}$ and $\alpha = 5.73 \times 10^{-7}$, respectively. The definition of the 5σ discovery potential is also illustrated in Figure 4.11.

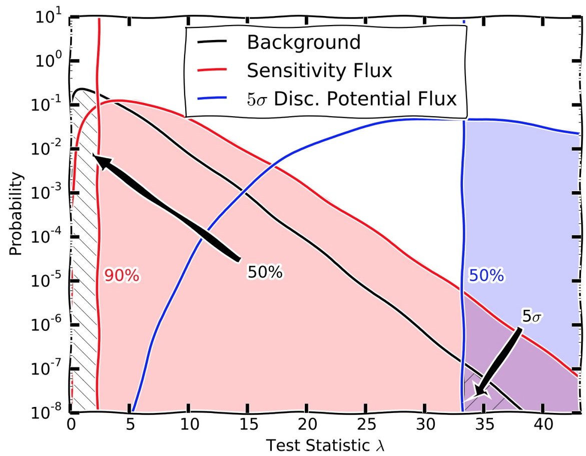

FIGURE 4.11: Schematic illustration defining the sensitivity and 5σ discovery potential [387]. The background-only PDF of the test statistic (denoted as λ) is shown in black. The red and blue vertical lines correspond with the median and 5σ threshold of the background-only PDF. The signal-plus-background PDFs of the sensitivity and discovery potential are shown in red and blue, respectively.

[18]One expects that the median background-only TS ≈ 0 (corresponding with a median $\hat{n}_s \approx 0$). Indeed, a median value TS = 0.07 in the 10^5 background-only trials presented here.

[19]As mentioned previously, a 5σ significance level is required to claim a discovery in particle physics. Between 3σ and 5σ we make the weaker claim that we have found evidence for a certain signal component in the data. Hence, the 3σ discovery potential might better be called the “3σ evidence potential.”

The above quantities each correspond with a certain mean number of injected signal events, μ_{inj}, and they depend on the assumed spectrum of the astrophysical signal. Here, the assumptions of Section 4.3.2 are followed, and the spectrum of ULIRGs is described by a power law with a single spectral index $\gamma = \gamma_{\mathrm{inj}}$ for all ULIRGs—see Equation (4.21). The sensitivities and discovery potentials are then computed using the efficiency curve method outlined below.

Computation

Let f_{thresh} be the fraction of trials with a $\mathrm{TS} \geq \mathrm{TS}_{\mathrm{thresh}}$, where the TS threshold is the median, 3σ value, or 5σ value of the background-only TS distribution (see Table 4.3). The aim is to find the value of μ_{inj} such that $f_{\mathrm{thresh}} = 0.9$ (resp. $f_{\mathrm{thresh}} = 0.5$) to obtain the sensitivity (resp. discovery potentials). For each γ_{inj} value of interest, first 10^3 trials are performed for selected pseudosignal strengths in the range $\mu_{\mathrm{inj}} \in [1, 500]$. Subsequently, an **efficiency curve** is fitted through f_{thresh} as a function of μ_{inj}. This curve is parameterized according to a χ^2_ν cumulative distribution function (CDF), with ν the degrees of freedom. The fit is limited to values $f_{\mathrm{thresh}} < 1.0$ for the sensitivity and $0.1 < f_{\mathrm{thresh}} < 0.9$ for the discovery potentials, in order to avoid biases due to the tails of the distributions.

To illustrate this method, Figure 4.12 shows the efficiency curves for the sensitivity, 3σ, and 5σ discovery potentials, respectively, for $\gamma_{\mathrm{inj}} \in \{2.0, 3.0\}$. The corresponding values of μ_{inj} of these quantities are listed in Table 4.3 for completeness. In addition, Figure 4.13 shows the signal-plus-background TS distributions corresponding with the sensitivity, 3σ, and 5σ discovery potentials for $\gamma \in \{2.0, 3.0\}$. Note that these PDFs correspond with the trials for μ_{inj} values that best approximate the sensitivities and discovery potentials obtained with the efficiency curve method.

$\mathrm{TS}_{\mathrm{thresh}}$	Quantity	μ_{inj} for $\gamma_{\mathrm{inj}} = 2.0$	μ_{inj} for $\gamma_{\mathrm{inj}} = 3.0$
0.07	Sensitivity	11.10	54.06
9.13	3σ disc. pot.	19.36	115.08
26.33	5σ disc. pot.	39.07	211.70

TABLE 4.3: Values of the sensitivities and discovery potentials in terms of the mean number of pseudosignal events, μ_{inj}, for injected power-law spectra with spectral indices $\gamma_{\mathrm{inj}} = 2.0$ and $\gamma_{\mathrm{inj}} = 3.0$. These values were obtained using the efficiency curve method shown in Figure 4.12. The corresponding TS thresholds, $\mathrm{TS}_{\mathrm{thresh}}$, are also given.

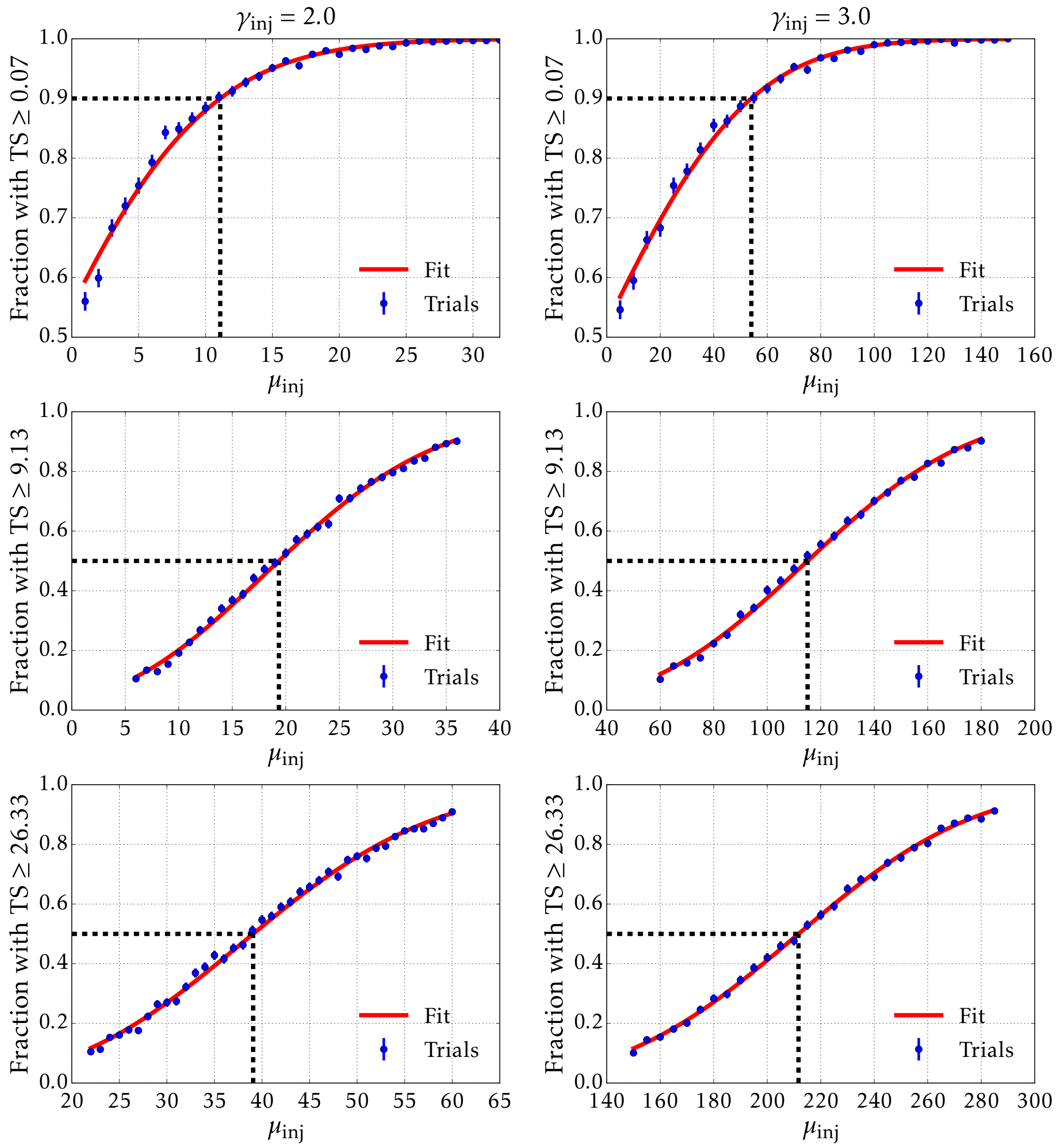

FIGURE 4.12: Efficiency curve method used to determine the sensitivity (top row), 3σ discovery potential (middle row), and 5σ discovery potential (bottom row) of the ULIRG stacking analysis (see Table 4.3 for the exact values). The left and right columns show the efficiency curves for injected pseudosignal following a power-law spectrum with spectral index $\gamma_{\rm inj} = 2.0$ and $\gamma_{\rm inj} = 3.0$, respectively. In each panel, the blue data points represent sets of 10^3 trials performed for different values of $\mu_{\rm inj}$, while the full red line indicates the χ^2 CDF fit through these trials. The dashed lines indicate which signal strength corresponds with the required fraction threshold.

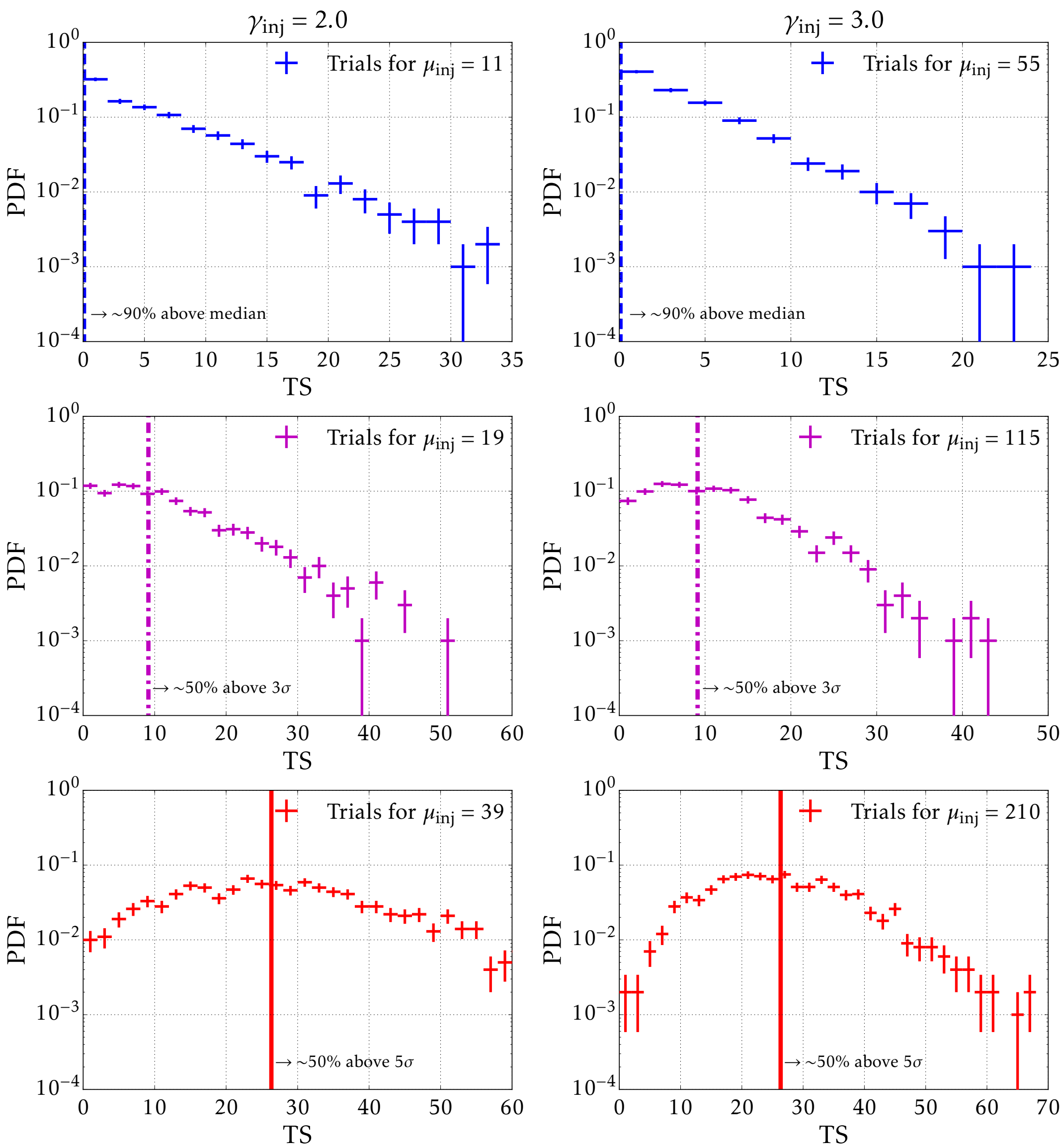

FIGURE 4.13: Signal-plus-background PDFs of the likelihood ratio test statistic (TS), each found by performing 10^3 trials. They correspond with the sensitivity, 3σ, and 5σ discovery potentials (blue, magenta, and red histograms, respectively) for injected spectral indices $\gamma_{inj} = 2.0$ (left column) and $\gamma_{inj} = 3.0$ (right column). These quantities are given in terms of the number of injected pseudosignal events, μ_{inj}, and the corresponding PDFs are shown in the top, middle, and bottom rows, respectively. The TS thresholds corresponding with the median, 3σ, and 5σ significance levels of the background-only TS PDF (Figure 4.8) are indicated with the blue dashed, magenta dash-dotted, and red full lines, respectively.

Blind Results

Figure 4.14 shows the sensitivity, 3σ, and 5σ discovery potentials for an astrophysical pseudosignal from the representative sample of 75 ULIRGs as a function its spectral index γ. Panel (a) of Figure 4.14 shows these quantities in terms of the stacked muon-neutrino flux at the normalization energy $E_0 = 10$ TeV. However, note that the shape of this plot can be misleading, since one might e.g. erroneously conclude that the analysis is more sensitive to an $E_\nu^{-3.2}$ spectrum than an $E_\nu^{-2.8}$ spectrum. Such a conclusion does not take into account the neutrino energy range over which the analysis is actually sensitive, which strongly depends on the spectral index γ. The energy ranges of the sensitivity shall be discussed in Section 5.1.2.

It is therefore more intuitive to plot the sensitivity and discovery potentials of the ULIRG analysis in terms of the mean number of injected neutrino events in 7.2 years of GFU data, as shown in Panel (b) of Figure 4.14. This number is related to the flux normalization via Equation (4.22). For $\gamma = 2.0$ (resp. $\gamma = 3.0$), the analysis is sensitive to $\sim$11 (resp. $\sim$55) ULIRG neutrinos, while $\sim$29 (resp. $\sim$160) events would be required to obtain a 50% probability for a 5σ discovery (see also Table 4.3). To put this into perspective, the total number of events in the GFU sample, which is dominated by atmospheric background, is about 1.5×10^6 (Table 3.2). The fact that the sensitivity and discovery potentials improve for harder spectra—less events are required to potentially observe a signal—is due to the fact that harder spectra are better distinguishable from the atmospheric background.[20]

Finally, one of the main assumptions of this analysis is shortly addressed, which is that all ULIRG emit neutrinos according to the same power-law spectrum. A more realistic scenario is one where each ULIRG has its own spectral index[21] γ_k, as

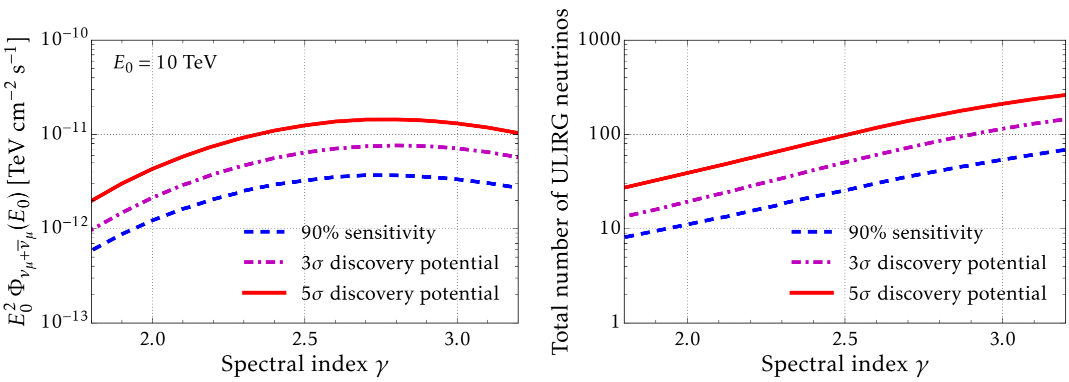

(a) Flux normalization

(b) Number of pseudosignal events

FIGURE 4.14: Sensitivity, 3σ, and 5σ discovery potentials (blue dashed, magenta dash-dotted, and red full lines, respectively) as a function of the spectral index γ, for injected pseudosignal following an unbroken $E_\nu^{-\gamma}$ power-law spectrum. Panels (a) and (b) show these quantities in terms of the stacked flux at the normalization energy $E_0 = 10$ TeV, $\Phi_{\nu_\mu+\bar{\nu}_\mu}(E_0)$, and the total number of injected pseudosignal events, respectively.

[20] Recall that the atmospheric neutrino background is well-described by an $E^{-3.7}$ spectrum (Section 3.1.5).

[21] It is reasonable to assume that each neutrino source would manifest some kind of power-law behavior. However, instead of being an unbroken power law, it is also possible that the neutrino spectrum features a break or a cutoff within the sensitive energy range of IceCube. A discussion of

in Equation (4.18). Such a variation in the spectral index could e.g. be the result of a different relative starburst-versus-AGN contribution to the neutrino flux, which depends on the IR luminosity (Figure 2.5). The stacked neutrino flux of the selected ULIRGs would then not be a simple power-law spectrum as in Equation (4.21). This effect is also known as **spectral-index blending** [150].

The effect of such a spectral-index blending scenario to this analysis is only performed qualitatively.[22] As mentioned in Section 4.2.2, the *fitted* spectral index $\hat{\gamma}$ is computationally limited to a single global value in the stacking likelihood. Consequently, the value of $\hat{\gamma}$ would be biased towards the *true* γ_k values of the sources that provide most of the neutrino flux at Earth. If all ULIRGs emit neutrinos, $\hat{\gamma}$ would be biased towards nearby northern sources due to the chosen stacking weights that enter the likelihood. Sources with a smaller stacking weight are not expected to strongly influence the value of $\hat{\gamma}$, although they can still significantly contribute to the fitted number of neutrinos, $\hat{n}_s$. Hence, the sensitivity of this analysis to such a spectral-index blending scenario is roughly expected to lie within the range of sensitivities presented in Figure 4.14.

4.3.4 Stacking 75 versus 189 ULIRGs

In the final analysis, 75 ULIRGs are stacked which were selected to obtain a representative sample of the local ULIRG population. As such, the analysis results can be extrapolated to study the neutrino emission of the full ULIRG population. A question that can be raised is whether stacking 75 objects instead of the initial selection of 189 ULIRGs has an impact on the sensitivity of this search. On average, stacking more sources improves the sensitivity of an analysis to observe fainter sources (Figure 4.5). However, this improvement is asymptotic, and also depends on the weights used in the stacking.

Let us therefore investigate the effect of stacking 75 versus 189 ULIRGs in the analysis. In contrast to the final analysis, where the sources are weighted according to their total IR flux F_{IR}, a theoretical weighting scheme $t_k = d_{L,k}^{-2}$ is used in this comparison (both in the likelihood fit as in the signal injection), where $d_{L,k}$ is the luminosity distance to source k. Since there is a strong correlation between F_{IR} and d_L^{-2}, as shown in Figure 4.7, the main conclusions of this comparison hold for the final analysis. Using the notations defined in Section 4.3.2, the average (single-flavor) neutrino luminosity per source can be determined between $E_1 = 10$ GeV and $E_2 = 10$ PeV,

$$\begin{aligned}
\langle L_\nu \rangle &= 4\pi d_{L,k}^2 \int_{E_1}^{E_2} E_\nu \Phi_k(E_\nu)\, \mathrm{d}E_\nu \\
&= \frac{4\pi\Phi_0}{\sum_{j=1}^{M} d_{L,j}^{-2}} \int_{E_1}^{E_2} \left(\frac{E_\nu}{E_0}\right)^{1-\gamma} \mathrm{d}E_\nu. \qquad (4.23)
\end{aligned}$$

Here, $E_\nu \Phi_k = E_\nu\, \mathrm{d}N_k/\mathrm{d}E_\nu$ is the muon-neutrino energy flux of source k.

these more elaborate spectral features is omitted here, since the aim of this study is to provide the first generic neutrino analysis of the ULIRG source class.

[22] In a quantitative approach, one could follow the method presented in [150] for the injection of pseudosignal. Here, each γ_k would be drawn randomly from a distribution of spectral indices. In [150], this distribution is found by fitting a Gaussian PDF through the resolved gamma-ray spectral indices of SFGs. Such a quantitative sensitivity estimation for a spectral-index blending scenario falls outside the scope of this work.

Using Equation (4.23), the sensitivity and discovery potential of the analysis can be translated from flux normalization, Φ_0, to average neutrino luminosity per source. The corresponding sensitivities and discovery potentials found by stacking $M = 75$ and $M = 189$ ULIRGs are compared in Figure 4.15. Stacking 75 sources does not have a major impact on the sensitivity of this search compared to stacking 189 sources. Typically, the latter improves the sensitivity and discovery potential of the analysis by ~20–40%. This relatively small impact can be attributed to the choice of stacking weights. As shown in Figure 4.7, the 75 ULIRGs with $z \leq 0.13$ are those which dominate the theoretical stacking weights—both in terms of d_L^{-2} and F_{IR}—in the case of stacking 189 sources. Hence, analyzing all 189 objects does not add a substantial cumulative weight to the stacking, and therefore only results in a minor improvement of the sensitivity.

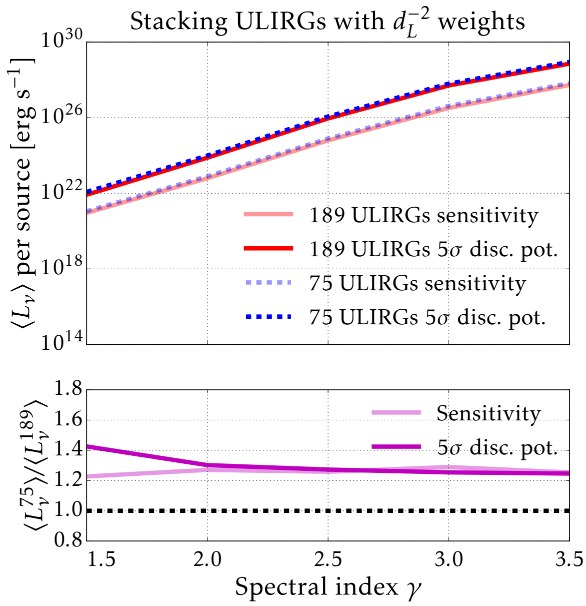

FIGURE 4.15: Comparison of the sensitivities (more transparent lines) and discovery potentials (more opaque lines) when stacking 189 and 75 ULIRGs, indicated with the red full lines and blue dashed lines, respectively. The top panel shows these quantities in terms of the average per-flavor neutrino luminosity per source, $\langle L_\nu \rangle$, as a function of the spectral index γ. The bottom panel shows the luminosity ratio of stacking 75 ULIRGs to stacking 189 ULIRGs, where the light and dark magenta lines represent the sensitivity and 5σ discovery potential ratios, respectively.

4.3.5 Crosscheck of Analysis Software

The ULIRG stacking analysis was developed using the SkyLab software framework. As a final consistency check before unblinding the data, an investigation is conducted on the compatibility of SkyLab with Csky,[23] which is the other main[24] software package used in IceCube analyses. Both SkyLab and Csky are written in Python,

[23] Available at https://github.com/icecube/csky.

[24] Currently, a novel analysis framework named SkyLLH is being developed within IceCube [388]. This software includes the non-Gaussian description to the spatial signal PDF discussed in Section 4.2.1.

although the latter also has some underlying structure written in C in order to gain computational performance. In any case, apart from some minor differences that are omitted here, the two software packages essentially apply the same analysis method that was described above. They are therefore expected to yield compatible sensitivities and discovery potentials for an astrophysical signal following the injection spectrum of Equation (4.21).

The two software packages are compared for a stacking analysis of the *initial* selection of 189 ULIRGs (Section 2.3.1) using a d_L^{-2} theoretical weighting scheme, as in Section 4.3.4. Note that this choice is again only relevant for the comparison presented here, and not representative of the final analysis. The sensitivities and 5σ discovery potentials obtained with SkyLab and Csky are shown in Figure 4.16. A good agreement is found between the two frameworks. The deviations in the sensitivities and discovery potentials computed with SkyLab and Csky lie between 5–20%, which is an expected range for the statistical fluctuations of these quantities.

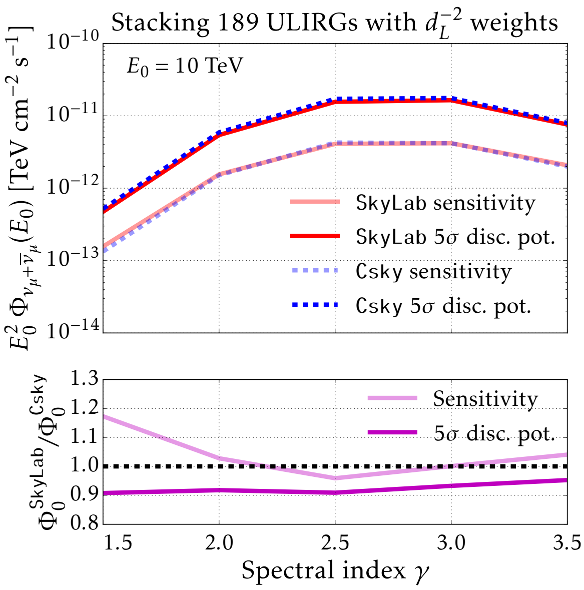

FIGURE 4.16: Comparison of the sensitivities (more transparent lines) and discovery potentials (more opaque lines) computed with SkyLab and Csky, indicated with the red full lines and blue dashed lines, respectively. The top panel shows these quantities terms of the stacked flux at the normalization energy E_0 = 10 TeV, $\Phi_{\nu_\mu+\bar{\nu}_\mu}(E_0) \equiv \Phi_0$, as a function of the spectral index γ (analogous to Panel (a) of Figure 4.14). The bottom panel shows the SkyLab-to-Csky ratios of these flux normalizations, where the light and dark magenta lines represent the sensitivity and 5σ discovery potential ratios, respectively.

Chapter 5

Results and Implications for Neutrino Emission from ULIRGs

> *Absence of evidence is not evidence of absence.*
>
> — **Carl Sagan**

> *The data is IceCube, but the interpretation is mine.*
>
> — **Francis Halzen**

Introduction

This Chapter presents the main scientific results of this thesis. First, the stacking-analysis method of Chapter 4 will be applied to search for astrophysical neutrinos from ULIRGs, selected in Chapter 2, in 7.2 years of IceCube GFU data, described in Chapter 3. As will be discussed in Section 5.1, the stacking analysis yields a null result, such that upper limits are computed on the neutrino flux originating from the selection of 75 nearby ULIRGs.

Subsequently, the null result will be interpreted in the context of the diffuse neutrino observations discussed in Chapter 1. In Section 5.2, ULIRGs will be excluded as the sole population of sources responsible for the diffuse astrophysical neutrino flux. Furthermore, in Section 5.3 these results shall be compared to the model predictions of diffuse neutrino emission from ULIRGs described in Chapter 2. More specifically, it will be shown that the null results of this search yield constraints on possible neutrino emission mechanisms in ULIRGs.

5.1 Unblinding Results

5.1.1 Best-Fit Parameters

Using the analysis method described in Section 4.2, the unscrambled 7.2 years of GFU data are used to test for any evidence of astrophysical neutrinos originating from the selection of 75 ULIRGs. The likelihood space of the **unblinded analysis** is shown in Figure 5.1. A best-fit value $\hat{n}_s = 0$ is found for the number of astrophysical signal events, such that the best-fit spectral index $\hat{\gamma}$ of a signal flux following an unbroken power law remains undetermined. Consequently, the observed test-statistic value is $\mathrm{TS}_{\mathrm{obs}} = 0$, which yields a p-value $p = 1.0$. Thus, it can be concluded that the GFU data is compatible[1] with a background-only scenario.

[1] Recall that in particle physics, we generally require a 3σ significance ($p \leq 2.70 \times 10^{-3}$) to report a first sign of evidence, and a 5σ significance ($p \leq 5.73 \times 10^{-7}$) to claim a discovery and reject the null hypothesis. A p-value $p = 1.0$ indicates that the data is "perfectly" compatible with the null hypothesis.

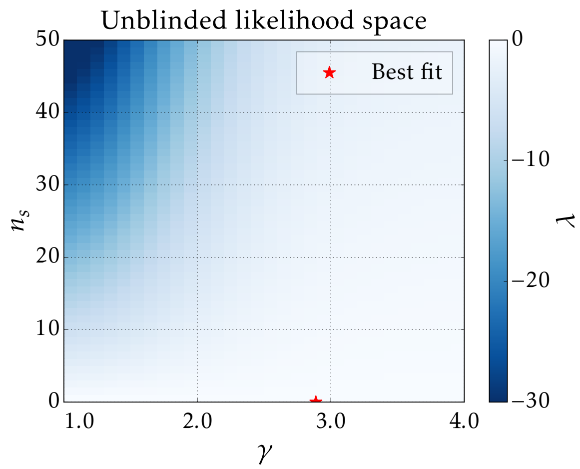

FIGURE 5.1: Likelihood space of the ULIRG stacking analysis using the unscrambled GFU data. Here, the likelihood ratio $\lambda \equiv \log[\mathcal{L}(n_s, \gamma)/\mathcal{L}(n_s = 0)]$, which is related to Equation (4.15), is shown as a function of the fit parameters n_s, the number of signal events, and γ, the spectral index for an $E_\nu^{-\gamma}$ signal flux. The best-fit parameters $(\hat{n}_s, \hat{\gamma})$ that maximize the likelihood are denoted by the red star. Note that $\hat{\gamma}$ is degenerate since $\hat{n}_s = 0$. The value of $\hat{\gamma}$ indicated here is the output of the likelihood maximization by SkyLab.

5.1.2 Integral Upper Limits

Computation and Interpretation

Since the analysis yields a null result, **upper limits** are set on the stacked muon-neutrino flux from the selection of 75 ULIRGs. The upper limits are determined by constructing single-sided confidence intervals using Neyman's frequentist method [389]. A detailed overview of this method was given in a previous work [384]; the discussion here is restricted to the application of Neyman's method in the context of this analysis. For a fixed spectral index γ, the **confidence level** of an upper limit on the stacked flux normalization is defined as

$$\mathrm{CL} = \int_{\mathrm{TS_{obs}}}^{\infty} \mathcal{T}_s(\mathrm{TS}'|\Phi_0^{\mathrm{CL}}, \gamma)\, \mathrm{d}(\mathrm{TS}'). \tag{5.1}$$

Here, $\mathcal{T}_s$ represents the signal-plus-background PDF of the test statistic. Given the observed value $\mathrm{TS_{obs}}$, the flux normalization Φ_0^{CL} is determined such that Equation (5.1) is satisfied for a given CL. In the following, the confidence level is set to CL = 90%, and the corresponding upper limit on the flux normalization is denoted by $\Phi_0^{90\%}$.

Practically, upper limits are determined in an analogous manner to the sensitivity (Section 4.3.3). For each γ, the signal-plus-background TS PDFs are constructed by performing 10^3 pseudo-experiments for each choice of the pseudosignal strength. The upper limit $\Phi_0^{90\%}$ then corresponds with the signal strength such that in 90% of the trials, $\mathrm{TS} \geq \mathrm{TS_{obs}}$. The smaller the value of $\mathrm{TS_{obs}}$ (i.e. the smaller $\hat{n}_s$), the more stringent this upper limit becomes. Generally, in IceCube searches a policy is applied where the most stringent upper limit that can be reported coincides with the sensitivity. That is, were we to observe a $\mathrm{TS_{obs}} < \mathrm{TS_{med}}$, which is the median of the background-only TS distribution, then we would report the value of $\Phi_0^{90\%}$ found by setting $\mathrm{TS_{obs}} = \mathrm{TS_{med}}$ in Equation (5.1). Usually, $\mathrm{TS_{med}} \approx 0$, such that the most stringent upper limit is obtained for an observed value $\mathrm{TS_{obs}} \approx 0$. Hence, this most stringent upper limit is obtained when $\hat{n}_s \approx 0$, as expected, since the likelihood fit was restricted to $\hat{n}_s \geq 0$ (Section 4.2.3).

In this analysis, a value $\mathrm{TS_{obs}} = 0$ is observed, while the median of the background-only TS distribution is $\mathrm{TS_{med}} = 0.07$, which is compatible with zero[2] for all practical purposes. Therefore, the upper limits at 90% CL are set equal to the sensitivities given in Figure 4.14. For completeness, Table 5.1 lists the upper limits on the stacked flux normalization at $E_0 = 10$ TeV, $\Phi_0^{90\%}$, for some specific values of the spectral index γ.

It should be noted that in general, upper limits such as those computed here should be interpreted with caution. An upper limit $\Phi_0^{90\%}$ at 90% CL means that if we were to repeat this experiment, the single-sided confidence interval defined by our upper limit, $[0, \Phi_0^{90\%}]$, would contain the true value of Φ_0^{true} in 90% of the experiments. Here it was already anticipated that the true flux is physically bound to $\Phi_0^{\mathrm{true}} \geq 0$. However, **underfluctuations**, i.e. $\hat{n}_s < 0$, were not allowed in the analysis (Section 4.2.2). As a post-unblinding check, the maximum-likelihood fit is recomputed, but now allowing for $\hat{n}_s < 0$. A best-fit $\hat{n}_s = -100$ is found, which roughly corresponds to a 2σ underfluctuation. If we were to compute $\Phi_0^{90\%}$ using Equation (5.1) with the corresponding $\mathrm{TS_{obs}} = -49.90$, we would obtain a negative value of $\Phi_0^{90\%}$, yielding an "empty" confidence interval, which is unphysical.

The reason why Neyman's method leads to such empty confidence intervals is because it is not designed to take into account any physical restrictions on the true flux normalization, i.e. $\Phi_0^{\mathrm{true}} \geq 0$. By setting the most stringent upper limit equal to the sensitivity in IceCube analyses, we somewhat artificially avoid this problem. As a consequence, our confidence intervals $[0, \Phi_0^{90\%}]$ are likely yielding some **overcoverage**. Overcoverage means that while we state that our CL is 90%, our confidence intervals would contain the true value of Φ_0^{true} in more than 90% of the experiments.

Spectral index γ	Upper limit $E_0^2 \Phi^{90\%}_{\nu_\mu+\bar{\nu}_\mu}(E_0)$ $[10^{-12}\ \mathrm{TeV\ cm^{-2}\ s^{-1}}]$
2.0	1.2
2.12	1.7
2.37	2.7
2.5	3.2
2.89	3.6
3.0	3.3

TABLE 5.1: Integral upper limits at 90% CL on the stacked astrophysical muon-neutrino flux of the 75 analyzed ULIRGs, $\Phi^{90\%}_{\nu_\mu+\bar{\nu}_\mu}$, at the normalization energy $E_0 = 10$ TeV, for various unbroken $E_\nu^{-\gamma}$ power-law spectra (see the sensitivity curve in Figure 4.14 for other values). Note that the limits are scaled with E_0^2. The value $\gamma = 2.37$ corresponds with the 9.5-yr best-fit diffuse muon-neutrino measurement in the Northern Sky [92]. The value $\gamma = 2.89$ corresponds with the 7.5-yr best-fit diffuse measurement using the high-energy starting event sample (HESE) [91]. The other spectral-index values will be used for further interpretation of these limits.

[2] If one estimates the uncertainty on $\mathrm{TS_{med}}$ as $\sigma_{\mathrm{TS}}\sqrt{\pi/2}$ [390], where σ_{TS} is the standard deviation of the background-only distribution, one finds that $\mathrm{TS_{med}} = 0.07 \pm 1.74$.

Therefore, the upper limits at 90% CL stated in this work can be seen as conservative. We do note that Feldman & Cousins developed a method of constructing confidence intervals that is able to take into account physical bounds on the statistical parameter in question [391]. They achieve this by computing a ratio of the likelihood for a range of *physically allowed* model parameters to the likelihood that best fits the data. These ratios are then ordered from large to small, until a required CL is obtained. Computing such Feldman-Cousins upper limits falls beyond the scope of this thesis,[3] but more details about this method can also be found in [384].

Central Energy Range

The upper limits on the stacked muon-neutrino flux from ULIRGs were determined by injecting pseudosignal neutrinos with energies 100 GeV $< E_\nu <$ 100 PeV according to an $E_\nu^{-\gamma}$ unbroken power-law spectrum. Using Equation (4.22), the mean number of injected events, μ_{inj}, was then related to the flux normalization, Φ_0. Since the spectrum was integrated over the complete 100 GeV–100 PeV energy range in Equation (4.22), these limits are also referred to as **integral limits**. However, not all neutrino energies within this range will contribute equally to the upper limit, due to the detection efficiency as reflected by the effective area A_{eff} (Section 3.3.2).

To quantize this effect, for each spectral index γ of interest, the so-called **90% central energy range** is determined, $[E_{\mathrm{min}}, E_{\mathrm{max}}]$, of pseudosignal neutrinos that contribute to 90% of the total sensitivity,[4] Φ_0. These bounds are defined such that

$$1 - \frac{\Phi_0}{\Phi_0^{E_\nu \geq E_{\mathrm{min}}}} = 1 - \frac{\Phi_0}{\Phi_0^{E_\nu \leq E_{\mathrm{max}}}} \equiv 5\%. \tag{5.2}$$

Here, $\Phi_0^{E_\nu \geq E_{\mathrm{min}}}$ is the sensitivity obtained by restricting the energies of injected pseudosignal neutrinos to $E_{\mathrm{min}} < E_\nu <$ 100 PeV in Equation (4.22),

$$\Phi_0^{E_\nu \geq E_{\mathrm{min}}} \propto \left[\int_{E_{\mathrm{min}}}^{100\ \mathrm{PeV}} A_{\mathrm{eff}}(E_\nu) \left(\frac{E_\nu}{E_0} \right)^{-\gamma} \mathrm{d}E_\nu \right]^{-1}. \tag{5.3}$$

Analogously, $\Phi_0^{E_\nu \leq E_{\mathrm{max}}}$ is the sensitivity obtained by restricting the energies of injected pseudosignal neutrinos to 100 GeV $< E_\nu < E_{\mathrm{max}}$,

$$\Phi_0^{E_\nu \leq E_{\mathrm{max}}} \propto \left[\int_{100\ \mathrm{GeV}}^{E_{\mathrm{max}}} A_{\mathrm{eff}}(E_\nu) \left(\frac{E_\nu}{E_0} \right)^{-\gamma} \mathrm{d}E_\nu \right]^{-1}. \tag{5.4}$$

Thus, the minimum (resp. maximum) bound is defined as the energy E_{min} (resp. E_{max}) such that the sensitivity flux computed by restricting pseudosignal neutrinos to energies $E_\nu \geq E_{\mathrm{min}}$ (resp. $E_\nu \leq E_{\mathrm{max}}$) increases[5] with 5% relative to the sensitivity flux integrated over the complete 100 GeV–100 PeV energy range.

In practice, the minimum energy bound (resp. maximum energy bound) is determined by gradually increasing E_{min} (resp. decreasing E_{max}) in steps of $\log_{10}(E_\nu/\mathrm{GeV}) = 0.2$. This process is illustrated in Figure 5.2 for a selection of spectral indices $\gamma \in [2.0, 3.0]$. As expected, we see that overall, increasing E_{min} (resp. decreasing

[3] It is also worth noting that a Bayesian approach [376], where so-called credibility intervals are constructed, could also deal with physical restrictions on statistical parameters.

[4] Recall that the upper limits at 90% CL are set equal to the sensitivity.

[5] An increase of the sensitivity flux with 5% means that the sensitivity worsens with 5%.

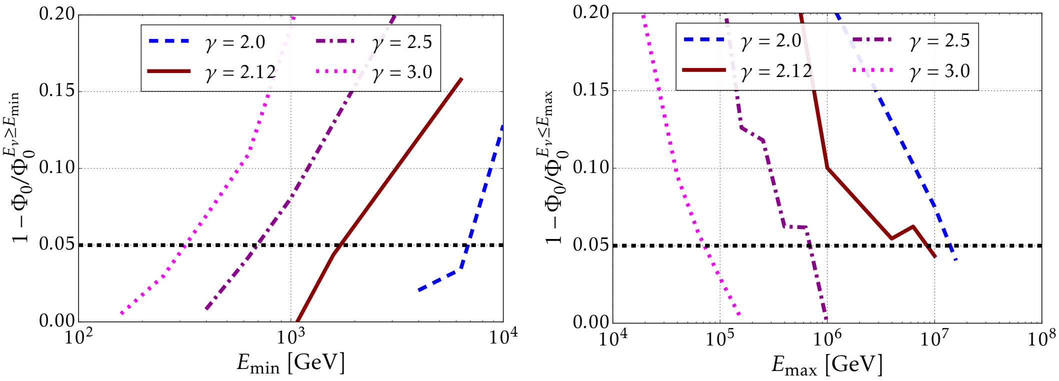

(a) Minimum energy bound

(b) Maximum energy bound

FIGURE 5.2: Determination of the 90% central energy range of the sensitivity for several spectral indices γ. Here, Φ_0 denotes the flux normalization of the sensitivity computed over the full [100 GeV,100 PeV] energy range. Panel (a) shows that as the minimum energy bound $E_{\min}$ is increased in steps of $\log_{10}(E_\nu/\text{GeV}) = 0.2$, the sensitivity flux normalization computed over the [$E_{\min}$,100 PeV] energy range, $\Phi_0^{E_\nu \geq E_{\min}}$, increases with respect to Φ_0. Analogously, Panel (b) shows that as the maximum energy bound $E_{\max}$ is decreased in steps of $\log_{10}(E_\nu/\text{GeV}) = 0.2$, the sensitivity flux normalization computed over the [100 GeV, $E_{\max}$] energy range, $\Phi_0^{E_\nu \leq E_{\max}}$, increases with respect to Φ_0. The 90% central energy ranges are defined by the smallest $E_{\min}$ values and largest $E_{\max}$ values for which this relative increase in flux is ≥5% (the 5% mark is denoted by the black dotted lines). These values are listed in Table 5.2.

$E_{\max}$) results in a relative increase of the sensitivity flux. The "kinks" that are sometimes observed between two neighboring steps are due to statistical fluctuations in the computation of the sensitivity. For harder spectra, the sensitivity is driven by very few pseudosignal events (Figure 4.14), such that a small fluctuations in this number can result in an upward "kink" as observed at $\log_{10}(E_{\max}/\text{GeV}) = 6.8$ for $\gamma = 2.12$. The minimum bound (resp. maximum bound) of the 90% central energy is obtained by finding the first value of $E_{\min}$ (resp. $E_{\max}$) for which Equation (5.2) yields a fraction ≥5%. The 90% central energy ranges[6] obtained with this method are listed in Table 5.2.

Spectral index γ	$\log_{10}(E_{\min}/\text{GeV})$	$\log_{10}(E_{\max}/\text{GeV})$
2.0	4.0	7.0
2.12	3.8	6.8
2.5	3.0	5.8
3.0	2.6	4.8

TABLE 5.2: The 90% central energy ranges, [$E_{\min}$, $E_{\max}$], of the sensitivities corresponding to some chosen values of the spectral index γ. These energy ranges were determined using the method illustrated in Figure 5.2.

[6]Note that in the case of e.g. an E_ν^{-3} spectrum, for which $\log_{10}(E_{\max}/\text{GeV}) = 4.8$, the central energy range does not imply that the analysis is not sensitive to an astrophysical PeV event. It means that statistically, for this spectrum, it is unlikely for such a PeV event to be observed in 7.2 years of GFU data.

5.1.3 Differential Upper Limits

As discussed in Section 5.1.2, integral limits are computed by normalizing the stacked flux to the number of pseudosignal events by integrating Equation (4.22) between 100 GeV and 100 PeV. This integration depends on the assumed spectrum of the pseudosignal—a power law in our case. Consequently, integral limits do not reflect the energy dependence of the IceCube experiment to any arbitrary signal spectrum. Thus, **differential limits** at 90% CL are also computed, which essentially correspond with the IceCube sensitivity to any astrophysical signal from ULIRGs at a specific energy.[7]

In practice, the differential[8] limits are determined by computing the sensitivity of this analysis in a certain energy bin $[E_i, E_{i+1}]$. This computation is done by generating pseudosignal events according to an $E_\nu^{-2.0}$ spectrum in that specific energy bin,[9] and calculating the corresponding flux normalization as

$$\Phi_0^{[E_i,E_{i+1}]} \propto \left[\int_{E_i}^{E_{i+1}} A_{\mathrm{eff}}(E_\nu)\left(\frac{E_\nu}{E_i}\right)^{-2.0} \mathrm{d}E_\nu\right]^{-1}. \tag{5.5}$$

The better the energy resolution of the detector, the smaller one can take the energy bins to describe the differential IceCube sensitivity. For tracks, the energy resolution is rather poor (Section 3.2.3), such that here, one bin is set equal to one decade in energy, $E_{i+1} = 10E_i$. Table 5.3 lists the differential limits of the ULIRG stacking analysis between 100 GeV and 100 PeV. As expected, the most stringent differential limit corresponds with the 100 TeV–1 PeV energy bin, which is where IceCube has most of its $\nu_\mu + \overline{\nu}_\mu$ point-source sensitivity [116].

Energy bin $[E_i, 10E_i]$ [TeV]	Upper limit $E_i^2\Phi^{90\%}_{\nu_\mu+\overline{\nu}_\mu}$ in bin $[10^{-12}$ TeV cm^{-2} s$^{-1}]$
$[10^{-1}, 10^0]$	2.9×10^2
$[10^0, 10^1]$	17
$[10^1, 10^2]$	3.7
$[10^2, 10^3]$	3.0
$[10^3, 10^4]$	7.6
$[10^4, 10^5]$	24

TABLE 5.3: Differential upper limits at 90% CL on the stacked astrophysical muon-neutrino flux of the 75 analyzed ULIRGs, $\Phi^{90\%}_{\nu_\mu+\overline{\nu}_\mu}$, per bin of energy decade, $[E_i, 10E_i]$, between 100 GeV–100 PeV. Note that each limit is scaled with the corresponding value of E_i^2.

[7] It is a common—and sometimes confusing—practice to describe both differential and integral *limits* in terms of a *differential flux* $\mathrm{d}N/\mathrm{d}E_\nu$ (as defined in Appendix A). By definition, differential limits are truly "differential." On the other hand, integral limits are normalized to the total number of injected events (i.e. the total flux according to Appendix A), for which $\mathrm{d}N/\mathrm{d}E_\nu \propto E_\nu^{-\gamma}$ is *assumed* as a differential shape.

[8] Due to the fact that we are limited by IceCube's energy resolution for the bin size, these are in fact *quasi-differential* limits, although the prefix "quasi" will be omitted in the following.

[9] The choice for an $E_\nu^{-2.0}$ spectrum is completely arbitrary and is only used in a practical sense for the generation of pseudosignal. When computing differential limits, we can in any case not distinguish a spectral shape per energy bin. One could also e.g. opt for an $E_\nu^{-3.0}$ spectrum for the signal generation and obtain equivalent results.

5.1.4 Systematic Uncertainties

As described above and in Section 4.3.2, upper limits and sensitivities are computed by injecting simulated pseudosignal events to scrambled data. The GFU effective area, which is a measure for the detector response after the GFU event selection, is used to translate the number of events to a neutrino flux under an assumed signal spectrum. This process requires MC simulations, which introduce **systematic uncertainties** through the usage of a certain ice model, the expected DOM efficiency, and other detection effects (see below). Note that systematic uncertainties from background are considered to be negligible, since the background is described using scrambled data in the analysis.

Practically, the effect of such systematic uncertainties is studied by varying one quantity of interest in the simulation. Subsequently, a new MC sample is generated and passed through the entire event selection. Finally, the complete blind analysis is repeated and the sensitivities are recomputed. As such, we can estimate the effect of any systematic variation at the sensitivity level. Here, the works of [116, 392] are quoted, in which detailed investigations were performed on the systematic uncertainties of time-integrated point-source searches, such as the one presented in this thesis.

The main systematic uncertainties that affect the ULIRG stacking analysis, for a $\nu_\mu + \overline{\nu}_\mu$ pseudosignal following an E_ν^{-2} power-law spectrum, are listed below:

- **DOM efficiency**. At a wavelength of 390 nm, the optimal quantum efficiency of typical IceCube DOMs is 25% (Section 3.1.2). However, the DOM efficiency for continuous Cherenkov radiation in the South Pole ice is not fully understood. In particular, if the DOM efficiency is lower, less per-event photon counts will yield a lower total deposited charge in the detector. Due to the charge cuts in the GFU event selection (Section 3.3.1), this will affect the number of expected signal events in the GFU sample. Moreover, less photon counts will worsen the overall quality of event reconstructions (Section 3.2). Using a conservative systematic uncertainty of 10% on the DOM efficiency, this affects the analysis sensitivity by ∼8%.

- **Ice properties**. As mentioned in Section 3.1.1, LED flashers on the DOMs are used to perform in-situ measurements of the optical properties of the glacial ice. The uncertainties on both the absorption and scattering coefficients are found to be $\lesssim$10%. These uncertainties then propagate through the ice models used in IceCube reconstructions. In particular, larger absorption coefficients would result in a smaller photon yield at the DOMs, resulting in poorer reconstruction qualities. Varying the scattering and absorption coefficients by 10% results in a systematic uncertainty of ∼6% on the analysis sensitivity.

- **Muon propagation**. Track reconstructions model the energy loss of muons that propagate through the ice, which is proportional to their light yield in the detector (Section 3.2). In particular, this requires a description of the photonuclear[10] interaction cross section in the highly stochastic regime, for which different models have been investigated. The resulting systematic error on the analysis sensitivity, which is determined by varying the photonuclear interaction model used in the reconstruction, is ∼6%.

[10] In this case, "photonuclear" stands for the exchange of a virtual photon between the muon and atomic nucleon [393].

The overall systematic effect on the E_ν^{-2} sensitivity of the ULIRG stacking analysis is found by computing the quadratic sum of the individual errors, yielding a total systematic uncertainty of ∼12%. This value may vary depending on the simulated signal spectrum, since the systematic effects described above are energy dependent. Nevertheless, the total systematic uncertainty is generally expected to be ≲15% [394]. This conservative value is adopted to scale the upper limits in the remainder of this work, although it should be noted that it does not affect the interpretation of the analysis results given in Sections 5.2 and 5.3.

5.2 Constraints on the ULIRG Source Population

5.2.1 Extrapolation of Analysis Results to Diffuse Upper Limits

Up to this point, upper limits have been obtained on the stacked muon-neutrino flux, $\Phi^{90\%}_{\nu_\mu+\bar{\nu}_\mu}$, from the representative sample of 75 ULIRGs. To interpret these results, upper limits will be determined on the cumulative diffuse muon-neutrino flux of the full ULIRG source population. These diffuse-flux limits will be extrapolated from the stacked-flux limits by effectively integrating the contribution of all ULIRGs to the neutrino emission over cosmic history. Such a cosmological integration is non-trivial, since one needs to take into account the expansion of the Universe, the redshift evolution of the source luminosity function, and the redshift effects on the energy spectra of the sources.

Diffuse Neutrino Flux of the ULIRG Source Population

Let us first consider the neutrino emission of a generic source population up to a maximum redshift $z_{\rm max}$. As shown in e.g. [145,146,150,243], the cumulative diffuse neutrino energy flux at Earth (per flavor assuming equipartition) originating from all sources in this population is given by[11,12]

$$E_\nu^2 \Phi^{z\leq z_{\rm max}}_{\nu_\ell+\bar{\nu}_\ell}(E_\nu) = \frac{1}{3}\int_0^{z_{\rm max}} \frac{d_L^2}{(1+z)^2}\frac{c}{H(z)}\,\mathrm{d}z \\ \times \int_{\log L_{\rm min}}^{\log L_{\rm max}} \frac{\langle \epsilon_\nu L_{\epsilon_\nu}(\epsilon_\nu, z)\rangle}{4\pi d_L^2}\,\rho_\nu(L_\nu, z)\,\mathrm{d}\log L_\nu. \tag{5.6}$$

Here, d_L is the luminosity distance, and $H(z) = H_0\sqrt{\Omega_m(1+z)^3+\Omega_\Lambda}$ represents the evolution of the Hubble parameter over cosmic history. The quantity $\langle \epsilon_\nu L_{\epsilon_\nu}\rangle$, where $\epsilon_\nu = (1+z)E_\nu$ takes into account the energy loss due to the cosmological expansion, is the average[13] differential all-flavor neutrino luminosity of a source at a redshift z with a total neutrino luminosity $L_\nu = \int L_{\epsilon_\nu}\,\mathrm{d}\epsilon_\nu$. This average is taken per bin of the

[11] The redshift integral in Equation (5.6) stems from an integration over comoving volume [145]. A comoving volume element can be written as $\mathrm{d}V_C = d_C^2\,\mathrm{d}(d_c)\,\mathrm{d}\Omega$, with the comoving distance given by $d_C = c\int_0^z \mathrm{d}z'/H(z')$, which is on its turn related to the luminosity distance via $d_C = d_L/(1+z)$. Since a diffuse flux is given per unit of solid angle $\mathrm{d}\Omega$, the solid-angle integration is omitted in Equation (5.6). In any case, since the Universe is isotropic [46], integrating over $\mathrm{d}\Omega$ would result in a factor 4π.

[12] A similar integral can be written down for gamma rays, although in this case, one has to take into account the optical depth $\tau_{\gamma\gamma}(E_\gamma, z)$ for gamma-ray interactions with the EBL and CMB [243].

[13] Such an average accounts for the different spectral shapes that contribute to the overall luminosity density of the source population at a redshift z. For example, in a spectral-index blending scenario where all sources are described by a power law but with a varying spectral index, one would average over the spectral-index distribution $p(\gamma)$ of the sources, $\langle \epsilon_\nu L_{\epsilon_\nu}\rangle = \int p(\gamma)\,\epsilon_\nu L_{\epsilon_\nu}(\epsilon_\nu|\gamma)\,\mathrm{d}\gamma$ [150].

neutrino luminosity function, $\rho_\nu(L_\nu, z) = \mathrm{d}n/\mathrm{d}\log L_\nu(z)$, which describes the redshift evolution of the source population over some range $L_{\min} \leq L_\nu \leq L_{\max}$. More precisely, the luminosity function yields the number density of sources per comoving volume element, per logarithmic interval in total neutrino luminosity.

In order to solve Equation (5.6) for the ULIRG source population and relate its solution to a diffuse upper limit, the results of this work are based on the following **set of assumptions**:

1. ULIRGs have identical properties of hadronic acceleration and neutrino production over cosmic history, $\epsilon_\nu L_{\epsilon_\nu}(\epsilon_\nu, z) = \epsilon_\nu L_{\epsilon_\nu}(\epsilon_\nu)$. In particular, all ULIRGs are assumed to emit neutrinos according to the same unbroken power-law spectrum, $\epsilon_\nu L_{\epsilon_\nu} \propto \epsilon_\nu^{2-\gamma}$. This assumption, already introduced in Section 4.2, is mostly motivated by the fact that the diffuse IceCube observations show no evidence for more intricate features in the neutrino spectrum (Section 1.2.1). Hence, the average differential neutrino luminosity can be simplified to $\langle \epsilon_\nu L_{\epsilon_\nu}(\epsilon_\nu) \rangle = \epsilon_\nu L_{\epsilon_\nu}(\epsilon_\nu)$, and it can be taken out of the luminosity integration. Note, however, that it is more realistic for ULIRGs to exhibit some form of spectral-index blending (Section 4.3.3) and for their spectrum to have some high-energy cutoff (Section 2.2.1). Nevertheless, the assumption made here will still allow for novel insights into the neutrino-production mechanisms of ULIRGs.

2. The total IR luminosity is a direct measure of the total neutrino luminosity, $L_\nu \propto L_{\mathrm{IR}}$. This assumption is motivated by the fact that non-thermal emission in ULIRGs and SFGs in general, which could be an indicator for hadronic acceleration and neutrino production, is strongly correlated to the IR luminosity (Section 2.1.2). Consequently, the ULIRGs neutrino luminosity function $\rho_\nu(L_\nu, z)$ is assumed to be fully described by the IR luminosity function $\rho_{\mathrm{IR}}(L_{\mathrm{IR}}, z)$,
$$\frac{\mathrm{d}n}{\mathrm{d}\log L_\nu}(z) \propto \frac{\mathrm{d}n}{\mathrm{d}\log L_{\mathrm{IR}}}(z). \tag{5.7}$$

3. The luminosity function of ULIRGs is characterized by one overall parameterization between[14] $12 \leq \log_{10}(L_{\mathrm{IR}}/L_\odot) \leq 13$, as motivated by the observations discussed in Section 2.1.3. These luminosities correspond with the luminosity range of the objects in our search (Figure 2.12). The luminosity integral can thus be simplified to
$$\begin{aligned}\int_{\log L_{\min}}^{\log L_{\max}} \frac{\mathrm{d}n}{\mathrm{d}\log L_\nu}(z)\,\mathrm{d}\log L_\nu &= \int_{12}^{13} \frac{\mathrm{d}n}{\mathrm{d}\log_{10}(L_{\mathrm{IR}}/L_\odot)}(z)\,\mathrm{d}\log_{10}(L_{\mathrm{IR}}/L_\odot) \\ &\equiv n(z),\end{aligned} \tag{5.8}$$
where $n(z) = n(0)\mathcal{H}(z)$ is the total number density of ULIRGs, with a redshift evolution parameterized by $\mathcal{H}(z)$. The quantity $\epsilon_\nu \mathcal{Q}_{\epsilon_\nu}(\epsilon_\nu, z) = \epsilon_\nu L_{\epsilon_\nu}(\epsilon_\nu) \times n(z)$ therefore represents the differential neutrino luminosity density, or differential neutrino energy generation rate, of ULIRGs at a redshift z (all-flavor).

The above assumptions imply that we can write $\epsilon_\nu \mathcal{Q}_{\epsilon_\nu}(\epsilon_\nu, z) = \epsilon_\nu \mathcal{Q}_{\epsilon_\nu}(\epsilon_\nu, 0)\mathcal{H}(z)$, where $\mathcal{H}(z)$ is the parameterization of the IR luminosity density evolution of ULIRGs,

[14] Since sources with higher luminosities—HyLIRGs and ELIRGs—are comparatively rare and distant (see the Introduction of Chapter 2), their contribution to the diffuse flux is in any case negligible under the assumptions made here.

$\mathcal{Q}_{\rm IR}(z) = \mathcal{Q}_{\rm IR}(0)\mathcal{H}(z)$, as described in Section 2.1.3. Thus, the spectrum of the observed diffuse ULIRG neutrino flux is completely described by the local ULIRG luminosity density, $\epsilon_\nu \mathcal{Q}_{\epsilon_\nu}(\epsilon_\nu, 0) \equiv E_\nu \mathcal{Q}_{E_\nu}(E_\nu)$. Moreover, as shown in [145], for unbroken power-law spectra, the redshift integral becomes independent of energy. The solution of Equation (5.6) is therefore given by

$$E_\nu^2 \Phi_{\nu_\ell+\bar{\nu}_\ell}^{z\le z_{\rm max}}(E_\nu) = \frac{1}{3}\frac{c}{4\pi H_0}\,\xi_{z_{\rm max}}\,E_\nu \mathcal{Q}_{E_\nu}(E_\nu), \tag{5.9}$$

where so-called **redshift evolution parameter** is defined according to the work of [70],

$$\xi_z(\gamma) = \int_0^z \frac{\mathcal{H}(z')\,(1+z')^{-\gamma}}{\sqrt{\Omega_m(1+z')^3+\Omega_\Lambda}}\,\mathrm{d}z'. \tag{5.10}$$

This parameter encompasses all information regarding the redshift evolution of the sources, and essentially describes the cumulative contribution of the full source population up to a redshift z to the diffuse flux. Figure 5.3 shows the redshift evolution parameter as a function of redshift for the following parameterizations $\mathcal{H}(z) \propto (1+z)^m$:

- ULIRG evolution, with $m = 4$ for $z \le 1$ and $m = 0$ for $1 < z \le 4$; see Equation (2.3).
- Star-formation rate (SFR) evolution, with $m = 3.4$ for $z \le 1$, $m = -0.3$ for $1 < z \le 4$; see Equation (2.4).
- Flat evolution, with $m = 0$ for all z; for reference.

As expected, the contribution of sources at higher redshifts is more significant for a population with an aggressive redshift evolution, such as ULIRGs, compared to sources evolving more moderately. Furthermore, Figure 5.3 indicates that the redshift-evolution parameter is significantly larger for $\gamma = 2.0$ compared to $\gamma = 3.0$. This illustrates the fact that for a fixed normalization of the luminosity density

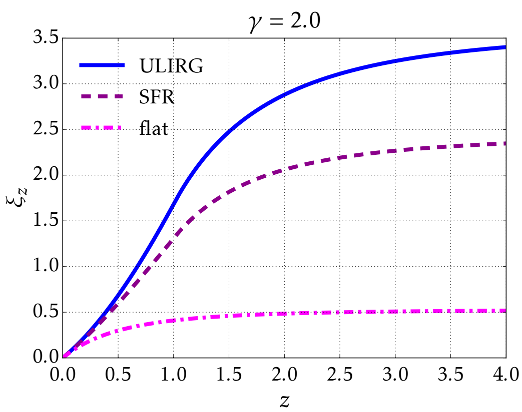

(a) $\gamma = 2.0$

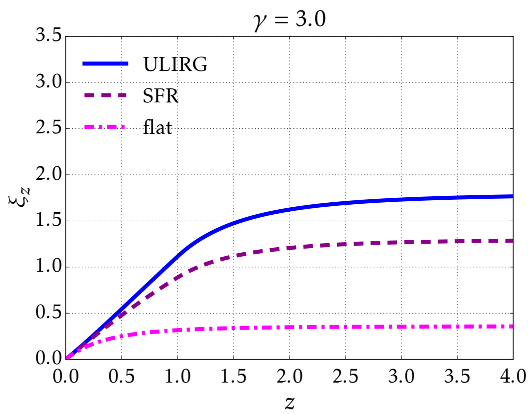

(b) $\gamma = 3.0$

FIGURE 5.3: Redshift evolution parameter $\xi_z(\gamma)$ as a function of the redshift z, shown for ULIRG, SFR, and flat source evolutions (blue full, dark-magenta dashed, and light-magenta dash-dotted lines, respectively). Panels (a) and (b) show the redshift evolution parameters for the spectral indices $\gamma = 2.0$ and $\gamma = 3.0$, respectively.

$E_\nu Q_{E_\nu}$, the contribution of high-redshift sources to the diffuse flux is more prominent for harder spectra compared to softer spectra.

Computing Diffuse Limits

Let us now translate our stacked-flux upper limits, corresponding with the cumulative flux of our representative ULIRG sample within $z \leq 0.13$, to limits on the diffuse muon-neutrino flux of the complete ULIRG population up to $z_{\max} = 0.13$,

$$\Phi^{z\leq 0.13}_{\nu_\mu+\bar{\nu}_\mu} = \frac{\epsilon_c}{4\pi\ \mathrm{sr}}\, \Phi^{90\%}_{\nu_\mu+\bar{\nu}_\mu}. \tag{5.11}$$

Here, the factor 4π sr stems from the fact that the distribution of ULIRGs on the sky is isotropic (see e.g. Figure 2.16). The **completeness-correction factor** ϵ_c is also introduced, which takes into account that the representative selection of ULIRGs is not complete. In Section 2.3.4, it was argued that this is a result of a limited sky coverage of the catalogs used to perform the ULIRG selection. The effect of this limited coverage was shown to be roughly 10%, such that the completeness-correction factor is set to $\epsilon_c = 1.1$.

Finally, Equation (5.9) and its underlying assumptions can be used to obtain upper limits on the diffuse muon-neutrino flux of the ULIRG source population up to a certain maximum redshift $z_{\max}$,

$$\Phi^{z\leq z_{\max}}_{\nu_\mu+\bar{\nu}_\mu} = \frac{\xi_{z_{\max}}(\gamma)}{\xi_{0.13}(\gamma)}\, \Phi^{z\leq 0.13}_{\nu_\mu+\bar{\nu}_\mu}. \tag{5.12}$$

Thus, the upper limit on the diffuse ULIRG population is fully determined by the redshift evolution parameter. More specifically, the ratio $\xi_{z_{\max}}/\xi_{0.13}$ is effectively a scaling factor, which yields the relative contribution of all ULIRGs up to $z_{\max}$ compared to those used in the analysis ($z \leq 0.13$). Panels (a) and (b) of Figure 5.4 show

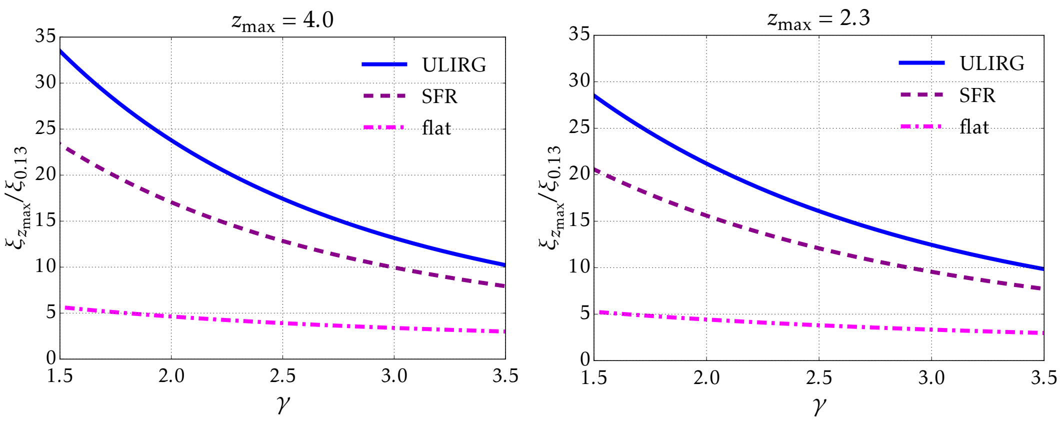

(a) $z_{\max} = 4.0$ (b) $z_{\max} = 2.3$

FIGURE 5.4: Ratio of the redshift-evolution parameter integrated up to a maximum redshift $z_{\max}$, $\xi_{z_{\max}}$, to the redshift-evolution parameter integrated up to the maximum redshift $z = 0.13$ used in the ULIRG stacking analysis, $\xi_{0.13}$. This ratio is shown as a function of the spectral index γ for ULIRG, SFR, and flat source evolutions (blue full, dark-magenta dashed, and light-magenta dash-dotted lines, respectively). Panels (a) and (b) show the ratio computed for $z_{\max} = 4.0$ and $z_{\max} = 2.3$, respectively.

this ratio for $z_{\max} = 4.0$ and $z_{\max} = 2.3$, respectively, as a function of the spectral index γ, for the ULIRG, SFR, and flat evolution schemes. The impact of the scaling factor is more significant for more aggressive source evolutions and harder spectra, which is consistent with our discussion of Figure 5.3.

5.2.2 Limits on Diffuse Neutrino Emission from ULIRGs

Using Equations (5.11) and (5.12), upper limits at 90% CL are obtained on the diffuse muon-neutrino flux from the full ULIRG source population. In what follows, the ULIRG evolution scheme will be assumed as well as a maximum redshift[15] $z_{\max} = 4.0$, unless explicitly mentioned otherwise.

First, the integral stacked-flux upper limits of Table 5.1 are extrapolated to integral diffuse-flux upper limits. These results are shown in Figure 5.5 for unbroken $E_\nu^{-2.0}$, $E_\nu^{-2.5}$, and $E_\nu^{-3.0}$ power-law spectra, where they are compared to the diffuse $\nu_\mu + \overline{\nu}_\mu$ and per-flavor HESE measurements[16] of IceCube. Each of these upper limits is plotted within its respective 90% central energy range, determined in Section 5.1.2. The limits under the $E_\nu^{-2.0}$ and $E_\nu^{-2.5}$ assumptions exclude ULIRGs as the sole contributors to the diffuse neutrino observations up to energies of ~3 PeV and ~600 TeV, respectively. More specifically, for an $E_\nu^{-2.5}$ spectrum, ULIRGs cannot contribute more than ~10% to the diffuse neutrino observations. The $E_\nu^{-3.0}$ limit mostly constrains the diffuse ULIRG flux at energies below the diffuse observations.

In addition, the differential stacked-flux limits of Table 5.3 are extrapolated to diffuse limits on the neutrino flux from the ULIRG source population. Equation (5.12) is used for this extrapolation as well; a spectral-index value $\gamma = 2.0$ is assumed for the computation of the redshift evolution parameter ξ_z. In other words, the true spectrum emitted by ULIRGs is assumed to be a power law with $\gamma = 2.0$ over cosmic history, which is a conservative choice (see Figure 5.4). These differential limits are shown in Figure 5.6, and should therefore be interpreted as limits on the diffuse neutrino flux of the ULIRG population per energy decade, assuming that this population emits neutrinos according to an $E_\nu^{-2.0}$ spectrum over cosmic history. The differential limits exclude ULIRGs as the sole contributors to the diffuse neutrino observations in the 10–100 TeV and 0.1–1 PeV bins, respectively.

The above results do *not* constrain the possible contribution of LIRGs ($10^{11} L_\odot \leq L_{\mathrm{IR}} < 10^{12} L_\odot$) to the diffuse neutrino flux. Within $z < 1$, the IR luminosity density of LIRGs evolves roughly the same with redshift as the IR luminosity density of ULIRGs, although the former is ~10–50 times larger (Section 2.1.3). Assuming that the correlation between the total IR and neutrino luminosities holds down to $L_{\mathrm{IR}} \geq 10^{11} L_\odot$, the contribution of LIRGs to the neutrino flux is expected to dominate with respect to ULIRGs by a factor ~10–50. Under this assumption, the diffuse neutrino observations would likely provide more stringent constraints than the stacking analysis. Nevertheless, note that the AGN contribution to the total IR luminosity seems to be smaller for LIRGs than for ULIRGs [227]. This difference of the AGN

[15] The choice of $z_{\max} = 4.0$, although arbitrary, is inspired by the work of [149]. It can also be motivated by the fact that the ULIRG redshift evolution of Equation (2.3) is only descriptive up to $z \sim 4$. For $z > 4$, a *negative* source evolution is expected for ULIRGs, as observed for the evolution of the SFR in Equation (2.4). The contribution of sources with $z > 4$ is therefore expected to be quasi negligible. For example, under the SFR evolution scheme given in Equation (2.4), a relative contribution $\xi_\infty/\xi_{4.0} = 1.02$ is found for $\gamma = 2.0$.

[16] Recall that HESE measures an all-flavor flux of neutrinos (Section 1.2.1). Since the observed astrophysical flavor ratio is consistent with $(\nu_e : \nu_\mu : \nu_\tau) = (1 : 1 : 1)$ (Section 1.2.2), the per-flavor HESE flux is found by dividing the all-flavor measurement by 3.

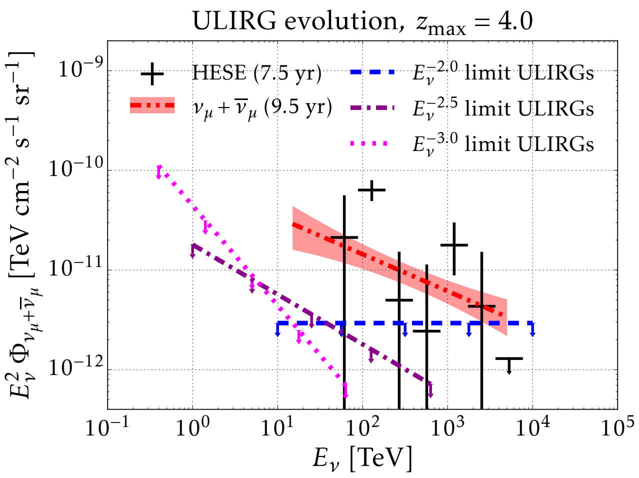

Figure 5.5: Integral limits at 90% confidence level on the contribution of the ULIRG population up to a redshift $z_{\mathrm{max}} = 4.0$ to the observed diffuse muon-neutrino flux. These integral limits are shown for unbroken $E_\nu^{-2.0}$ (dashed blue line), $E_\nu^{-2.5}$ (dash-dotted dark magenta line), and $E_\nu^{-3.0}$ (dotted light magenta line) power-law spectra. The integral limits are plotted within their respective 90% central energy ranges. The diffuse neutrino observations are shown in terms of the 7.5-yr differential per-flavor measurements using the high-energy starting event (HESE) sample (black data points) [91]. They are also shown in terms of the 9.5-yr best-fit unbroken power-law spectrum of astrophysical muon neutrinos from the Northern hemisphere (dash-double-dotted red line), where the ±68% confidence region is also indicated (red band) [92].

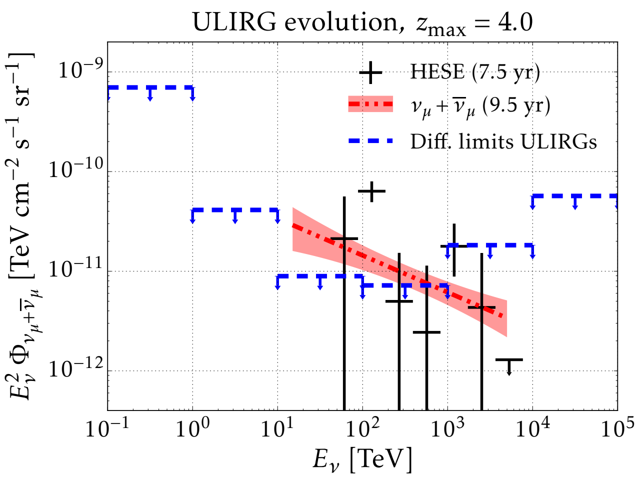

Figure 5.6: Differential limits at 90% confidence level (dashed blue line) on the contribution of the ULIRG population up to a redshift $z_{\mathrm{max}} = 4.0$ to the observed diffuse muon-neutrino flux. These differential limits are found by determining the limit for an $E_\nu^{-2.0}$ spectrum in each decade of energy. The diffuse neutrino observations are described in Figure 5.5.

contribution suggests that the hadronic acceleration properties of LIRGs may differ from those of ULIRGs. A dedicated study searching for high-energy neutrinos from LIRGs would provide further insights on the possible acceleration mechanisms within these objects.[17]

5.3 Comparison with Model Predictions

The diffuse-flux upper limits, determined according to the method of Section 5.2.1, can be compared to model predictions of the diffuse neutrino flux originating from the ULIRG source population (Section 2.2). It should be remarked that in each of the model comparisons, all ULIRGs are assumed to have the physical properties described by the model in question. Consequently, neutrino production in ULIRGs is implicitly assumed to occur either via a starburst reservoir or an AGN beam dump throughout cosmic history, without considering a combination of both scenarios.

5.3.1 Constraints on Starburst Reservoir Models

To start, the ULIRG analysis results are compared to the cosmic-ray reservoir models discussed in Section 2.2.1. The first reservoir model, by He et al. [272], proposes that the enhanced hypernova rate in ULIRGs accelerates cosmic rays up to ∼100 PeV. They predict a diffuse neutrino flux from ULIRGs up to a redshift $z_{\text{max}} = 2.3$ consistent with an $E_\nu^{-2.0}$ power-law spectrum, with a cutoff at ∼2 PeV. Hence, their prediction is compared to the integral $E_\nu^{-2.0}$ upper limit on the diffuse ULIRG neutrino flux up to a redshift $z_{\text{max}} = 2.3$. This comparison is shown in Figure 5.7. The upper limit at 90% CL using 7.2 years of IceCube data is roughly at the level of the predicted flux of He et al. A follow-up study using additional years of data is required to further investigate the validity of this model.

The analysis results are also compared to the work of Palladino et al. [149], who construct a generic model of neutrino emission from a population of hadronically powered gamma-ray galaxies (HAGS), such as ULIRGs. They find that power laws with spectral indices $\gamma \leq 2.12$ and a variable cutoff at several PeV are able to explain a significant fraction of the diffuse neutrino observations without violating the non-blazar EGB bound above 50 GeV (Section 1.3.4). For their prediction, Palladino et al. assume that HAGS evolve according to the SFR over cosmic history up to $z_{\text{max}} = 4.0$. Thus, their most optimistic prediction, i.e. for $\gamma = 2.12$, is compared to the integral $E_\nu^{-2.12}$ upper limit on the diffuse ULIRG neutrino flux up to a redshift $z_{\text{max}} = 4.0$. The limits exclude ULIRGs at 90% CL as the sole population of HAGS that can be responsible for the diffuse neutrino observations. However, it should be noted that this result does not have any implications for other candidate HAGS, such as starburst galaxies with $L_{\text{IR}} < 10^{12} L_\odot$.

5.3.2 Constraints on AGN Beam-Dump Model

The results of the ULIRG analysis can also be used to constrain the Compton-thick AGN beam-dump model of Vereecken & de Vries [145, 146], which was discussed in Section 2.2.2. In this model, the authors applied two methods to normalize the

[17] A data-driven model [263] of neutrino emission from LIRGs is currently being developed in collaboration with the Great Observatories All-sky LIRG Survey (GOALS) [133]. The eventual goal—pun intended—is to test this model in a dedicated IceCube analysis, and as such expand the GOALS survey to become the first multimessenger catalog of LIRGs [395].

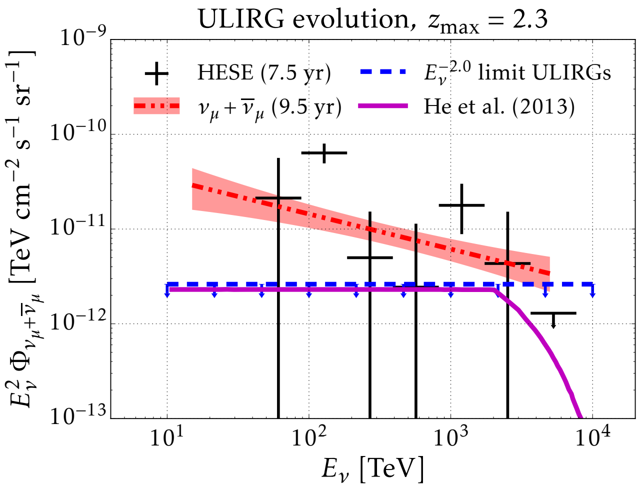

FIGURE 5.7: Comparison of the prediction by [272] of a diffuse muon-neutrino flux from hypernovae in ULIRGs (full magenta line; see Figure 2.8) with the integral $E_\nu^{-2.0}$ upper limit at 90% confidence level of the ULIRG stacking search (dashed blue line). The limit is plotted within its 90% central energy range. For this comparison, an ULIRG source evolution is assumed and integrated up to a redshift $z_{\max} = 2.3$. The diffuse neutrino observations are described in Figure 5.5.

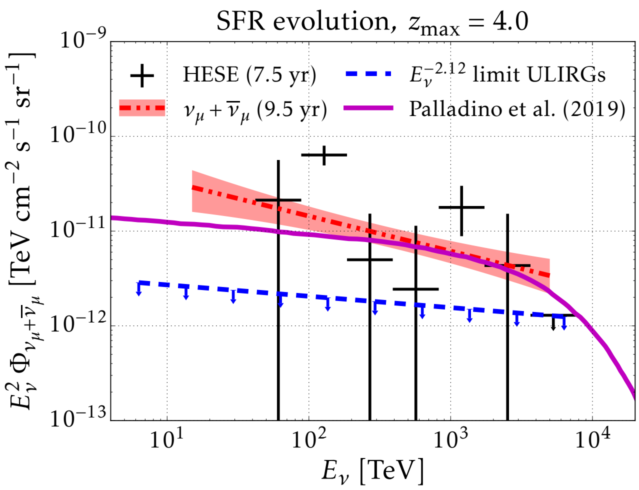

FIGURE 5.8: Comparison of the prediction by [149] of a diffuse muon-neutrino flux, normalized to the IceCube observations, from HAGS (full magenta line; see Figure 2.9) and the integral $E_\nu^{-2.12}$ upper limit at 90% confidence level of the ULIRG stacking search (dashed blue line). The limit is plotted within its 90% central energy range. For this comparison, a source evolution according to the star-formation rate (SFR) is assumed and integrated up to a redshift $z_{\max} = 4.0$. The diffuse neutrino observations are described in Figure 5.5.

proton luminosity of Compton-thick AGN in ULIRGs. On the one hand, they fitted the proton luminosity to the diffuse IceCube observations, where it was found that for column densities $N_H \gtrsim 5 \times 10^{25}$ cm^{-2}, ULIRGs can fit the diffuse IceCube without violating the non-blazar EGB bound above 50 GeV (Section 1.3.4). On the other hand, by normalizing the proton luminosity to the radio luminosity via Equation (2.5), it was found that ULIRGs are unlikely to be responsible for the bulk of the diffuse neutrino observations. However, the latter method required an estimate for the electron-to-proton luminosity ratio, f_e, which is the most uncertain parameter in the model.

Using Equation (2.5), a lower limit on f_e is set by fixing all other parameters in the model. This estimation is achieved by performing the following steps:

- Fix the electron-to-radio luminosity ratio to $\chi = 100$, according to Vereecken & de Vries.
- Set an upper limit on the local proton energy generation rate of ULIRGs, $\mathcal{Q}_p$. The beam-dump model is fit to the integral $E_\nu^{-2.0}$ diffuse-flux upper limit for the ULIRG source evolution up to $z_{\max} = 4.0$. Using Equation (5.9), this is converted to an upper limit on the total neutrino energy generation rate, $\mathcal{Q}_\nu$, and subsequently to an upper limit on $\mathcal{Q}_p$.
- Estimate the radio luminosity density of ULIRGs, $\mathcal{Q}_R$. The typical radio luminosity of ULIRGs, L_R, is determined using Equation (2.2). For this, the method of Vereecken & de Vries is followed by fixing the IR luminosity as well as the IR-to-radio luminosity ratio to $L_{\mathrm{IR}} = 10^{12} L_\odot$ and $q_{\mathrm{IR}} = 2.6$, respectively. It is also assumed that all ULIRGs host a Compton-thick AGN with $N_H \gtrsim 5 \times 10^{25}$ cm^{-2} and that their contribution to the total IR luminosity is 10%, as motivated by Figure 2.5. This estimate is then converted to the local radio luminosity density as $\mathcal{Q}_R = n_0 L_R$, with n_0 the local ULIRG source number density. The value used by Vereecken & de Vries is adopted, $n_0 = 5 \times 10^{-7}$ Mpc^{-3}, which is also compatible with Figure 2.7.

More details regarding these computations can be found in Appendix E.

The resulting lower limit on the electron-to-proton luminosity ratio of the ULIRG source population is

$$f_e \gtrsim 10^{-3}. \tag{5.13}$$

Note that this lower limit was determined under various assumptions, as described in the steps above and in Section 5.2.1. Furthermore, among the model parameters that were kept fixed, some have significant uncertainties, such as the electron-to-radio luminosity ratio, χ, and the local ULIRG source density, n_0. Hence, the lower limit on f_e should be regarded as an order-of-magnitude estimation. Nevertheless, this estimated lower limit can be compared to previous results. Vereecken & de Vries performed a similar lower-limit estimation for 14 individual obscured flat-spectrum radio AGN that were also studied with IceCube [281, 282]. Their lower limits on the electron-to-proton luminosity ratio range between $f_e \gtrsim 10^{-4}$ and $f_e \gtrsim 10^{-2}$, which are consistent[18] with the lower limit that was determined for the ULIRG source

[18] This result can also be seen as a sanity check of the model developed by Vereecken & de Vries. This model can namely applied to obtain predictions of individual sources (e.g. obscured flat-spectrum radio AGN) and to obtain predictions of a generic source population (e.g. ULIRGs). The ULIRG stacking analysis yields the first ever constraint on f_e for the case of a source population, which falls in the same ballpark as previous constraints on f_e for individual objects of another source class.

class. However, a more dedicated IceCube analysis on Compton-thick AGN, which is currently being developed [396], could provide more stringent constraints on the f_e parameter.

Conclusions and Outlook

This thesis presented the first dedicated search for high-energy (TeV–PeV) neutrinos from ultra-luminous infrared galaxies (ULIRGs; $L_{\mathrm{IR}} \geq 10^{12} L_{\odot}$), which has led to the publication of a peer-reviewed article [1] and several conference proceedings [2–5]. The motivation behind this study was the yet unknown origin of the diffuse high-energy neutrino flux measured by the IceCube Neutrino Observatory at the South Pole. ULIRGs are powered by strong starburst nuclei ($\gtrsim 100\ M_{\odot}\ \mathrm{yr}^{-1}$) with secondary contributions from (obscured) active galactic nuclei (AGN) [183], both of which are plausible hadronic accelerators where high-energy neutrinos could be produced [146, 149, 272]. Moreover, the ULIRG source population—which is relatively numerous and expected to be relatively dim in terms of neutrino emission—is unconstrained by limits set in previous IceCube point-source studies. In fact, ULIRGs could supply a large fraction of the diffuse IceCube observations without violating the non-blazar extragalactic gamma-ray background (EGB) measured by *Fermi*-LAT above 50 GeV [83].

First, a selection of ULIRGs was performed using three catalogs that are primarily based on data of the Infrared Astronomical Satellite (IRAS) [215, 227, 246]. An initial sample of 189 ULIRGs was obtained, after correcting for the overlap between the three catalogs. The selection biases of these catalogs were also investigated, and found to be consistent with a lack of sky coverage. Furthermore, a redshift cut was applied at $z = 0.13$, up to which the initial ULIRG selection was estimated to be complete. The resulting final sample of 75 ULIRGs is distributed over the whole sky and indeed found to be representative for the local ULIRG source population within $z \leq 0.13$, after correcting for the selection biases.

Subsequently, a dedicated IceCube point-source analysis was developed using the gamma-ray follow-up (GFU) event selection, which consists of high-quality track data recorded between 2011–2018 [132, 340]. A short comparative study was presented between the GFU sample and another dataset widely used in point-source searches, in terms of their effective area and the median resolution. For the analysis itself, which was performed within the `SkyLab` software framework, a stacking technique was applied to target the cumulative neutrino emission of the selected ULIRGs. Here, the candidate sources were weighted according to their total infrared flux, which was found to be a reasonable proxy for their neutrino flux. By blinding the data, the analysis performance in the recovery of a simulated astrophysical signal from ULIRGs was tested for various unbroken $E_{\nu}^{-\gamma}$ power-law spectra. The corresponding sensitivities and discovery potentials were crosschecked with the `Csky` software framework, which were found to be compatible with the `SkyLab` results. Additionally, it was tested whether stacking 189 instead of 75 ULIRGs would yield significant improvements to these quantities, but such improvements were determined to be marginal.

The stacking analysis yielded a p-value $p = 1.0$, such that the IceCube data was found to be consistent with atmospheric-background expectations. In other words, no high-energy astrophysical muon neutrinos were identified from the representative sample of 75 ULIRGs within $z \leq 0.13$ using 7.2 years of GFU data. Both integral and differential upper limits at 90% confidence level (CL) were therefore computed on the muon-neutrino flux of this ULIRG selection. The integral limits were obtained for unbroken $E_\nu^{-\gamma}$ power-law spectra, and the central 90% energy ranges contributing to these limits were also determined. In addition, the relative effect of systematic uncertainties on all upper limits was studied qualitatively, and found to be $\lesssim$15%. Overall, these upper limits constitute the first ever constraints on the neutrino emission from ULIRGs.

Finally, for the purposes of interpretation, the above results were extrapolated to upper limits on the diffuse high-energy neutrino flux expected from the full ULIRG source population. As such, ULIRGs were excluded at 90% CL as the sole population of sources that could be responsible for the diffuse IceCube observations. In particular, the integral upper limits for an $E_\nu^{-2.5}$ spectrum constrain the contribution of ULIRGs to the diffuse muon-neutrino measurements of [92] to $\lesssim$10%. Furthermore, these results were compared to model predictions of diffuse neutrino emission from ULIRGs. He et al. [272] predict a neutrino flux from ULIRGs that is at the level of the $E_\nu^{-2.0}$ upper limit, and a follow-up study with additional years of IceCube data is required to validate or exclude this starburst-reservoir model. Nevertheless, ULIRGs were excluded as the sole hadronically-powered gamma-ray galaxies (HAGS) responsible for the diffuse observations in the starburst-reservoir model by Palladino et al. [149]. Lastly, the results of this search were compared to the obscured-AGN beam-dump model by Vereecken & de Vries [145,146], where the electron-to-proton luminosity ratio—a measure for the cosmic-ray content of these sources—was roughly restricted to $f_e \gtrsim 10^{-3}$. This beam-dump model could further be tested in an upcoming IceCube study targeting hard X-ray AGN, which can show typical signs of AGN obscuration [396].

It should be remarked that the above results do not constrain the possible contribution of luminous infrared galaxies (LIRGs; $L_{\mathrm{IR}} \geq 10^{11} L_\odot$) to the diffuse observations. They are less luminous but much more numerous compared to ULIRGs, and their contribution to the total infrared luminosity density in the Universe is roughly a factor 10–50 larger [258]. Since the mechanisms powering LIRGs and ULIRGs are similar [183], LIRGs could be significant contributors to the diffuse neutrino measurements. In fact, a model of neutrino production in LIRGs, driven by data of the Great Observatories All-Sky LIRG Survey (GOALS) [133], is currently under development [263]. This model, as well as the contribution of LIRGs to the diffuse neutrino flux, is planned to be tested in a dedicated IceCube search [395].

In a broader context, the future of the field of neutrino astronomy looks promising [151]. Currently, km^3 counterparts of IceCube are being instrumented in the Mediterranean Sea (KM3NeT) and Lake Baikal (Baikal-GVD), and P-ONE has been proposed to be built near the West Coast of Canada. These experiments will complement IceCube observations, particularly in the Southern Sky. Moreover, IceCube-Gen2 is planned to take form in the coming decades [141]. This 8-km^3 array is designed to identify the yet unknown sources of TeV–PeV astrophysical neutrinos. Lastly, apart from these optical Cherenkov telescopes, various projects are being developed that target ultra-high-energy (UHE; $\geq$ 100 PeV) neutrinos [151]. The discovery of UHE neutrinos would not only allow to directly probe the sources of cosmic rays at the highest energies, but it could also reveal the existence of cosmogenic neutrinos produced via the GZK effect.

Contributions during the PhD

Research

The main research outlined in this thesis, which was conducted under a PhD Fellowship awarded by the Flemish Research Foundation (FWO), resulted in a peer-reviewed publication [1] and a number of conference proceedings [2–5]. Complementary to this work, I was also actively involved in a phenomenological study regarding the construction of a data-driven starburst model in LIRGs [263]. A publication of these efforts is foreseen in the near future. Furthermore, I performed several internal contributions as a member of the IceCube collaboration. These included detector monitoring, some minor improvements to the `SkyLab` code, as well as the first comparison of `SkyLab` and `Csky` in the context of a stacking analysis. Apart from that, I was also an internal IceCube reviewer of two neutrino-source analyses, two conference proceedings [396, 397], and one article which was recently submitted for publication [142].

Teaching

During my PhD, I was the teaching assistant for the courses Subatomic Physics I (BA3; 2017–2018) and Experimental Physics (BA1; 2018–2021). In addition, I supervised the BSc theses of Yarno Merckx [398] and Tanguy Aerts [399], as well as the MSc thesis of Yarno Merckx [263]. The research of the latter is currently being continued, as Yarno Merckx was awarded a PhD Fellowship by the FWO.

Outreach

I was actively involved in a variety of outreach activities, mostly targeting children and adolescents. I was the main organizer of the annual IceCube Masterclass[1] and South Pole Experiment contest[2] between 2019–2021, and I also contributed to the organization of the 2018 and 2022 editions of these events. Furthermore, I organized a variety of workshops, ranging from summer-camp events to expositions about the local research activities, generally for interested students. In addition, I was one of the main Dutch translators of the *Rosie & Gibbs* comics[3] created by members of the IceCube collaboration.

[1] See https://iihe.ac.be/masterclass and https://masterclass.icecube.wisc.edu.

[2] See https://iihe.ac.be/polar-science-challenge and https://spexperiment.icecube.wisc.edu/.

[3] Available at https://icecube.wisc.edu/outreach/activities/rosie-gibbs/.

Academic Representation

I participated in a number of academic councils and organizations during the course of my PhD. I was a PhD representative in the council (2019–2021) and board (2017–2021) of the Faculty of Sciences & Bio-Engineering Sciences, as well as in the managing and education councils of the Department of Physics (2017–2022). Apart from that, between 2019–2021, I was also a co-organizer of colloquia promoted by the International Solvay Institutes.[4]

[4]See http://www.solvayinstitutes.be/html/colloquia.html.

Appendix A

Conventions for Flux and Luminosity

It is worth devoting some words on the conventions for flux and luminosity that are used throughout this work. Let us first consider an astrophysical source of electromagnetic radiation. When observing this source, we usually measure the energy flux of this source that reaches Earth at a certain frequency. Such a **differential energy flux**, or flux density, is the amount of energy per unit time, $\mathrm{d}E/\mathrm{d}t$, that passes through a surface area $\mathrm{d}A$ at Earth,[1] per unit of frequency[2] $\mathrm{d}\nu$,

$$f_\nu \equiv \frac{\mathrm{d}E}{\mathrm{d}A\,\mathrm{d}t\,\mathrm{d}\nu}. \tag{A.1}$$

Typical units are $1\ \mathrm{Jy} = 10^{-26}\ \mathrm{W\ m^{-2}\ Hz^{-1}}$. The **total energy flux** observed by the source is then found by integrating over the frequency spectrum,

$$F \equiv \frac{\mathrm{d}E}{\mathrm{d}A\,\mathrm{d}t} = \int_{\nu_1}^{\nu_2} f_\nu\ \mathrm{d}\nu, \tag{A.2}$$

typically given in units of $\mathrm{W\ m^{-2}}$. The total energy flux is usually determined over a specific band in frequency, $[\nu_1, \nu_2]$. Note that historically, some parts of the electromagnetic spectrum are characterized by their wavelength $\lambda = c/\nu$ instead of their frequency. For example, the infrared band is usually defined as $[\lambda_2 = 8\ \mu\mathrm{m}, \lambda_1 = 1000\ \mu\mathrm{m}]$, which corresponds to $[\nu_1 = 3.0 \times 10^2\ \mathrm{GHz}, \nu_2 = 3.7 \times 10^4\ \mathrm{GHz}]$.

If we assume that the source is spherical and its energy output is isotropic, such as e.g. a star, we can determine the **differential intrinsic luminosity** and **total intrinsic luminosity**—integrated over a given waveband—of the source via the well-known relations

$$f_\nu = \frac{L_{\nu_s}}{4\pi d_L^2}, \quad F = \frac{L}{4\pi d_L^2}, \tag{A.3}$$

where d_L is the luminosity distance to the source, and where

$$L = \int_{(1+z)\nu_1}^{(1+z)\nu_2} L_\nu\ \mathrm{d}\nu. \tag{A.4}$$

Here we take into account that due to the expansion of the Universe, radiation emitted at a frequency ν_s in the rest frame of the source will be observed at the redshifted frequency $\nu = \nu_s/(1+z)$. Typically, L_ν is given in units of $\mathrm{W\ Hz^{-1}}$, while L is usually given in terms of the bolometric solar luminosity $L_\odot = 3.828 \times 10^{26}$ W. Equation (A.3)

[1] It is important to notice that "flux" is generally used to describe the energy output of the source that reaches Earth. It is typically not meant to describe the detection rate of a certain experiment. To convert the actual detection rate to the flux that reaches Earth requires a detailed understanding of the detector. For IceCube, this information is incorporated into the effective area, as discussed in Section 3.3.2.

[2] Recall that frequency, wavelength, and energy are related to each other as $E = h\nu = hc/\lambda$. Hence, a differential flux can always be converted into a flux per unit of wavelength, $\mathrm{d}\lambda$, or a flux per unit of energy, $\mathrm{d}E$.

is generally also used to estimate the luminosity of sources that are not spherical (e.g. a spiral galaxy) or do not emit their radiation isotropically (e.g. an active galactic nucleus). In this case, we in fact determine the apparent isotropic luminosity of the source. However, we typically just refer to it as the source luminosity, as done in this work. Note that Equation (A.3) does not take into account any absorption effects that might occur between the source and the observer.

Note that the luminosity distance d_L is defined such that Equation (A.3) holds over cosmological distances. As mentioned above, a consequence of the expansion of the Universe is that the emitted energy (or frequency) at the source, $\mathrm{d}\epsilon$, is redshifted when observed at Earth, $\mathrm{d}E = \mathrm{d}\epsilon/(1+z)$. Moreover, the time interval over which radiation or particles are observed, $\mathrm{d}t = (1+z)\,\mathrm{d}\tau$, is stretched w.r.t. the time interval over which they were emitted, $\mathrm{d}\tau$. In other words, $\mathrm{d}E/\mathrm{d}t = (1+z)^{-2}\,\mathrm{d}\epsilon/\mathrm{d}\tau$. This redshift factor is essentially absorbed in the luminosity distance, which is related to the comoving distance $d_C = c\int_0^z \mathrm{d}z'/H(z')$, where $H(z)$ is the redshift-dependent Hubble parameter, as $d_L = (1+z)\,d_C$.

In astroparticle physics, we tend to use different notations for flux and luminosity. Since we are now explicitly focused on measuring particles, we define a **differential particle flux** of an astrophysical source as the particle rate $\mathrm{d}N/\mathrm{d}t$ that passes through a surface area $\mathrm{d}A$ at Earth, per unit of particle energy $\mathrm{d}E$,

$$\Phi(E) \equiv \frac{\mathrm{d}N}{\mathrm{d}E\,\mathrm{d}A\,\mathrm{d}t}. \tag{A.5}$$

This quantity has typical units of $\mathrm{GeV}^{-1}\ \mathrm{cm}^{-2}\ \mathrm{s}^{-1}$ and is also commonly denoted as $\mathrm{d}N/\mathrm{d}E$. The corresponding **differential energy flux**[3] is then given by

$$E\,\Phi(E) = E\frac{\mathrm{d}N}{\mathrm{d}E\,\mathrm{d}A\,\mathrm{d}t}, \tag{A.6}$$

which is equivalent to f_ν in our previous notation. The total energy flux over a certain energy range $[E_1, E_2]$ is then given by[4]

$$F = \int_{E_1}^{E_2} E\,\Phi(E)\,\mathrm{d}E. \tag{A.7}$$

The differential energy flux is related to the (apparent isotropic) differential rest-frame luminosity of the source as

$$E\,\Phi(E) = \frac{L_\epsilon}{4\pi d_L^2}, \tag{A.8}$$

with $\epsilon = (1+z)E$, and where the total luminosity is given by

$$L = \int_{\epsilon_1}^{\epsilon_2} L_E\,\mathrm{d}E. \tag{A.9}$$

Note that it is common to define the differential luminosity as EL_E, such that it has the same units, typically $\mathrm{erg\ s}^{-1}$, as the total luminosity L.

[3] Note that in this work both particle and energy fluxes are generally referred to as "flux." The adjectives "differential" and "total" are also typically omitted when describing a flux or luminosity, unless required for clarity.

[4] For transient sources, it is common to consider the differential fluence of the source, $S_E \equiv \mathrm{d}N/\mathrm{d}A\,\mathrm{d}E = \int \Phi(E)\,\mathrm{d}t$, with the total fluence given by $S = \int S_E\,\mathrm{d}E$.

We can also define the **differential energy flux per logarithmic energy interval** $\mathrm{d}\log E = \mathrm{d}E/E$ as

$$E^2\Phi(E) = E\,\frac{\mathrm{d}N}{\mathrm{d}\log E\,\mathrm{d}A\,\mathrm{d}t}, \tag{A.10}$$

which has typical units of GeV cm^{-2} s^{-1}. In our previous notation, this quantity is usually denoted as νf_ν, and given in units of Jy Hz. As we will discuss below, $E^2\Phi$ is closely related to a **differential luminosity density**, which is defined as the differential luminosity per unit of volume $\mathrm{d}V$,

$$E\mathcal{Q}_E(E) \equiv E\frac{\mathrm{d}L_E}{\mathrm{d}V}. \tag{A.11}$$

This quantity is also referred to as the **differential energy generation rate**.[5] As usual, we define the **total luminosity density**, or total energy generation rate, as

$$\mathcal{Q} \equiv \frac{\mathrm{d}L}{\mathrm{d}V} = \int_{\epsilon_1}^{\epsilon_2} \mathcal{Q}_E \;\mathrm{d}E. \tag{A.12}$$

Both $E\mathcal{Q}_E$ and $\mathcal{Q}$ have typical units of erg Mpc^{-3} yr^{-1}.

High-energy astrophysical phenomena are typically characterized by power-law fluxes of the form

$$\Phi(E) \propto E^{-\gamma}, \tag{A.13}$$

where γ is called the spectral index. An elegant property of power laws is that they are directly associated with scale-free systems, since a power law is the only distribution whose shape remains unchanged under a scale transformation[6] [61]. One particularly important value of the spectral index is $\gamma = 2$, which is predicted by the first-order Fermi acceleration mechanism (Section 1.1.1), and for which $E^2\Phi$ is constant. Thus, for a source emitting particles according to an E^{-2} spectrum, the total energy budget is distributed equally per energy decade. For non-E^{-2} power-law spectra and broken power-law spectra (i.e. spectra characterized by multiple spectral indices), it is also common to consider $E^\alpha\Phi(E)$, where the value of α is chosen such that it highlights the spectral features of the flux.

Lastly, we point out the distinction between the following three types of fluxes:

- **Individual-source flux.** This is the flux originating from one specific astrophysical source, which can either be a point source or an extended source on the sky.

- **Stacked flux.** When considering multiple astrophysical sources, one can stack their individual fluxes Φ_k as

$$\Phi_{\mathrm{stack}}(E) = \sum_k \Phi_k(E). \tag{A.14}$$

[5] This term is typically used to describe the energy that goes into the production of particles that do not fully escape their source environment. For example, only a fraction of the cosmic rays produced in a source will escape and contribute to the cosmic-ray luminosity output of that source. In contrast, a neutrino energy generation rate can also be seen as the energy output in neutrinos of that source.

[6] More precisely, a power law $p(x)$ is the only distribution for which $p(bx) = g(b)p(x)$, where $g(b)$ is a constant in x [61].

A stacked flux is typically used to describe the cumulative flux of a well-defined set of sources that are too faint to be observed individually. However, in this sense, stacking the contribution of different sources relies on some physical assumption of the sources and their relative contribution to the total stacked flux. The reader is referred to Chapter 4 for a detailed example of a stacked-flux interpretation.

- **Diffuse flux.** When observing a patch of solid angle on the sky, $\mathrm{d}\Omega$, it is possible to observe a flux without being able to associate it to any astrophysical sources in that patch. A diffuse flux is therefore defined as

$$\Phi_{\text{diffuse}}(E) \equiv \frac{\mathrm{d}N}{\mathrm{d}E\,\mathrm{d}A\,\mathrm{d}t\,\mathrm{d}\Omega}, \tag{A.15}$$

with typical units[7] $\mathrm{GeV}^{-1}\ \mathrm{cm}^{-2}\ \mathrm{s}^{-1}\ \mathrm{sr}^{-1}$. On the one hand, such a diffuse flux consists of the cumulative contribution of unresolved sources in that patch of the sky. On the other hand, it can contain a contribution of secondary particles that are produced in interactions of the primary source particles on their trajectory to Earth.[8] Typically, a diffuse flux is measured isotropically over a fraction of the full sky, $\Delta\Omega$, such that it can be related to our usual notation of a particle flux as

$$\Phi(E) = \int \Phi_{\text{diffuse}}(E)\,\mathrm{d}\Omega = \Phi_{\text{diffuse}}(E)\,\Delta\Omega. \tag{A.16}$$

Although by definition, a diffuse flux cannot be associated to any sources directly, we can still infer the overall energy budget required to produce this diffuse flux. Assume that our diffuse flux of particles moving at a velocity c is isotropic over the full sky. The energy flux per logarithmic energy interval, $E^2\Phi_{\text{diffuse}}$, can be converted to an overall energy density by multiplying it with $(4\pi\ \mathrm{sr})/c$. By dividing this energy density with a characteristic timescale τ over which the particles are produced—typically set to the Hubble time $t_H \equiv H_0^{-1}$ for extragalactic sources [145]—we find

$$EQ_E = \frac{4\pi\ \mathrm{sr}}{c\,\tau}\,E^2\Phi_{\text{diffuse}}. \tag{A.17}$$

This quantity can be regarded as the differential luminosity density required to produced the observed diffuse flux.

[7] Note that a diffuse flux has the dimensions of an *intensity*. This quantity remains constant as a function of the distance d_L, since the solid angle scales with d_L^2.

[8] For example, primary gamma rays can interact with the extragalactic background light (EBL), where they cascade into secondary gamma rays with lower energy.

Appendix B

Elementary Particles, Decay Rates, and Cross Sections

The Standard Model is a theory that describes elementary particles and their interplay with three of the four fundamental interactions of nature, namely the electromagnetic force as well as the weak and strong nuclear forces. Although many of its predictions have been verified experimentally (up to great precision), the Standard Model does not provide a complete picture of particle physics. For example, it cannot explain why neutrinos have a non-zero mass, and it does not describe gravity, the fourth fundamental force of nature. A review of the Standard Model and its limitations falls beyond the scope of this work but can be found in e.g. [14, 321, 400–402]. Instead, based on these references, a short description is given of some of the particles relevant to this thesis. The concepts of particle lifetimes and cross sections are also briefly introduced.

Particles of the Standard Model

Figure B.1 shows a summary of the elementary particles that constitute the Standard Model. These particles are classified into various categories, as outlined below.

Gauge and Scalar Bosons

When two particles interact, they do so via the exchange of a gauge boson, which has a spin[1] of 1. Gluons g and photons γ are the massless and chargeless mediators of the strong and electromagnetic forces, respectively, while the weak force is mediated by the massive $W^{\pm}$ (charged current) and Z^0 bosons (neutral current). The Brout-Englert-Higgs boson H is the scalar boson (spin 0) responsible for particles having mass.

Matter and Antimatter

Most elementary particles are fermions, which are characterized by a spin of 1/2. Each of these fermions has an antiparticle counterpart with the same mass and spin but with otherwise opposite physical properties, such as the electric charge. They are classified into (anti)quarks and (anti)leptons, where the former correspond to matter capable of interacting via the strong force. Each of these classes is categorized into three generations of (anti)matter. Note that all (anti)quarks and (anti)leptons can interact weakly, and those with a non-zero electric charge can also interact electromagnetically.

[1] Particles with non-zero half-integer spins are called fermions, and particles with integer spins are called bosons. In particular, scalar bosons have spin 0, while vector bosons have spin 1.

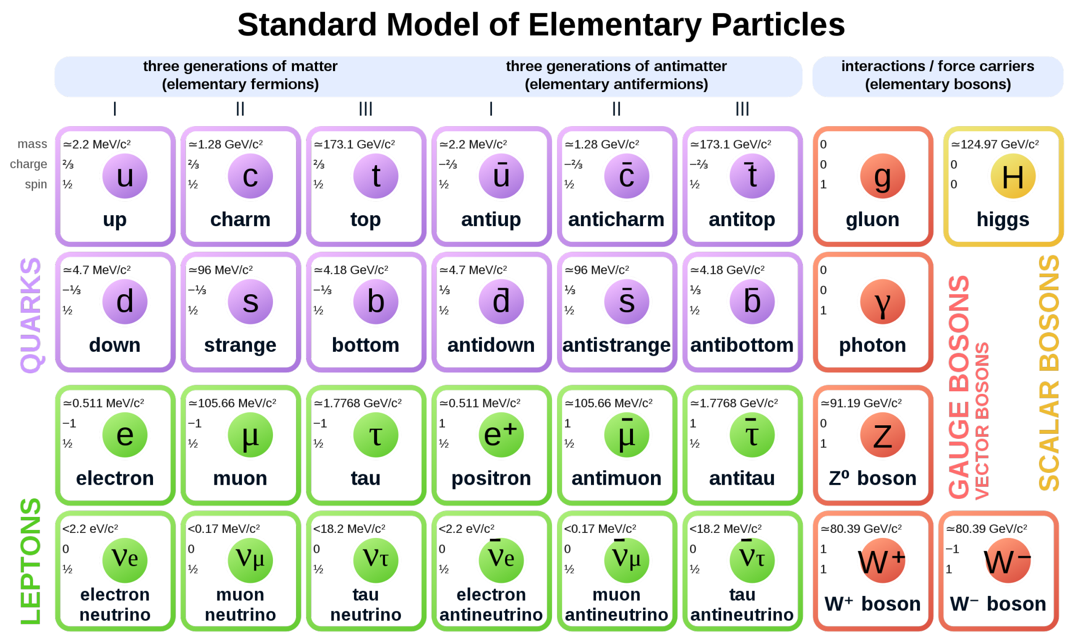

FIGURE B.1: The Standard Model of particle physics, based on data from [14], showing both particles and antiparticles, as well as their mass, electric charge (in units of the elementary charge $e = 1.602 \times 10^{-19}$ C), and spin. Image taken from [403].

Hadrons

Due to the nature of the strong force, quarks q and antiquarks $\overline{q}$ typically exist in composite states, called hadrons.[2] The most common hadronic states are:

- **Baryons ($q\,q\,q$) and antibaryons ($\overline{q}\,\overline{q}\,\overline{q}$).** Examples are (anti)protons ($p = u\,u\,d$ and $\overline{p} = \overline{u}\,\overline{u}\,\overline{d}$) and (anti)neutrons ($n = u\,d\,d$ and $\overline{n} = \overline{u}\,\overline{u}\,\overline{d}$). Note that baryons are fermions.
- **Mesons ($q\,\overline{q}$).** Examples are charged pions ($\pi^+ = u\,\overline{d}$ and $\pi^- = d\,\overline{u}$) and neutral pions ($\pi^0 = u\,\overline{u}$ or $d\,\overline{d}$). Note that mesons are bosons.

Leptons

Leptons and antileptons do not interact via the strong force. While charged (anti)-leptons can also interact electromagnetically, neutral (anti)leptons, i.e. (anti)neutrinos, can only interact via the weak force. Note that (anti)neutrinos can oscillate between their respective generations—also known as neutrino flavors—which cannot be explained by the Standard Model (see also Section 1.2.2).

Particle Decays and Interactions

Apart from (anti)electrons, (anti)neutrinos, and photons, all particles in the Standard Model are unstable.[3] The probability for a particle to decay after some time t

[2] Note that the electric charges add up in these composite-quark states. For example, a proton has an electric charge of $+1e$, whereas a neutron is electrically neutral.

[3] Protons are also stable, although neutrons are *unstable*. However, the strong force ensures that neutrons do not decay when they form part of an atomic nucleus.

in the particle's rest frame is given by

$$\mathcal{P}(t) = 1 - e^{-t/\tau}, \tag{B.1}$$

where τ is defined as the mean particle **lifetime**, and $1/\tau$ is therefore the mean decay rate of the particle, which can be measured in experiments. Table B.1 presents values of particle lifetimes relevant to this work (see Section 1.1.2 and Section 3.1.4), as well as their most common decay modes.

The probability that a certain particle interaction occurs is proportional the **cross section**, σ, which is a measurable quantity. With units of area, the cross section can be interpreted as the effective surface area encountered by a particle undergoing the interaction.[4] In particular, if one considers a beam of particles with an initial intensity I_0 that is shot into a medium with density n, the beam intensity at some distance x into the medium is given by

$$I(x) = I_0 \, e^{-x/\lambda}. \tag{B.2}$$

Here, $\lambda = (n\sigma)^{-1}$ is the **mean free path** of the particles passing through that particular medium, and $1/\lambda$ is also called the absorptivity or scattering coefficient, depending on the type of interaction. Examples of cross sections relevant to this work are shown in Section 1.1.2 (pp and $p\gamma$-interactions) and Section 3.1.1 (neutrino-ice and photon-ice interactions).

Particle	Lifetime [s]	Main Decay Modes
n	$8.8 \times 10^{+2}$	$p\,e^-\,\overline{\nu}_e$
π^- π^+	2.6×10^{-8}	$\mu^-\,\overline{\nu}_\mu$ $\mu^+\,\nu_\mu$
π^0	8.5×10^{-17}	$\gamma\,\gamma$
μ^- μ^+	2.2×10^{-6}	$e^-\,\overline{\nu}_e\,\nu_\mu$ $e^+\,\nu_e\,\overline{\nu}_\mu$
τ^- τ^+	2.9×10^{-13}	ν_τ + hadrons [64.8%] $\nu_\tau\,e^-\,\overline{\nu}_e$ [17.8%] $\nu_\tau\,\mu^-\,\overline{\nu}_\mu$ [17.4%] $\overline{\nu}_\tau$ + hadrons [64.8%] $\overline{\nu}_\tau\,e^+\,\nu_e$ [17.8%] $\overline{\nu}_\tau\,\mu^+\,\nu_\mu$ [17.4%]

TABLE B.1: Lifetimes and main decay modes of some particles relevant to this work. Data taken from [14].

[4] Imagine a game of throwing darts—it is quite easy to hit the overall target, which has a relatively large cross section, but it is much more difficult to hit the bullseye due to its smaller area.

Appendix C
List of Selected ULIRGs

Table C.1 contains a list of all the 189 ULIRGs used in this work. The table contains the following columns, ordered from left to right:

- **NED identification** of the ULIRG [193]. Objects denoted in bold have a redshift $z \leq 0.13$ and thus form part of the representative ULIRG sample used for the IceCube stacking analysis.
- **Right ascension** α and **declination** δ (in J2000 coordinates). Taken from NED.
- **Redshift** z. Taken from NED.
- **Luminosity distance** d_L. Computed from the redshift using the cosmological parameters in [6].
- **IR flux density at 60 μm** f_{60}. Taken from the IRAS RBGS [215] if available; taken from the IRAS FSC [286] if not available in the RBGS; taken from the IRAS PSC [288] if not available in the RBGS or FSC. Data from the FSC and PSC is obtained from NED.
- **Total IR luminosity** L_{IR} (8–1000 μm).
- **Reference** of the ULIRG catalog from which the object and its value of the total IR luminosity are selected.

NED identification	α [°]	δ [°]	z	d_L [Mpc]	f_{60} [Jy]	$\log_{10}(L_{\mathrm{IR}}/L_{\odot})$	Ref.
2MASX J00002427-5250313	0.10	−52.84	0.125	604	1.89 ± 0.13	12.20	[227]
2MASX J00114330-0722073	2.93	−7.37	0.118	570	2.63 ± 0.18	12.19	[246]
2MASS J00203472-7055262	5.14	−70.92	0.327	1769	1.20 ± 0.08	12.95	[227]
2MASX J00212652-0839261	5.36	−8.66	0.128	622	2.59 ± 0.23	12.33	[246]
2MASX J00220698-7409418	5.53	−74.16	0.096	457	4.16 ± 0.21	12.33	[227]
[HB89] 0027-289 NED02	7.52	−28.71	0.278	1468	0.69 ± 0.06	12.65	[227]
2MASX J00300908-0027441	7.54	−0.46	0.242	1253	0.62 ± 0.08	12.53	[227]
GALEXASC J004215.50-125603.2	10.56	−12.93	0.262	1370	1.83 ± 0.13	12.90	[246]
GALEXASC J004303.20-311050.3	10.76	−31.18	0.342	1866	0.72 ± 0.06	12.81	[227]
2MASX J00480675-2848187	12.03	−28.81	0.110	526	2.60 ± 0.18	12.12	[246]
GALEXASC J005040.35-270440.6	12.67	−27.08	0.129	626	1.13 ± 0.14	12.00	[246]
GALEXASC J010250.01-222157.4	15.71	−22.37	0.118	567	2.29 ± 0.16	12.24	[246]
2MASX J01190760-0829095	19.78	−8.49	0.118	569	1.74 ± 0.10	12.03	[246]
IRAS 01199-2307	20.59	−22.87	0.156	770	1.61 ± 0.10	12.26	[246]
GALEXASC J013221.29-072909.5	23.09	−7.49	0.136	663	2.47 ± 0.15	12.27	[246]
GALEXASC J013757.48-175920.6	24.49	−17.99	0.192	966	1.40 ± 0.08	12.39	[246]
2MASX J01405591-4602533	25.23	−46.05	0.090	426	2.91 ± 0.20	12.12	[227]
2MASX J01515140-1830464	27.96	−18.51	0.158	779	1.29 ± 0.09	12.23	[246]
2MASX J01590262+2542367	29.76	+25.71	0.166	821	0.81 ± 0.06	12.24	[227]
2MASX J01591372-2924356	29.81	−29.41	0.140	683	1.73 ± 0.14	12.15	[246]
MRK 1014	29.96	+0.39	0.163	807	2.22 ± 0.18	12.53	[246]
2MASX J02042730-2049413	31.11	−20.83	0.116	557	1.45 ± 0.12	12.01	[246]
GALEXASC J021332.93-292337.3	33.39	−29.39	0.192	968	0.94 ± 0.08	12.41	[227]

Table C.1: List of ULIRGs used in this work. See text in Appendix C for a detailed description of this table.

(Continued on next page)

NED identification	α [°]	δ [°]	z	d_L [Mpc]	f_{60} [Jy]	$\log_{10}(L_{\rm IR}/L_{\odot})$	Ref.
2MASX J02434617+0406377	40.94	+4.11	0.144	702	1.37 ± 0.08	12.19	[246]
IRAS 02456-2220	41.96	−22.13	0.296	1577	0.82 ± 0.05	12.72	[227]
2MASS J02500170-3732441	42.51	−37.55	0.165	817	1.25 ± 0.06	12.23	[246]
2MASX J03021145-2707263	45.55	−27.12	0.221	1133	0.92 ± 0.08	12.55	[227]
IRAS 03158+4227	49.80	+42.64	0.134	653	4.26 ± 0.51	12.61	[227]
SDSS J032322.86-075615.2	50.85	−7.94	0.166	825	1.00 ± 0.08	12.19	[246]
2MASX J03274981+1616594	51.96	+16.28	0.129	625	1.38 ± 0.08	12.06	[246]
2MASS J03542522-6423445	58.61	−64.40	0.301	1606	0.99 ± 0.05	12.79	[227]
2MASX J03544214+0037033	58.68	+0.62	0.152	746	2.64 ± 0.24	12.45	[246]
GALEXASC J040930.40-275343.0	62.38	−27.90	0.154	756	1.33 ± 0.11	12.14	[246]
2MASX J04121945-2830252	63.08	−28.51	0.117	565	1.82 ± 0.09	12.15	[246]
2MASX J04124420-5109402	63.18	−51.16	0.125	602	2.09 ± 0.10	12.26	[227]
IRAS 04313-1649	68.40	−16.73	0.268	1407	1.01 ± 0.05	12.55	[246]
2MASS J04395082-4843165	69.96	−48.72	0.203	1031	0.99 ± 0.05	12.41	[227]
2MASS J04411405-3734369	70.31	−37.58	0.236	1221	0.82 ± 0.07	12.56	[227]
GALEXASC J050400.67-293654.5	76.00	−29.62	0.154	760	1.93 ± 0.08	12.28	[246]
2MASX J05043657-1937028	76.15	−19.62	0.192	966	1.06 ± 0.06	12.43	[246]
2MASX J05173257-3021126	79.39	−30.35	0.172	855	1.16 ± 0.07	12.20	[246]
2MASX J05210136-2521450	80.26	−25.36	0.043	194	13.25 ± 0.03	12.11	[215]
2MASX J05583717-7716393	89.65	−77.28	0.117	562	1.42 ± 0.06	12.05	[227]
2MASX J06025406-7103104	90.73	−71.05	0.079	373	5.13 ± 0.15	12.23	[227]
2MASX J06210118-6317238	95.26	−63.29	0.092	437	3.96 ± 0.12	12.22	[227]
2MASS J06264206-7936302	96.68	−79.61	0.156	771	1.92 ± 0.06	12.39	[227]

Table C.1: List of ULIRGs used in this work. See text in Appendix C for a detailed description of this table.
(Continued on next page)

NED identification	α [°]	δ [°]	z	d_L [Mpc]	f_{60} [Jy]	$\log_{10}(L_{IR}/L_{\odot})$	Ref.
2MASX J06301333+3507498	97.56	+35.13	0.170	844	0.94 ± 0.07	12.34	[227]
2MASS J06363586-6220335	99.15	−62.34	0.160	788	1.66 ± 0.08	12.41	[227]
IRAS 06487+2208	102.94	+22.07	0.143	701	2.07 ± 0.17	12.44	[227]
2MASX J07273754-0254540	111.91	−2.92	0.088	413	6.49 ± 0.03	12.32	[215]
IRAS 07246+6125	112.30	+61.31	0.137	668	0.93 ± 0.08	12.06	[227]
2MASX J07595974+0524513	120.00	+5.41	0.190	955	0.95 ± 0.08	12.47	[227]
IRAS 07598+6508	121.14	+65.00	0.148	727	1.69 ± 0.09	12.46	[246]
SDSS J082312.61+275139.8	125.80	+27.86	0.168	833	1.17 ± 0.07	12.23	[246]
2MASX J08380365+5055090	129.52	+50.92	0.097	459	2.14 ± 0.11	12.01	[227]
IRAS 08449+2332	131.96	+23.35	0.151	744	0.87 ± 0.07	12.14	[227]
SDSS J085018.31+180200.9	132.58	+18.03	0.145	712	1.28 ± 0.12	12.13	[246]
2MASX J08584172+1041223	134.67	+10.69	0.148	726	1.12 ± 0.07	12.16	[246]
IRAS 08572+3915	135.11	+39.07	0.058	270	7.30 ± 0.03	12.10	[215]
IRAS 08592+5248	135.70	+52.61	0.158	779	1.01 ± 0.09	12.14	[246]
2MASX J09041268-3627007	136.05	−36.45	0.060	276	11.64 ± 0.06	12.26	[215]
2MASX J09063400+0451271	136.64	+4.86	0.125	605	1.48 ± 0.09	12.07	[246]
2MASX J09133888-1019196	138.41	−10.32	0.054	249	6.75 ± 0.04	12.00	[215]
2MASX J09141380+0322009	138.56	+3.37	0.145	710	1.09 ± 0.07	12.11	[246]
UGC 05101	143.96	+61.35	0.039	179	11.54 ± 0.81	11.99	[227]
2MASX J09452133+1737533	146.34	+17.63	0.128	621	0.89 ± 0.06	12.08	[227]
2MASX J09530021+8127282	148.25	+81.46	0.156	769	1.43 ± 0.06	12.29	[246]
GALEXASC J095634.42+084306.0	149.14	+8.72	0.129	624	1.44 ± 0.10	12.03	[246]
2MASX J10062631+2725464	151.61	+27.43	0.166	820	1.14 ± 0.13	12.22	[246]

Table C.1: List of ULIRGs used in this work. See text in Appendix C for a detailed description of this table.
(Continued on next page)

NED identification	α [°]	δ [°]	z	d_L [Mpc]	f_{60} [Jy]	$\log_{10}(L_{\mathrm{IR}}/L_{\odot})$	Ref.
GALEXASC J101216.80+464942.9	153.07	+46.83	0.246	1277	1.18 ± 0.07	12.67	[246]
IRAS 10190+1322	155.43	+13.12	0.077	358	3.33 ± 0.27	12.00	[246]
GALEXASC J103638.01+153241.7	159.16	+15.55	0.197	996	0.98 ± 0.06	12.41	[227]
2MASX J10402919+1053178	160.12	+10.89	0.136	663	2.28 ± 0.14	12.26	[246]
IRAS 10485-1447	162.76	−15.06	0.133	646	1.73 ± 0.23	12.17	[246]
2MASX J10522356+4408474	163.10	+44.15	0.092	435	3.53 ± 0.21	12.13	[246]
SDSS J105839.29+382906.5	164.66	+38.49	0.208	1058	0.62 ± 0.05	12.24	[227]
2MASX J10591815+2432343	164.83	+24.54	0.043	197	12.10 ± 0.03	12.02	[215]
FBQS J110214.0+380234	165.56	+38.04	0.158	779	1.29 ± 0.08	12.24	[246]
SDSS J110537.53+311432.1	166.41	+31.24	0.199	1004	1.02 ± 0.07	12.32	[246]
LCRS B110930.3-023804	168.01	−2.91	0.107	509	3.25 ± 0.16	12.20	[246]
B2 1111+32	168.66	+32.69	0.189	950	1.59 ± 0.17	12.58	[246]
AM 1113-270	168.88	−27.27	0.136	662	1.21 ± 0.22	12.05	[246]
GALEXASC J112041.74+160656.7	170.17	+16.12	0.166	823	1.19 ± 0.10	12.24	[246]
IRAS 11223-1244	171.21	−13.02	0.199	1006	1.52 ± 0.11	12.59	[246]
2MASXi J1141220+405950	175.34	+41.00	0.149	729	1.02 ± 0.06	12.18	[246]
2MASX J11531422+1314276	178.31	+13.24	0.127	616	2.58 ± 0.15	12.28	[246]
IRAS 11524+1058	178.76	+10.70	0.179	892	0.82 ± 0.07	12.23	[227]
2MASX J11575822+4540240	179.49	+45.67	0.147	718	0.80 ± 0.06	12.09	[227]
SDSS J120046.83+300414.1	180.20	+30.07	0.223	1143	1.13 ± 0.17	12.56	[246]
2MASX J12022678-0129155	180.61	−1.49	0.151	740	2.41 ± 0.27	12.43	[246]
SDSS J120424.53+192509.7	181.10	+19.42	0.169	837	1.76 ± 0.12	12.44	[246]
2MASX J12054771+1651085	181.45	+16.85	0.218	1113	1.36 ± 0.10	12.57	[246]

Table C.1: List of ULIRGs used in this work. See text in Appendix C for a detailed description of this table.
(Continued on next page)

NED identification	α [°]	δ [°]	z	d_L [Mpc]	f_{60} [Jy]	$\log_{10}(L_{\mathrm{IR}}/L_{\odot})$	Ref.
IRAS 12071-0444	182.44	−5.02	0.128	621	2.46 ± 0.15	12.35	[246]
IRAS 12112+0305	183.44	+2.81	0.073	342	8.18 ± 0.03	12.28	[215]
IRAS 12127-1412	183.83	−14.50	0.133	646	1.54 ± 0.09	12.10	[246]
3C 273	187.28	+2.05	0.158	781	2.06 ± 0.14	12.73	[246]
2MASSi J1238316-074225	189.63	−7.71	0.138	672	1.32 ± 0.09	12.11	[246]
FBQS J124707.7+370536	191.78	+37.09	0.158	779	1.04 ± 0.15	12.06	[246]
SDSS J125400.80+101112.3	193.50	+10.19	0.319	1719	0.71 ± 0.06	12.73	[227]
MRK 0231	194.06	+56.87	0.042	193	30.80 ± 0.04	12.51	[215]
IRAS 13106-0922	198.31	−9.64	0.175	869	1.66 ± 0.20	12.32	[246]
WKK 2031	198.78	−55.16	0.031	139	41.11 ± 0.07	12.26	[215]
[HB89] 1321+058	201.08	+5.62	0.205	1040	1.17 ± 0.08	12.63	[246]
2MASX J13331651-1755106	203.32	−17.92	0.148	727	1.16 ± 0.09	12.21	[246]
IRAS 13335-2612	204.09	−26.46	0.125	604	1.40 ± 0.11	12.06	[246]
2MASX J13362406+3917305	204.10	+39.29	0.179	896	1.11 ± 0.13	12.37	[246]
IRAS 13352+6402	204.21	+63.78	0.237	1221	0.99 ± 0.05	12.54	[227]
MRK 0273	206.18	+55.89	0.038	172	22.51 ± 0.04	12.14	[215]
2MASX J13465107+0747184	206.71	+7.79	0.135	658	1.30 ± 0.14	12.15	[246]
4C +12.50	206.89	+12.29	0.122	587	1.92 ± 0.21	12.28	[246]
IRAS 13454-2956	207.08	−30.20	0.129	625	2.16 ± 0.11	12.21	[246]
2MASX J13484011+5818522	207.17	+58.31	0.158	778	1.27 ± 0.06	12.15	[246]
SDSS J135331.57+042805.2	208.38	+4.47	0.136	662	1.56 ± 0.09	12.27	[246]
2MASX J13561001+2905355	209.04	+29.09	0.108	518	1.83 ± 0.13	12.00	[246]
[HB89] 1402+436	211.16	+43.45	0.323	1746	0.62 ± 0.06	12.96	[227]

Table C.1: List of ULIRGs used in this work. See text in Appendix C for a detailed description of this table.

(Continued on next page)

NED identification	α [°]	δ [°]	z	d_L [Mpc]	f_{60} [Jy]	$\log_{10}(L_{\rm IR}/L_\odot)$	Ref.
IRAS 14054-1958	212.05	−20.21	0.161	796	1.02 ± 0.06	12.12	[246]
2MASXJ 14081899+2904474	212.08	+29.08	0.117	561	1.61 ± 0.16	12.03	[246]
SDSS J140931.25+051131.2	212.38	+5.19	0.264	1385	1.45 ± 0.09	12.76	[246]
2MASX J14144550-0140550	213.69	−1.68	0.150	737	1.39 ± 0.11	12.23	[246]
SDSS J142211.65+075927.9	215.55	+7.99	0.131	635	1.10 ± 0.09	12.00	[246]
2MASX J14223136+2602049	215.63	+26.03	0.159	783	1.49 ± 0.10	12.39	[246]
2MASX J14280106-1603400	217.00	−16.06	0.150	734	1.15 ± 0.13	12.15	[246]
IRAS 14348-1447	219.41	−15.01	0.083	390	6.82 ± 0.04	12.30	[215]
2MASX J14405901-3704322	220.25	−37.08	0.068	315	6.72 ± 0.04	12.15	[215]
2MASX J14410437+5320088	220.27	+53.34	0.105	498	1.95 ± 0.08	12.04	[246]
IRAS 14484-2434	222.85	−24.78	0.148	726	1.02 ± 0.07	12.04	[246]
2MASX J15023198+1421352	225.63	+14.36	0.163	805	1.87 ± 0.09	12.38	[246]
SDSS J150539.53+574307.1	226.41	+57.72	0.151	739	1.02 ± 0.04	12.05	[246]
2MASX J15155520-2009172	228.98	−20.15	0.109	520	1.92 ± 0.13	12.09	[246]
SBS 1517+522	229.78	+52.10	0.139	678	0.78 ± 0.05	12.15	[227]
SDSS J152238.10+333135.8	230.66	+33.53	0.124	601	1.77 ± 0.09	12.18	[246]
2MASX J15244389+2340099	231.18	+23.67	0.139	678	1.30 ± 0.09	12.10	[246]
IRAS 15250+3609	231.75	+35.98	0.055	254	7.10 ± 0.04	12.02	[215]
ARP 220	233.74	+23.50	0.018	81	104.09 ± 0.11	12.21	[215]
IRAS 15462-0450	237.24	−4.99	0.100	474	2.92 ± 0.20	12.16	[246]
2MASX J16114042-0147062	242.92	−1.79	0.134	649	3.61 ± 0.14	12.49	[246]
GALEXASC J161809.36+013922.3	244.54	+1.66	0.132	641	1.13 ± 0.07	12.04	[246]
IRAS 16255+2801	246.91	+27.91	0.134	649	0.89 ± 0.09	12.04	[227]

Table C.1: List of ULIRGs used in this work. See text in Appendix C for a detailed description of this table.
(Continued on next page)

NED identification	α [°]	δ [°]	z	d_L [Mpc]	f_{60} [Jy]	$\log_{10}(L_{\mathrm{IR}}/L_{\odot})$	Ref.
SDSS J163221.37+155145.4	248.09	+15.86	0.242	1252	1.48 ± 0.13	12.63	[246]
GALEXASC J163452.60+462453.1	248.72	+46.41	0.191	961	1.19 ± 0.06	12.35	[246]
SDSS J164658.91+454824.3	251.75	+45.81	0.191	959	0.94 ± 0.07	12.37	[227]
GALEXASC J164801.56+515545.3	252.01	+51.93	0.150	736	1.01 ± 0.05	12.02	[246]
2MASX J16491420+3425096	252.31	+34.42	0.111	534	2.27 ± 0.11	12.11	[246]
SBS 1648+547	252.45	+54.71	0.104	494	2.88 ± 0.12	12.12	[246]
2MASX J16551989+5256348	253.83	+52.94	0.194	975	0.68 ± 0.05	12.25	[227]
2MASX J17034196+5813443	255.92	+58.23	0.106	506	2.43 ± 0.15	12.10	[246]
IRAS 17044+6720	256.12	+67.27	0.135	656	1.28 ± 0.06	12.13	[246]
SDSS J170831.96+402328.0	257.13	+40.39	0.179	894	1.33 ± 0.08	12.30	[246]
2MASX J17185436+5441486	259.73	+54.70	0.147	720	1.36 ± 0.07	12.20	[246]
2MASX J17232194-0017009	260.84	−0.28	0.043	196	32.13 ± 0.06	12.39	[215]
IRAS 17463+5806	266.77	+58.09	0.309	1657	0.65 ± 0.04	12.64	[227]
IRAS 18030+0705	271.36	+7.10	0.146	714	0.84 ± 0.07	12.38	[227]
2MASX J18383543+3552197	279.65	+35.87	0.116	558	2.23 ± 0.13	12.29	[227]
IRAS 18443+7433	280.73	+74.61	0.135	655	2.11 ± 0.10	12.33	[227]
IRAS 18531-4616	284.22	−46.21	0.141	687	1.42 ± 0.13	12.33	[227]
VII Zw 852	284.56	+65.52	0.176	880	0.76 ± 0.04	12.21	[227]
IRAS 18588+3517	285.17	+35.36	0.107	510	1.47 ± 0.10	11.97	[227]
Superantennae	292.84	−72.66	0.062	286	5.48 ± 0.22	12.10	[227]
2MASX J19322229-0400010	293.09	−4.00	0.086	404	7.32 ± 0.11	12.37	[215]
IRAS 19458+0944	297.07	+9.87	0.100	475	3.95 ± 0.40	12.37	[227]
IRAS 19542+1110	299.15	+11.32	0.065	301	6.18 ± 0.04	12.04	[215]

Table C.1: List of ULIRGs used in this work. See text in Appendix C for a detailed description of this table.

(Continued on next page)

NED identification	α [°]	δ [°]	z	d_L [Mpc]	f_{60} [Jy]	$\log_{10}(L_{\mathrm{IR}}/L_{\odot})$	Ref.
GALEXASC J200631.82-153906.5	301.63	−15.65	0.192	966	1.65 ± 0.12	12.58	[227]
2MASX J20112386-0259503	302.85	−3.00	0.106	504	4.70 ± 0.28	12.44	[227]
2MASX J20132950-4147354	303.37	−41.79	0.130	628	5.23 ± 0.31	12.64	[227]
IRAS 20286+1846	307.73	+18.95	0.136	660	0.92 ± 0.07	12.20	[227]
IRAS 20414-1651	311.08	−16.67	0.087	410	4.36 ± 0.26	12.14	[246]
ESO 286-IG 019	314.61	−42.65	0.043	196	12.19 ± 0.03	12.00	[215]
IRAS 21208-0519	320.87	−5.12	0.130	630	1.17 ± 0.07	12.01	[246]
[HB89] 2121-179	321.17	−17.75	0.112	536	1.07 ± 0.09	12.06	[246]
2MASX J21354580-2332359	323.94	−23.54	0.125	604	1.65 ± 0.08	12.09	[246]
GALEXASC J215016.25+051603.4	327.57	+5.27	0.171	850	1.14 ± 0.15	12.24	[246]
2MASX J22074966+3039393	331.96	+30.66	0.127	614	1.87 ± 0.36	12.29	[227]
IRAS 22088-1832	332.89	−18.29	0.170	846	1.73 ± 0.10	12.31	[246]
2MASX J22232890-2700034	335.87	−27.00	0.131	637	1.75 ± 0.10	12.19	[246]
IRAS 22491-1808	342.96	−17.87	0.078	364	5.54 ± 0.04	12.11	[215]
IRAS 22542+0833	344.18	+8.82	0.166	823	1.20 ± 0.19	12.23	[246]
2MASX J23042114+3421477	346.09	+34.36	0.108	516	1.42 ± 0.10	11.99	[227]
2MASX J23083397+0521293	347.14	+5.36	0.173	861	1.15 ± 0.08	12.44	[246]
2MASSi J2315213+260432	348.84	+26.08	0.179	894	1.81 ± 0.14	12.38	[246]
ESO 148-IG 002	348.94	−59.05	0.045	204	10.94 ± 0.04	12.00	[215]
2MASX J23254938+2834208	351.46	+28.57	0.114	547	1.26 ± 0.13	12.00	[246]
2MASX J23255611+1002500	351.48	+10.05	0.128	619	1.56 ± 0.09	12.05	[246]
2MASX J23260362-6910185	351.52	−69.17	0.107	509	3.74 ± 0.15	12.31	[227]
AM 2325-541	352.03	−53.98	0.130	630	2.30 ± 0.18	12.36	[227]

Table C.1: List of ULIRGs used in this work. See text in Appendix C for a detailed description of this table.

(Continued on next page)

NED identification	α [°]	δ [°]	z	d_L [Mpc]	f_{60} [Jy]	$\log_{10}(L_{\mathrm{IR}}/L_{\odot})$	Ref.
2MASX J23351192+2930000	353.80	+29.50	0.107	511	2.10 ± 0.13	12.06	[246]
2MASX J23390127+3621087	354.76	+36.35	0.064	299	7.44 ± 0.05	12.13	[215]
4C +03.60	355.38	+3.29	0.145	709	1.23 ± 0.15	12.09	[246]
2MASX J23522589+2440164	358.11	+24.67	0.212	1079	1.02 ± 0.08	12.40	[246]
IRAS 23515-2917	358.53	−29.02	0.335	1819	0.65 ± 0.06	12.81	[227]

Table C.1: List of ULIRGs used in this work. See text in Appendix C for a detailed description of this table.

Appendix D

Details of the Stacking Analysis

In Section 4.3.1, 10^5 scrambles of the GFU data were performed in order to obtain the background-only TS distribution of the ULIRG stacking analysis. Here we take a look at the distribution of the likelihood fit parameters $(\hat{n}_s, \hat{\gamma})$ of these background-only trials, shown in Figure D.1. Their relation to the TS values is presented in Figure D.2. In these plots, the trials for which $\mathrm{TS} = \hat{n}_s = 0$ are omitted since then $\hat{\gamma}$ becomes degenerate. As expected, a strong correlation is found between TS and $\hat{n}_s$, and $\hat{\gamma}$ is relatively degenerate for low TS and $\hat{n}_s$ values. However, as $\hat{n}_s$ and TS increase, the fitted spectral index converges to a value $\hat{\gamma} \sim 3$. The reason behind this convergence is that the data itself consists mostly of atmospheric background, which follows an $E^{-3.7}$ energy spectrum [344]. The fact that the analysis converges towards a slightly stronger $E^{-3.0}$ spectrum for the background is a consequence of the GFU event selection (Section 3.3), which is biased towards high-energy events (especially in the Southern Hemisphere) as these are more likely to be of astrophysical origin.

When injecting pseudosignal to the trials in Section 4.3.2, it was found that the likelihood fit parameters are biased due to the limited description of the background energy PDF that enters the likelihood. In particular, the bias was discussed using 10^3 trials for each combination of the mean number of injected pseudosignal events $\mu_{\mathrm{inj}} \in \{5, 10, \ldots, 500\}$ and injected spectral index $\gamma_{\mathrm{inj}} \in \{2.0, 3.0\}$. Here, similar bias plots are shown in Figure D.3, Figure D.4, and Figure D.5 for the complementary injected spectral indices $\gamma_{\mathrm{inj}} \in \{1.5, 2.5, 3.5\}$, respectively. Note that for low values of μ_{inj}, and in general for $\gamma_{\mathrm{inj}} = 3.5$, the fitted $\hat{\gamma}$ is driven more by the background value of $\sim$3.0 rather than the injected value of γ_{inj}.

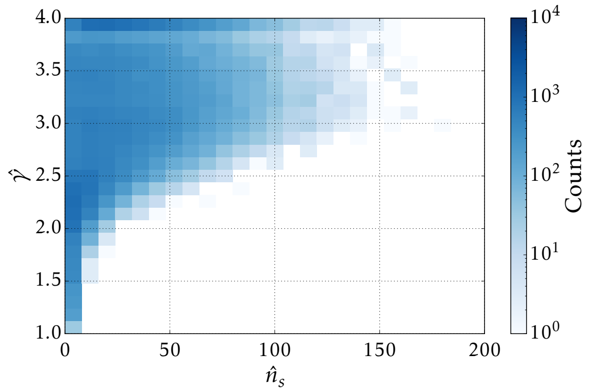

Figure D.1: Distribution of the likelihood fit parameters for nonzero background-only trials. Here, $\hat{n}_s$ and $\hat{\gamma}$ are the fitted number of signal events and spectral index, respectively.

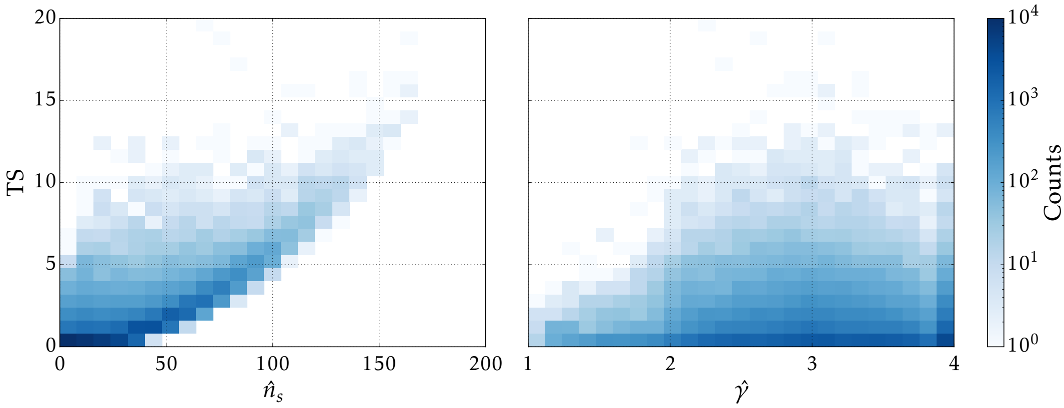

FIGURE D.2: Distribution of the test statistic (TS) as a function of the likelihood fit parameters for nonzero background-only trials. The left and right panels show the TS distribution as a function of the number of signal events, $\hat{n}_s$, and the spectral index, $\hat{\gamma}$, respectively.

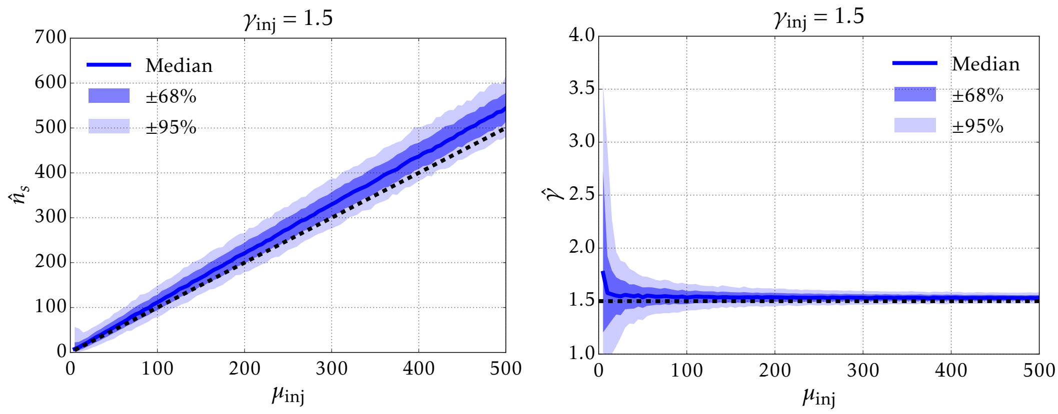

(a) $\hat{n}_s$ bias

(b) $\hat{\gamma}$ bias

FIGURE D.3: Bias plots for the fitted number of signal events, $\hat{n}_s$, and fitted spectral index, $\hat{\gamma}$, shown in Panels (a) and (b), respectively. Both are shown as a function of the mean number of injected signal events, $\mu_{\rm inj}$, for an injected spectral index $\gamma_{\rm inj} = 1.5$. In each plot, the median of the fit parameter is indicated (blue solid line), as well as the ±68% and 95% contours (dark blue and light blue bands, respectively), while the black dashed line represents the ideal non-bias scenario.

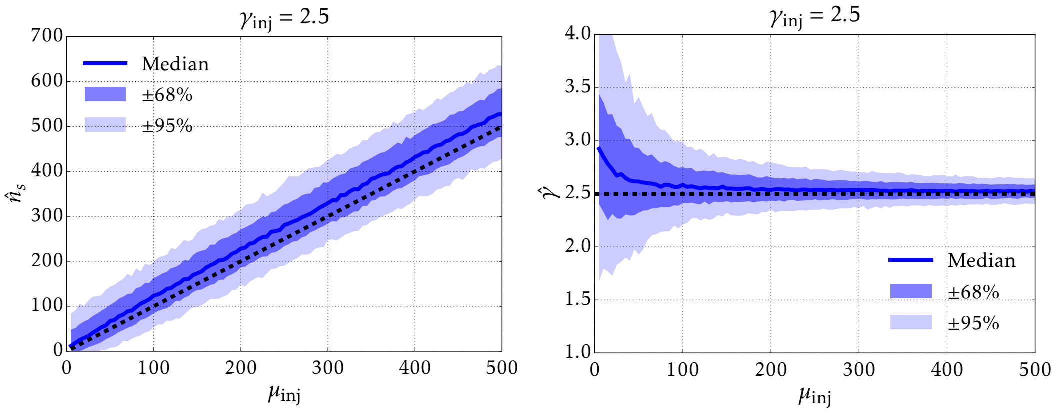

(a) $\hat{n}_s$ bias

(b) $\hat{\gamma}$ bias

FIGURE D.4: Same as Figure D.3 for $\gamma_{inj} = 2.5$.

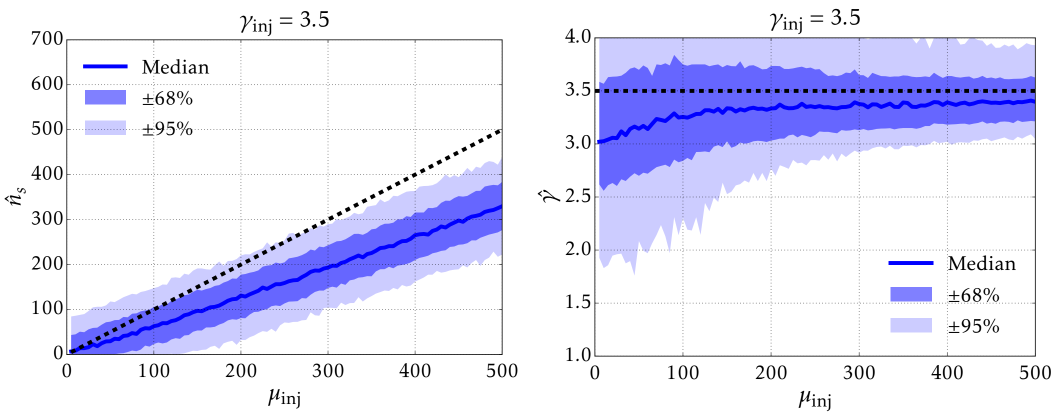

(a) $\hat{n}_s$ bias

(b) $\hat{\gamma}$ bias

FIGURE D.5: Same as Figure D.3 for $\gamma_{inj} = 3.5$.

Appendix E

Constraining the AGN Beam-Dump Model

This Appendix is devoted to the details behind the constraints on the AGN beam-dump model by Vereecken & de Vries [145, 146], discussed in Section 5.3.2. Equation (2.5) is used to calculate the lower limit on the electron-to-proton luminosity ratio,

$$f_e^{90\%} = \chi \frac{\mathcal{Q}_R}{\mathcal{Q}_p^{90\%}}. \tag{E.1}$$

Here, $\mathcal{Q}_p^{90\%}$ is the proton energy generation rate of ULIRGs normalized to the upper limit at 90% CL on the diffuse muon-neutrino flux determined in the analysis, $\Phi^{90\%}_{\nu_\mu+\bar{\nu}_\mu}$. The value of electron-to-radio luminosity ratio is fixed at $\chi = 100$, as done by Vereecken & de Vries.

The radio luminosity density of ULIRGs is given by $\mathcal{Q}_R \equiv n_0 L_R$, where n_0 is the local ULIRG source density, and L_R is the typical radio luminosity of ULIRGs determined using Equation (2.2),

$$\log\left(\frac{L_{1.4\ \mathrm{GHz}}}{\mathrm{W\ Hz^{-1}}}\right) = \log\left(\frac{L_{\mathrm{IR}}^{\mathrm{AGN}}}{3.75\times10^{12}\ \mathrm{W}}\right) - q_{\mathrm{IR}}. \tag{E.2}$$

Here, $L_{\mathrm{IR}}^{\mathrm{AGN}} = 0.1 L_{\mathrm{IR}}$ is the estimated contribution of AGN to the total IR luminosity of ULIRGs, motivated by Figure 2.5. As such, the ULIRG radio luminosity is estimated which is attributed to the AGN. As done by Vereecken & de Vries, the total IR luminosity is fixed to $L_{\mathrm{IR}} = 10^{12} L_\odot$ and the IR-to-radio luminosity ratio to $q_{\mathrm{IR}} = 2.6$. The latter is also motivated by the discussion in Section 2.1.2. Following the authors, the total radio luminosity is related to the differential luminosity at 1.4 GHz as $L_R = 1.4\ \mathrm{GHz} \times L_{1.4\ \mathrm{GHz}}$. Their value of the local ULIRG source density is also adopted, $n_0 = 5\times10^{-7}\ \mathrm{Mpc^{-3}}$, which is consistent with the observations presented in Figure 2.7. After putting everything together, the following estimate for the radio luminosity density of ULIRGs is obtained: $\mathcal{Q}_R = 5.6\times10^{39}\ \mathrm{erg\ Mpc^{-3}\ yr^{-1}}$.

Next, $\mathcal{Q}_p^{90\%} = \mathcal{Q}_\nu^{90\%}/f_\nu$ needs to be determined, using the definition

$$f_\nu \equiv \mathcal{Q}_\nu/\mathcal{Q}_p, \tag{E.3}$$

which is the fraction of the proton energy generation rate that is converted into neutrinos. Following the method of Vereecken & de Vries, the average single-flavor neutrino energy generation rate is determined via Equation (5.9),

$$\begin{aligned}\mathcal{Q}_\nu^{90\%} &= \frac{4\pi H_0}{c\xi_{z_{\max}}} \int_{E_1}^{E_2} E_\nu \Phi^{90\%}_{\nu_\mu+\bar{\nu}_\mu}(E_\nu)\, \mathrm{d}E_\nu \\ &= \frac{4\pi H_0}{c\xi_{z_{\max}}} \Phi_0^{90\%} \int_{E_1}^{E_2} \left(\frac{E_\nu}{E_0}\right)^{1-\gamma} \mathrm{d}E_\nu,\end{aligned} \tag{E.4}$$

with $E_0 = 10$ TeV and $\Phi_0^{90\%}$ taken from the sensitivity line in Figure 4.14. The redshift evolution parameter $\xi_{z_{\max}}$ is determined for a source evolution following that of ULIRGs—see Equation (2.3)—and a maximum redshift $z_{\max} = 4.0$. The energy bounds of the integration were not explicitly mentioned by Vereecken & de Vries, such that they are set to correspond to the energy range of the neutrino prediction line in Figure 2.10, i.e. $E_1 = 100$ MeV and $E_2 = 10$ PeV. Table E.1 lists the inferred values of $\mathcal{Q}_\nu^{90\%}$ for $\gamma = 2.0$ and $\gamma = 2.1$, which are the two spectral indices considered by Vereecken & de Vries for their predictions.

The remaining parameter that needs to be determined is f_ν. The proton energy generation rates reported by Vereecken & de Vries are the starting point, $\mathcal{Q}_p^{\mathrm{HESE}}$, which are fitted to the 6-year diffuse HESE observations of [275]. These values are listed in Table E.2 for all combinations of the spectral index[1] $\gamma \in \{2.0, 2.1\}$ and dust column density $N_H/(10^{25}\ \mathrm{cm}^{-2}) \in \{5, 10\}$ considered by Vereecken & de Vries. The neutrino-flux line[2] Φ_ν^{HESE} of Figure 2.10 is used—as well as the corresponding plots found in [145, 146] for other combinations of γ and N_H—to determine the average single-flavor[3] neutrino generation rate that fits the HESE data, $\mathcal{Q}_\nu^{\mathrm{HESE}}$,

$$\mathcal{Q}_\nu^{\mathrm{HESE}} = \frac{4\pi H_0}{c\xi_{z_{\max}}} \int_{E_1}^{E_2} E_\nu \Phi_\nu^{\mathrm{HESE}}(E_\nu)\, \mathrm{d}E_\nu. \tag{E.5}$$

The resulting values of $f_\nu = \mathcal{Q}_\nu^{\mathrm{HESE}}/\mathcal{Q}_p^{\mathrm{HESE}}$ are listed in Table E.3. The fact that $f_\nu \sim 5\%$ indicates that effectively no protons are able to escape the source environment. They all interact with the extremely dense dust columns, and since ~5% of the proton energy is converted into neutrino energy in hadronic interactions [14], the neutrino energy generation rate of the source is ~5% of the proton energy generation rate. This computation serves as a consistency check of the discussions found in [145, 146]. Finally, using Equations (E.1) and (E.3), the lower limits on the electron-to-proton luminosity ratio are obtained for the different combinations of γ and N_H, which are listed in Table E.4.

Spectral index γ	$\mathcal{Q}_\nu^{90\%}$ [10^{43} erg Mpc^{-3} yr^{-1}]
2.0	1.3
2.1	2.3

TABLE E.1: Upper limits on the average single-flavor neutrino energy generation rate, $\mathcal{Q}_\nu^{90\%}$, of the AGN beam-dump model for two values of the spectral index γ. These values are found by fitting the model of Vereecken & de Vries to the corresponding diffuse-flux upper limits (90% CL) of the ULIRG stacking analysis via Equation (E.4).

[1] The values for $\gamma = 2.1$ were obtained after private communications with M. Vereecken.

[2] Note that Φ_ν^{HESE} does not refer to the HESE measurements, but rather to the prediction of Vereecken & de Vries that fits the HESE observations.

[3] This assumes a flavor ratio $(\nu_e : \nu_\mu : \nu_\tau) = (1 : 1 : 1)$, consistent with IceCube observations (Section 1.2.2).

Q_p^{HESE} [10^{45} erg Mpc^{-3} yr^{-1}]	$\gamma = 2.0$	$\gamma = 2.1$
$N_H = 5 \times 10^{25}$ cm^{-2}	1.6	3.0
$N_H = 10^{26}$ cm^{-2}	1.5	2.8

TABLE E.2: Proton energy generation rates, Q_p^{HESE}, reported by Vereecken & de Vries in [145, 146], that fit their AGN beam-dump model to the diffuse neutrino observations of the 6-year HESE analysis [275]. These are given for different combinations of the spectral index γ and dust column density N_H.

$f_\nu \equiv Q_\nu/Q_p$ [%]	$\gamma = 2.0$	$\gamma = 2.1$
$N_H = 5 \times 10^{25}$ cm^{-2}	4.9	5.3
$N_H = 10^{26}$ cm^{-2}	6.6	6.2

TABLE E.3: Fractions of the neutrino energy generation rate to the proton energy generation rate, f_ν, for different combinations of the spectral index γ and dust column density N_H. These values were determined using the proton generation rates that were fitted to the HESE data, found in Table E.2, and the neutrino energy generation rates found using Equation (E.5) and (the equivalents of) Figure 2.10 (given in [145, 146]).

$f_e^{90\%}$ [‰]	$\gamma = 2.0$	$\gamma = 2.1$
$N_H = 5 \times 10^{25}$ cm^{-2}	2.2	1.3
$N_H = 10^{26}$ cm^{-2}	2.9	1.5

TABLE E.4: Lower limits on the electron-to-proton luminosity ratio, $f_e^{90\%}$, of the ULIRG source population. These limits are given for different combinations of the spectral index γ and dust column density N_H.

Bibliography

[1] R. Abbasi et al. (2022) [IceCube collaboration]. *Search for High-energy Neutrinos from Ultraluminous Infrared Galaxies with IceCube*. The Astrophysical Journal, **926**, 59, doi:10.3847/1538-4357/ac3cb6, arXiv:2107.03149.

[2] P. Correa, K. D. de Vries, and N. van Eijndhoven (2021) [for the IceCube collaboration]. *Investigation of Ultra-Luminous Infrared Galaxies as Obscured High-Energy Neutrino Source Candidates*. Proceedings of Science, **ICRC2019**, 860, doi:10.22323/1.358.0860.

[3] P. Correa, K. D. de Vries, and N. van Eijndhoven (2022) [for the IceCube collaboration]. *IceCube Search for High-Energy Neutrinos from Ultra-Luminous Infrared Galaxies*. Proceedings of Science, **ICRC2021**, 1115, doi:10.22323/1.395.1115.

[4] P. Correa (2022) [for the IceCube collaboration]. *Searching for High-Energy Neutrinos from Ultra-Luminous Infrared Galaxies with IceCube*. Proceedings of Science, **EPS-HEP2021**, 92, doi:10.22323/1.398.0092.

[5] P. Correa (2022) [for the IceCube collaboration]. *Searching for High-Energy Neutrinos from Ultra-Luminous Infrared Galaxies with IceCube*. Journal of Physics: Conference Series, **2156**, 012087, doi:10.1088/1742-6596/2156/1/012087.

[6] P. A. R. Ade et al. (2016) [*Planck* collaboration]. *Planck 2015 results. XIII. Cosmological parameters*. Astronomy & Astrophysics, **594**, A13, doi:10.1051/0004-6361/201525830, arXiv:1502.01589.

[7] M. Aartsen et al. (2013) [IceCube collaboration]. *Evidence for High-Energy Extraterrestrial Neutrinos at the IceCube Detector*. Science, **342**, 1242856, doi:10.1126/science.1242856, arXiv:1311.5238.

[8] M. Aartsen et al. (2014) [IceCube collaboration]. *Observation of High-Energy Astrophysical Neutrinos in Three Years of IceCube Data*. Physical Review Letters, **113**, 101101, doi:10.1103/PhysRevLett.113.101101, arXiv:1405.5303.

[9] B. P. Abbott et al. (2016) [LIGO Scientific and Virgo collaborations]. *Observation of Gravitational Waves from a Binary Black Hole Merger*. Physical Review Letters, **116**, 061102, doi:10.1103/PhysRevLett.116.061102, arXiv:1602.03837.

[10] B. P. Abbott et al. (2017) [LIGO Scientific and Virgo collaborations]. *GW170817: Observation of Gravitational Waves from a Binary Neutron Star Inspiral*. Physical Review Letters, **119**, 161101, doi:10.1103/PhysRevLett.119.161101, arXiv:1710.05832.

[11] B. P. Abbott et al. (2017) [LIGO Scientific collaboration and others]. *Gravitational Waves and Gamma-rays from a Binary Neutron Star Merger:*

GW170817 and GRB 170817A. Astrophysical Journal Letters, **848**, L13, doi:10.3847/2041-8213/aa920c, arXiv:1710.05834.

[12] M. G. Aartsen et al. (2018) [IceCube collaboration and others]. *Multimessenger observations of a flaring blazar coincident with high-energy neutrino IceCube-170922A*. Science, **361**, eaat1378, doi:10.1126/science.aat1378, arXiv:1807.08816.

[13] M. G. Aartsen et al. (2018) [IceCube collaboration]. *Neutrino emission from the direction of the blazar TXS 0506+056 prior to the IceCube-170922A alert*. Science, **361**, 147–151, doi:10.1126/science.aat2890, arXiv:1807.08794.

[14] R. L. Wockman (2022) [Particle Data Group]. *Review of Particle Physics*. Progress of Theoretical and Experimental Physics, **2022**, 083C01, doi:10.1093/ptep/ptac097.

[15] V. F. Hess (1912). *Über Beobachtungen der durchdringenden Strahlung bei sieben Freiballonfahrten*. Physikalische Zeitschrift, **13**, 1084–1091, arXiv:1808.02927.

[16] S. Bravo (for the IceCube collaboration). *Neutrinos and gamma rays, a partnership to explore the extreme universe*. Online, accessed 2 June 2022, URL: https://icecube.wisc.edu/news/research/2016/10/.

[17] S. Ting (2013). *The Alpha Magnetic Spectrometer on the International Space Station*. Nuclear Physics B – Proceeding Supplements, **243–244**, 12–24, doi:10.1016/j.nuclphysbps.2013.09.028.

[18] R. Abbasi et al. (2013) [IceCube collaboration]. *IceTop: The surface component of IceCube*. Nuclear Instruments and Methods in Physics Research A, **700**, 188–220, doi:10.1016/j.nima.2012.10.067, arXiv:1207.6326.

[19] A. Aab et al. (2015) [Pierre Auger collaboration]. *The Pierre Auger Cosmic Ray Observatory*. Nuclear Instruments and Methods in Physics Research A, **798**, 172–213, doi:10.1016/j.nima.2015.06.058, arXiv:1502.01323.

[20] T. Abu-Zayyad et al. (2013) [Telescope Array collaboration]. *The surface detector array of the Telescope Array experiment*. Nuclear Instruments and Methods in Physics Research A, **689**, 87–97, doi:10.1016/j.nima.2012.05.079, arXiv:1201.4964.

[21] M. Malacari et al. (2020). *The First Full-Scale Prototypes of the Fluorescence detector Array of Single-pixel Telescopes*. Astroparticle Physics, **119**, 102430, doi:10.1016/j.astropartphys.2020.102430, arXiv:1911.05285.

[22] T. Huege (2019) [Pierre Auger collaboration]. *Radio detection of cosmic rays with the Auger Engineering Radio Array*. European Physical Journal Web of Conferences, **210**, 05011, doi:10.1051/epjconf/201921005011, arXiv:1905.04986.

[23] T. Winchen et al. (2019). *Cosmic Ray Physics with the LOFAR Radio Telescope*. Journal of Physics: Conference Series, **1181**, 012020, doi:10.1088/1742-6596/1181/1/012020, arXiv:1903.08474.

[24] M. G. Aartsen et al. (2020) [IceCube collaboration]. *Cosmic ray spectrum from 250 TeV to 10 PeV using IceTop*. Physical Review D, **102**, 122001, doi:10.1103/PhysRevD.102.122001, arXiv:2006.05215.

[25] R. U. Abbasi et al. (2018) [Telescope Array collaboration]. *The Cosmic-Ray Energy Spectrum between 2 PeV and 2 EeV Observed with the TALE detector in monocular mode*. The Astrophysical Journal, **865**, 74, doi:10.3847/1538-4357/aada05, arXiv:1803.01288.

[26] A. Aab et al. (2020) [Pierre Auger collaboration]. *Features of the Energy Spectrum of Cosmic Rays above* 2.5×10^{18} *eV Using the Pierre Auger Observatory*. Physical Review Letters, **125**, 121106, doi:10.1103/PhysRevLett.125.121106, arXiv:2008.06488.

[27] P. Abreu et al. (2021) [Pierre Auger collaboration]. *The energy spectrum of cosmic rays beyond the turn-down around* 10^{17} *eV as measured with the surface detector of the Pierre Auger Observatory*. European Physical Journal C, **81**, 966, doi:10.1140/epjc/s10052-021-09700-w, arXiv:2109.13400.

[28] V. Novotný (2022) [for the Pierre Auger collaboration]. *Energy spectrum of cosmic rays measured using the Pierre Auger Observatory*. Proceedings of Science, **ICRC2021**, 324, doi:10.22323/1.395.0324.

[29] D. Ivanov et al. (2022) [for the Telescope Array collaboration]. *Recent measurement of the Telescope Array energy spectrum and observation of the shoulder feature in the Northern Hemisphere*. Proceedings of Science, **ICRC2021**, 341, doi:10.22323/1.395.0341.

[30] Y. Tsunesada (2022) [for the Pierre Auger and Telescope Array collaborations]. *Joint analysis of the energy spectrum of ultra-high-energy cosmic rays measured at the Pierre Auger Observatory and the Telescope Array*. Proceedings of Science, **ICRC2021**, 337, doi:10.22323/1.395.0337.

[31] A. Coleman et al. (2022). *Ultra-High-Energy Cosmic Rays: The Intersection of the Cosmic and Energy Frontiers*, arXiv:2205.05845.

[32] D. J. Bird et al. (1995). *Detection of a cosmic ray with measured energy well beyond the expected spectral cutoff due to cosmic microwave radiation*. The Astrophysical Journal, **441**, 144–150, doi:10.1086/175344, arXiv:astro-ph/9410067.

[33] T. K. Gaisser, R. Engel, and E. Resconi (2016). *Cosmic Rays and Particle Physics*, 2nd edition, Cambridge University Press, ISBN 978-1-13-919219-4, doi:10.1017/CBO9781139192194.

[34] M. S. Longair (2011). *High Energy Astrophysics*, 3rd edition, Cambridge University Press, ISBN 978-0-51-177834-6, doi:10.1017/CBO9780511778346.

[35] K.-H. Kampert (2013). *Ultrahigh-Energy Cosmic Rays: Results and Prospects*. Brazilian Journal of Physics, **43**, 375–382, doi:10.1007/s13538-013-0150-1, arXiv:1305.2363.

[36] T. Abu-Zayyad, et al. (2018). *The Knee and the Second Knee of the Cosmic-Ray Energy Spectrum*, arXiv:1803.07052.

[37] D. Maoz (2016). *Astrophysics in a Nutshell*, 2$^{\text{nd}}$ edition, Princeton University Press, ISBN 978-0-69-116479-3.

[38] A. Aab et al. (2018) [Pierre Auger collaboration]. *An indication of anisotropy in arrival directions of ultra-high-energy cosmic rays through comparison to the flux pattern of extragalactic gamma-ray sources*. Astrophysical Journal Letters, **853**, L29, doi:10.3847/2041-8213/aaa66d, arXiv:1801.06160.

[39] A. García Arámburo, et al. (2021). *Ultrahigh energy cosmic ray deflection by the intergalactic magnetic field*. Physical Review D, **104**, 083017, doi:10.1103/PhysRevD.104.083017, arXiv:2101.07207.

[40] C. Blaksley, et al. (2013). *Ultra-high-energy cosmic ray source statistics in the GZK energy range*. Astronomy & Astrophysics, **552**, A125, doi:10.1051/0004-6361/201220178.

[41] R. Aloisio, V. Berezinsky, and A. Gazizov (2012). *Transition from galactic to extragalactic cosmic rays*. Astroparticle Physics, **39-40**, 129–143, doi:10.1016/j.astropartphys.2012.09.007, arXiv:1211.0494.

[42] A. Haungs (2015). *Cosmic Rays from the Knee to the Ankle*. Physics Procedia, **61**, 425–434, doi:10.1016/j.phpro.2014.12.094, arXiv:1504.01859.

[43] A. Yushkov (2021) [for the Pierre Auger collaboration]. *Mass Composition of Cosmic Rays with Energies above* $10^{17.2}$ *eV from the Hybrid Data of the Pierre Auger Observator*. Proceedings of Science, **ICRC2019**, 482, doi:10.22323/1.358.0482.

[44] Y. Zhezher (2022) [for the Telescope Array collaboration]. *Cosmic-ray mass composition with the TA SD 12-year data*. Proceedings of Science, **ICRC2021**, 300, doi:10.22323/1.395.0300.

[45] E. Guido (2022) [for the Pierre Auger collaboration]. *Combined fit of the energy spectrum and mass composition across the ankle with the data measured at the Pierre Auger Observatory*. Proceedings of Science, **ICRC2021**, 311, doi:10.22323/1.395.0311.

[46] Y. Akrami et al. (2020) [*Planck* collaboration]. *Planck 2018 results. XVI. Isotropy and statistics of the CMB*. Astronomy & Astrophysics, **641**, A7, doi:10.1051/0004-6361/201935201, arXiv:1906.02552.

[47] K. Greisen (1966). *End to the cosmic ray spectrum?* Physical Review Letters, **16**, 748–750, doi:10.1103/PhysRevLett.16.748.

[48] G. T. Zatsepin and V. A. Kuzmin (1966). *Upper limit of the spectrum of cosmic rays*. Journal of Experimental and Theoretical Physics Letters, **4**, 78–80.

[49] E. Khan, et al. (2005). *Photodisintegration of ultra-high-energy cosmic rays revisited*. Astroparticle Physics, **23**, 191–201, doi:10.1016/j.astropartphys.2004.12.007, arXiv:astro-ph/0412109.

[50] A. M. Hillas (1984). *The Origin of Ultrahigh-Energy Cosmic Rays*. Annual Review of Astronomy and Astrophysics, **22**, 425–444, doi:10.1146/annurev.aa.22.090184.002233.

[51] J. Matthews, A. Bell, and K. Blundell (2020). *Particle acceleration in astrophysical jets*. New Astronomy Reviews, **89**, 101543, doi:10.1016/j.newar.2020.101543, arXiv:2003.06587.

[52] M. G. Aartsen et al. (2018) [IceCube collaboration]. *Astrophysical neutrinos and cosmic rays observed by IceCube*. Advances in Space Research, **62**, 2902–2930, doi:10.1016/j.asr.2017.05.030, arXiv:1701.03731.

[53] R. A. Treumann (2009). *Fundamentals of collisionless shocks for astrophysical application, 1. Non-relativistic shocks*. The Astronomy and Astrophysics Review, **17**, 409–535, doi:10.1007/s00159-009-0024-2.

[54] A. M. Bykov and R. A. Treumann (2011). *Fundamentals of collisionless shocks for astrophysical application, 2. Relativistic shocks*. The Astronomy and Astrophysics Review, **19**, 42, doi:10.1007/s00159-011-0042-8, arXiv:1105.3221.

[55] E. Fermi (1949). *On the Origin of the Cosmic Radiation*. Physical Review, **75**, 1169–1174, doi:10.1103/PhysRev.75.1169.

[56] A. R. Bell (1978). *The acceleration of cosmic rays in shock fronts – I*. Monthly Notices of the Royal Astronomical Society, **182**, 147–156, doi:10.1093/mnras/182.2.147.

[57] A. R. Bell (1978). *The acceleration of cosmic rays in shock fronts – II*. Monthly Notices of the Royal Astronomical Society, **182**, 443–455, doi:10.1093/mnras/182.3.443.

[58] J. A. Peacock (1981). *Fermi acceleration by relativistic shock waves*. Monthly Notices of the Royal Astronomical Society, **196**, 135–152, doi:10.1093/mnras/196.2.135.

[59] A. Bykov, et al. (2012). *Particle acceleration in relativistic outflows*. Space Science Reviews, **173**, 309–339, doi:10.1007/s11214-012-9896-y, arXiv:1205.2208.

[60] A. Achterberg, et al. (2001). *Particle acceleration by ultrarelativistic shocks: Theory and simulations*. Monthly Notices of the Royal Astronomical Society, **328**, 393, doi:10.1046/j.1365-8711.2001.04851.x, arXiv:astro-ph/0107530.

[61] M. E. J. Newman (2005). *Power laws, Pareto distributions and Zipf's law*. Contemporary Physics, **46**, 323–351, doi:10.1080/00107510500052444.

[62] K. Koyama, et al. (1995). *Evidence for shock acceleration of high-energy electrons in the supernova remnant SN1006*. Nature, **378**, 255–258, doi:10.1038/378255a0.

[63] S. Hümmer, et al. (2010). *Simplified models for photohadronic interactions in cosmic accelerators*. The Astrophysical Journal, **721**, 630–652, doi:10.1088/0004-637X/721/1/630, arXiv:1002.1310.

[64] N. van Eijndhoven (2008). *On the observability of high-energy neutrinos from gamma-ray bursts*. Astroparticle Physics, **28**, 540–546, doi:10.1016/j.astropartphys.2007.10.002, arXiv:astro-ph/0702029.

[65] K. Mannheim and R. Schlickeiser (1994). *Interactions of Cosmic Ray Nuclei*. Astronomy & Astrophysics, **286**, 983–996, arXiv:astro-ph/9402042.

[66] L. A. Anchordoqui, et al. (2004). *Galactic point sources of TeV antineutrinos*. Physics Letters B, **593**, 42, doi:10.1016/j.physletb.2004.04.054, arXiv:astro-ph/0311002.

[67] S. Hümmer, et al. (2010). *Energy dependent neutrino flavor ratios from cosmic accelerators on the Hillas plot*. Astroparticle Physics, **34**, 205–224, doi:10.1016/j.astropartphys.2010.07.003, arXiv:1007.0006.

[68] C. A. García Canal, S. J. Sciutto, and T. Tarutina (2009). *Testing hadronic interaction packages at cosmic ray energies*. Physical Review D, **79**, 054006, doi:10.1103/PhysRevD.79.054006, arXiv:0903.2409.

[69] E. Waxman and J. N. Bahcall (1999). *High-energy neutrinos from astrophysical sources: An upper bound*. Physical Review D, **59**, 023002, doi:10.1103/PhysRevD.59.023002, arXiv:hep-ph/9807282.

[70] M. Ahlers and F. Halzen (2014). *Pinpointing Extragalactic Neutrino Sources in Light of Recent IceCube Observations*. Physical Review D, **90**, 043005, doi:10.1103/PhysRevD.90.043005, arXiv:1406.2160.

[71] C. Winkler et al. (2003) [INTEGRAL collaboration]. *The INTEGRAL mission*. Astronomy & Astrophysics, **411**, L1–L6, doi:10.1051/0004-6361:20031288.

[72] C. Pittori and M. Tavani (2004) [for the AGILE collaboration]. *Scientific goals and instrument performance of the gamma-ray imaging detector AGILE*. Nuclear Physics B – Proceedings Supplements, **134**, 72–74, doi:10.1016/j.nuclphysbps.2004.08.010.

[73] W. Atwood et al. (2009) [*Fermi*-LAT collaboration]. *The Large Area Telescope on the Fermi Gamma-ray Space Telescope Mission*. The Astrophysical Journal, **697**, 1071–1102, doi:10.1088/0004-637X/697/2/1071, arXiv:0902.1089.

[74] C. Meegan et al. (2009) [*Fermi*-GBM collaboration]. *The Fermi Gamma-Ray Burst Monitor*. The Astrophysical Journal, **702**, 791–804, doi:10.1088/0004-637X/702/1/791, arXiv:0908.0450.

[75] A. J. Smith (2016) [for the HAWC collaboration]. *HAWC: Design, Operation, Reconstruction and Analysis*. Proceedings of Science, **ICRC2015**, 966, doi:10.22323/1.236.0966, arXiv:1508.05826.

[76] Z. Cao et al. (2010) [LHAASO collaboration]. *A future project at Tibet: The large high altitude air shower observatory (LHAASO)*. Chinese Physics C, **34**, 249–252, doi:10.1088/1674-1137/34/2/018.

[77] Z. Cao et al. (2021) [LHAASO collaboration]. *Ultrahigh-energy photons up to 1.4 petaelectronvolts from 12 γ-ray Galactic sources*. Nature, **594**, 33–36, doi:10.1038/s41586-021-03498-z.

[78] W. Hofmann (2003) [for the HESS collaboration]. *Status of the H.E.S.S. Project*. In T. Kajita et al. (eds.), *Proceedings of the 28th International Cosmic Ray Conference*, Universal Academy Press, 2811–2814, URL: http://www-rccn.icrr.u-tokyo.ac.jp/icrc2003/.

[79] J. Aleksic et al. (2012) [MAGIC collaboration]. *Performance of the MAGIC stereo system obtained with Crab Nebula data*. Astroparticle Physics, **35**, 435–448, doi:10.1016/j.astropartphys.2011.11.007, arXiv:1108.1477.

[80] J. Holder et al. (2006) [VERITAS collaboration]. *The first VERITAS telescope*. Astroparticle Physics, **25**, 391–401, doi:10.1016/j.astropartphys.2006.04.002, arXiv:astro-ph/0604119.

[81] A. De Angelis, G. Galanti, and M. Roncadelli (2013). *Transparency of the Universe to gamma rays*. Monthly Notices of the Royal Astronomical Society, **432**, 3245–3249, doi:10.1093/mnras/stt684, arXiv:1302.6460.

[82] A. Franceschini, G. Rodighiero, and M. Vaccari (2008). *The extragalactic optical-infrared background radiations, their time evolution and the cosmic photon-photon opacity*. Astronomy & Astrophysics, **487**, 837, doi:10.1051/0004-6361:200809691, arXiv:0805.1841.

[83] M. Ackermann et al. (2015) [*Fermi*-LAT collaboration]. *The spectrum of isotropic diffuse gamma-ray emission between 100 MeV and 820 GeV*. The Astrophysical Journal, **799**, 86, doi:10.1088/0004-637X/799/1/86, arXiv:1410.3696.

[84] M. Ajello et al. (2017) [*Fermi*-LAT collaboration]. *3FHL: The Third Catalog of Hard Fermi-LAT Sources*. Astrophysical Journal Supplement Series, **232**, 18, doi:10.3847/1538-4365/aa8221, arXiv:1702.00664.

[85] A. A. Abdo et al. (2010) [*Fermi*-LAT collaboration]. *The Spectrum of the Isotropic Diffuse Gamma-Ray Emission Derived From First-Year Fermi Large Area Telescope Data*. Physical Review Letters, **104**, 101101, doi:10.1103/PhysRevLett.104.101101, arXiv:1002.3603.

[86] S. Abdollahi et al. (2020) [*Fermi*-LAT collaboration]. *Fermi Large Area Telescope Fourth Source Catalog*. Astrophysical Journal Supplement Series, **247**, 33, doi:10.3847/1538-4365/ab6bcb, arXiv:1902.10045.

[87] J. Ballet, et al. (2020) [*Fermi*-LAT collaboration]. *Fermi Large Area Telescope Fourth Source Catalog Data Release 2*, arXiv:2005.11208.

[88] M. Ackermann et al. (2011) [*Fermi*-LAT collaboration]. *The Second Catalog of Active Galactic Nuclei Detected by the Fermi Large Area Telescope*. The Astrophysical Journal, **743**, 171, doi:10.1088/0004-637X/743/2/171, arXiv:1108.1420.

[89] M. Ajello et al. (2020) [*Fermi*-LAT collaboration]. *The Fourth Catalog of Active Galactic Nuclei Detected by the Fermi Large Area Telescope*. The Astrophysical Journal, **892**, 105, doi:10.3847/1538-4357/ab791e, arXiv:1905.10771.

[90] M. G. Aartsen et al. (2017) [IceCube collaboration]. *The contribution of Fermi-2LAC blazars to the diffuse TeV-PeV neutrino flux*. The Astrophysical Journal, **835**, 45, doi:10.3847/1538-4357/835/1/45, arXiv:1611.03874.

[91] R. Abbasi et al. (2021) [IceCube collaboration]. *The IceCube high-energy starting event sample: Description and flux characterization with 7.5 years of data*. Physical Review D, **104**, 022002, doi:10.1103/PhysRevD.104.022002, arXiv:2011.03545.

[92] R. Abbasi et al. (2022) [IceCube collaboration]. *Improved Characterization of the Astrophysical Muon–neutrino Flux with 9.5 Years of IceCube Data*. The Astrophysical Journal, **928**, 50, doi:10.3847/1538-4357/ac4d29, arXiv:2111.10299.

[93] M. G. Aartsen et al. (2020) [IceCube collaboration]. *Characteristics of the diffuse astrophysical electron and tau neutrino flux with six years of IceCube high energy cascade data*. Physical Review Letters, **125**, 121104, doi:10.1103/PhysRevLett.125.121104, arXiv:2001.09520.

[94] M. G. Aartsen et al. (2019) [IceCube collaboration]. *Measurements using the inelasticity distribution of multi-TeV neutrino interactions in IceCube*. Physical Review D, **99**, 032004, doi:10.1103/PhysRevD.99.032004, arXiv:1808.07629.

[95] M. G. Aartsen et al. (2015) [IceCube collaboration]. *A combined maximum-likelihood analysis of the high-energy astrophysical neutrino flux measured with IceCube*. The Astrophysical Journal, **809**, 98, doi:10.1088/0004-637X/809/1/98, arXiv:1507.03991.

[96] M. G. Aartsen et al. (2021) [IceCube collaboration]. *Detection of a particle shower at the Glashow resonance with IceCube*. Nature, **591**, 220–224, doi:10.1038/s41586-021-03256-1, arXiv:2110.15051.

[97] M. G. Aartsen et al. (2015) [IceCube collaboration]. *Atmospheric and astrophysical neutrinos above 1 TeV interacting in IceCube*. Physical Review D, **91**, 022001, doi:10.1103/PhysRevD.91.022001, arXiv:1410.1749.

[98] L. A. Fusco and F. Versari (2021) [for the ANTARES collaboration]. *Study of the high-energy diffuse neutrino signal with the ANTARES telecope*. Proceedings of Science, **ICRC2019**, 891, doi:10.22323/1.358.0891.

[99] E. Ganster, R. Naab, and Z. Zhang (2022) [for the IceCube collaboration]. *A Combined Fit of the Diffuse Neutrino Spectrum using IceCube Muon Tracks and Cascades*. Proceedings of Science, **ICRC2021**, 1129, doi:10.22323/1.395.1129.

[100] Y. Fukuda et al. (1998) [Super-Kamiokande collaboration]. *Evidence for oscillation of atmospheric neutrinos*. Physical Review Letters, **81**, 1562–1567, doi:10.1103/PhysRevLett.81.1562, arXiv:hep-ex/9807003.

[101] Y. Farzan and M. Tortola (2018). *Neutrino oscillations and Non-Standard Interactions*. Frontiers in Physics, **6**, 10, doi:10.3389/fphy.2018.00010, arXiv:1710.09360.

[102] I. Esteban, et al. (2020). *The fate of hints: updated global analysis of three-flavor neutrino oscillations*. Journal of High Energy Physics, **09**, 178, doi:10.1007/JHEP09(2020)178, arXiv:2007.14792.

[103] HIDDeν (2021). *NuFIT 5.1*. Online, accessed 17 June 2022, URL: https://nu-fit.org.

[104] J. G. Learned and S. Pakvasa (1995). *Detecting tau-neutrino oscillations at PeV energies*. Astroparticle Physics, **3**, 267–274, doi:10.1016/0927-6505(94)00043-3, arXiv:hep-ph/9405296.

[105] R. Abbasi et al. (2020) [IceCube collaboration]. *Measurement of Astrophysical Tau Neutrinos in IceCube's High-Energy Starting Events*, arXiv:2011.03561.

[106] D. F. Cowen (2007) [IceCube collaboration]. *Tau neutrinos in IceCube*. Journal of Physics: Conference Series, **60**, 227–230, doi:10.1088/1742-6596/60/1/048.

[107] H. Athar, C. S. Kim, and J. Lee (2006). *The intrinsic and oscillated astrophysical neutrino flavor ratios*. Modern Physics Letters A, **21**, 1049–1066, doi:10.1142/S021773230602038X, arXiv:hep-ph/0505017.

[108] J. F. Beacom, et al. (2003). *Measuring flavor ratios of high-energy astrophysical neutrinos*. Physical Review D, **68**, 093005, doi:10.1103/PhysRevD.68.093005, arXiv:hep-ph/0307025.

[109] A. Palladino (2019). *The flavor composition of astrophysical neutrinos after 8 years of IceCube: an indication of neutron decay scenario?* European Physical Journal C, **79**, 500, doi:10.1140/epjc/s10052-019-7018-7, arXiv:1902.08630.

[110] A. Albert et al. (2022) [ANTARES collaboration and others]. *Search for Spatial Correlations of Neutrinos with Ultra-High-Energy Cosmic Rays*, arXiv:2201.07313.

[111] R. Abbasi et al. (2021) [IceCube collaboration]. *Search for GeV neutrino emission during intense gamma-ray solar flares with the IceCube Neutrino Observatory*. Physical Review D, **103**, 102001, doi:10.1103/PhysRevD.103.102001, arXiv:2101.00610.

[112] R. Abbasi et al. (2021) [IceCube collaboration]. *Probing neutrino emission at GeV energies from compact binary mergers with the IceCube Neutrino Observatory*, arXiv:2105.13160.

[113] E. Pinat (2017). *The IceCube Neutrino Observatory: search for extended sources of neutrinos and preliminary study of a communication protocol for its future upgrade*. PhD thesis, Université Libre de Bruxelles, URL: https://iihe.ac.be/research/theses.

[114] R. Abbasi et al. (2021) [IceCube collaboration]. *The IceCube Collaboration – Contributions to the 37th International Cosmic Ray Conference (ICRC2021)*, arXiv:2107.06966.

[115] M. G. Aartsen et al. (2019) [IceCube collaboration]. *The IceCube Collaboration – Contributions to the 36th International Cosmic Ray Conference (ICRC2019)*, arXiv:1907.11699.

[116] M. G. Aartsen et al. (2019) [IceCube collaboration]. *Search for steady point-like sources in the astrophysical muon neutrino flux with 8 years of IceCube data*. European Physical Journal C, **79**, 234, doi:10.1140/epjc/s10052-019-6680-0, arXiv:1811.07979.

[117] R. Abbasi et al. (2021) [IceCube collaboration]. *IceCube Data for Neutrino Point-Source Searches Years 2008-2018*. doi:10.21234/CPKQ-K003, arXiv:2101.09836.

[118] M. Aartsen et al. (2020) [IceCube collaboration]. *Time-Integrated Neutrino Source Searches with 10 Years of IceCube Data*. Physical Review Letters, **124**, 051103, doi:10.1103/PhysRevLett.124.051103, arXiv:1910.08488.

[119] M. Ageron et al. (2011) [ANTARES collaboration]. *ANTARES: the first undersea neutrino telescope*. Nuclear Instruments and Methods in Physics Research A, **656**, 11–38, doi:10.1016/j.nima.2011.06.103, arXiv:1104.1607.

[120] J. Aublin, G. Illuminati, and S. Navas (2021) [for the ANTARES collaboration]. *Searches for point-like sources of cosmic neutrinos with 11 years of ANTARES data*. Proceedings of Science, **ICRC2019**, 920, doi:10.22323/1.358.0920.

[121] M. G. Aartsen et al. (2019) [IceCube collaboration]. *Search for Sources of Astrophysical Neutrinos Using Seven Years of IceCube Cascade Events*. The Astrophysical Journal, **886**, 12, doi:10.3847/1538-4357/ab4ae2, arXiv:1907.06714.

[122] S. Sclafani and M. Hünnefeld (2022) [for the IceCube collaboration]. *A Search for Neutrino Sources with Cascade Events in IceCube*. Proceedings of Science, **ICRC2021**, 1150, doi:10.22323/1.395.1150.

[123] R. Abbasi et al. (2021) [IceCube collaboration]. *Search for neutrino emission from cores of active galactic nuclei*. Physical Review D, **106**, 022005, doi:10.1103/PhysRevD.106.022005, arXiv:2111.10169.

[124] M. Huber (2021) [for the IceCube collaboration]. *Searches for steady neutrino emission from 3FHL blazars using eight years of IceCube data from the Northern hemisphere*. Proceedings of Science, **ICRC2019**, 916, doi:10.22323/1.358.0916.

[125] R. Abbasi et al. (2011) [IceCube collaboration]. *Time-Integrated Searches for Point-like Sources of Neutrinos with the 40-String IceCube Detector*. The Astrophysical Journal, **732**, 18, doi:10.1088/0004-637X/732/1/18, arXiv:1012.2137.

[126] R. Abbasi et al. (2021) [IceCube collaboration]. *Search for Multi-flare Neutrino Emissions in 10 yr of IceCube Data from a Catalog of Sources*. Astrophysical Journal Letters, **920**, L45, doi:10.3847/2041-8213/ac2c7b, arXiv:2109.05818.

[127] M. G. Aartsen et al. (2020) [IceCube collaboration]. *IceCube Search for Neutrinos Coincident with Compact Binary Mergers from LIGO-Virgo's First Gravitational-wave Transient Catalog*. Astrophysical Journal Letters, **898**, L10, doi:10.3847/2041-8213/ab9d24, arXiv:2004.02910.

[128] P. Coppin (2022). *Investigation of the precursor phase of gamma-ray bursts through gamma-ray and high-energy neutrino observations*. PhD thesis, Vrije Universiteit Brussel, URL: https://iihe.ac.be/research/theses.

[129] R. Abbasi et al. (2022) [IceCube collaboration]. *Searches for Neutrinos from Gamma-Ray Bursts using the IceCube Neutrino Observatory*, arXiv:2205.11410.

[130] C. Raab (2022). *Searches for neutrino emission from blazar flares with IceCube*. PhD thesis, Université Libre de Bruxelles, URL: https://iihe.ac.be/research/theses.

[131] R. Stein (2021) [for the IceCube collaboration]. *Search for Neutrinos from Populations of Optical Transients*. Proceedings of Science, **ICRC2019**, 1016, doi:10.22323/1.358.1016.

[132] M. Aartsen et al. (2017) [IceCube collaboration]. *The IceCube Realtime Alert System*. Astroparticle Physics, **92**, 30–41, doi:10.1016/j.astropartphys.2017.05.002, arXiv:1612.06028.

[133] L. Armus et al. (2009). *GOALS: The Great Observatories All-Sky LIRG Survey*. Publications of the Astronomical Society of the Pacific, **121**, 559, doi:10.1086/600092, arXiv:0904.4498.

[134] C. Bellenghi et al. (2022) [for the IceCube collaboration]. *A New Search for Neutrino Point Sources with IceCube*. Proceedings of Science, **ICRC2021**, 1138, doi:10.22323/1.395.1138.

[135] R. Stein et al. (2021). *A tidal disruption event coincident with a high-energy neutrino*. Nature Astronomy, **5**, 510–518, doi:10.1038/s41550-020-01295-8, arXiv:2005.05340.

[136] A. Plavin, et al. (2020). *Observational Evidence for the Origin of High-energy Neutrinos in Parsec-scale Nuclei of Radio-bright Active Galaxies*. The Astrophysical Journal, **894**, 101, doi:10.3847/1538-4357/ab86bd, arXiv:2001.00930.

[137] M. Ajello et al. (2014). *The Cosmic Evolution of Fermi BL Lacertae Objects*. The Astrophysical Journal, **780**, 73, doi:10.1088/0004-637X/780/1/73, arXiv:1310.0006.

[138] C. Guépin, et al. (2018). *Ultra-High Energy Cosmic Rays and Neutrinos from Tidal Disruptions by Massive Black Holes*. Astronomy & Astrophysics, **616**, A179, doi:10.1051/0004-6361/201732392, arXiv:1711.11274.

[139] K. Murase and E. Waxman (2016). *Constraining High-Energy Cosmic Neutrino Sources: Implications and Prospects*. Physical Review D, **94**, 103006, doi:10.1103/PhysRevD.94.103006, arXiv:1607.01601.

[140] K. Murase and M. Fukugita (2019). *Energetics of High-Energy Cosmic Radiations*. Physical Review D, **99**, 063012, doi:10.1103/PhysRevD.99.063012, arXiv:1806.04194.

[141] M. G. Aartsen et al. (2021) [IceCube-Gen2 collaboration]. *IceCube-Gen2: the window to the extreme Universe*. Journal of Physics G, **48**, 060501, doi:10.1088/1361-6471/abbd48, arXiv:2008.04323.

[142] R. Abbasi et al. (2022) [IceCube collaboration]. *Searching for High-Energy Neutrino Emission from Galaxy Clusters with IceCube*, arXiv:2206.02054.

[143] K. Murase, D. Guetta, and M. Ahlers (2016). *Hidden Cosmic-Ray Accelerators as an Origin of TeV-PeV Cosmic Neutrinos*. Physical Review Letters, **116**, 071101, doi:10.1103/PhysRevLett.116.071101, arXiv:1509.00805.

[144] K. Bechtol, et al. (2017). *Evidence against star-forming galaxies as the dominant source of IceCube neutrinos*. The Astrophysical Journal, **836**, 47, doi:10.3847/1538-4357/836/1/47, arXiv:1511.00688.

[145] M. Vereecken (2019). *Aspects of astrophysical particle production and beyond the Standard Model phenomenology*. PhD thesis, Vrije Universiteit Brussel, arXiv:1911.12244.

[146] M. Vereecken and K. D. de Vries (2020). *Obscured pp-channel neutrino sources*, arXiv:2004.03435.

[147] K. Murase, M. Ahlers, and B. C. Lacki (2013). *Testing the Hadronuclear Origin of PeV Neutrinos Observed with IceCube*. Physical Review D, **88**, 121301, doi:10.1103/PhysRevD.88.121301, arXiv:1306.3417.

[148] I. Tamborra, S. Ando, and K. Murase (2014). *Star-forming galaxies as the origin of diffuse high-energy backgrounds: Gamma-ray and neutrino connections, and implications for starburst history*. Journal of Cosmology and Astroparticle Physics, **09**, 043, doi:10.1088/1475-7516/2014/09/043, arXiv:1404.1189.

[149] A. Palladino, et al. (2019). *IceCube Neutrinos from Hadronically Powered Gamma-Ray Galaxies*. Journal of Cosmology and Astroparticle Physics, **09**, 004, doi:10.1088/1475-7516/2019/09/004, arXiv:1812.04685.

[150] A. Ambrosone, et al. (2021). *Starburst galaxies strike back: a multi-messenger analysis*. Monthy Notices of the Royal Astronomical Society, **503**, doi:10.1093/mnras/stab659, arXiv:2011.02483.

[151] M. Ackermann et al. (2022). *High-Energy and Ultra-High-Energy Neutrinos*, arXiv:2203.08096.

[152] S. Adrian-Martinez et al. (2016) [KM3Net collaboration]. *Letter of intent for KM3NeT 2.0*. Journal of Physics G, **43**, 084001, doi:10.1088/0954-3899/43/8/084001, arXiv:1601.07459.

[153] A. D. Avrorin et al. (2017) [Baikal collaboration]. *Baikal-GVD*. EPJ Web of Conferences, **136**, 04007, doi:10.1051/epjconf/201713604007.

[154] M. Agostini et al. (2020) [P-ONE collaboration]. *The Pacific Ocean Neutrino Experiment*. Nature Astronomy, **4**, 913–915, doi:10.1038/s41550-020-1182-4, arXiv:2005.09493.

[155] A. van Vliet, R. Alves Batista, and J. R. Hörandel (2019). *Determining the fraction of cosmic-ray protons at ultrahigh energies with cosmogenic neutrinos*. Physical Review D, **100**, 021302, doi:10.1103/PhysRevD.100.021302, arXiv:1901.01899.

[156] M. S. Muzio, G. R. Farrar, and M. Unger (2022). *Probing the environments surrounding ultrahigh energy cosmic ray accelerators and their implications for astrophysical neutrinos*. Physical Review D, **105**, 023022, doi:10.1103/PhysRevD.105.023022, arXiv:2108.05512.

[157] J. A. Aguilar et al. (2021) [RNO-G collaboration]. *Design and Sensitivity of the Radio Neutrino Observatory in Greenland (RNO-G)*. Journal of Instrumentation, **16**, P03025, doi:10.1088/1748-0221/16/03/P03025, arXiv:2010.12279.

[158] P. Allison et al. (2012) [ARA collaboration]. *Design and Initial Performance of the Askaryan Radio Array Prototype EeV Neutrino Detector at the South Pole*. Astroparticle Physics, **35**, 457–477, doi:10.1016/j.astropartphys.2011.11.010, arXiv:1105.2854.

[159] A. Anker et al. (2020) [ARIANNA collaboration]. *White Paper: ARIANNA-200 high energy neutrino telescope*, arXiv:2004.09841.

[160] O. Scholten et al. (2016). *Measurement of the circular polarization in radio emission from extensive air showers confirms emission mechanisms*. Physical Review D, **94**, 103010, doi:10.1103/PhysRevD.94.103010, arXiv:1611.00758.

[161] K. D. de Vries and S. Prohira (2022) [for the RET collaboration]. *The Radar Echo Telescope for Neutrinos*. Proceedings of Science, **ICRC2021**, 1195, doi:10.22323/1.395.1195.

[162] P. W. Gorham et al. (2009) [ANITA collaboration]. *The Antarctic Impulsive Transient Antenna Ultra-high Energy Neutrino Detector Design, Performance, and Sensitivity for 2006-2007 Balloon Flight*. Astroparticle Physics, **32**, 10–41, doi:10.1016/j.astropartphys.2009.05.003, arXiv:0812.1920.

[163] Q. Abarr et al. (2021) [PUEO collaboration]. *The Payload for Ultrahigh Energy Observations (PUEO): a white paper*. Journal of Instrumentation, **16**, P08035, doi:10.1088/1748-0221/16/08/P08035, arXiv:2010.02892.

[164] S. Wissel et al. (2020). *Prospects for high-elevation radio detection of >100 PeV tau neutrinos*. Journal of Cosmology and Astroparticle Physics, **11**, 065, doi:10.1088/1475-7516/2020/11/065, arXiv:2004.12718.

[165] J. Álvarez-Muñiz et al. (2020) [GRAND collaboration]. *The Giant Radio Array for Neutrino Detection (GRAND): Science and Design*. Science China Physics, Mechanics & Astronomy, **63**, 219501, doi:10.1007/s11433-018-9385-7, arXiv:1810.09994.

[166] J. W. Nam et al. (2016). *Design and implementation of the TAROGE experiment*. International Journal of Modern Physics D, **25**, 1645013, doi:10.1142/S0218271816450139.

[167] S. Wissel (2020). *Expanding the Reach of Tau Neutrino Telescopes with the Beamforming Elevated Array for COsmic Neutrinos (BEACON)*. Bulletin of the American Astronomical Society, **51**, 1148, URL: https://baas.aas.org/pub/2020n7i191.

[168] A. M. Brown et al. (2022). *Trinity: An Imaging Air Cherenkov Telescope to Search for Ultra-High-Energy Neutrinos*. Proceedings of Science, **ICRC2021**, 1179, doi:10.22323/1.395.1179.

[169] A. Romero-Wolf et al. (2020). *An Andean Deep-Valley Detector for High-Energy Tau Neutrinos*. Latin American Strategy Forum for Research Infrastructure, arXiv:2002.06475.

[170] A. V. Olinto et al. (2021) [POEMMA collaboration]. *The POEMMA (Probe of Extreme Multi-Messenger Astrophysics) observatory*. Journal of Cosmology and Astroparticle Physics, **06**, 007, doi:10.1088/1475-7516/2021/06/007, arXiv:2012.07945.

[171] M. G. Aartsen et al. (2018) [IceCube collaboration]. *Differential limit on the extremely-high-energy cosmic neutrino flux in the presence of astrophysical background from nine years of IceCube data*. Physical Review D, **98**, 062003, doi:10.1103/PhysRevD.98.062003, arXiv:1807.01820.

[172] P. Abreu et al. (2013) [Pierre Auger collaboration]. *Ultrahigh Energy Neutrinos at the Pierre Auger Observatory*. Advances in High Energy Physics, **2013**, 708680, doi:10.1155/2013/708680, arXiv:1304.1630.

[173] P. W. Gorham et al. (2019) [ANITA collaboration]. *Constraints on the ultrahigh-energy cosmic neutrino flux from the fourth flight of ANITA*. Physical Review D, **99**, 122001, doi:10.1103/PhysRevD.99.122001, arXiv:1902.04005.

[174] A. Anker et al. (2020) [ARIANNA collaboration]. *A search for cosmogenic neutrinos with the ARIANNA test bed using 4.5 years of data*. Journal of Cosmology and Astroparticle Physics, **03**, 053, doi:10.1088/1475-7516/2020/03/053, arXiv:1909.00840.

[175] P. Allison et al. (2020) [ARA collaboration]. *Constraints on the diffuse flux of ultrahigh energy neutrinos from four years of Askaryan Radio Array data in two stations*. Physical Review D, **102**, 043021, doi:10.1103/PhysRevD.102.043021, arXiv:1912.00987.

[176] G. W. Krampah et al. (2022). *The NuMoon Experiment: Lunar Detection of Cosmic Rays and Neutrinos with LOFAR*. Proceedings of Science, **ICRC2021**, 1148, doi:10.22323/1.395.1148.

[177] I. Esteban, S. Prohira, and J. F. Beacom (2022). *Detector Requirements for Model-Independent Measurements of Ultrahigh Energy Neutrino Cross Sections*. Physical Review D, **106**, 023021, doi:10.1103/PhysRevD.106.023021, arXiv:2205.09763.

[178] R. F. Webbink and W. Q. Jeffers (1969). *Infrared Astronomy*. Space Science Reviews, **10**, 191–216, doi:10.1007/BF00212684.

[179] H. J. Walker (2000). *A brief history of infrared astronomy*. Astronomy & Geophysics, **41**, 10, doi:10.1046/j.1468-4004.2000.41510.x.

[180] G. H. Rieke and F. J. Low (1972). *Infrared Photometry of Extragalactic Sources*. The Astrophysical Journal, **176**, L95, doi:10.1086/181031.

[181] S. van den Bergh (1999). *The local group of galaxies*. The Astronomy and Astrophysics Review, **9**, 273–318, doi:10.1007/s001590050019.

[182] G. Neugebauer et al. (1984). *The Infrared Astronomical Satellite (IRAS) mission*. Astrophysical Journal Letters, **278**, L1–L6, doi:10.1086/184209.

[183] C. J. Lonsdale, D. Farrah, and H. E. Smith (2006). *Ultraluminous Infrared Galaxies*. In J. W. Mason (ed.), *Astrophysics Update 2*, Springer Berlin Heidelberg, 285–336, doi:10.1007/3-540-30313-8_9.

[184] S. G. Kleinmann et al. (1988). *The Properties and Environment of the Giant, Infrared-Luminous Galaxy IRAS 09104+4109*. The Astrophysical Journal, **328**, 161, doi:10.1086/166276.

[185] M. F. Kessler et al. (1996). *The Infrared Space Observatory (ISO) mission*. Astronomy & Astrophysics, **315**, L27, URL: https://ui.adsabs.harvard.edu/abs/1996A%26A...315L..27K/.

[186] M. W. Werner et al. (2004). *The Spitzer Space Telescope mission*. The Astrophysical Journal Supplement Series, **154**, 1–9, doi:10.1086/422992, arXiv:astro-ph/0406223.

[187] H. Murakami et al. (2007). *The Infrared Astronomical Mission AKARI*. Publications of the Astronomical Society of Japan, **59**, 369–376, doi:10.1093/pasj/59.sp2.S369, arXiv:0708.1796.

[188] G. L. Pilbratt et al. (2010). *Herschel Space Observatory - An ESA facility for far-infrared and submillimetre astronomy*. Astronomy & Astrophysics, **518**, L1, doi:10.1051/0004-6361/201014759, arXiv:1005.5331.

[189] E. L. Wright et al. (2010). *The Wide-field Infrared Survey Explorer (WISE): Mission Description and Initial On-orbit Performance*. The Astronomical Journal, **140**, 1868, doi:10.1088/0004-6256/140/6/1868, arXiv:1008.0031.

[190] C.-W. Tsai et al. (2015). *The Most Luminous Galaxies Discovered by WISE*. The Astrophysical Journal, **805**, 90, doi:10.1088/0004-637X/805/2/90, arXiv:1410.1751.

[191] J. P. Gardner et al. (2006). *The James Webb Space Telescope*. Space Science Reviews, **123**, 485, doi:10.1007/s11214-006-8315-7, arXiv:astro-ph/0606175.

[192] M. Rowan-Robinson (2000). *Hyperluminous infrared galaxies*. Monthly Notices of the Royal Astronomical Society, **316**, 885, doi:10.1046/j.1365-8711.2000.03588.x, arXiv:astro-ph/9912286.

[193] NASA/IPAC Extragalactic Database (NED), URL: https://ned.ipac.caltech.edu/.

[194] European Space Agency (ESA). *Arp 220*. Online, accessed 12 July 2021, URL: https://esahubble.org/images/heic0810bf/.

[195] National Aeronautics and Space Administration (NASA). *Hubble interacting galaxy Mrk 273*. Online, accessed 12 July 2021, URL: https://hubblesite.org/contents/media/images/2008/16/2307-Image.html.

[196] M. García-Marín et al. (2009). *Integral field optical spectroscopy of a representative sample of ULIRGs: I. The Data*. Astronomy & Astrophysics, **505**, 1319–1343, doi:10.1051/0004-6361/200811324, arXiv:0907.2408.

[197] C.-W. Hung et al. (2014). *A comparison of the morphological properties between local and $z \sim 1$ infrared luminous galaxies. Are local and high-z (U)LIRGs different?* The Astrophysical Journal, **971**, 63, doi:10.1088/0004-637X/791/1/63, arXiv:1406.4509.

[198] K. L. Larson et al. (2016). *Morphology and Molecular Gas Fractions of Local Luminous Infrared Galaxies as a Function of Infrared Luminosity and Merger Stage*. The Astrophysical Journal, **825**, 128, doi:10.3847/0004-637X/825/2/128, arXiv:1605.05417.

[199] D. B. Sanders, et al. (1988). *Ultraluminous infrared galaxies and the origin of quasars*. The Astrophysical Journal, **325**, 74–91, doi:10.1086/165983.

[200] Cosmic Assembly Near-infrared Deep Extragalactic Legacy Survey (CANDELS). *The Curious History of Luminous Infrared Galaxies*. Online, accessed 12 July 2021, URL: http://candels-collaboration.blogspot.com/2012/07/luminous-infrared-galaxies.html.

[201] D. L. Clements et al. (2017). *HERUS: the far-IR/submm spectral energy distributions of local ULIRGs and photometric atlas*. Monthly Notices of the Royal Astronomical Society, **475**, 2097–2121, doi:10.1093/mnras/stx3227, arXiv:1712.04843.

[202] T. P. Robitaille and B. A. Whitney (2010). *The present-day star formation rate of the Milky-Way determined from Spitzer detected young stellar objects*. Astrophysical Journal Letters, **710**, L11–L15, doi:10.1088/2041-8205/710/1/L11, arXiv:1001.3672.

[203] G. Rieke et al. (2009). *Determining Star Formation Rates for Infrared Galaxies*. The Astrophysical Journal, **692**, 556–573, doi:10.1088/0004-637X/692/1/556, arXiv:0810.4150.

[204] E. da Cunha et al. (2010). *Exploring the physical properties of local star-forming ULIRGs from the ultraviolet to the infrared*. Astronomy & Astrophysics, **523**, A78, doi:10.1051/0004-6361/201014498, arXiv:1008.2000.

[205] J. Piqueras López et al. (2016). *VLT-SINFONI sub-kpc study of the star formation in local LIRGs and ULIRGs - Analysis of the global Σ_{SFR} structure and characterisation of individual star-forming clumps*. Astronomy & Astrophysics, **590**, A67, doi:10.1051/0004-6361/201527671, arXiv:1603.03707.

[206] R. C. Kennicutt, Jr. (1998). *The Global Schmidt Law in Star Forming Galaxies*. The Astrophysical Journal, **498**, 541, doi:10.1086/305588, arXiv:astro-ph/9712213.

[207] M. Schmidt (1959). *The Rate of Star Formation*. The Astrophysical Journal, **129**, 243, doi:10.1086/146614.

[208] R. C. Kennicutt, Jr. (1989). *The Star Formation Law in Galactic Disks*. The Astrophysical Journal, **344**, 685, doi:10.1086/167834.

[209] N. M. Nagar et al. (2003). *The AGN content of ultraluminous IR galaxies: High resolution VLA imaging of the IRAS 1Jy ULIRG sample*. Astronomy & Astrophysics, **409**, 115–122, doi:10.1051/0004-6361:20031069, arXiv:astro-ph/0309298.

[210] D. L. Clements, L. Dunne, and S. A. Eales (2010). *The Submillimetre Properties of Ultraluminous Infrared Galaxies*. Monthy Notices of the Royal Astronomical Society, **403**, 274, doi:10.1111/j.1365-2966.2009.16064.x, arXiv:0911.3593.

[211] D. Fadda et al. (2010). *Ultra-deep Spitzer Mid-Infrared Spectroscopy of LIRGs and ULIRGs at $z \sim 1$–2*. The Astrophysical Journal, **719**, 425–450, doi:10.1088/0004-637X/719/1/425, arXiv:1006.2873.

[212] K. Akiyama et al. (2022) [Event Horizon Telescope collaboration]. *First Sagittarius A* Event Horizon Telescope Results. I. The Shadow of the Supermassive*

Black Hole in the Center of the Milky Way. Astrophysical Journal Letters, **930**, L12, doi:10.3847/2041-8213/ac6674.

[213] M. Su, T. R. Slatyer, and D. P. Finkbeiner (2010). *Giant Gamma-ray Bubbles from Fermi-LAT: AGN Activity or Bipolar Galactic Wind?* The Astrophysical Journal, **724**, 1044–1082, doi:10.1088/0004-637X/724/2/1044, arXiv:1005.5480.

[214] H. Netzer (2015). *Revisiting the Unified Model of Active Galactic Nuclei*. Annual Review of Astrononomy and Astrophysics, **53**, 365–408, doi:10.1146/annurev-astro-082214-122302, arXiv:1505.00811.

[215] D. B. Sanders, et al. (2003). *The IRAS Revised Bright Galaxy Sample (RBGS)*. The Astrophysical Journal, **126**, 1607, doi:10.1086/376841, arXiv:astro-ph/0306263.

[216] R. C. Hickox and D. M. Alexander (2018). *Obscured Active Galactic Nuclei*. Annual Review of Astrononomy and Astrophysics, **56**, 625–671, doi:10.1146/annurev-astro-081817-051803, arXiv:1806.04680.

[217] National Radio Astronomy Observatory (NRAO). *A Unified AGN Model*. Online, accessed 5 May 2022, URL: https://public.nrao.edu/gallery/a-unified-agn-model/.

[218] S. Veilleux et al. (1995). *Optical Spectroscopy of Luminous Infrared Galaxies. II. Analysis of the Nuclear and Long-Slit Data*. Astrophysical Journal Supplement Series, **98**, 171, doi:10.1086/192158.

[219] D. C. Kim, S. Veilleux, and D. B. Sanders (1998). *The IRAS 1-Jy survey of ultraluminous infrared galaxies. 2. Optical spectroscopy*. The Astrophysical Journal, **508**, 627, doi:10.1086/306409, arXiv:astro-ph/9806149.

[220] S. Veilleux, D. C. Kim, and D. B. Sanders (1999). *Optical spectroscopy of the IRAS 1-Jy sample of ultraluminous infrared galaxies*. The Astrophysical Journal, **522**, 113–138, doi:10.1086/307634, arXiv:astro-ph/9904149.

[221] T. Goto (2005). *Optical properties of 4248 IRAS galaxies*. Monthy Notices of the Royal Astronomical Society, **360**, 322–339, doi:10.1111/j.1365-2966.2005.09036.x, arXiv:astro-ph/0504080.

[222] M. Imanishi et al. (2008). *Systematic infrared 2.5-5 micron spectroscopy of nearby ultraluminous infrared galaxies with AKARI*. Publications of the Astronomical Society of Japan, **60**, 489, doi:10.1093/pasj/60.sp2.S489, arXiv:0808.0363.

[223] L. G. Hou, X.-B. Wu, and J. L. Han (2009). *Ultra-luminous Infrared galaxies in SDSS Data Release 6*. The Astrophysical Journal, **704**, 789–802, doi:10.1088/0004-637X/704/1/789, arXiv:0908.2297.

[224] D. Farrah et al. (2003). *Starburst and AGN activity in ultraluminous infrared galaxies*. Monthy Notices of the Royal Astronomical Society, **343**, 585, doi:10.1046/j.1365-8711.2003.06696.x, arXiv:astro-ph/0304154.

[225] S. Veilleux et al. (2009). *Spitzer Quasar and ULIRG Evolution Study (QUEST). IV. Comparison of 1 Jy Ultraluminous Infrared Galaxies with Palomar-Green Quasars*. Astrophysical Journal Supplement Series, **182**, 628–666, doi:10.1088/0067-0049/182/2/628, arXiv:0905.1577.

[226] M. Imanishi, R. Maiolino, and T. Nakagawa (2010). *Spitzer Infrared Low-Resolution Spectroscopic Study of Buried AGNs in a Complete Sample of Nearby Ultraluminous Infrared Galaxies*. The Astrophysical Journal, **709**, 801–815, doi:10.1088/0004-637X/709/2/801, arXiv:0912.2748.

[227] E. Nardini, et al. (2010). *The role of nuclear activity as the power source of ultraluminous infrared galaxies*. Monthy Notices of the Royal Astronomical Society, **405**, 2505, doi:10.1111/j.1365-2966.2010.16618.x, arXiv:1003.0858.

[228] T.-T. Yuan, L. J. Kewley, and D. B. Sanders (2010). *The Role of Starburst-AGN composites in Luminous Infrared Galaxy Mergers: Insights from the New Optical Classification Scheme*. The Astrophysical Journal, **709**, 884–911, doi:10.1088/0004-637X/709/2/884, arXiv:0911.3728.

[229] E. Nardini and G. Risaliti (2011). *Compton-thick active galactic nuclei inside local ultraluminous infrared galaxies*. Monthy Notices of the Royal Astronomical Society, **415**, 619, doi:10.1111/j.1365-2966.2011.18732.x, arXiv:1103.3212.

[230] A. Comastri (2004). *Compton thick AGN: The Dark side of the X-ray background*. Astrophysics and Space Science Library, **308**, 245, doi:10.1007/978-1-4020-2471-9_8, arXiv:astro-ph/0403693.

[231] C. D. Wilson et al. (2014). *Extreme Dust Disks in Arp 220 as Revealed by ALMA*. Astrophysical Journal Letters, **789**, L36, doi:10.1088/2041-8205/789/2/L36, arXiv:1406.4530.

[232] A. Franceschini et al. (2003). *An XMM-Newton Hard X-ray Survey of ULIRGs*. Monthly Notices of the Royal Astronomical Society, **343**, 1181, doi:10.1046/j.1365-8711.2003.06744.x, arXiv:astro-ph/0304529.

[233] K. Iwasawa et al. (2012). *Fe K emission from active galaxies in the COSMOS field*. Astronomy & Astrophysics, **537**, A86, doi:10.1051/0004-6361/201118203, arXiv:1111.2447.

[234] M. S. Clemens, et al. (2008). *Modeling the spectral energy distribution of ULIRGs I: the radio spectra*. Astronomy & Astrophysics, **477**, 95, doi:10.1051/0004-6361:20077224, arXiv:0708.0149.

[235] P. Kornecki, et al. (2022). *Exploring the physics behind the non-thermal emission from star-forming galaxies detected in gamma rays*. Astronomy & Astrophysics, **657**, A49, doi:10.1051/0004-6361/202141295, arXiv:2107.00823.

[236] T. A. Thompson, et al. (2006). *Magnetic fields in starburst galaxies and the origin of the FIR-radio correlation*. The Astrophysical Journal, **645**, 186–198, arXiv:astro-ph/0601626.

[237] W. Ishibashi and T. J. L. Courvoisier (2011). *Synchrotron radio emission in radio-quiet AGNs*. Astronomy & Astrophysics, **525**, A118, doi:10.1051/0004-6361/201014987, arXiv:1010.5591.

[238] T. J. Hayashi, Y. Hagiwara, and M. Imanishi (2021). *Radio properties of 10 nearby ultraluminous infrared galaxies with signatures of luminous buried active galactic nuclei*. Monthly Notices of the Royal Astronomical Society, **504**, 2675–2686, doi:10.1093/mnras/stab1084, arXiv:2101.12058.

[239] F.-K. Peng, et al. (2016). *First detection of GeV emission from an ultraluminous infrared galaxy: Arp 220 as seen with the Fermi Large Area Telescope*. Astrophysical Journal Letters, **821**, L20, doi:10.3847/2041-8205/821/2/L20, arXiv:1603.06355.

[240] G. Helou, B. T. Soifer, and M. Rowan-Robinson (1985). *Thermal infrared and nonthermal radio – Remarkable correlation in disks of galaxies*. Astrophysical Journal Letters, **298**, L7–L11, doi:10.1086/184556.

[241] M. T. Sargent et al. (2010). *No Evolution in the IR-Radio Relation for IR-Luminous Galaxies at z<2 in the COSMOS Field*. Astrophysical Journal Letters, **714**, L190, doi:10.1088/2041-8205/714/2/L190, arXiv:1003.4271.

[242] B. Magnelli et al. (2015). *The far-infrared/radio correlation and radio spectral index of galaxies in the SFR-M_* plane up to $z \sim 2$*. Astronomy & Astrophysics, **573**, A45, doi:10.1051/0004-6361/201424937, arXiv:1410.7412.

[243] M. Ajello, et al. (2020). *The γ-Ray Emission of Star-forming Galaxies*. The Astrophysical Journal, **894**, 88, doi:10.3847/1538-4357/ab86a6, arXiv:2003.05493.

[244] J. Wu et al. (2012). *Submillimeter Follow-up of WISE-Selected Hyperluminous Galaxies*. The Astrophysical Journal, **756**, 96, doi:10.1088/0004-637X/756/1/96, arXiv:1208.5518.

[245] S. Frey et al. (2016). *Four hot DOGs in the microwave*. Monthly Notices of the Royal Astronomical Society, **455**, 2058–2065, doi:10.1093/mnras/stv2399, arXiv:1510.04179.

[246] D.-C. Kim and D. B. Sanders (1998). *The IRAS 1-Jy Survey of Ultraluminous Infrared Galaxies. 1. The Sample and luminosity function*. The Astrophysical Journal Supplement Series, **119**, 41–58, doi:10.1086/313148, arXiv:astro-ph/9806148.

[247] A. W. Blain, et al. (1999). *The history of star formation in dusty galaxies*. Monthly Notices of the Royal Astronomical Society, **302**, 632–648, doi:10.1046/j.1365-8711.1999.02178.x, arXiv:astro-ph/9806062.

[248] R. Genzel and C. J. Cesarsky (2000). *Extragalactic results from the infrared space observatory*. Annual Review of Astronomy and Astrophysics, **38**, 761–814, doi:10.1146/annurev.astro.38.1.761, arXiv:astro-ph/0002184.

[249] S. C. Chapman, et al. (2005). *A Redshift Survey of the Submillimeter Galaxy Population*. The Astrophysical Journal, **622**, 772–796, doi:10.1086/428082, arXiv:astro-ph/0412573.

[250] N. A. Reddy, et al. (2008). *Multi-Wavelength Constraints on the Cosmic Star Formation History from Spectroscopy: The Rest-Frame UV, H-alpha, and Infrared Luminosity Functions at Redshifts* $1.9 \lesssim z \lesssim 3.4$. The Astrophysical Journal Supplement Series, **175**, 48, doi:10.1086/521105, arXiv:0706.4091.

[251] L. L. Cowie, et al. (2004). *The Evolution of the Ultraluminous Infrared Galaxy Population from Redshift 0 to 1.5*. Astrophysical Journal Letters, **603**, L69–L72, doi:10.1086/383198, arXiv:astro-ph/0402235.

[252] P. F. Hopkins, et al. (2006). *A Unified, Merger-driven Model of the Origin of Starbursts, Quasars, the Cosmic X-Ray Background, Supermassive Black Holes, and Galaxy Spheroids*. The Astrophysical Journal Supplement Series, **163**, 1–49, doi:10.1086/499298, arXiv:astro-ph/0506398.

[253] E. Le Floc'h et al. (2005). *Infrared luminosity functions from the Chandra Deep Field South: The Spitzer view on the history of dusty star formation at* $0 < z < 1$. The Astrophysical Journal, **632**, 169–190, doi:10.1086/432789, arXiv:astro-ph/0506462.

[254] K. I. Caputi, et al. (2007). *The infrared luminosity function of galaxies at redshifts* $z = 1$ *and* $z = 2$ *in the GOODS fields*. The Astrophysical Journal, **660**, 97–116, doi:10.1086/512667, arXiv:astro-ph/0701283.

[255] B. Magnelli, et al. (2009). *The* $0.4 < z < 1.3$ *star formation history of the Universe as viewed in the far-infrared*. Astronomy & Astrophysics, **496**, 57, doi:10.1051/0004-6361:200811443, arXiv:0901.1543.

[256] T. Goto et al. (2011). *Luminosity Functions of Local Infrared Galaxies with AKARI: Implications to the Cosmic Star Formation History and AGN Evolution*. Monthly Notices of the Royal Astronomical Society, **410**, 573, doi:10.1111/j.1365-2966.2010.17466.x, arXiv:1008.0859.

[257] C. M. Casey et al. (2012). *A Redshift Survey of Herschel Far-Infrared Selected Starbursts and Implications for Obscured Star Formation*. The Astrophysical Journal, **761**, 140, doi:10.1088/0004-637X/761/2/140, arXiv:1210.4928.

[258] B. Magnelli, et al. (2011). *Evolution of the dusty infrared luminosity function from* $z = 0$ *to* $z = 2.3$ *using observations from Spitzer*. Astronomy & Astrophysics, **528**, A35, doi:10.1051/0004-6361/200913941, arXiv:1101.2467.

[259] C. Gruppioni et al. (2013). *The Herschel PEP/HerMES Luminosity Function. I: Probing the Evolution of PACS selected Galaxies to* $z \sim 4$. Monthly Notices of the Royal Astronomical Society, **432**, 23, doi:10.1093/mnras/stt308, arXiv:1302.5209.

[260] A. M. Hopkins and J. F. Beacom (2006). *On the normalisation of the cosmic star formation history*. The Astrophysical Journal, **651**, 142–154, doi:10.1086/506610, arXiv:astro-ph/0601463.

[261] H. Yüksel, et al. (2008). *Revealing the High-Redshift Star Formation Rate with Gamma-Ray Bursts*. Astrophysical Journal Letters, **683**, L5–L8, doi:10.1086/591449, arXiv:0804.4008.

[262] P. Madau and M. Dickinson (2014). *Cosmic Star Formation History*. Annual Review of Astronomy and Astrophysics, **52**, 415–486, doi:10.1146/annurev-astro-081811-125615, arXiv:1403.0007.

[263] Y. Merckx (2021). *Modeling of Neutrino Production in Starburst-Driven (Ultra)-Luminous Infrared Galaxies*. MSc thesis, Vrije Universiteit Brussel, URL: https://iihe.ac.be/research/theses.

[264] R. Budnik, et al. (2008). *Cosmic rays from trans-relativistic supernovae*. The Astrophysical Journal, **673**, 928–933, doi:10.1086/524923, arXiv:0705.0041.

[265] Y.-Z. Fan (2008). *Cosmic ray protons in $10^{16} - 10^{18.5}$ eV: Stochastic gyroresonant acceleration in hypernova shocks?* Monthy Notices of the Royal Astronomical Society, **389**, 1306, doi:10.1111/j.1365-2966.2008.13632.x, arXiv:0807.0029.

[266] E. Peretti, et al. (2019). *Cosmic ray transport and radiative processes in nuclei of starburst galaxies*. Monthy Notices of the Royal Astronomical Society, **487**, 168–180, doi:10.1093/mnras/stz1161, arXiv:1812.01996.

[267] A. Loeb and E. Waxman (2006). *The Cumulative background of high energy neutrinos from starburst galaxies*. Journal of Cosmology and Astroparticle Physics, **05**, 003, doi:10.1088/1475-7516/2006/05/003, arXiv:astro-ph/0601695.

[268] A. L. Kyriacou (2018). *Starbursts and Star-forming Galaxies as the sources of Cosmic Neutrinos measured by the IceCube Neutrino Observatory*. MPhil thesis, Adelaide University, URL: https://digital.library.adelaide.edu.au/dspace/handle/2440/113620.

[269] C. Lunardini, et al. (2019). *Are starburst galaxies a common source of high energy neutrinos and cosmic rays?* Journal of Cosmology and Astroparticle Physics, **10**, 073, doi:10.1088/1475-7516/2019/10/073, arXiv:1902.09663.

[270] E. Peretti, et al. (2020). *Contribution of starburst nuclei to the diffuse gamma-ray and neutrino flux*. Monthy Notices of the Royal Astronomical Society, **493**, 5880–5891, doi:10.1093/mnras/staa698, arXiv:1911.06163.

[271] D. Downes and P. M. Solomon (1998). *Rotating nuclear rings and extreme starbursts in ultraluminous galaxies*. The Astrophysical Journal, **507**, 615, doi:10.1086/306339, arXiv:astro-ph/9806377.

[272] H.-N. He, et al. (2013). *Diffuse PeV neutrino emission from ultraluminous infrared galaxies*. Physical Review D, **87**, 063011, doi:10.1103/PhysRevD.87.063011, arXiv:1303.1253.

[273] P. A. Mazzali, et al. (2004). *Properties of two hypernovae entering the nebular phase: SN 1997ef and SN 1997dq*. The Astrophysical Journal, **614**, 858–863, doi:10.1086/423888, arXiv:astro-ph/0409575.

[274] C. Haack and C. Wiebusch (2018) [for the IceCube collaboration]. *A measurement of the diffuse astrophysical muon neutrino flux using eight years of IceCube data*. Proceedings of Science, **ICRC2017**, 1005, doi:10.22323/1.301.1005.

[275] C. Kopper (2018) [for the IceCube collaboration]. *Observation of Astrophysical Neutrinos in Six Years of IceCube Data*. Proceedings of Science, **ICRC2017**, 981, doi:10.22323/1.301.0981.

[276] M. Lisanti, et al. (2016). *Deciphering Contributions to the Extragalactic Gamma-Ray Background from 2 GeV to 2 TeV*. The Astrophysical Jounal, **832**, 117, doi:10.3847/0004-637X/832/2/117, arXiv:1606.04101.

[277] H.-S. Zechlin, et al. (2016). *Statistical Measurement of the Gamma-ray Source-count Distribution as a Function of Energy*. Astrophysical Journal Letters, **826**, L31, doi:10.3847/2041-8205/826/2/L31, arXiv:1605.04256.

[278] K. Murase (2017). *Active Galactic Nuclei as High-Energy Neutrino Sources*. In T. Gaisser and A. Karle (eds.), *Neutrino Astronomy: Current Status, Future Prospects*, World Scientific, 15–31, doi:10.1142/9789814759410_0002, arXiv:1511.01590.

[279] Y. Inoue, et al. (2019). *On high-energy particles in accretion disk coronae of supermassive black holes: implications for MeV gamma rays and high-energy neutrinos from AGN cores*. The Astrophysical Journal, **880**, 40, doi:10.3847/1538-4357/ab2715, arXiv:1904.00554.

[280] A. Kheirandish, K. Murase, and S. S. Kimura (2021). *High-Energy Neutrinos from Magnetized Coronae of Active Galactic Nuclei and Prospects for Identification of Seyfert Galaxies and Quasars in Neutrino Telescopes*. The Astrophysical Journal, **922**, 45, doi:10.3847/1538-4357/ac1c77, arXiv:2102.04475.

[281] G. Maggi, et al. (2016). *Obscured flat spectrum radio active galactic nuclei as sources of high-energy neutrinos*. Physical Review D, **94**, 103007, doi:10.1103/PhysRevD.94.103007, arXiv:1608.00028.

[282] G. Maggi, K. D. de Vries, and N. van Eijndhoven (2018) [for the IceCube collaboration]. *Investigation of Obscured Flat Spectrum Radio AGN with the IceCube Neutrino Observatory*. Proceedings of Science, **ICRC2017**, 1000, doi:10.22323/1.301.1000.

[283] J. Becker Tjus, et al. (2014). *High-energy neutrinos from radio galaxies*. Physical Review D, **89**, 123005, doi:10.1103/PhysRevD.89.123005, arXiv:1406.0506.

[284] L. Merten, et al. (2017). *On the non-thermal electron-to-proton ratio at cosmic ray acceleration sites*. Astroparticle Physics, **90**, 75–84, doi:10.1016/j.astropartphys.2017.02.007, arXiv:1702.07523.

[285] D. B. Sanders and I. F. Mirabel (1996). *Luminous Infrared Galaxies*. Annual Review of Astronomy and Astrophysics, **34**, 749–792, doi:10.1146/annurev.astro.34.1.749.

[286] M. Moshir, et al. (1992). *IRAS Faint Source Survey, Explanatory supplement version 2*, URL: https://ui.adsabs.harvard.edu/abs/1992ifss.book.....M.

[287] W. Saunders et al. (2000). *The PSCz catalogue*. Monthy Notices of the Royal Astronomical Society, **317**, 55, doi:10.1046/j.1365-8711.2000.03528.x, arXiv:astro-ph/0001117.

[288] C. A. Beichman et al. (1988). *Infrared Astronomical Satellite (IRAS) Catalogs and Atlases. Volume 1: Explanatory Supplement*, URL: https://ui.adsabs.harvard.edu/abs/1988iras....1.....B.

[289] J. R. Houck et al. (2004) [*Spitzer*/IRS collaboration]. *The Infrared spectrograph on the Spitzer Space Telescope*. The Astrophysical Journal Supplement Series, **154**, 18–24, doi:10.1086/423134, arXiv:astro-ph/0406167.

[290] J. Chadwick (1932). *Possible Existence of a Neutron*. Nature, **129**, 312, doi:10.1038/129312a0.

[291] E. Amaldi (1984). *From the discovery of the neutron to the discovery of nuclear fission*. Physics Reports, **111**, 1–332, doi:10.1016/0370-1573(84)90214-X.

[292] L. M. Brown (1978). *The idea of the neutrino*. Physics Today, **31**, 23, doi:10.1063/1.2995181.

[293] G. Aad et al. (2012) [ATLAS collaboration]. *Observation of a new particle in the search for the Standard Model Higgs boson with the ATLAS detector at the LHC*. Physics Letters B, **716**, 1–29, doi:10.1016/j.physletb.2012.08.020, arXiv:1207.7214.

[294] S. Chatrchyan et al. (2012) [CMS collaboration]. *Observation of a New Boson at a Mass of 125 GeV with the CMS Experiment at the LHC*. Physics Letters B, **716**, 30–61, doi:10.1016/j.physletb.2012.08.021, arXiv:1207.7235.

[295] B. P. Abbott et al. (2016) [LIGO and Virgo collaborations]. *Observation of Gravitational Waves from a Binary Black Hole Merger*. Physical Review Letters, **116**, 061102, doi:10.1103/PhysRevLett.116.061102, arXiv:1602.03837.

[296] C. L. Cowan et al. (1956). *Detection of the Free Neutrino: a Confirmation*. Science, **124**, 103–104, doi:10.1126/science.124.3212.103.

[297] F. Reines, et al. (1965). *Evidence for high-energy cosmic ray neutrino interactions*. Physical Review Letters, **15**, 429–433, doi:10.1103/PhysRevLett.15.429.

[298] C. V. Achar et al. (1965). *Detection of muons produced by cosmic ray neutrinos deep underground*. Physics Letters, **18**, 196–199, doi:10.1016/0031-9163(65)90712-2.

[299] R. Davis, Jr., D. S. Harmer, and K. C. Hoffman (1968). *Search for neutrinos from the sun*. Physical Review Letters, **20**, 1205–1209, doi:10.1103/PhysRevLett.20.1205.

[300] W. D. Arnett, et al. (1989). *Supernova SN1987A*. Annial Review of Astronomy and Astrophysics, **27**, 629–700, doi:10.1146/annurev.aa.27.090189.003213.

[301] M. A. Markov (1960). *On high-energy neutrino physics*. In E. C. Sudarshan, G. Tinlot, and A. C. Melissinos (eds.), *Proceedings of the 1960 Annual International Conference on High-Energy Physics*, University of Rochester, 578, URL: https://s3.cern.ch/inspire-prod-files-f/f515e30d1396ca1bfea09fee946b122f.

[302] A. Roberts (1992). *The birth of high-energy neutrino astronomy: A personal history of the DUMAND project*. Reviews of Modern Physics, **64**, 259, doi:10.1103/RevModPhys.64.259.

[303] F. Halzen and S. R. Klein (2008). *Astronomy and astrophysics with neutrinos*. Physics Today, **61**, 29–35, doi:10.1063/1.2930733.

[304] I. A. Belolaptikov et al. (1997) [Baikal collaboration]. *The Baikal underwater neutrino telescope: Design, performance and first results*. Astroparticle Physics, **7**, 263–282, doi:10.1016/S0927-6505(97)00022-4.

[305] R. Wischnewski et al. (2005) [Baikal collaboration]. *The Baikal Neutrino Telescope - Results and plans*. International Journal of Modern Physics A, **20**, 6932–6936, doi:10.1142/S0217751X0503051X, arXiv:astro-ph/0507698.

[306] E. Andres et al. (2000) [AMANDA collaboration]. *The AMANDA neutrino telescope: Principle of operation and first results*. Astroparticle Physics, **13**, 1–20, doi:10.1016/S0927-6505(99)00092-4, arXiv:astro-ph/9906203.

[307] R. Wischnewski (2002) [for the AMANDA collaboration]. *The AMANDA-II neutrino telescope*. Nuclear Physics B – Proceedings Supplements, **110**, 510–512, doi:10.1016/S0920-5632(02)01550-5, arXiv:astro-ph/0204268.

[308] G. Riccobene (2001). *NEMO: NEutrino Mediterranean Observatory*. In M. M. Shapiro, T. Stanev, and J. P. Wefel (eds.), *Astrophysical Sources of High Energy Particles and Radiation*, Springer Berlin Heidelberg, 355–361, doi:10.1007/978-94-010-0560-9_32.

[309] S. E. Tzamarias (2005) [for the NESTOR collaboration]. *Operation and performance of the NESTOR test detector: A measurement of the atmospheric muon flux*. Nuclear Physics B – Proceedings Supplements, **143**, 355–358, doi:10.1016/j.nuclphysbps.2005.01.129.

[310] M. Aartsen et al. (2017) [IceCube collaboration]. *The IceCube Neutrino Observatory: Instrumentation and Online Systems*. Journal of Instrumentation, **12**, P03012, doi:10.1088/1748-0221/12/03/P03012, arXiv:1612.05093.

[311] R. Abbasi et al. (2012) [IceCube collaboration]. *The Design and Performance of IceCube DeepCore*. Astroparticle Physics, **35**, 615–624, doi:10.1016/j.astropartphys.2012.01.004, arXiv:1109.6096.

[312] A. Ishihara (2021) [for the IceCube collaboration]. *The IceCube Upgrade - Design and Science Goals*. Proceedings of Science, **ICRC2019**, 1031, doi:10.22323/1.358.1031.

[313] L. Classen, A. Kappes, and T. Karg (2021) [for the IceCube collaboration]. *A multi-PMT Optical Module for the IceCube Upgrade*. Proceedings of Science, **ICRC2019**, 855, doi:10.22323/1.358.0855.

[314] A. Ishihara (2020) [for the IceCube collaboration]. *D-Egg: new optical sensors for the IceCube Upgrade and Gen2*. Journal of Physics Conference Series, **1468**, 012166, doi:10.1088/1742-6596/1468/1/012166.

[315] L. Classen, A. Kappes, and T. Karg (2022) [for the IceCube-Gen2 collaboration]. *A next-generation optical sensor for IceCube-Gen2*. Proceedings of Science, **ICRC2021**, 1062, doi:10.22323/1.395.1062.

[316] D. Hebecker et al. (2016). *A Wavelength-shifting Optical Module (WOM) for in-ice neutrino detectors*. European Physical Journal Web of Conferences, **116**, 01006, doi:10.1051/epjconf/201611601006.

[317] M. G. Aartsen et al. (2014) [IceCube collaboration]. *Energy Reconstruction Methods in the IceCube Neutrino Telescope*. Journal of Instrumentation, **9**, P03009, doi:10.1088/1748-0221/9/03/P03009, arXiv:1311.4767.

[318] B. Zhou and J. F. Beacom (2020). *W-boson and trident production in TeV–PeV neutrino observatories*. Physical Review D, **101**, 036010, doi:10.1103/PhysRevD.101.036010, arXiv:1910.10720.

[319] M. G. Aartsen et al. (2017) [IceCube]. *Measurement of the multi-TeV neutrino cross section with IceCube using Earth absorption*. Nature, **551**, 596–600, doi:10.1038/nature24459, arXiv:1711.08119.

[320] R. Abbasi et al. (2020) [IceCube collaboration]. *Measurement of the high-energy all-flavor neutrino-nucleon cross section with IceCube*. Physical Review D, **104**, 022001, doi:10.1103/PhysRevD.104.022001, arXiv:2011.03560.

[321] F. Mandl and G. Shaw (2010). *Quantum Field Theory*, 2$^{\text{nd}}$ edition, John Wiley and Sons, ISBN 978-0-47-149684-7.

[322] S. L. Glashow (1960). *Resonant Scattering of Antineutrinos*. Physical Review, **118**, 316–317, doi:10.1103/PhysRev.118.316.

[323] M. F. L'Annunziata (2012). *Cherenkov Counting*. In M. F. L'Annunziata (ed.), *Handbook of Radioactivity Analysis*, Elsevier, 935–1019, doi:10.1016/C2009-0-64509-8.

[324] P. A. Cherenkov (1934). *Visible light from clear liquids under the actrion of gamma radiation*. Proceedings of the USSR Academy of Sciences, **2**, 451–454, doi:10.3367/UFNr.0093.196710n.0385.

[325] P. A. Cherenkov (1937). *Visible Radiation Produced by Electrons Moving in a Medium with Veolocities Exceeding that of Light*. Physical Review, **52**, 378, doi:10.1103/PhysRev.52.378.

[326] P. B. Price and D. C. Woschnagg (2000). *Role of group and phase velocity in High-Energy Neutrino Observatories*. Astroparticle Physics, **15**, 97–100, doi:10.1016/S0927-6505(00)00142-0, arXiv:arXiv:hep-ex/0008001.

[327] J. Ahrens et al. (2004) [AMANDA collaboration]. *Muon track reconstruction and data selection techniques in AMANDA*. Nuclear Instruments and Methods in Physics Research A, **524**, 169–194, doi:10.1016/j.nima.2004.01.065, arXiv:astro-ph/0407044.

[328] E. Branger et al. (2017). *On Cherenkov light production by irradiated nuclear fuel rods*. Journal of Instrumentation, **12**, T06001, doi:10.1088/1748-0221/12/06/T06001.

[329] P. Askebjer et al. (1997). *Optical properties of deep ice at the South Pole: Absorption*. Applied Optics, **36**, 4168–4180, doi:10.1364/AO.36.004168, arXiv:physics/9701025.

[330] M. Ackermann et al. (2006) [AMANDA collaboration]. *Optical properties of deep glacial ice at the South Pole*. Journal of Geophysical Research, **111**, D13203, doi:10.1029/2005JD006687.

[331] P. B. Price and L. Bergström (1997). *Optical properties of deep ice at the South Pole: Scattering*. Applied Optics, **36**, 4181–4194, doi:10.1364/AO.36.004181.

[332] N. E. Bramall et al. (2005). *A deep high-resolution optical log of dust, ash, and stratigraphy in South Pole glacial ice*. Geophysical Research Letters, **32**, L21815, doi:10.1029/2005GL024236.

[333] P. B. Price and D. C. Woschnagg (2000). *Age vs depth of glacial ice at South Pole*. Geophysical Research Letters, **27**, 2129–2132, doi:10.1029/2000GL011351.

[334] M. G. Aartsen et al. (2013) [IceCube collaboration]. *Measurement of South Pole ice transparency with the IceCube LED calibration system*. Nuclear Instruments and Methods in Physics Research A, **711**, 73–89, doi:10.1016/j.nima.2013.01.054, arXiv:1301.5361.

[335] D. Chirkin (2014) [for the IceCube collaboration]. *Evidence of optical anisotropy of the South Pole ice*. Brazilian Journal of Physics, **44**, 0580, arXiv:1309.7010.

[336] D. Chirkin and M. Rongen (2021) [for the IceCube collaboration]. *Light diffusion in birefringent polycristals and the IceCube ice anisotropy*. Proceedings of Science, **ICRC2019**, 854, doi:10.22323/1.358.0854.

[337] R. Abbasi et al. (2010) [IceCube collaboration]. *Calibration and Characterization of the IceCube Photomultiplier Tube*. Nuclear Instruments and Methods in Physics Research A, **618**, 139–152, doi:10.1016/j.nima.2010.03.102, arXiv:1002.2442.

[338] R. Abbasi et al. (2009) [IceCube collaboration]. *The IceCube Data Acquisition System: Signal Capture, Digitization, and Timestamping*. Nuclear Instruments and Methods in Physics Research A, **601**, 294–316, doi:10.1016/j.nima.2009.01.001, arXiv:0810.4930.

[339] T. Benson et al. (2014). *IceCube Enhanced Hot Water Drill functional description*. Annals of Glaciology, **55**, 105–114, doi:10.3189/2014AoG68A032.

[340] T. Kintscher (2020). *Rapid Response to Extraordinary Events: Transient Neutrino Sources with the IceCube Experiment*. PhD thesis, Humbholdt University of Berlin, doi:10.18452/21948.

[341] L. Radel and C. Wiebusch (2013). *Calculation of the Cherenkov light yield from electromagnetic cascades in ice with Geant4*. Astroparticle Physics, **44**, 102–113, doi:10.1016/j.astropartphys.2013.01.015, arXiv:1210.5140.

[342] L. Wille and D. Xu (2021) [for the IceCube collaboration]. *Astrophysical Tau Neutrino Identification with IceCube Waveforms*. Proceedings of Science, **ICRC2019**, 1036, doi:10.22323/1.358.1036.

[343] M. G. Aartsen et al. (2016) [IceCube collaboration]. *Characterization of the Atmospheric Muon Flux in IceCube*. Astroparticle Physics, **78**, 1–27, doi:10.1016/j.astropartphys.2016.01.006, arXiv:1506.07981.

[344] R. Abbasi et al. (2011) [IceCube collaboration]. *Measurement of the atmospheric neutrino energy spectrum from 100 GeV to 400 TeV with IceCube*. Physical Review D, **83**, 012001, doi:10.1103/PhysRevD.83.012001, arXiv:1010.3980.

[345] M. G. Aartsen et al. (2015) [IceCube collaboration]. *Measurement of the Atmospheric ν_e Spectrum with IceCube*. Physical Review D, **91**, 122004, doi:10.1103/PhysRevD.91.122004, arXiv:1504.03753.

[346] A. Gazizov and M. P. Kowalski (2005). *ANIS: High energy neutrino generator for neutrino telescopes*. Computer Physics Communications, **172**, 203–213, doi:10.1016/j.cpc.2005.03.113, arXiv:astro-ph/0406439.

[347] M. Usner (2018). *Search for Astrophysical Tau-Neutrinos in Six Years of High-Energy Starting Events in the IceCube Detector*. PhD thesis, Humbholdt University of Berlin, doi:10.18452/19458.

[348] D. A. Chirkin (2003). *Cosmic ray energy spectrum measurement with the Antarctic Muon and Neutrino Detector Array (AMANDA)*. PhD thesis, University of California, Berkeley, URL: https://www.proquest.com/docview/305338997.

[349] D. Chirkin and W. Rhode (2004). *Propagating leptons through matter with Muon Monte Carlo (MMC)*, arXiv:hep-ph/0407075.

[350] J. H. Koehne, et al. (2013). *PROPOSAL: A tool for propagation of charged leptons*. Computer Physics Communications, **184**, 2070–2090, doi:10.1016/j.cpc.2013.04.001.

[351] M. G. Aartsen et al. (2014). *Improvement in Fast Particle Track Reconstruction with Robust Statistics*. Nuclear Instruments and Methods in Physics Research A, **736**, 143–149, doi:10.1016/j.nima.2013.10.074, arXiv:1308.5501.

[352] P. J. Huber (1964). *Robust Estimation of a Location Parameter*. Annals of Statistics, **53**, 73–101, doi:10.1214/aoms/1177703732.

[353] D. Pandel (1996). *Bestimmung von Wasser- und Detektorparametern und Rekonstruktion von Myonen bis 100 TeV mit dem Baikal-Neutrinoteleskop NT-72*. MSc thesis, Humbholdt University of Berlin, URL: https://docushare.wipac.wisc.edu/dsweb/Get/Rendition-128757/pandel-diplom.ps.gz.

[354] N. van Eijndhoven, O. Fadiran, and G. Japaridze (2007). *Implementation of a Gauss convoluted Pandel PDF for track reconstruction in Neutrino Telescopes*. Astroparticle Physics, **28**, 456–462, doi:10.1016/j.astropartphys.2007.09.001, arXiv:0704.1706.

[355] J. Lundberg, et al. (2007). *Light tracking for glaciers and oceans: Scattering and absorption in heterogeneous media with Photonics*. Nuclear Instruments and Methods in Physics Research A, **581**, 619–631, doi:10.1016/j.nima.2007.07.143, arXiv:astro-ph/0702108.

[356] N. Whitehorn, J. van Santen, and S. Lafebre (2013). *Penalized Splines for Smooth Representation of High-dimensional Monte Carlo Datasets*. Computer Physics Communications, **184**, 2214–2220, doi:10.1016/j.cpc.2013.04.008, arXiv:1301.2184.

[357] K. Schatto (2014). *Stacked searches for high-energy neutrinos from blazars with IceCube*. PhD thesis, Mainz University, doi:10.25358/openscience-2897.

[358] R. Abbasi et al. (2021) [IceCube collaboration]. *A muon-track reconstruction exploiting stochastic losses for large-scale Cherenkov detectors*. Journal of Instrumentation, **16**, P08034, doi:10.1088/1748-0221/16/08/P08034, arXiv:2103.16931.

[359] R. A. Fisher (1922). *On the mathematical foundations of theoretical statistics*. Philosophical Transactions of the Royal Society of London A, **222**, 309–368, doi:10.1098/rsta.1922.0009.

[360] H. Cramér (1999). *Mathematical Methods of Statistics (PMS-9), Volume 9*, 1st edition, Princeton University Press.

[361] C. R. Rao (1945). *Information and the accuracy attainable in the estimation of statistical parameters*. Bulletin of Calcutta Mathematical Society, **37**, 81–89.

[362] M. Richman (2015). *A Search for Muon Neutrinos coincident with Northern Gamma-Ray Bursts using IceCube*. PhD thesis, University of Maryland, doi:10.13016/M2CS5W.

[363] J. Lünemann (2014). *Suche nach Dunkler Materie in Galaxien und Galaxienhaufen mit dem Neutrinoteleskop IceCube*. PhD thesis, Mainz University, doi:10.25358/openscience-4219.

[364] T. Neunhöffer (2003). *Die Entwicklung eines neuen Verfahrens zur Suche nach kosmischen Neutrino-Punktquellen mit dem AMANDA-Neutrinoteleskop*. PhD thesis, Mainz University, doi:10.25358/openscience-2482.

[365] T. Neunhöffer (2006). *Estimating the angular resolution of tracks in neutrino telescopes based on a likelihood analysis*. Astroparticle Physics, **25**, 220–225, doi:10.1016/j.astropartphys.2006.01.002, arXiv:astro-ph/0403367.

[366] B. Efron (1979). *Bootstrap Methods: Another Look at the Jackknife*. The Annals of Statistics, **7**, 1–26.

[367] S. Grullon et al. (2008) [for the IceCube collaboration]. *Reconstruction of high energy muon events in IceCube using waveforms*. In R. Caballero et al. (eds.), *Proceedings of the 30th International Cosmic Ray Conference*, Universidad Nacional Autónoma de México, 1457–1460, URL: https://indico.nucleares.unam.mx/event/4/contributions.

[368] J. d. D. Zornoza and D. Chirkin (2008) [for the IceCube collaboration]. *Muon energy reconstruction and atmospheric neutrino spectrum unfolding with the IceCube detector*. In R. Caballero et al. (eds.), *Proceedings of the 30th International Cosmic Ray Conference*, Universidad Nacional Autónoma de México, 1275–1278, arXiv:0711.0353.

[369] D. Chirkin (2013). *Photon tracking with GPUs in IceCube*. Nuclear Instruments and Methods in Physics Research A, **725**, 141–143, doi:10.1016/j.nima.2012.11.170.

[370] R. Franke, E. Bernardini, and D. Góra (2014) [for the IceCube collaboration]. *High-Energy Gamma-Ray Follow-Up Program Using Neutrino Triggers from IceCube*. In A. Saa (ed.), *Proceedings, 33rd International Cosmic Ray Conference (ICRC 2013)*, Brazilian Journal of Physics, **4**, 415–608, URL: https://inspirehep.net/literature/1412973.

[371] M. Voge (2016). *Searches for Neutrinos from Supernovae Using Cherenkov In-Ice Detectors*. PhD thesis, University of Bonn, URL: hdl.handle.net/20.500.11811/7138.

[372] L. Breiman et al. (1984). *Classification and Regression Trees*, 1st edition, Routledge, ISBN 978-1-31-513947-0, doi:10.1201/9781315139470.

[373] T. Kintscher (2017). *A GFU Sample from Pass2*. Online, accessed 26 May 2022, URL: https://docushare.icecube.wisc.edu/dsweb/Get/Document-81337/2017-09-11%20-%20Muon%20Call%20-%20MuEx.pdf.

[374] F. James (2006). *Statistical Methods in Experimental Physics*, 2nd edition, World Scientific Publishing, ISBN 978-9-81-310184-5, doi:10.1142/6096.

[375] A. Agresti and C. Franklin (2009). *Statistics: The Art and Science of Learning from Data*, 2nd edition, Pearson Education, ISBN 978-0-13-135746-4.

[376] D. Bose et al. (2013). *Bayesian approach for counting experiment statistics applied to a neutrino point source analysis*. Astroparticle Physics, **50–52**, 57–64, doi:10.1016/j.astropartphys.2013.09.009, arXiv:1212.2008.

[377] S. S. Wilks (1938). *The Large-Sample Distribution of the Likelihood Ratio for Testing Composite Hypotheses*. Annals of Mathematical Statistics, **9**, 60–62, doi:10.1214/aoms/1177732360.

[378] J. Neyman and E. S. Pearson (1933). *On the problem of the most efficient tests of statistical hypotheses*. Philosophical Transactions of the Royal Society of London A, **231**, 289–337, doi:10.1098/rsta.1933.0009.

[379] J. Braun, et al. (2008). *Methods for point source analysis in high energy neutrino telescopes*. Astroparticle Physics, **29**, 299–305, doi:10.1016/j.astropartphys.2008.02.007, arXiv:0801.1604.

[380] A. Poluektov (2015). *Kernel density estimation of a multidimensional efficiency profile*. Journal of Instrumentation, **10**, P02011, doi:10.1088/1748-0221/10/02/P02011, arXiv:1411.5528.

[381] C. Boscolo Meneguolo (2021). *GFU Dataset – Approval Request*. Online, accessed 26 May 2022, URL: https://drive.google.com/file/d/1WIfOKibjf86-IbpMMHvnSs8uvgTyyXMY/view?usp=sharing.

[382] A. Achterberg et al. (2006) [IceCube collaboration]. *On the selection of AGN neutrino source candidates for a source stacking analysis with neutrino telescopes*. Astroparticle Physics, **26**, 282–300, doi:10.1016/j.astropartphys.2006.06.012, arXiv:astro-ph/0609534.

[383] M. G. Aartsen et al. (2020) [IceCube collaboration]. *IceCube Search for High-Energy Neutrino Emission from TeV Pulsar Wind Nebulae*. The Astrophysical Journal, **898**, 117, doi:10.3847/1538-4357/ab9fa0, arXiv:2003.12071.

[384] P. Correa (2017). *Comparison of Statistical Methods in order to Evaluate the IceCube Discovery Potential for Steady Point Sources*. MSc thesis, Vrije Universiteit Brussel, URL: https://iihe.ac.be/research/theses.

[385] L. Brayeur (2015). *Search for High-Energy Neutrinos Associated with Long Gamma Ray Bursts using the IceCube Detector*. PhD thesis, Vrije Universiteit Brussel, URL: https://iihe.ac.be/research/theses.

[386] F. Bradascio (2020). *n_s bias for large catalogues while searching for neutrinos from AGN cores*. Online, accessed 30 June 2022, URL: https://drive.google.com/file/d/1MY5A-nI3fZrEy_H62m9-sKK40I_Ype2W/view.

[387] R. Reimann (2019). *Search for the sources of the astrophysical high-energy muon-neutrino flux with the IceCube neutrino observatory*. PhD thesis, RWTH Aachen University, URL: http://publications.rwth-aachen.de/record/773297.

[388] M. Wolf (2021) [for the IceCube collaboration]. *SkyLLH – A generalized Python-based tool for log-likelihood analyses in multi-messenger astronomy*. Proceedings of Science, **ICRC2019**, 1035, doi:10.22323/1.358.1035.

[389] J. Neyman (1937). *Outline of a Theory of Statistical Estimation Based on the Classical Theory of Probability*. Philosophical Transactions of the Royal Society A, **236**, 333–380, doi:10.1098/rsta.1937.0005.

[390] J. F. Kenney and E. S. Keeping (1962). *Mathematics of Statistics: Volume 1*, 3rd edition, Van Nostrand.

[391] G. J. Feldman and R. D. Cousins (1998). *A unified approach to the classical statistical analysis of small signals*. Physical Review D, **57**, 3873–3889, doi:10.1103/PhysRevD.57.3873, arXiv:physics/9711021.

[392] M. G. Aartsen et al. (2017) [IceCube collaboration]. *All-sky Search for Time-integrated Neutrino Emission from Astrophysical Sources with 7 yr of IceCube Data*. The Astrophysical Journal, **835**, 151, doi:10.3847/1538-4357/835/2/151, arXiv:1609.04981.

[393] E. V. Bugaev and Y. V. Shlepin (2003). *Photonuclear interaction of high-energy muons and tau leptons*. Physical Review D, **67**, 034027, doi:10.1103/PhysRevD.67.034027, arXiv:hep-ph/0203096.

[394] E. A. Friedman (2021). *All-Sky Search for Neutrinos Correlated with Gamma-Ray Bursts in Extended Time Windows Using Eight Years of IceCube Data*. PhD thesis, University of Maryland, doi:10.13016/yqa1-0vmh.

[395] Y. Merckx (2022). *Luminous infrared galaxies with the Great Observatory All-Sky LIRG Survey (GOALS)*. Online, accessed 30 June 2022, URL: https://drive.google.com/file/d/1xJZJa4FpUlJ12KJuN-UrnD5ykFeqZ3qI/view.

[396] S. Goswami, G. C. Privon, and M. Santander (2021) [for the IceCube collaboration]. *Search for high-energy neutrino emission from hard X-ray AGN with IceCube*. Proceedings of Science, **ICRC2021**, 1142, doi:10.22323/1.395.1142.

[397] M. Un Nisa and A. Ludwig (2021) [for the IceCube collaboration]. *A time-independent search for neutrinos from galaxy clusters with IceCube*. Proceedings of Science, **ICRC2021**, 1133, doi:10.22323/1.395.1133.

[398] Y. Merckx (2019). *Determining dust properties in X-ray obscured galaxies through infrared emission*. BSc thesis, Vrije Universiteit Brussel, URL: https://drive.google.com/file/d/1-ofyFH6-omJ_bR5QLyjt3w6qdtBwrEIk/view.

[399] T. Aerts (2020). *Neutrino production via beam dumps in ultra-luminous infrared galaxies*. BSc thesis, Vrije Universiteit Brussel, URL: https://drive.google.com/file/d/13eItLuXNkJnMSL37GNRY9NoelmXVWTym/view.

[400] J. Butterworth (2016). *The Standard Model: How far can it go and how can we tell?* Philosophical Transactions of the Royal Society A, **374**, 20150260, doi:10.1098/rsta.2015.0260, arXiv:1601.02759.

[401] D. Griffiths (2008). *Introduction to Elementary Particles*, 2nd revised edition, WILEY-VCH, ISBN 978-3-52-740601-2.

[402] M. Thomson (2013). *Modern Particle Physics*, 1st edition, Cambridge University Press, ISBN 978-1-10-703426-6.

[403] Wikipedia (The Free Encyclopedia). *Standard Model*. Online, accessed 18 June 2022, URL: https://en.wikipedia.org/wiki/Standard_Model.